

# **Modeling the random walk and chemotaxis of bacteria: Aspects of biofilm formation**

vorgelegt von  
Diplom-Physiker

**Johannes Taktikos**  
geboren in Detmold

Von der Fakultät II - Mathematik und Naturwissenschaften  
der Technischen Universität Berlin  
zur Erlangung des akademischen Grades  
*Doktor der Naturwissenschaften (Dr. rer. nat.)*  
genehmigte Dissertation

Promotionsausschuss:

Vorsitzender: Prof. Dr. Martin Schoen  
Erster Gutachter: Prof. Dr. Holger Stark  
Zweiter Gutachter: Dr. Vasily Zaburdaev  
Externer Gutachter: Prof. Dr. Carsten Beta

Tag der wissenschaftlichen Aussprache: 17.10.2012  
Berlin 2013  
D 83



# Contents

<b>1</b>	<b>Introduction</b>	<b>1</b>
<b>2</b>	<b>Active particles and random walks</b>	<b>5</b>
2.1	Brownian motion . . . . .	5
2.1.1	Langevin equation . . . . .	5
2.1.2	Fokker-Planck equation . . . . .	7
2.2	Microorganisms as overdamped particles . . . . .	10
2.3	Active particles . . . . .	13
2.3.1	Rotational diffusion of the velocity direction . . . . .	15
2.3.2	Rotational diffusion with constant drift . . . . .	18
2.3.3	Simple run-and-tumble dynamics . . . . .	19
2.4	Chemotaxis . . . . .	21
2.4.1	Keller-Segel approach . . . . .	23
2.4.2	Chemotactic collapse . . . . .	26
<b>3</b>	<b>Swimming strategies of bacteria</b>	<b>29</b>
3.1	Introduction . . . . .	29
3.1.1	Run-and-tumble strategy ( <i>E. coli</i> ) . . . . .	29
3.1.2	Run-reverse strategy . . . . .	31
3.1.3	Run-reverse-flick strategy ( <i>V. alginolyticus</i> ) . . . . .	32
3.1.4	Outline of the chapter . . . . .	33
3.2	Diffusion coefficient for a random walk with two alternating tumbling events . . . . .	34
3.2.1	Without rotational diffusion . . . . .	35
3.2.2	Rotational diffusion included . . . . .	40
3.2.3	Discussion . . . . .	42
3.3	Chemotactic drift speed . . . . .	44
3.3.1	For <i>E. coli</i> . . . . .	44
3.3.2	For <i>V. alginolyticus</i> . . . . .	47
3.3.3	Comparison: <i>E. coli</i> versus <i>V. alginolyticus</i> . . . . .	49
3.3.4	Derivation of the chemotactic drift speed for the run-tumble-flick strategy . . . . .	50
3.3.5	Different approaches for the tumbling rate . . . . .	53

3.4	Mean run times in a chemical gradient . . . . .	56
3.4.1	For <i>E. coli</i> . . . . .	57
3.4.2	For <i>V. alginolyticus</i> . . . . .	59
3.5	Summary . . . . .	60
<b>4</b>	<b>Modeling an autochemotactic active walker</b>	<b>63</b>
4.1	Introduction . . . . .	63
4.2	Model of the autochemotactic walker . . . . .	65
4.2.1	Dynamic equation for the velocity direction . . . . .	65
4.2.2	Constant chemotactic field . . . . .	68
4.2.3	Chemotactic field of the autochemotactic walker . . . . .	70
4.3	Diffusion coefficient of the autochemotactic walker . . . . .	72
4.3.1	Weak chemotactic coupling . . . . .	72
4.3.2	Strong chemotactic coupling . . . . .	75
4.3.3	Comparison of analytical and numerical results . . . . .	79
4.4	Summary . . . . .	83
<b>5</b>	<b>Collective dynamics of autochemotactic active walkers</b>	<b>85</b>
5.1	Introduction . . . . .	85
5.2	The model . . . . .	86
5.2.1	Autochemotactic active walkers . . . . .	86
5.2.2	Collisions of autochemotactic walkers . . . . .	88
5.2.3	Rescaled units and simulation parameters . . . . .	91
5.3	Analysis of the two-walker system . . . . .	92
5.3.1	Typical trajectories . . . . .	93
5.3.2	State diagram . . . . .	96
5.3.3	Mean life time . . . . .	98
5.4	Properties of a many-walker system . . . . .	100
5.4.1	State diagram and cluster stability . . . . .	101
5.4.2	Relaxation dynamics of stable clusters . . . . .	101
5.4.3	Microcolonies merge into a central cluster . . . . .	105
5.4.4	Microorganisms in confined geometry with fixed area fraction	107
5.5	Summary . . . . .	109
5.6	Appendix I. Probability for a particle distance below a given value .	110
5.7	Appendix II. Radius of gyration for hexagonal closest packing .	111
<b>6</b>	<b>Kinetic equation for autochemotactic walkers</b>	<b>115</b>
6.1	Kinetic equation . . . . .	115
6.2	Derivation of the kinetic equation . . . . .	117
6.3	Mean-field approximation and discussion . . . . .	118
6.4	Conclusion and outlook . . . . .	120

<b>7 Pili-induced clustering of <i>N. gonorrhoeae</i> bacteria</b>	<b>121</b>
7.1 Basics about gonococci and type IV pili . . . . .	121
7.2 Experimental setup and results . . . . .	122
7.2.1 Clustering dynamics . . . . .	123
7.2.2 Image analysis . . . . .	125
7.3 Modeling of “pili-taxis” . . . . .	126
7.3.1 Diffusion coefficient as a function of cluster size . . . . .	126
7.3.2 Cell growth . . . . .	128
7.3.3 Merging rule for pili-mediated interaction . . . . .	128
7.4 Comparison of experimental and numerical results . . . . .	130
7.5 Summary . . . . .	132
7.6 Appendix: A different model for pili-mediated cluster interaction . .	133
<b>8 Conclusions</b>	<b>135</b>
<b>List of Publications</b>	<b>139</b>
<b>Bibliography</b>	<b>140</b>
<b>Acknowledgments</b>	<b>157</b>
<b>Zusammenfassung in deutscher Sprache</b>	<b>159</b>



# 1 Introduction

A bacterial biofilm is an aggregation of bacteria encased in self-produced polymer matrix that forms on surfaces [1, 2]. One encounters a large variety of biofilms in nature and daily life, ranging from attached bacteria in fresh water pipes, to pathogens in medical devices, and dental plaques. In general, one can classify biofilms into the categories of beneficial and harmful. Examples of the latter category illustrate why much effort of biofilm research is devoted to developing strategies to prevent or control the formation of biofilms: Bacterial biofilms that form in water pipes contaminate drinking water. The bacterium *Pseudomonas aeruginosa* forms biofilms in medical devices such as catheters; it is a dangerous pathogen that may cause lethal pneumonia and is responsible for hospital-acquired infections [3]. Another example of unwanted biofilms is plaque on teeth, which results in dental caries. In contrast, one also finds situations where the bacteria of a biofilm perform a useful job: Acting as a natural sewage plant, certain bacteria can clean water by digesting toxic substances. This process is a paradigm for the efficiency of bioremediation, where bacteria destroy pollutants in their natural environment [4].

Although these examples just represent a tiny part of ubiquitous biofilms, they indicate that a thorough understanding of biofilms is necessary to solve problems related to biofilms in industrial applications, engineering, and daily life. In addition, scientific research has significantly increased over the past decades because of fundamental interest in this challenging topic at the interface of biology, chemistry, pharmacology, and physics [5].

The aim of this thesis is to elucidate selected aspects of the early stages of biofilm formation with tools of statistical physics. On that account, we briefly discuss essential features of biofilms in the following. A major constituent of a bacterial biofilm are bacteria; however, bacteria contribute for less than 10% of the total mass of most biofilms. The remaining mass stems from extracellular polymeric substances (EPS), also characterized as the “dark matter of the biofilm”, which mediate interactions among the bacteria themselves and with the colonized surface [6]. It is known that this slimy matrix of hydrated biopolymers forms a protecting barrier for bacteria living within a biofilm. This barrier is one of the reasons why many antibiotics have little success in destroying or dissolving stable biofilms, as the antibiotics are mechanically and chemically hindered to approach the bacteria [7]. Another protection factor for bacteria in a biofilm is the reduction of their metabolic activity.

An important question in biofilm research deals with intra- and intercellular mechanisms, which make a biofilm a robust multicellular organism that can survive under

extreme conditions. A possible means for communication between individuals is the exchange of diffusing chemical substances. Different types of bacterial signaling comprise chemotaxis, chemokinesis, and quorum sensing. Whereas chemotaxis denotes the directed motion of cells towards regions of high or low concentration of a certain chemical, in chemokinesis the chemical stimulus alters only the speed of cells [8]. Quorum sensing triggers physiological activities, such as motility, virulence, or biofilm formation, via gene expression if the bacterial density exceeds a threshold value [9].

The formation of a biofilm is a complex dynamical process. According to the literature, one usually separates the formation of a biofilm into four distinct phases: Surface attachment, cell proliferation, matrix production, and detachment, to be discussed below [7]. Initially, bacteria are in the so-called planktonic state and freely swim in the vicinity of a surface, until they settle down and attach to the surface. To swim most bacteria have thin and long appendages on their cell body, called flagella, which rotate and thereby push the cell forward.

Once attached to a surface, bacteria respond to the new environment and change their phenotype, *e.g.* by developing a different sort of motility [2]. Special cell appendages, type IV pili, are grown that provide a form of bacterial motility, called “twitching”. According to Bradley’s extraction model, a single pilus is thrown like an anchor, attaches to the surface, and by retraction pulls the cell forward [10, 11]. During colonization bacteria agglomerate on the surface into microcolonies. After the production of extracellular polymeric substances has started, the full three-dimensional biofilm grows. In general, a single natural biofilm consists of different bacterial species; when encountering unfavorable conditions, some bacteria may detach from the biofilm and search for better living conditions.

A vivid picture for biofilms is given by Watnick and Kolter in their review “Biofilm, city of microbes” [12], where the authors compare the formation of a biofilm to the colonization of a city by humans. In both “societies”, the overall driving force which determines where to live, in which neighborhood to settle down, and how to arrange with other individuals, is to find and guarantee optimal living conditions.

There are already models of biofilm growth that contain a large number of parameters to incorporate known details from biology and chemistry [13, 14]. However, these models are usually only solved numerically due to their complexity. In this thesis, we pursue a different approach and consider the formation of biofilms as a motivation to construct minimal models of idealized microorganisms, where we concentrate on physical principles and neglect biochemical details. We set our focus on the random walks of swimming bacteria, model chemotactic signaling between cells, and try to understand the pilus-mediated formation of bacterial microcolonies.

This work is mainly theoretical, except for Chapter 7. Our results are obtained by analytical as well as by numerical methods. In the following, we briefly summarize the contents of each chapter.

- 
- Chapter 2** In Chapter 2, we introduce basic concepts of statistical physics, which are fundamental throughout this thesis. After discussing Brownian motion in terms of Langevin and Fokker-Planck equations, we comment on the locomotion of microorganisms at the micrometer scale, where friction fully dominates inertia. We present the concept of active particles that have an intrinsic propulsion mechanism and serve as an idealization of moving biological entities, such as bacteria, amoebae or other cells. As the motion of microorganisms contains stochastic contributions, one includes noise into the dynamical equations. Particles subject to stochastic forces or torques perform random walks in space and diffuse for large times. Finally, we give a short introduction to chemotaxis, which is universal for most microorganisms. If a cell is exposed to a chemical gradient, it biases its random walk and moves along or against the gradient. In particular, we present the classical approach by Keller and Segel for the time evolution of the cell density of chemotactic microorganisms.
- Chapter 3** Before the biofilm formation starts with the surface recruitment of cells, planktonic bacteria are freely swimming. In Chapter 3, we discuss different swimming strategies of bacteria. While the well-known motion of the enteric bacterium *Escherichia coli* is described by “run-and-tumble” dynamics, the marine bacterium *Vibrio alginolyticus* adopts the “run-reverse-flick” strategy; besides, the majority of bacteria in the oceans swims in a “run-reverse” mode. We describe these swimming patterns as a generalized random walk, and calculate the diffusion coefficient and the chemotactic drift velocity with which the cells move along a chemical gradient. A large diffusion coefficient indicates that cells effectively explore their environment; a large chemotactic drift speed is beneficial for the cells, as it allows them to quickly approach nutrient sources.
- Chapter 4** In Chapter 4, we propose a model for the dynamics of a microorganism that aligns its direction of motion to the gradient of a self-generated chemical field. The microorganism is modeled as an active particle with constant speed whose velocity direction diffuses on the unit circle. We study the autochemotactic response of the active walker and show that its long-time dynamics is always diffusive. For the diffusion coefficient we analytically derive approximations, which agree well with our results from numerical simulations.

- Chapter 5** In Chapter 5, we study the collective dynamics of an ensemble of autochemotactic walkers, which communicate via chemotactic signaling. To account for the size of a cell, each microorganism is treated as a soft disk. Its velocity is modified when it overlaps with other walkers according to a linear force-velocity relation and a harmonic repulsion force. We analyze two-walker collisions by presenting typical trajectories and determine a state diagram that distinguishes between free walker, metastable, and bound cluster states. Finally, we investigate relevant properties of many-walker systems and describe characteristics of cluster formation in unbounded geometry and in confinement.
- Chapter 6** Whereas the model for the autochemotactic walkers in Chapter 5 is formulated in terms of Langevin equations for each individual, in Chapter 6 we introduce an equivalent probabilistic description. We consider an ensemble of autochemotactic point particles for which we derive a kinetic equation and perform a mean-field approximation of the model. Note that the chapters 4, 5, and 6 are closely related and constitute a coherent unit.
- Chapter 7** In Chapter 7, we present our experimental results for the bacterium *Neisseria gonorrhoeae*, the etiological agent of gonorrhea. We study the surface attachment of *N. gonorrhoeae* cells, which is mediated by their filamentous appendages of type IV pili. Cells that are initially dispersed on a surface agglomerate into spherical microcolonies within hours. Our analysis, supported by results from our model for pili-induced cell aggregation, suggests that the clustering is driven entirely by the interaction of pili without additional chemotactic signaling.
- Chapter 8** We give a summary of our work and an outlook in Chapter 8.

# 2 Active particles and random walks

In this chapter, we summarize the essential concepts from statistical physics, which will be applied in this thesis. In Sec. 2.1, we give a short introduction to Brownian motion and diffusion in the framework of Langevin, Fokker-Planck and Smoluchowski equations. We show in Secs. 2.2 and 2.3 how these tools, originally derived for colloids in thermal equilibrium, have been generalized to active particles out of equilibrium. In particular, we focus on the motion of microorganisms, which we mimic as particles with constant speed and rotational diffusion of the velocity direction. Finally, we present basics about chemotaxis in Sec. 2.4 and demonstrate the Keller-Segel approach as a classical model for chemotaxis; for illustration, we motivate the model and explain the chemotactic collapse as an interesting property.

## 2.1 Brownian motion

### 2.1.1 Langevin equation

Brownian motion describes the random motion of a small colloidal particle in a bath of much smaller fluid particles [15]. The characteristic size of a colloid ranges from several nanometers up to micrometers. Due to the collisions with the fluid particles, the Brownian particle of mass  $m$  experiences a Stokes friction force  $-\gamma\mathbf{v}$  that is proportional to its velocity  $\mathbf{v}$  with a constant friction coefficient  $\gamma > 0$ . For instance, one has  $\gamma = 6\pi\eta a$  for a sphere of radius  $a$  in a medium of viscosity  $\eta$ . Furthermore, to account for the random collisions with the surrounding fluid particles, one effectively introduces a stochastic force  $\boldsymbol{\Gamma}(t)$ . Without additional external forces on the particle, Newton's equations of motion for the position  $\mathbf{r}(t)$  of the colloid read

$$\frac{d}{dt}\mathbf{r}(t) = \mathbf{v} \quad \text{and} \quad m \frac{d}{dt}\mathbf{v}(t) = -\gamma\mathbf{v} + \sqrt{2q}\boldsymbol{\Gamma}(t). \quad (2.1)$$

Whereas the first equation simply defines velocity  $\mathbf{v}(t)$ , the second is called the Langevin equation of Brownian motion. We will determine the noise strength  $q > 0$  below, and the Cartesian components of  $\boldsymbol{\Gamma}(t)$  are independent sources of Gaussian white noise that satisfy

$$\langle \Gamma_i(t) \rangle = 0, \quad \langle \Gamma_i(t)\Gamma_j(t') \rangle = \delta_{ij}\delta(t-t'), \quad (2.2)$$

where the brackets  $\langle \dots \rangle$  denote an ensemble average over many realizations of the stochastic process. The vanishing mean indicates that the stochastic force is

isotropic on average; according to the second moment, the force is “delta-correlated” and the force correlation at different times is thus zero. The assumption of a Gaussian distribution for the noise is motivated by the central limit theorem [16]; it states that the sum of a large number of independent random variables with finite variance is a Gaussian distributed variable.

To determine the noise strength  $q$ , we employ the equipartition theorem for systems in equilibrium at temperature  $T$ ,

$$\frac{m}{2} \langle \mathbf{v}^2 \rangle = d \frac{k_B T}{2}, \quad (2.3)$$

where  $d$  is the number of spatial dimensions and  $k_B$  denotes the Boltzmann constant. Introducing the time constant  $\tau_v = m/\gamma$ , we obtain the particle velocity  $\mathbf{v}(t)$  by integrating Eq. (2.1) as

$$\mathbf{v}(t) = e^{-t/\tau_v} \left( \mathbf{v}_0 + \frac{\sqrt{2q}}{m} \int_0^t dt' \mathbf{\Gamma}(t') e^{t'/\tau_v} \right). \quad (2.4)$$

The ensemble average  $\langle \mathbf{v}(t) \rangle = \mathbf{v}_0 \exp(-t/\tau_v)$  reveals that the mean velocity exponentially decays to zero on the time scale  $\tau_v$ . From Eq. (2.4), we calculate the velocity correlation function using Eq. (2.2):

$$\langle \mathbf{v}(t) \cdot \mathbf{v}(t') \rangle = \mathbf{v}_0^2 e^{-(t+t')/\tau_v} + \frac{dq}{\gamma m} (e^{-|t-t'|/\tau_v} - e^{-(t+t')/\tau_v}). \quad (2.5)$$

For large times,  $t \gg \tau_v$ , one finds  $\langle \mathbf{v}^2 \rangle = dq/(\gamma m)$ , and together with Eq. (2.3),  $q = \gamma k_B T$ . The microscopic noise strength  $q$  is thus connected to the macroscopic friction coefficient  $\gamma$ , as both properties arise from the interactions of the colloid with the fluid particles of the bath. The fact that  $q$  and  $\gamma$  are not independent of each other provides an example for the more general fluctuation-dissipation theorem [17].

Now, we investigate the dynamics of the Brownian particle that performs a random walk in space. We use  $\mathbf{r}(t) = \mathbf{r}(0) + \int_0^t dt' \mathbf{v}(t')$  to first calculate the mean displacement  $\langle \mathbf{r}(t) - \mathbf{r}(0) \rangle = \mathbf{v}_0 \tau_v (1 - e^{-t/\tau_v})$ , which becomes constant for large times  $t \gg \tau_v$ . To characterize the random walk, one uses the mean-squared displacement (MSD) of the particle,

$$\langle [\mathbf{r}(t) - \mathbf{r}(0)]^2 \rangle \quad (2.6a)$$

$$= \left\langle \left[ \int_0^t dt' \mathbf{v}(t') \right] \cdot \left[ \int_0^t dt'' \mathbf{v}(t'') \right] \right\rangle \quad (2.6b)$$

$$= \int_0^t dt' \int_0^t dt'' \langle \mathbf{v}(t') \cdot \mathbf{v}(t'') \rangle \quad (2.6c)$$

$$= \frac{2dq\tau_v}{\gamma^2} \left( \frac{t}{\tau_v} - 1 + e^{-t/\tau_v} \right) + \left( \mathbf{v}_0^2 - \frac{dq}{\gamma m} \right) \left( \frac{1 - e^{-t/\tau_v}}{\tau_v^{-1}} \right)^2. \quad (2.6d)$$

According to Eq. (2.6c), the MSD can be calculated if the velocity correlation function  $\langle \mathbf{v}(t) \cdot \mathbf{v}(t') \rangle$  from Eq. (2.5) is known. Replacing the initial value  $\mathbf{v}_0^2$  by velocities with stationary mean  $\langle \mathbf{v}^2 \rangle$  from Eq. (2.3), the second term in Eq. (2.6d) vanishes. A Taylor expansion of the MSD for short times  $t \ll \tau_v$  gives ballistic motion with  $\langle [\mathbf{r}(t) - \mathbf{r}(0)]^2 \rangle \simeq (\tilde{v}t)^2$  and speed  $\tilde{v} = \sqrt{dk_B T/m}$ . For large times  $t \gg \tau_v$ , the MSD grows linearly in time and the Brownian particle in  $d$  dimensions diffuses with the diffusion coefficient

$$D = \lim_{t \rightarrow \infty} \frac{\langle [\mathbf{r}(t) - \mathbf{r}(0)]^2 \rangle}{2dt}. \quad (2.7)$$

From Eq. (2.6), we obtain  $D = q/\gamma^2$  or

$$D = \frac{k_B T}{\gamma}. \quad (2.8)$$

This equation is the Stokes-Einstein relation, which relates the diffusion coefficient of a Brownian particle to its friction coefficient. In particular,  $D$  is independent of the particle mass  $m$  and spatial dimension  $d$ .

## 2.1.2 Fokker-Planck equation

The Langevin equation (2.1) of a Brownian particle was obtained by adding a stochastic term of Gaussian white noise to Newton's equation of motion. An alternative description introduces an equation for the probability density  $P(\mathbf{r}, \mathbf{v}, t)$  to find the particle at time  $t$  at position  $\mathbf{r}$  with velocity  $\mathbf{v}$ . In the following, we recall how the corresponding Fokker-Planck equation for the time evolution of  $P$  is obtained.

For that purpose, we consider a general Langevin equation, which is a system of stochastic differential equations for  $n$  random variables  $\mathbf{x} = (x_1, \dots, x_n)$ . The equation for the dynamic variable  $x_i(t)$  reads

$$\frac{d}{dt} x_i(t) = h_i(\mathbf{x}, t) + g_{ij}(\mathbf{x}, t) \Gamma_j(t), \quad (2.9)$$

where  $h_i(\mathbf{x}, t)$  and  $g_{ij}(\mathbf{x}, t)$  are given functions of  $\mathbf{x}$  and  $t$ , the Gaussian white noise  $\Gamma_i(t)$  is again characterized by Eq. (2.2), and summation over double indices is understood [18, 19]. If  $g_{ij}$  does not depend on  $\mathbf{x}$ , the noise term is called additive. In the case of multiplicative noise,  $g_{ij}$  explicitly depends on  $\mathbf{x}$ , and Eq. (2.9) is not fully specified from a mathematical point of view. This is a consequence of the non-differentiable and unbounded noise. We will motivate below that the stochastic differential equation (2.9) becomes well-defined when one chooses an “interpretation parameter”  $\lambda \in [0, 1]$ , which will enter in Eq. (2.12a). The most common choices are

$\lambda = 0$  following Ito and  $\lambda = 1/2$  following Stratonovich, which we will also adopt in this thesis.

For a given Langevin equation (2.9), there are various methods [18, 20, 21] to derive the Fokker-Planck equation for the probability density

$$P = P(\mathbf{x}, t) = \left\langle \prod_{i=1}^n \delta[x_i - x_i(t)] \right\rangle. \quad (2.10)$$

Using  $\partial_t = \partial/\partial t$  and  $\partial_i = \partial/\partial x_i$ , one obtains the partial differential equation [22]

$$\partial_t P = -\partial_i (D_i P) + \partial_i \partial_j (D_{ij} P), \quad (2.11)$$

where the “drift vector”  $D_i(\mathbf{x}, t)$  and “diffusion tensor”  $D_{ij}(\mathbf{x}, t)$  read

$$D_i(\mathbf{x}, t) = h_i + \lambda g_{kj} \partial_k g_{ij}, \quad (2.12a)$$

$$D_{ij}(\mathbf{x}, t) = \frac{1}{2} g_{ik} g_{jk}. \quad (2.12b)$$

The Fokker-Planck equation (2.11) can be understood as a continuity equation for the probability density  $P$  with probability current  $\mathbf{j} = \mathbf{j}(\mathbf{x}, t)$ ,

$$\partial_t P + \partial_i j_i = 0, \quad j_i(\mathbf{x}, t) = [D_i - (\partial_j D_{ij})] P - D_{ij} \partial_j P. \quad (2.13)$$

In  $j_i(\mathbf{x}, t)$ , the term proportional to  $P$  (in square brackets) describes the drift current, which depends on the interpretation parameter  $\lambda$ , and the second contribution proportional to  $\partial_j P$  is the diffusive current. As already mentioned, the Fokker-Planck equation becomes independent of  $\lambda$  only if  $g_{ij}$  is independent of  $\mathbf{x}$ . For the Brownian particle, described by the Langevin equation (2.1), we obtain the following Fokker-Planck equation for the probability density  $P = P(\mathbf{r}, \mathbf{v}, t)$ :

$$\frac{\partial}{\partial t} P = \left( -\frac{\partial}{\partial r_i} + \frac{\gamma}{m} \frac{\partial}{\partial v_i} \right) v_i P + \frac{q}{m^2} \frac{\partial^2}{\partial v_i \partial v_i} P. \quad (2.14)$$

Next, we sketch why different “interpretations” exist for a single random variable  $x(t)$ . We introduce  $dW(t) = \Gamma(t) dt$  as the noise increment of the so-called Wiener process at time  $t$  during the interval  $dt$ . To determine the increment  $dx(t)$ , it makes a difference at which point of the interval  $[t, t + dt]$  the function  $g(x(t), t)$  is evaluated [23],

$$dx(t) = h(x(t_\lambda), t_\lambda) dt + g(x(t_\lambda), t_\lambda) dW(t), \quad t_\lambda = t + \lambda dt, \quad \lambda \in [0, 1]. \quad (2.15)$$

If  $\Gamma(t)$  were a continuous and differentiable function, expression (2.15) would be independent of  $\lambda$  for  $dt \rightarrow 0$ ; however, for the Gaussian white noise this is not true any longer, as  $\langle [dW(t)]^2 \rangle = dt$  and  $dW(t) \simeq \sqrt{dt}$ . We use the Taylor expansions

$$g(x(t_\lambda), t_\lambda) \approx g(x(t) + \lambda dx(t), t_\lambda) \approx g(x(t), t_\lambda) + g'(x(t), t_\lambda) \lambda dx(t), \quad (2.16)$$

and rearrange terms up to order of  $\sqrt{dt}$ ,

$$dx(t) = \left[ h(x(t), t) + \lambda g(x(t), t) g'(x(t), t) \right] dt + g(x(t), t) dW(t). \quad (2.17)$$

The drift term in square brackets depends on  $\lambda$  and corresponds to the drift vector from Eq. (2.12a). For physical models where the Gaussian white noise approximates stochastic forces with finite correlation time, the Stratonovich interpretation ( $\lambda = 1/2$ , “mid-point”) is the appropriate one, as stated by the Wong-Zakai theorem [24]. When modeling discrete systems, the Ito interpretation ( $\lambda = 0$ , “pre-point”) is often correct [25]. A third interpretation due to Klimontovich ( $\lambda = 1$ , “post-point”) can be chosen for systems, where one requires generalized Stokes-Einstein relations [cf. Eq. (2.8)] to hold [26]. Finally, we point out that only the Stratonovich interpretation has the convenient property that the classical rules of calculus apply; in contrast, the Ito formalism requires a new set of “rules” for manipulating stochastic differential equations.

Langevin equations can be obtained in a straight-forward way by adding noise to a deterministic equation. Moreover, these equations are easily solved numerically. In this work, we will deal with Langevin equations with additive noise of strength  $g$ ,  $\frac{d}{dt} x(t) = h(x(t), t) + g\Gamma(t)$ . Its discretized version according to the Euler scheme [25] with time step  $\Delta t$  reads

$$x_{n+1} = x_n + h(x_n, t_n) \Delta t + g Z_n \sqrt{\Delta t}, \quad (2.18)$$

where  $Z_n$  is a random number drawn from a standard normal distribution with mean  $\langle Z_n \rangle = 0$  and variance  $\langle Z_n^2 \rangle = 1$ .

In contrast to the Langevin equation, the Fokker-Planck formalism sometimes better helps to study a stochastic process analytically. There are situations where one is not interested in solving the Fokker-Planck equation for  $P$ , but in calculating the expectation value of a function  $f(\mathbf{x})$  of the dynamic random variables  $\mathbf{x}$ ,

$$\langle f(\mathbf{x}) \rangle (t) = \int d^n x P(\mathbf{x}, t) f(\mathbf{x}). \quad (2.19)$$

Even without knowledge of  $P(\mathbf{x}, t)$ , it is possible to determine  $\langle f(\mathbf{x}) \rangle$  in many practical cases. We get a moment equation by multiplying the Fokker-Planck equation (2.11) with  $f(\mathbf{x})$  and integrating over all variables:

$$\frac{d}{dt} \langle f(\mathbf{x}) \rangle = - \int d^n x f(\mathbf{x}) \partial_i (D_i P) + \int d^n x f(\mathbf{x}) \partial_i \partial_j (D_{ij} P). \quad (2.20)$$

In the best case, one ends up with a closed differential equation in time for  $\langle f(\mathbf{x}) \rangle$  after performing partial integrations on the right-hand side of Eq. (2.20) [19]. We will use this technique later on in this thesis.

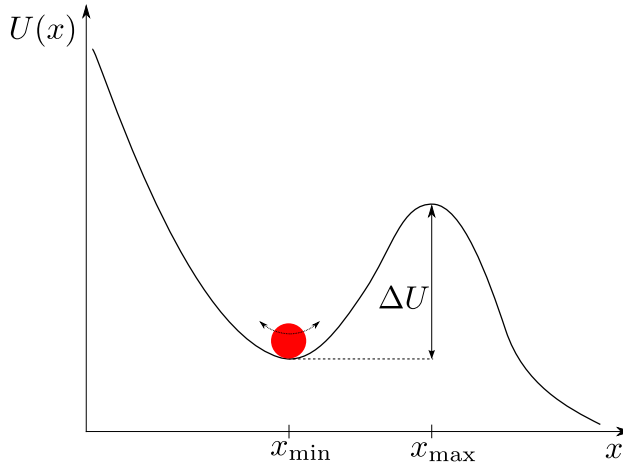


Figure 2.1 ■ A Brownian particle is initially trapped in a potential minimum at  $x_{\min}$ . Due to thermal noise, it escapes across the energy barrier  $\Delta U \gg k_B T$  in finite time. The escape rate in Eq. (2.21) was first derived by Kramers in 1940.

Ultimately, we refer to the Kramers escape problem [27], which we will encounter in a modified way in Chapter 5. As indicated in Fig. 2.1, a Brownian particle of mass  $m$  moves in a one-dimensional potential  $U(x)$  and is subject to a force  $F(x) = -U'(x)$ . Initially, it is trapped at  $x_{\min}$  in a deep potential minimum of height  $\Delta U \gg k_B T$ , but it can cross the barrier through thermal fluctuations. Using the Fokker-Planck equation, the mean escape time  $r^{-1}$  of the particle to leave the trap is determined as [28]

$$r = \frac{\sqrt{U''(x_{\min}) |U''(x_{\max})|}}{2\pi\gamma} \exp\left(-\frac{\Delta U}{k_B T}\right). \quad (2.21)$$

The escape rate  $r$  is non-zero for finite temperature and decays exponentially with the Boltzmann factor of the potential barrier height.

## 2.2 Microorganisms as overdamped particles

The first Langevin equation (2.1) was introduced in 1908 to describe the stochastic motion of a Brownian particle in a bath of fluid particles at temperature  $T$  [29]. Meanwhile, one finds numerous applications of Langevin equations (2.9) in physics, biology, engineering, and finance [16, 25, 30]. In particular, Langevin equations can be used to describe the stochastic motion of cells, as observed under a microscope [31, 32]. The striking similarity between the trajectories of Brownian particles and microorganisms was first pointed out by Przibram in his article “Über die ungeordnete Bewegung niederer Tiere” from 1913 [33]; the original data is reprinted in Fig. 2.2.

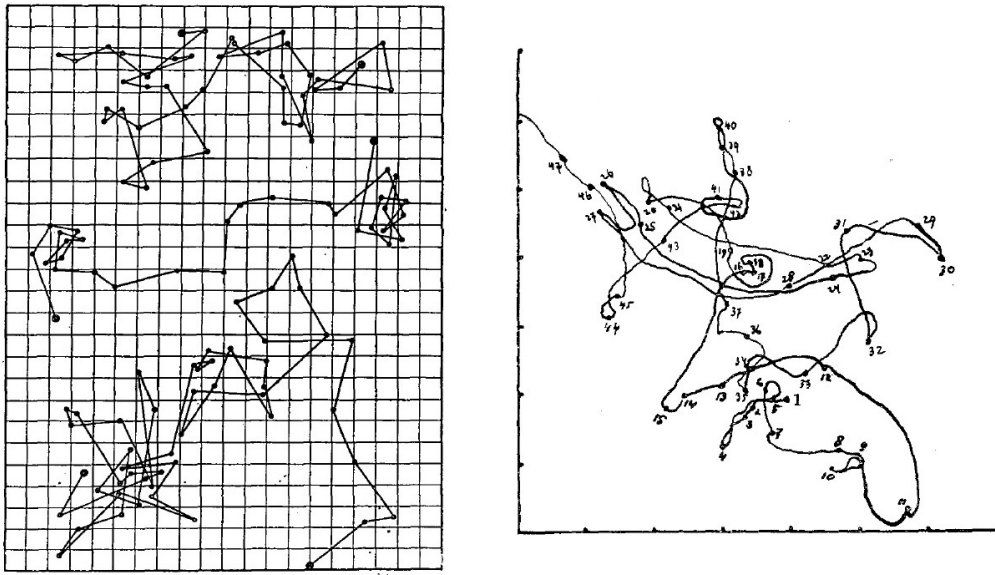


**Figure 2.2** ■ Left: Three random walk trajectories of a Brownian particle of putty by Perrin (1909) from Ref. [34]. Right: Trajectory of the microorganism *Paramecium* by Przibram (1913) from Ref. [33]. The time intervals between single dots are 30 s (left) and 4 s (right).

In this spirit, we attempt to describe the dynamics of microorganisms in terms of stochastic differential equations. In these equations, we will include noise terms for random forces and torques. On the one hand, the noise mimics collisions of the microorganism with particles of the surrounding medium, on the other hand, it represents stochasticity due to internal cell processes that have an effect on the locomotion. As a consequence, the fluctuation dissipation theorem or Stokes-Einstein relation (2.8) does not hold any longer.

A feature of microorganisms in motion is that inertial forces can be neglected compared to viscous forces. According to Berg [35], a microorganism, say a bacterium, is modeled as a spherical colloid of radius  $a = 1 \mu\text{m}$ , diffusing in water with viscosity  $\eta = 10^{-3} \text{ kg m}^{-1} \text{ s}^{-1}$  at thermal energy  $k_B T \sim 4 \text{ pN nm}$ . For a mass density of  $\rho_m \sim 10^3 \text{ kg m}^{-3}$ , the bacterial mass reads  $m = \rho_m \times \frac{4}{3}\pi a^3 = 4 \times 10^{-15} \text{ kg}$ , and the friction coefficient is  $\gamma = 6\pi\eta a = 2 \times 10^{-8} \text{ kg s}^{-1}$ . Without thermal forces in Eq. (2.4), the velocity of the particle decays to zero during the momentum relaxation time  $\tau_v = m/\gamma = 2\rho_m a^2/(9\eta) = 2 \times 10^{-7} \text{ s}$ .

We compare  $\tau_v$  to the time  $t_0 = a/v = 10^{-2} \text{ s} \dots 10^{-1} \text{ s}$  that it takes a bacterium to drift its own size  $a$  with a characteristic speed of  $v \sim (10 \dots 100) \mu\text{m s}^{-1}$ , and obtain the small ratio  $\tau_v/t_0 = 10^{-6} \dots 10^{-5}$ . Hence, the world of swimming organisms at the micrometer scale is governed by Aristotelian dynamics where any motion immediately stops when forces and torques are not applied.

The hydrodynamics of fluids is described by the Navier-Stokes equations [36]. To characterize the flow of an object of size  $a$  in a fluid of density  $\rho$  and viscosity  $\eta$ , one defines the

$$\text{Reynolds number} \quad \text{Re} = \frac{\rho v a}{\eta}, \quad (2.22)$$

where  $v$  is a characteristic flow velocity. The Reynolds number compares inertial to viscous forces, similar to our ratio  $\tau_v/t_0$  for a colloidal particle from above. Typical values for swimming microorganisms in water are  $\text{Re} \sim 10^{-5} \dots 10^{-4}$  for bacteria, such as *E. coli*,  $\text{Re} \sim 10^{-2}$  for human spermatozoa, and up to  $\text{Re} \sim 10^{-1}$  for larger microorganisms like ciliates [36]. Note that for small  $\text{Re} \ll 1$ , the Navier-Stokes equations simplify to the linear and time-independent Stokes equations for times  $t \gg \tau_v(\text{water})$ . In this thesis, however, we do not explicitly take hydrodynamics into account.

As the viscous forces dominate the inertial forces,  $m \frac{d}{dt} \mathbf{v}(t) \ll \gamma \mathbf{v}(t)$ , the dynamics of microorganisms is well described by an overdamped Langevin equation where we set  $m \frac{d}{dt} \mathbf{v}(t) = 0$ . Eq. (2.1) then becomes

$$\frac{d}{dt} \mathbf{r}(t) = \sqrt{2D} \mathbf{\Gamma}(t), \quad (2.23)$$

and as a consequence of Eq. (2.2), one obtains delta-correlations for the velocity  $\langle \mathbf{v}(t) \cdot \mathbf{v}(t') \rangle = 2dD\delta(t - t')$ . Using Eq. (2.6c), we find immediately that the overdamped particle diffuses for all times  $t$ :

$$\langle [\mathbf{r}(t) - \mathbf{r}(0)]^2 \rangle = \int_0^t dt' \int_0^t dt'' \langle \mathbf{v}(t') \cdot \mathbf{v}(t'') \rangle = 2dDt. \quad (2.24)$$

For overdamped systems, the Fokker-Planck equation is also called a Smoluchowski equation, and the probability density is only a function of position,  $P = P(\mathbf{r}, t)$ . The Smoluchowski equation corresponding to Eq. (2.23) reduces to the diffusion equation,

$$\partial_t P(\mathbf{r}, t) = D \nabla^2 P(\mathbf{r}, t), \quad (2.25)$$

where  $\nabla^2$  is the Laplacian in  $d$  dimensions. For the initial condition  $P(\mathbf{r}, t = 0) = \delta(\mathbf{r})$ , one obtains the Gaussian propagator

$$P(\mathbf{r}, t) = (4\pi Dt)^{-d/2} \exp\left(-\frac{\mathbf{r}^2}{4Dt}\right) \quad (2.26)$$

as the fundamental solution. The density  $P(\mathbf{r}, t)$  describes how an overdamped Brownian particle delocalizes with increasing time. Using spherical coordinates and  $\int_{\mathbb{R}^d} d^d r = \frac{2\pi^{d/2}}{\Gamma(d/2)} \int_0^\infty dr r^{d-1}$ , we confirm that the MSD is given by Eq. (2.24) since

$$\langle \mathbf{r}^2(t) \rangle = \int_{\mathbb{R}^d} d^d r P(\mathbf{r}, t) \mathbf{r}^2 = 2dDt. \quad (2.27)$$

Note that a third derivation of the MSD in Eq. (2.27) is provided by multiplying Eq. (2.25) with  $\mathbf{r}^2$  and integrating over the space coordinates; the resulting moment equation of the form (2.20) is then solved for  $\langle \mathbf{r}^2(t) \rangle$ .

Using the parameters from above, we determine the diffusion coefficient of a sphere with radius  $a = 1\text{ }\mu\text{m}$  as  $D = k_{\text{B}}T/\gamma = 0.2\text{ }\mu\text{m}^2\text{s}^{-1}$ . In Sec. 3.2.3, we will show that this value is more than two orders of magnitude smaller than the diffusion coefficient of an actively swimming bacterium with the same size, such as *E. coli*.

In nature, Gaussian diffusion is ubiquitous. Yet, there are plenty of examples where diffusion is “anomalous”. For a large class of random walks, the MSD asymptotically scales as a power law with exponent  $\Lambda$  as

$$\langle [\mathbf{r}(t) - \mathbf{r}(0)]^2 \rangle \sim t^\Lambda \quad \text{for large times } t. \quad (2.28)$$

For  $\Lambda = 1$ , one recovers normal Gaussian diffusion,  $0 < \Lambda < 1$  is called subdiffusion,  $\Lambda > 1$  corresponds to superdiffusion, and the special case  $\Lambda = 2$  is ballistic motion [37]. For instance, subdiffusion of proteins is observed in living cells, as the free diffusion is perturbed due to cytoplasmic crowding effects [38]; also colloidal particles in entangled actin filaments show subdiffusion [39]. On the contrary, superdiffusion is currently debated as a possible foraging strategy of animals [40].

## 2.3 Active particles

In spite of the similarity between the random walks of colloids and active microorganisms, there is a huge physical difference. The classical Brownian particle is a passive colloid in thermal equilibrium, and its diffusion coefficient  $D$  obeys the Stokes-Einstein relation (2.8). According to Eq. (2.4), the mean velocity  $\langle \mathbf{v} \rangle$  tends to zero for large times. This result somehow contradicts the intuitive picture of a living microorganism that actively moves in its environment, such that we assign a characteristic speed to it. We will therefore present several approaches to how the activity of a self-propelled particle can be explicitly taken into account in a Langevin description.

Biological particles, *i.e.* microorganisms, have the ability to absorb energy from their environment and store it in an internal depot. The conversion of this internal energy into kinetic energy makes the particle move [41]. As summarized in Refs. [42, 43], it is possible to model the activity of the particle by replacing  $\gamma$  in the Langevin equation (2.1) by an effective friction coefficient  $\gamma(\mathbf{r}, \mathbf{v})$  that depends on position and velocity in general. In addition, existence of energy or nutrient sources can be modeled by a potential  $U(\mathbf{r})$  that generates an attractive force  $-\nabla U(\mathbf{r})$ .

Prominent examples for a speed-dependent  $\gamma(v)$  read [43]:

$$\gamma(v) = \gamma - \frac{A}{B+Cv^2}, \quad \text{Schweitzer-Ebeling-Tilch,} \quad (2.29a)$$

$$\gamma(v) = \gamma \left( \frac{v^2}{v_0^2} - 1 \right), \quad \text{Rayleigh,} \quad (2.29b)$$

$$\gamma(v) = \gamma \left( 1 - \frac{v_0}{v} \right), \quad \text{Schienbein-Gruler.} \quad (2.29c)$$

They all have in common that for large speeds  $v$ , energy dissipation results in  $\gamma(v) > 0$ ; for small  $v$ , one has “active friction” with  $\gamma(v) < 0$ , as internal energy is “pumped” into active motion.

We will pursue a different approach, which is based on the observation that for various microorganisms fluctuations in the direction of motion are independent of fluctuations in the speed [44, 45]. Therefore, we express the time-dependent velocity vector of an active particle as

$$\mathbf{v}(t) = v(t)\mathbf{e}(t) \quad (2.30)$$

with speed  $v(t) = |\mathbf{v}(t)| \geq 0$ . The  $d$ -dimensional unit vector  $\mathbf{e}(t)$  indicates the direction of motion and contains  $d-1$  angles, denoted as  $\Omega(t)$  in  $d$ -dimensional spherical coordinates. For example, in  $d=3$ ,  $\Omega = (\varphi, \theta)$  and  $\mathbf{e} = (\cos \varphi \sin \theta, \sin \varphi \sin \theta, \cos \theta)$ . Since we consider speed  $v(t)$  and angle  $\Omega(t)$  as independent random variables, the probability density  $p(v, \Omega, t)$  and the joint distribution  $p(v, \Omega, t; v', \Omega', t')$  factorize

$$p(v, \Omega, t) = p(v, t)p(\Omega, t), \quad p(v, \Omega, t; v', \Omega', t') = p(v, t; v', t')p(\Omega, t; \Omega', t'). \quad (2.31)$$

Eq. (2.31) results in a factorization of the velocity correlations:

$$\langle \mathbf{v}(t) \cdot \mathbf{v}(t') \rangle = \int d^d v \int d^d v' p(v, \Omega, t; v', \Omega', t') v \mathbf{e} \cdot v' \mathbf{e}' \quad (2.32a)$$

$$= \langle v(t)v(t') \rangle \langle \mathbf{e}(t) \cdot \mathbf{e}(t') \rangle. \quad (2.32b)$$

Hence, for a particle with trajectory  $\mathbf{r}(t) = \mathbf{r}(0) + \int_0^t dt' v(t')\mathbf{e}(t')$  the MSD is determined as

$$\langle [\mathbf{r}(t) - \mathbf{r}(0)]^2 \rangle = \int_0^t dt' \int_0^t dt'' \langle v(t')v(t'') \rangle \langle \mathbf{e}(t') \cdot \mathbf{e}(t'') \rangle. \quad (2.33)$$

Peruani and Morelli discuss the MSD of a random walker in two dimensions where correlations decay exponentially on characteristic time scales [45]. In this case, the MSD exhibits several regimes with different local slopes in a double-logarithmic plot.

In the next section, we investigate a random walker with constant speed and rotational diffusion of its velocity direction, which will be the basis for our main model throughout the thesis. A possible Langevin equation for the speed of granulocytes

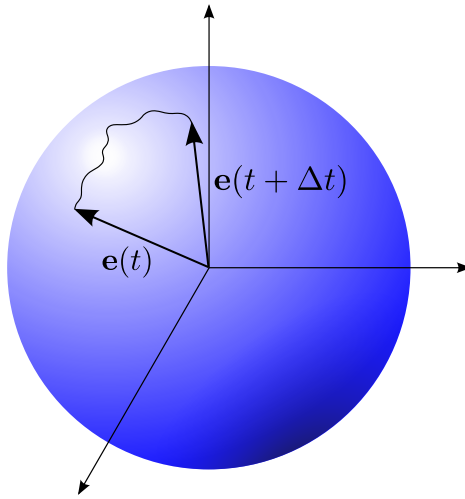


Figure 2.3 ■ Rotational diffusion of the unit vector  $\mathbf{e}(t)$  on the surface of a  $d$ -dimensional unit sphere. For small time intervals  $\Delta t$ , the surface looks flat and the unit vector shows translational diffusion in  $d - 1$  dimensions.

is found in Ref. [44]; it contains the friction function from Eq. (2.29c) and features a Gaussian speed distribution.

To conclude, we mention that a lot of research in statistical physics is dedicated to the understanding of active matter. Collective motion in a system of self-propelled particles was first investigated by Vicsek *et al.* [46] and numerous studies on pattern formation followed [47, 48, 49]. For elaborate reviews on active matter and collective motion, we refer to Refs. [50, 51, 52].

Apart from biological organisms, active particles are nowadays realized in a variety of artificial swimmers, which have been designed experimentally for scientific and engineering purposes [53]. The driving force of these autonomous nano- and micro-scale swimmers stems, for instance, from chemical reactions on their surface [54, 55].

### 2.3.1 Rotational diffusion of the velocity direction

In this section, we introduce an active particle with constant speed  $v$  whose direction of motion  $\mathbf{e}(t)$  is driven by Gaussian white noise. As sketched in Fig. 2.3, we consider rotational diffusion of the unit vector  $\mathbf{e}(t)$ , that is  $\mathbf{e}(t)$  diffuses on the surface of a  $d$ -dimensional unit sphere. The strength of rotational diffusion is specified by the rotational diffusion constant  $D_r$  with unit of inverse time. Here, we will present a calculation of the directional correlation function for arbitrary dimension  $d \geq 2$ , following Doi and Edwards [56]:

$$\langle \mathbf{e}(t) \cdot \mathbf{e}(t') \rangle = e^{-|t-t'|/\tau_{\text{rot}}}, \quad \tau_{\text{rot}} = \frac{1}{(d-1)D_r}. \quad (2.34)$$

To derive Eq. (2.34), we consider a stationary and uniform distribution for the orientation  $\mathbf{e}(t)$ ,

$$p(\Omega, t) = \frac{1}{\Omega_0} = \text{const.}, \quad (2.35)$$

where  $\Omega_0 = 2\pi$  for  $d = 2$  and  $\Omega_0 = 4\pi$  for  $d = 3$ . We express the joint distribution  $p(\Omega, t; \Omega', t') = p(\Omega, t|\Omega', t')p(\Omega', t')$  in terms of the conditional probability  $p(\Omega, t|\Omega', t')$ . The latter solves by definition the rotational diffusion equation

$$\partial_t p(\Omega, t|\Omega', t') = D_r \nabla_\Omega^2 p(\Omega, t|\Omega', t'), \quad (2.36)$$

where  $\nabla_\Omega^2$  denotes the angular part of the  $d$ -dimensional Laplace operator. Eq. (2.36) is solved with the initial condition  $p(\Omega, t'|\Omega', t') = \delta(\Omega - \Omega')$ . For  $d = 2$  and  $d = 3$ , explicit solutions are

$$p(\varphi, t|\varphi', t') = \frac{1}{2\pi} + \frac{1}{\pi} \sum_{m=1}^{\infty} e^{-m^2 D_r |t-t'|} \cos[m(\varphi - \varphi')], \quad (2.37a)$$

$$p(\Omega, t|\Omega', t') = \sum_{l=0}^{\infty} \sum_{m=-l}^{+l} e^{-l(l+1)D_r |t-t'|} Y_{lm}^*(\Omega') Y_{lm}(\Omega), \quad (2.37b)$$

where  $Y_{lm}(\Omega)$  are the spherical harmonics [45, 57]. For large times with  $|t - t'| \gg D_r^{-1}$ , the expressions in Eq. (2.37) tend to  $p(\Omega, t) = 1/\Omega_0$ .

In the following, we calculate  $\langle \mathbf{e}(t) \cdot \mathbf{e}(t') \rangle$  in arbitrary dimension  $d$  by deriving a moment equation as described in Eq. (2.20). We start with the correlation function

$$\langle \mathbf{e}(t) \cdot \mathbf{e}(t') \rangle = \int d\mathbf{e} \int d\mathbf{e}' \mathbf{e} \cdot \mathbf{e}' p(\Omega, t|\Omega', t') p(\Omega', t') \quad (2.38)$$

for  $t \geq t'$ , take the time derivative with respect to  $t$  and use Eq. (2.36):

$$\partial_t \langle \mathbf{e}(t) \cdot \mathbf{e}(t') \rangle = D_r \int d\mathbf{e} \int d\mathbf{e}' \mathbf{e} \cdot \mathbf{e}' \nabla_\Omega^2 p(\Omega, t|\Omega', t') p(\Omega', t'). \quad (2.39)$$

Next, we perform two partial integrations with respect to  $\Omega$  and arrive at

$$\partial_t \langle \mathbf{e}(t) \cdot \mathbf{e}(t') \rangle = D_r \int d\mathbf{e} \int d\mathbf{e}' \nabla_\Omega^2 \mathbf{e} \cdot \mathbf{e}' p(\Omega, t|\Omega', t') p(\Omega', t'). \quad (2.40)$$

The appendix of Ref. [58] contains the proof that

$$\nabla_\Omega^2 \mathbf{e} = -(d-1)\mathbf{e}, \quad (2.41)$$

and hence

$$\begin{aligned} \partial_t \langle \mathbf{e}(t) \cdot \mathbf{e}(t') \rangle &= -(d-1)D_r \int d\mathbf{e} \int d\mathbf{e}' \mathbf{e} \cdot \mathbf{e}' p(\Omega, t|\Omega', t') p(\Omega', t') \\ &= -(d-1)D_r \langle \mathbf{e}(t) \cdot \mathbf{e}(t') \rangle. \end{aligned} \quad (2.42)$$

Solving the ordinary differential equation (2.42) with the initial condition  $\langle \mathbf{e}(t') \cdot \mathbf{e}(t') \rangle = 1$  yields  $\langle \mathbf{e}(t) \cdot \mathbf{e}(t') \rangle = e^{-(d-1)D_r(t-t')}$ , which is generalized to Eq. (2.34) for arbitrary times  $t'$ ,  $t''$ .

The time scale for rotational diffusion is set by  $\tau_{\text{rot}} = \frac{1}{(d-1)D_r}$ , after which initial directional correlations are vanished. For larger spatial dimension  $d$ ,  $\tau_{\text{rot}}$  becomes smaller and correlations decay faster, as there is a larger degree of freedom for directional reorientations. For further illustration, we consider  $\langle \mathbf{e}(t) \cdot \mathbf{e}(0) \rangle = \langle \cos \delta_t \rangle$  for  $d = 3$ . Using  $\langle [\mathbf{e}(t) - \mathbf{e}(0)]^2 \rangle = 2(1 - \langle \mathbf{e}(t) \cdot \mathbf{e}(0) \rangle)$  and expanding both the exponential and cosine for small times  $t > 0$  and small angles, respectively, shows that the angle  $\delta_t$  diffuses on a two-dimensional surface according to

$$\langle \delta_t^2 \rangle \approx 4D_r t \quad \text{for } t \ll \frac{1}{2D_r}. \quad (2.43)$$

Note that there is also an Einstein relation that connects the rotational diffusion coefficient  $D_r$  of a Brownian particle in thermal equilibrium to its rotational friction coefficient  $\gamma_r$ . The analog to translational diffusion with  $D = k_B T / \gamma$  [Eq. (2.8)] reads  $D_r = k_B T / \gamma_r$ . For instance, one has  $\gamma_r = 8\pi\eta a^3$  for a sphere of radius  $a$ .

Finally, we apply our result to an active walker with rotational diffusion of its velocity direction in two dimensions. The direction of motion  $\mathbf{e}(t) = (\cos \varphi(t), \sin \varphi(t))$  is parametrized by the angle  $\varphi(t) \in (-\pi, \pi]$  relative to the  $x$  axis. Here, we denote the rotational diffusion coefficient as  $q_\varphi > 0$  and the corresponding Langevin and Fokker-Planck equation read

$$\frac{d}{dt} \varphi(t) = \sqrt{2q_\varphi} \Gamma(t) \quad \Leftrightarrow \quad \partial_t p(\varphi, t | \varphi', t') = q_\varphi \partial_\varphi^2 p(\varphi, t | \varphi', t'). \quad (2.44)$$

According to Eq. (2.34), directional correlations decay as

$$\langle \mathbf{e}(t) \cdot \mathbf{e}(t') \rangle = e^{-q_\varphi |t-t'|} \quad (2.45)$$

on the time scale  $\tau_{\text{rot}} = q_\varphi^{-1}$ . Using Eq. (2.33), the mean-squared displacement becomes

$$\langle [\mathbf{r}(t) - \mathbf{r}(0)]^2 \rangle = v^2 \int_0^t dt' \int_0^t dt'' \langle \mathbf{e}(t') \cdot \mathbf{e}(t'') \rangle \quad (2.46a)$$

$$= \frac{2v^2}{q_\varphi^2} (q_\varphi t - 1 + e^{-q_\varphi t}). \quad (2.46b)$$

For small times  $t \ll \tau_{\text{rot}}$ , the random walk is persistent and the walker moves in the same direction on the persistence length  $s_{\text{per}} = v\tau_{\text{rot}}$ . Note that the time dependence of the MSD in Eq. (2.46b) is the same as for the classical Brownian particle from

Eq. (2.6d). A Taylor expansion for  $q_\varphi t \ll 1$  gives ballistic motion for small times, and for large times  $q_\varphi t \gg 1$ , the motion is diffusive with diffusion coefficient

$$D = \lim_{t \rightarrow \infty} \frac{\langle [\mathbf{r}(t) - \mathbf{r}(0)]^2 \rangle}{4t} = \frac{v^2}{2q_\varphi}. \quad (2.47)$$

The diffusion coefficient of an active walker thus scales quadratically with speed  $v$ .

### 2.3.2 Rotational diffusion with constant drift

In Chapter 4, we will encounter an active walker with speed  $v$  whose Langevin dynamics for rotational diffusion of the velocity direction contains a constant angular drift  $\omega$ :

$$\frac{d}{dt} \varphi(t) = \omega + \sqrt{2q_\varphi} \Gamma(t). \quad (2.48)$$

Without noise, the walker performs circular motion and the mean-squared displacement is zero. Under the influence of noise, the perfect circles are disturbed such that the circle's center diffuses for large times.

Here, we derive an expression for the MSD of the active walker. First, we compute the directional correlation function  $\langle \mathbf{e}(t) \cdot \mathbf{e}(0) \rangle = \langle \cos[\varphi(t) - \varphi(0)] \rangle$ . The formal solution of Eq. (2.48) with initial condition  $\varphi(t=0) = \varphi(0)$  is given by  $\varphi(t) = \varphi(0) + \omega t + \sqrt{2q_\varphi} \int_0^t dt' \Gamma(t')$ . Using a trigonometric identity, it follows that

$$\begin{aligned} \langle \mathbf{e}(t) \cdot \mathbf{e}(0) \rangle &= \cos(\omega t) \left\langle \cos \left[ \sqrt{2q_\varphi} \int_0^t dt' \Gamma(t') \right] \right\rangle \\ &\quad - \sin(\omega t) \left\langle \sin \left[ \sqrt{2q_\varphi} \int_0^t dt' \Gamma(t') \right] \right\rangle. \end{aligned} \quad (2.49)$$

For delta-correlated Gaussian white noise with zero mean, we obtain [18]:

$$\left\langle \exp \left[ i \sqrt{2q_\varphi} \int_0^t dt' \Gamma(t') \right] \right\rangle = \exp \left[ -q_\varphi \int_0^t dt' \int_0^t dt'' \langle \Gamma(t') \Gamma(t'') \rangle \right] = e^{-q_\varphi t}. \quad (2.50)$$

The imaginary part of Eq. (2.50) is zero, so that Eq. (2.49) becomes  $\langle \mathbf{e}(t) \cdot \mathbf{e}(0) \rangle = \cos(\omega t) \exp(-q_\varphi t)$ . Generalized for arbitrary times  $t, t'$ , one has

$$\langle \mathbf{e}(t) \cdot \mathbf{e}(t') \rangle = \cos(\omega|t-t'|) e^{-q_\varphi|t-t'|}, \quad (2.51)$$

and the exponential decay due to rotational diffusion is multiplied with an oscillation of frequency  $\omega$ . The mean-squared displacement [according to Eq. (2.46a)] becomes

$$\begin{aligned} \langle [\mathbf{r}(t) - \mathbf{r}(0)]^2 \rangle &= \frac{2v^2 q_\varphi t}{q_\varphi^2 + \omega^2} - \frac{2v^2 (q_\varphi^2 - \omega^2)}{(q_\varphi^2 + \omega^2)^2} \\ &\quad + \frac{2v^2 e^{-q_\varphi t}}{(q_\varphi^2 + \omega^2)^2} \left[ (q_\varphi^2 - \omega^2) \cos(\omega t) - 2q_\varphi \omega \sin(\omega t) \right]. \end{aligned} \quad (2.52)$$

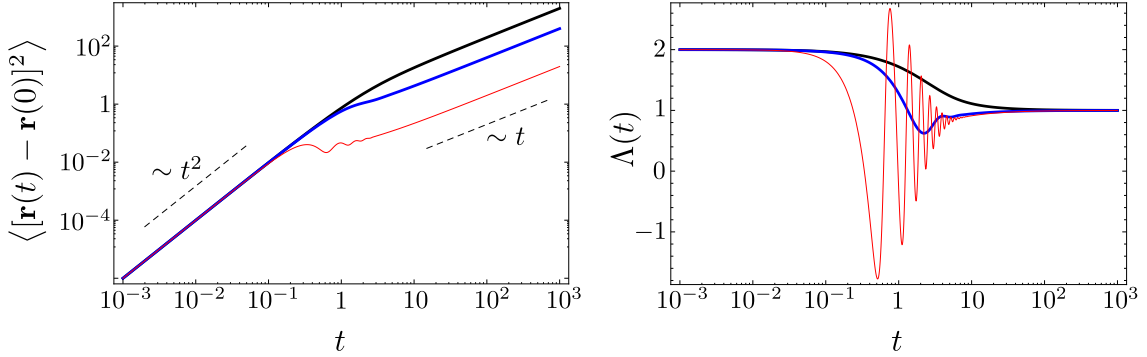


**Figure 2.4** ■ Mean-squared displacement  $\langle |\mathbf{r}(t) - \mathbf{r}(0)|^2 \rangle$  and its slope  $\Lambda(t)$  of an active walker with rotational diffusion and constant drift in arbitrary units. Speed  $v = 1$  and noise strength  $q_\varphi = 1$  are constant, and  $\omega$  takes the values 0 (black), 2 (blue), and 10 (red).

We will discuss this result in detail together with the diffusion coefficient in Chapter 4.3.2; a plot of the MSD is given on the left of Fig. 2.4.

As mentioned in Eq. (2.28), one can classify stochastic motion by writing the MSD as  $\langle |\mathbf{r}(t) - \mathbf{r}(0)|^2 \rangle \sim t^\Lambda$  for large times. The exponent  $\Lambda$  gives the slope of the MSD in a double-logarithmic plot. More generally, one defines the local slope  $\Lambda(t) = d \ln \langle |\mathbf{r}(t) - \mathbf{r}(0)|^2 \rangle / d \ln t$ . For the random walker with MSD from Eq. (2.52), we find

$$\Lambda(t) = \frac{t(q_\varphi^2 + \omega^2) [q_\varphi e^{q_\varphi t} - q_\varphi \cos(\omega t) + \omega \sin(\omega t)]}{e^{q_\varphi t} [q_\varphi^2 (q_\varphi t - 1) + \omega^2 (1 + q_\varphi t)] + (q_\varphi^2 - \omega^2) \cos(\omega t) - 2q_\varphi \omega \sin(\omega t)}, \quad (2.53)$$

which is plotted on the right of Fig. 2.4. For small times  $t \rightarrow 0$ , one always finds ballistic motion with  $\Lambda = 2$ ; for large times  $t \gg q_\varphi^{-1}, \omega^{-1}$ , the particle diffuses with  $\Lambda = 1$ . Without angular drift,  $\omega = 0$ ,  $\Lambda(t)$  shows a smooth transition between both regimes at intermediate time  $t \simeq q_\varphi^{-1}$ . On the contrary, an angular drift  $\omega \gg q_\varphi$  results in an oscillating MSD in the intermediate regime.

### 2.3.3 Simple run-and-tumble dynamics

We now comment on a generic random walk pattern, which describes the motion of various bacteria, such as *Escherichia coli*, but also of larger eukaryotic organisms, such as the unicellular alga *Chlamydomonas* [59, 60]. Both microorganisms perform “run-and-tumble” motion: During the “run”, these cells swim in an almost straight line, which is then interrupted by a “tumble” event. After the tumbling event, the cell starts a new run with a random direction of propagation. Note that the underlying swimming mechanisms that generate this motion are different for *E. coli* and *Chlamydomonas*; the details of *E. coli*’s run-and-tumble motion will be presented in Chapter 3.1.1.

The aim of this section is to show that an active swimmer that applies the run-and-tumble strategy diffuses for large times. In other words, we investigate how a sequence of ballistic runs is transformed into diffusive motion by the reorienting tumbling events. In particular, we will see that the mean-squared displacement has the same analytical form as that of an active walker, whose direction of motion performs continuous rotational diffusion, see Eq. (2.46).

To describe the run-and-tumble motion in a simplistic way, we assume that each run starts in a completely random direction and is interrupted after some time. Following the experimental results for *E. coli* and *Chlamydomonas*, the duration of runs is exponentially distributed with the probability density  $f(t) = \lambda e^{-\lambda t}$ , where  $\lambda$  is the “tumbling rate” and  $\tau_{\text{run}} = \int_0^\infty dt f(t)t = \lambda^{-1}$  is the mean run time. For example,  $\tau_{\text{run}} \sim 1$  s for *E. coli* and  $\tau_{\text{run}} \sim 11$  s for *Chlamydomonas* [59, 60].

An important property of the exponential run time distribution is that the probability for a cell to tumble at a given time is independent of all previous tumbling events. To see this, we determine the conditional probability  $P$  that tumbling occurs in the interval  $[t, t + \Delta t]$ , provided that it has not occurred during  $[0, t]$ . For small time intervals  $\Delta t \ll \lambda^{-1}$ ,  $P$  becomes

$$P = \frac{\int_t^{t+\Delta t} dt' f(t')}{1 - \int_0^t dt' f(t')} = 1 - e^{-\lambda \Delta t} \approx \lambda \Delta t, \quad (2.54)$$

and is independent of time  $t$ . Similarly, one shows that the probability  $p_k$  that  $k$  tumbling events occur during a time interval of length  $t$  is given by the Poisson distribution [35],

$$p_k = \frac{(\lambda t)^k}{k!} e^{-\lambda t}, \quad (2.55)$$

which we will encounter again in Eq. (3.7) of Sec. 3.2.1.

In the following, we adopt the approach by Condat *et al.* from Ref. [61]. Each tumbling event generates a random reorientation of the velocity direction, and afterwards the particle performs a run, which we specify only by its associated mean-squared displacement  $Q_{\text{run}}(t)$ . We consider the MSD  $Q_{\text{run}}(t)$  during a run as a known function; for straight ballistic runs, it is given by  $Q_{\text{run}}(t) = v^2 t^2$ . The MSD  $Q(t)$  for the integrated random walk process with run and tumbling events is determined by the integral equation

$$Q(t) = F(t)Q_{\text{run}}(t) + \int_0^t dt' f(t') \left[ Q_{\text{run}}(t') + Q(t - t') \right], \quad (2.56)$$

where we introduced the “survival probability”  $F(t) = 1 - \int_0^t dt' f(t') = e^{-\lambda t}$  that a run starting at time  $t = 0$  is not interrupted before time  $t$ . The first term on the right-hand side of Eq. (2.56) is the contribution of a single, non-interrupted run; the

second term describes a run which is interrupted at time  $t' < t$ , together with all successive run contributions.

To solve Eq. (2.56), we write

$$Q(t) - \int_0^t dt' f(t') Q(t-t') = F(t) Q_{\text{run}}(t) + \int_0^t dt' f(t') Q_{\text{run}}(t') =: Z(t), \quad (2.57)$$

where we have defined the auxiliary function  $Z(t)$ . The Laplace transform of a function  $g(t)$  reads  $\tilde{g}(s) = \int_0^\infty dt g(t)e^{-st}$ . Applying the convolution theorem, we first solve Eq. (2.57) for the MSD in Laplace space, and obtain  $Q(t)$  after an inverse Laplace transform:

$$\tilde{Q}(s) = \frac{\tilde{Z}(s)}{1 - \tilde{f}(s)} \quad \Leftrightarrow \quad Q(t) = \frac{2v^2}{\lambda^2} (\lambda t - 1 + e^{-\lambda t}). \quad (2.58)$$

The mean-squared displacement  $Q(t)$  is identical to the MSD of an active walker with rotational diffusion of the velocity direction [Eq. (2.46)], when the noise strength  $q_\varphi$  is replaced by the tumbling rate  $\lambda$ . For times  $t \ll \lambda^{-1}$  smaller than the mean run time  $\lambda^{-1}$ , the motion is ballistic; for large times  $t \gg \lambda^{-1}$ , the motion is purely diffusive with diffusion coefficient  $D = v^2/(2\lambda)$ .

In a more detailed view, the runs are not completely straight and described by ballistic motion, but in addition there is rotational diffusion of the velocity direction, such that the mean-squared displacement during a run is given by Eq. (2.46). Hence, we can define this MSD as  $Q_{\text{run}}(t)$  and perform the analogous calculation for the integrated MSD  $Q(t)$ : Remarkably, the time dependence of  $Q(t)$  remains the same as in Eq. (2.58) and the inverse time scale  $\lambda^{-1}$  is replaced by  $\lambda^{-1} + q_\varphi$ . We will revisit this result in Chapter 3.2, where we present a more precise and quantitative description of run-and-tumble motion.

## 2.4 Chemotaxis

So far, we have considered non-directional random walks that are characterized by a diffusion coefficient  $D$ . For these random walks, the drift velocity  $\mathbf{v}_{\text{drift}} = \lim_{t \rightarrow \infty} \frac{\langle \mathbf{r}(t) - \mathbf{r}(0) \rangle}{t}$  is zero. This is usually true for microorganisms in a homogeneous environment.

In a non-homogeneous system, most microorganisms are able to bias their motion in response to an external stimulus. That means they move along the gradient of a guiding field with non-vanishing drift speed. This directed motion is denoted as “taxis” and specified by the type of guiding field. To convey an impression of nature’s ideas, we present some examples for stimuli and the resulting taxis in Table 2.1, which is taken from Ref. [8].

In this work, we focus exclusively on chemotaxis, which is the directed motion of microorganisms to spatial regions of higher or lower concentration of a chemical

Term	Stimulus	Examples of responsive species
Chemotaxis	Chemical	Bacteria, amoebae, leukocytes, sperm cells
Phototaxis	Light	Bacteria, archaea, amoebae
Thermotaxis	Temperature	Bacteria, ciliates, nematodes, leukocytes
Galvanotaxis	Electrical current	Bacteria, spermatozoa
Magnetotaxis	Magnetic field	Bacteria
Gravitaxis	Gravity	Bacteria, Paramecium, flagellates

Table 2.1 ■ Examples for directed motion (“taxis”) of microorganisms in response to external stimuli. All data is taken from Eisenbach’s book on chemotaxis [8].

substance. The first case refers to positive chemotaxis in response to a chemoattractant, the latter to negative chemotaxis in response to a chemorepellent. Chemotaxis is a ubiquitous phenomenon in nature: Wound healing in the human body is enabled by the directed motion of granulocytes to the region of injury, chemotaxis makes sperm cells find their way to the ovum, and almost all kinds of primitive organisms can detect food sources [8, 62].

If the chemical is produced by the microorganisms themselves, the system exhibits “autochemotaxis”, which serves as a possible mechanism for communication between the cells. Examples for autochemotaxis are found in the bacteria *Escherichia coli* and *Salmonella typhimurium*, and the social amoeba *Dictyostelium discoideum* (*Dicty*) [63, 64, 65]. In Chapter 4, we formulate a model for a self-propelled autochemotactic walker; this model is extended in Chapter 5 to study the collective dynamics of an ensemble of autochemotactic individuals.

It is important to realize that the microscopic mechanisms to perform chemotaxis are basically different for bacteria and eukaryotic microorganisms, like amoebae, slime moulds, or algae. Eukaryotic cells, *e.g.* *Dicty* or white blood cells, are large enough so that they can detect a chemical gradient by comparing the concentration at the front and back of their cell body [65]. For our model microorganisms of Chapter 4, we assume this ability of spatial sensing. Most bacteria, however, are believed to be too small for spatial sensing, and instead use temporal sensing where the concentration is monitored over a few seconds [66]. For the bacterium *E. coli*, the temporal average is performed over the past four seconds; when the cell swims towards regions of higher concentration of chemoattractant, the run time becomes larger. We will present *E. coli*’s chemotactic response system in more detail in Chapter 3.

In the next section, we present the classical, continuum approach by Keller and Segel to describe the dynamics of chemotactic microorganisms. Though many variants and generalizations have already been developed [67, 68, 69, 70, 71], we will focus on the essential idea that the density of microorganisms is described in terms of partial differential equations.

### 2.4.1 Keller-Segel approach

In a continuum approach, the dynamics of microorganisms is described by a space- and time-dependent cell density  $\rho(\mathbf{r}, t)$ . We will mainly follow the presentation of Murray from Ref. [62]. If the total number of cells does not change over time due to proliferation or death of cells,  $\rho(\mathbf{r}, t)$  satisfies the continuity equation

$$\partial_t \rho(\mathbf{r}, t) + \nabla \cdot \mathbf{j}(\mathbf{r}, t) = 0, \quad (2.59)$$

where the flux  $\mathbf{j}(\mathbf{r}, t)$  contains contributions of diffusion and chemotactic interaction,

$$\mathbf{j}(\mathbf{r}, t) = \mathbf{j}(\mathbf{r}, t)_{\text{diffusion}} + \mathbf{j}(\mathbf{r}, t)_{\text{chemotaxis}}. \quad (2.60)$$

According to Fick's law, the diffusive component is given by  $\mathbf{j}(\mathbf{r}, t)_{\text{diffusion}} = -D_\rho \nabla \rho$  and  $D_\rho > 0$  is the macroscopic diffusion coefficient of the cells. As the cells respond to a chemical substance of concentration  $c(\mathbf{r}, t)$ , the chemotactic flux is written as a convective term, “density  $\times$  velocity”,  $\mathbf{j}(\mathbf{r}, t)_{\text{chemotaxis}} = \rho \mathbf{v}_{\text{chemotaxis}}$ , and one introduces the macroscopic chemotactic drift velocity

$$\mathbf{v}_{\text{chemotaxis}} = \chi(c) \nabla c, \quad (2.61)$$

where  $\chi(c)$  is the chemotactic sensitivity. In general,  $\chi(c)$  depends on the concentration  $c(\mathbf{r}, t)$  and we will give specific examples for  $\chi(c)$  below. Note that Eq. (2.61) assumes that the drift motion is along the gradient of the chemical.

To obtain a closed system of equations, we need a balance equation for the chemical. As the chemical diffuses with diffusion coefficient  $D_c$ , a general ansatz for  $c(\mathbf{r}, t)$  is a reaction-diffusion equation,

$$\partial_t c(\mathbf{r}, t) = D_c \nabla^2 c + \text{“reaction term”}, \quad (2.62)$$

where the “reaction term” is a function of  $c$  and  $\rho$ . A minimal model for autochemotaxis contains the production of chemical by the cells at a constant rate  $h$ . In addition, one includes an overall decay of chemical due to enzymatic reactions in the environment which, for simplicity, also occurs at a constant rate  $k$ . In this case, the reaction term reads  $h\rho - kc$ . Both equations for  $\rho$  and  $c$  constitute the Keller-Segel model for chemotaxis:

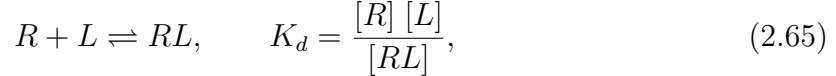
$$\partial_t \rho = D_\rho \nabla^2 \rho - \nabla[\rho \chi(c) \nabla c], \quad (2.63a)$$

$$\partial_t c = D_c \nabla^2 c + h\rho - kc. \quad (2.63b)$$

In the simplest approach,  $\chi(c) = \chi_0$  is constant. The absolute value of  $\chi_0$  measures the strength of chemotaxis, while its sign distinguishes between attractive ( $> 0$ ) and repulsive ( $< 0$ ) interactions. More evolved models for  $\chi(c)$  take into account that the chemotactic sensitivity decreases for larger  $c$ , *e.g.*,

$$\text{log law } \chi(c) = \frac{\chi_0}{c}, \quad \text{receptor law } \chi(c) = \frac{\chi_0 K_d}{(K_d + c)^2}, \quad (2.64)$$

with constant  $K_d > 0$ . Here, we sketch how the receptor law stems from changes of occupied receptors of the microorganisms, see also Refs. [72, 73]. Say, each cell has a constant number of chemoreceptors on its surface. Each receptor is either in empty state or occupied by a ligand molecule of the chemical. The concentrations of free receptors  $[R]$ , ligands  $[L]$ , and receptor-ligand complexes  $[RL]$  are connected by the law of mass action,



where  $K_d > 0$  is the binding dissociation constant. Using Eq. (2.65) and  $[L] = c$ , the fraction of occupied receptors  $f$  becomes

$$f = \frac{[RL]}{[RL] + [R]} = \frac{c}{K_d + c}. \quad (2.66)$$

Taking the total time derivative and applying the chain rule gives

$$\frac{df}{dt} = \frac{df}{dc} \frac{dc}{dt} = \frac{K_d}{(K_d + c)^2} \frac{dc}{dt}, \quad (2.67)$$

where we recover the concentration dependence of the receptor law. For small  $c$ , the chemotactic sensitivity is almost constant, while for large  $c$  all receptors are occupied such that a chemotactic response disappears and  $\chi(c) \rightarrow 0$ .

Later on, in Chapters 4 and 5, we will use the balance equation (2.63b). To characterize the diffusion of the chemical substance, we briefly focus on the case where  $\rho$  is a delta-peaked density, centered at the origin:

$$\partial_t c(\mathbf{r}, t) = D_c \nabla^2 c(\mathbf{r}, t) + h\delta(\mathbf{r}) - kc(\mathbf{r}, t). \quad (2.68)$$

Integrating Eq. (2.68) over the  $d$ -dimensional space gives a balance equation for the total amount of chemical  $C(t) = \int d^d r c(\mathbf{r}, t)$ , which is readily solved:

$$\partial_t C(t) = h - kC(t) \quad \Rightarrow \quad C(t) = \frac{h}{k} (1 - e^{-kt}). \quad (2.69)$$

For large times  $t \gg k^{-1}$ ,  $C(t) = h/k$  saturates; for vanishing decay rate  $k = 0$ , the amount of chemical increases linearly with time as  $C(t) = ht$ .

To identify a characteristic length scale of Eq. (2.68), we look for stationary solutions  $c_{\text{stat}}(\mathbf{r})$ . For  $\partial_t c_{\text{stat}} = 0$ , one obtains a Helmholtz differential equation (also called a screened Poisson equation),

$$\left( \nabla^2 - \frac{1}{l_c^2} \right) c_{\text{stat}}(\mathbf{r}) = -\frac{h}{D_c} \delta(\mathbf{r}), \quad (2.70)$$

where we have introduced the “screening length”  $l_c = \sqrt{D_c/k}$ . The fundamental solutions of Eq. (2.70) in  $d$  dimensions read

$$c_{\text{stat}}(\mathbf{r}) = \begin{cases} \frac{h}{2D_c} l_c \exp(-|\mathbf{r}|/l_c), & d = 1, \\ \frac{h}{2\pi D_c} K_0(|\mathbf{r}|/l_c), & d = 2, \\ \frac{h}{4\pi D_c} \frac{1}{|\mathbf{r}|} \exp(-|\mathbf{r}|/l_c) & d = 3, \end{cases} \quad (2.71)$$

where  $K_0$  denotes the modified Bessel function of the second kind and zeroth order. According to Eq. (2.71),  $l_c$  is indeed the characteristic length of chemical spread. For  $k = 0$ ,  $l_c$  diverges and the Helmholtz equation reduces to the Poisson equation. In analogy to electrostatics, the concentration corresponds to the electric potential  $\Phi(\mathbf{r})$  that is generated by a point charge  $q$  at the origin with charge density  $q\delta(\mathbf{r})$ . In SI units, the Poisson equation reads  $\nabla^2\Phi(\mathbf{r}) = -q/\varepsilon_0\delta(\mathbf{r})$ , so we identify  $h/D_c$  with the term  $q/\varepsilon_0$  where  $\varepsilon_0$  is the vacuum permittivity. For  $d = 3$ , the solution (2.71) is the Yukawa potential of a screened charge, and for  $k = 0$  it reduces to the Coulomb potential.

The solution of the full time-dependent balance equation (2.63b) is expressed in terms of the Green’s function

$$G(\mathbf{r}, t) = \frac{1}{(4\pi D_c t)^{d/2}} \exp\left(-\frac{\mathbf{r}^2}{4D_c t} - kt\right) \quad (2.72)$$

by a convolution with the density  $\rho(\mathbf{r}, t)$  as

$$c(\mathbf{r}, t) = \int_{\mathbb{R}^d} d^d r' \int_{-\infty}^t dt' h\rho(\mathbf{r}', t') G(\mathbf{r} - \mathbf{r}', t - t'). \quad (2.73)$$

The Keller-Segel equations describe the dynamics of the macroscopic densities of microorganisms and chemical. However, recent experimental techniques, which allow for a better single-cell tracking, have raised the interest to model also the dynamics of individual cells in a particle-based approach, for instance, by formulating Langevin equations for each cell [74]. A lot of research has gone into how equations for macroscopic cell densities, such as the Keller-Segel model, are strictly derived from the more “fundamental” microscopic approach for single cells. For example, though Eq. (2.61) for the macroscopic chemotactic drift velocity looks physically intuitive, its rigorous derivation from microscopic single-cell quantities is not obvious *a priori* [75].

In the model for chemotactic aggregation of Ref. [76], Newman and Grima study the overdamped Langevin dynamics of individual cells that continuously emit a chemical of concentration  $c$  according to Eq. (2.63b). Each point-particle is driven by the chemotactic force  $\propto \chi \nabla c(\mathbf{r}, t)$  with constant  $\chi$ , which is the microscopic version of the chemotactic drift speed from Eq. (2.61),

$$\frac{d}{dt} \mathbf{r}(t) = \chi \nabla c + \sqrt{2D} \boldsymbol{\Gamma}(t), \quad (2.74)$$

and  $\boldsymbol{\Gamma}(t)$  denotes the normalized Gaussian white noise as in Eq. (2.2). Rewriting the dynamics in a kinetic equation, which is similar to a Fokker-Planck equation, it is shown in Ref. [76] that a mean-field approximation of the model gives the Keller-Segel equations (2.63). The mean-field approach neglects correlations between the cells. It is remarkable that this derivation of the Keller-Segel model is independent of the number of cells, *i.e.*, it does not require a “thermodynamic” limit of a large number of cells. Note that we will present a calculation similar to the derivation of the kinetic equation in Chapter 6.

Depending on the kind of microorganisms, the Keller-Segel equations can be taken as a starting point to model specific experimental results. For the autochemotactic bacteria *Escherichia coli* and *Salmonella typhimurium*, a variety of chemotactic patterns, such as swarming rings and symmetrical arrays of high-density aggregates, were observed [77, 78, 64]; many of these patterns were described theoretically by extended Keller-Segel models, see *e.g.* Refs. [79, 80].

### 2.4.2 Chemotactic collapse

An interesting property of the simple Keller-Segel model is the “chemotactic collapse”. If the density of cells exceeds a critical threshold, the density will collapse into a single delta-peaked distribution [81, 82]. Equivalently, for fixed density, there exists a minimal chemotactic sensitivity that induces the collapse. The chemotactic collapse occurs within finite time and is independent of initial conditions for the densities of cells and chemical.

Here, we prove the condition for the collapse in a simplified version of the Keller-Segel model in two dimensions, where the decay rate of the chemical is zero ( $k = 0$ ). The following calculation can be found, for instance, in Ref. [81]. The reduced Keller-Segel model is obtained for the biologically relevant case that the diffusion of the chemical is much faster compared to the diffusion of the cells,  $D_c/D_\rho \ll 1$  [83]. Thus, we consider a stationary distribution of chemical and set  $\partial_t c = 0$  in Eq. (2.63b),

$$\partial_t \rho = D_\rho \nabla^2 \rho - \chi \nabla [\rho \nabla c], \quad (2.75a)$$

$$0 = D_c \nabla^2 c + h \rho, \quad (2.75b)$$

where the chemotactic sensitivity  $\chi > 0$  is constant. The continuity equation (2.75a) together with vanishing density at infinity results in a constant number of particles  $N = \int d^2r \rho(\mathbf{r}, t)$ . We will show that the chemotactic collapse occurs if the sensitivity  $\chi$  is larger than

$$\chi_{\text{collapse}} = 8\pi \frac{D_\rho D_c}{hN}. \quad (2.76)$$

To identify the chemotactic collapse, we show that the second moment of the density

$$A(t) = \int d^2r \rho(\mathbf{r}, t) \mathbf{r}^2, \quad (2.77)$$

becomes negative within finite time. The solution of Eq. (2.75b) for  $c$  reads

$$c(\mathbf{r}, t) = -\frac{h}{2\pi D_c} \int d^2 r' \rho(\mathbf{r}', t) \ln(|\mathbf{r} - \mathbf{r}'|/r_0), \quad (2.78)$$

where  $r_0 > 0$  is a constant. We will evaluate the time derivative of  $A(t)$  and show that it becomes negative for  $\chi > \chi_{\text{collapse}}$ . First, we find

$$\frac{d}{dt} A(t) = \int d^2 r \mathbf{r}^2 \frac{\partial}{\partial t} \rho(\mathbf{r}, t) \quad (2.79a)$$

$$= \int d^2 r \mathbf{r}^2 \nabla [D_\rho \nabla \rho - \chi \rho \nabla c] \quad (2.79b)$$

$$= 4D_\rho \int d^2 r \rho + 2\chi \int d^2 r \mathbf{r} \rho(\mathbf{r}, t) \nabla c(\mathbf{r}, t), \quad (2.79c)$$

where we used Eq. (2.75a) and performed two partial integrations. To evaluate the second term in Eq. (2.79c), we insert the gradient  $\nabla c(\mathbf{r}, t)$  and symmetrize the integrand with respect to  $\mathbf{r}$  and  $\mathbf{r}'$ :

$$2 \int d^2 r \int d^2 r' \frac{\mathbf{r} \cdot (\mathbf{r} - \mathbf{r}')}{|\mathbf{r} - \mathbf{r}'|^2} \rho(\mathbf{r}, t) \rho(\mathbf{r}', t) \quad (2.80a)$$

$$= \int d^2 r \int d^2 r' [\mathbf{r} \cdot (\mathbf{r} - \mathbf{r}') + \mathbf{r}' \cdot (\mathbf{r}' - \mathbf{r})] \frac{\rho(\mathbf{r}, t) \rho(\mathbf{r}', t)}{|\mathbf{r} - \mathbf{r}'|^2} \quad (2.80b)$$

$$= \int d^2 r \rho(\mathbf{r}, t) \int d^2 r' \rho(\mathbf{r}', t) \quad (2.80c)$$

$$= N^2. \quad (2.80d)$$

Finally, we arrive at

$$\frac{d}{dt} A(t) = 4D_\rho N - \frac{\chi h N^2}{2\pi D_c}, \quad (2.81)$$

which leads to  $\frac{d}{dt} A(t) < 0$  and  $A(t) < 0$  for  $\chi h N > 8\pi D_\rho D_c$ . This proves the proposition from Eq. (2.76). For fixed  $\chi$ , one can also determine a critical particle number  $N$  above which the collapse occurs.

The presented calculation also works in the limit of a small decay rate  $k$ . According to Eq. (2.71), the solution to  $0 = D_c \nabla^2 c + h\rho - kc$  is

$$c(\mathbf{r}, t) = \frac{h}{2\pi D_c} \int d^2 r' \rho(\mathbf{r}', t) K_0(|\mathbf{r} - \mathbf{r}'|/l_c). \quad (2.82)$$

Using  $\frac{d}{dx} K_0(x) = -K_1(x)$ , the analogous equation to (2.81) reads

$$\begin{aligned} \frac{d}{dt} A(t) &= 4D_\rho N - \frac{\chi h}{2\pi D_c l_c} \\ &\times \int d^2 r \int d^2 r' |\mathbf{r} - \mathbf{r}'| K_1(|\mathbf{r} - \mathbf{r}'|/l_c) \rho(\mathbf{r}, t) \rho(\mathbf{r}', t). \end{aligned} \quad (2.83)$$

For small  $k$  or large chemotactic range  $l_c = \sqrt{D_c/k}$ , we use the expansion  $K_1(x) \approx 1/x$  for  $x \ll 1$  [84]; as a consequence, Eq. (2.83) coincides with Eq. (2.81), and we obtain the same critical condition.

To close our analysis of the Keller-Segel model, we explain how macroscopic pattern formation is recognized. Details of the linear stability analysis are found in Refs. [85, 80]. We consider the full Keller-Segel model (2.63) with constant  $\chi$  and non-vanishing decay rate of chemical  $k \neq 0$ . For both densities, homogeneous solutions exist, which we denote as  $\rho_0$  and  $c_0$ . We expand a perturbation of the homogeneous solutions in plane waves,

$$\rho(\mathbf{r}, t) = \rho_0 + \varepsilon \sum_{\mathbf{q}} f_{\mathbf{q}}(t) e^{i\mathbf{q} \cdot \mathbf{r}}, \quad c(\mathbf{r}, t) = c_0 + \varepsilon \sum_{\mathbf{q}} g_{\mathbf{q}}(t) e^{i\mathbf{q} \cdot \mathbf{r}}, \quad (2.84)$$

where  $0 < \varepsilon \ll 1$ , and the sums extend over all possible “wave vectors”  $\mathbf{q}$ . Next, we insert the expressions (2.84) into the Keller-Segel equations and derive equations for the amplitudes  $f_{\mathbf{q}}(t)$  and  $g_{\mathbf{q}}(t)$  up to first order in  $\varepsilon$ . When we search for solutions  $f_{\mathbf{q}}(t)$ ,  $g_{\mathbf{q}}(t)$  of exponential form  $\propto \exp(\lambda t)$ , we determine the parameter  $\lambda$  explicitly. If the homogeneous solutions are stable the real part of  $\lambda$  must be negative; in contrast, pattern formation corresponds to stable non-homogeneous solutions and requires a positive real part of  $\lambda$ . In the long-wavelength limit with  $|\mathbf{q}| \rightarrow 0$ , the condition for pattern formation becomes  $\chi h \rho_0 > k D_\rho$ . This means that pattern formation requires a chemotactic sensitivity  $\chi$  above

$$\chi_{\text{pattern}} = \frac{k D_\rho}{h \rho_0}. \quad (2.85)$$

For a system with confined area  $A$ , we can write the homogeneous density as  $\rho_0 = \frac{1}{A} \int_A d^2 r \rho(\mathbf{r}, t) = N/A$ . Hence, the critical sensitivity for pattern formation scales with the particle number  $N$  as  $\chi_{\text{pattern}} \propto 1/N$ .

# 3 Swimming strategies of bacteria

## 3.1 Introduction

For the initial stage of biofilm formation, swimming of bacteria marks a relevant step. It enables the cells to approach the surface where the biofilm forms. This fact motivates us to study different swimming strategies of bacteria.

We focus on the enteric bacterium *Escherichia coli* and the marine bacterium *Vibrio alginolyticus*. Both species have been investigated experimentally and theoretically and serve as a role model for the “run-and-tumble” and “run-reverse-flick” swimming strategies. In addition, a large number of marine bacteria, *e.g.* *Shewanella putrefaciens* or *Pseudoalteromonas haloplanktis*, performs the so-called “run-reverse” motion. Before we give the outline of this chapter in Sec. 3.1.4, we present the basic principles of these three swimming mechanisms. We illustrate why we are interested in comparing the different strategies in terms of the cells’ diffusion coefficient and chemotactic drift speed with which they can swim towards a food source. Put differently, we will explain that our rigorous analysis of diffusion coefficient and chemotactic drift speed allows us to assess the “swimming performance” of bacteria.

### 3.1.1 Run-and-tumble strategy (*E. coli*)

The bacterium *E. coli* is one of the best-studied microorganisms and its genome and biochemistry of internal processes are completely deciphered [86, 8]. The research in the 1970s, when physicists around Howard Berg began to study the motility of *E. coli*, contributed to the establishment of biophysics as a new branch of soft condensed matter physics. *E. coli* is a rod-shaped bacterium of about  $1\text{ }\mu\text{m}$  in diameter and  $2\text{ }\mu\text{m}$  in length [35]. Over the entire cell body, appendages called flagella are located, which are up to  $10\text{ }\mu\text{m}$  long and only  $20\text{ nm}$  thin. Each flagellum is anchored to a motor, which makes it rotate counterclockwise (CCW) or clockwise (CW). When all flagella rotate CCW (when looking from behind the bacterium), hydrodynamic interactions result in the formation of a flagellar bundle and the bacterium is pushed forward in an almost straight line with a characteristic speed of  $v = 15 \dots 30\text{ }\mu\text{m s}^{-1}$ . This motion lasts for  $\sim 1\text{ s}$  and is called a “run”. It is interrupted when at least one flagellum rotates CW and the bundle comes apart [87]. This event of  $\sim 0.1\text{ s}$  duration is called “tumbling”, during which the bacterium’s center of mass almost does not move, but which reorients its swimming direction.

$D_r$	[rad $^2$ s $^{-1}$ ]	0.062	Ref. [59]	0.2	Ref. [88]	0.32	Ref. [89]
$\tau_{\text{rot}}$	[s]	8.1		2.5		1.6	

Table 3.1 ■ Rotational diffusion coefficients  $D_r$  of *E. coli* found in the literature, together with the corresponding time scales  $\tau_{\text{rot}} = 1/(2D_r)$ , on which directional correlations decay.

If the new swimming direction after a tumbling event were randomly chosen the mean angular change between successive runs would be 90°; however, *E. coli* prefers swimming in the forward hemisphere with a mean angular change of  $\Delta\varphi \sim 70^\circ$ . The persistence of motion can be captured by the parameter  $\alpha = \langle \cos \Delta\varphi \rangle \in [-1, 1]$ , which is the mean cosine of the angle  $\Delta\varphi$  between successive runs. For totally random reorientations one obtains  $\alpha = 0$ , whereas for *E. coli*  $\alpha = 0.33$ .

The idealized swimming pattern of *E. coli* thus consists of two alternating steps and is called run-and-tumble. In the simplest modeling approach, swimming during a run follows a straight line. However, rotational diffusion due to thermal noise is always present and during a single run of  $\sim 1$  s the direction of motion can change up to  $\sim 30^\circ$ . This corresponds to a rotational diffusion coefficient  $D_r$  on the order of 0.1 rad $^2$  s $^{-1}$  (or, 0.1 s $^{-1}$  in short notation). If we model the bacterium as a colloidal sphere of radius  $a = 1$   $\mu\text{m}$ , we can estimate  $D_r$  by using the Stokes-Einstein relation  $D_r = k_B T / \gamma_r$  for thermal diffusion with the rotational friction coefficient  $\gamma_r = 8\pi\eta a^3$ . For experiments at room temperature, in water with viscosity  $\eta = 10^{-3}$  kg m $^{-1}$  s $^{-1}$ , and with a thermal energy  $k_B T = 4$  pN nm, one obtains  $D_r = 0.16$  s $^{-1}$ . This value is close to the standard reference  $D_r = 0.062$  s $^{-1}$  taken from Berg's seminal experiments. According to Eq. (2.34), the characteristic time scale on which directional correlations decay exponentially is given by  $\tau_{\text{rot}} = 1/(2D_r)$ . Values for the rotational diffusion coefficient of *E. coli* may strongly depend on experimental conditions and therefore vary in the literature. For this reason, we have summarized possible values of  $D_r$  and  $\tau_{\text{rot}}$  in Table 3.1.

Finally, the run time is not constant, but a random variable, which is exponentially distributed and depends on the “tumbling rate”  $\lambda = 1$  s $^{-1}$ , corresponding to a mean run time of  $\tau_{\text{run}} = \lambda^{-1} = 1$  s [59]. Throughout this chapter, we will assume an exponential run time distribution. Note, however, that recent experiments have revealed a power law distribution of run times for *E. coli* [90]. As a tumbling event is one order of magnitude shorter than a run event, we model tumbling to happen instantaneously and neglect the tumbling time. Finite tumbling times have been considered in some theoretical investigations, *e.g.* in Ref. [91], and can also easily be implemented in numerical simulations of a random walk.

In a homogeneous environment, the random walk of *E. coli* is unbiased and its motility is described by the diffusion coefficient  $D$ . For run-and-tumble motion in three dimensions with constant speed  $v$  and persistence parameter  $\alpha$ , Lovely and

Dahlquist [92] have calculated the diffusion coefficient

$$D = \frac{v^2}{3[\lambda(1 - \alpha) + 2D_r]} . \quad (3.1)$$

The first term in the denominator stems from the run-and-tumble motion and the second accounts for rotational diffusion during the runs; we discuss this result also later on.

A food source usually acts as a chemoattractant for bacteria. The chemotactic apparatus of *E. coli* enables it to bias its random walk such that it approaches a food source with a chemotactic drift velocity. Most bacteria are assumed to be too small to directly measure a spatial concentration gradient of a chemical, and instead perform temporal sensing. *E. coli* compares the concentration of a chemical sensed over the past second with that from the preceding three seconds [93]. When *E. coli* swims in the favorable direction of the gradient  $\nabla c$ , *i.e.* towards an increasing concentration, the runs become longer [59]. The presence of a chemoattractant altering the tumbling rate is accounted for by a convolution of the concentration with an internal response function of the cell, as described by de Gennes [94]. This modulation of the tumbling rate generates a chemotactic drift speed  $v_d$  in the direction of the gradient, which can be up to 10...20% of the swimming speed  $v$  [35, 95]. De Gennes' calculation of  $v_d$  for small gradients neglects rotational diffusion during runs and persistence of direction between successive runs. These features have been incorporated later on by Locsei [96]: His results show that a higher persistence parameter  $\alpha$  enhances  $v_d$ , while the presence of rotational diffusion decreases  $v_d$ .

Both the chemotactic drift speed  $v_d$  and the diffusion coefficient  $D$  are important measures to compare the performance of bacteria. For an optimal performance, transiently, bacteria should quickly approach a nutrient source; once they have accumulated close to the source, they should remain localized at the same place [97]. The first requirement is equivalent to maximizing  $v_d$ , and the second –in a rough picture— corresponds to a small diffusion coefficient  $D$ . In a homogeneous environment, a large diffusion coefficient enables a bacterium to effectively explore its environment for foraging.

### 3.1.2 Run-reverse strategy

In the oceans, a variety of marine bacteria, such as *Shewanella putrefaciens* or *Pseudoalteromonas haloplanktis*, is found that swim with a run-reverse strategy [98]. Whereas their size is comparable to *E. coli*, the majority of marine bacteria has only a single flagellum attached to one end of the cell body. This simply provides one gear for swimming: CCW rotation of the flagellum results in forward motion, CW rotation results in backward motion. Very high swimming speeds of up to  $400 \mu\text{m s}^{-1}$  have been reported for marine bacteria, *i.e.*, they may exceed *E. coli*'s speed by one order of magnitude [99].

Conceptually, the run-reverse swimming pattern is identical to the run-and-tumble pattern. Again, a run denotes motion with almost constant speed, along with rotational diffusion of the swimming direction. However, in contrast to *E. coli*, the direction of motion between successive runs is reversed with  $\Delta\varphi = 180^\circ$ . This anti-correlation corresponds to a minimal value for the persistence parameter  $\alpha = -1$  and the result for the diffusion coefficient of run-and-tumble motion is still valid [Eq. (3.1)]. The benefits of run-reverse for marine bacteria as compared to run-and-tumble motion are still a subject of current research; for instance, theoretical studies showed that run-reverse motion under high shear in the turbulent regime of an ocean allows cells to stay closer to nutrient sources, compared to run-and-tumble swimmers [100].

Another important bacterium that uses the run-reverse strategy is the pathogen *Pseudomonas aeruginosa* [101, 102]; due to its clinical relevance, the characteristic biofilm formation of *P. aeruginosa* has been thoroughly studied [3, 103]. Finally, we refer to the species of myxobacteria and their most famous representative, the rod-shaped soil bacterium *Myxococcus xanthus* [104]. Though the underlying motility that enables these cells to glide over moist surfaces is entirely different from swimming, we mention that also myxobacteria periodically reverse their direction of motion [105].

#### 3.1.3 Run-reverse-flick strategy (*V. alginolyticus*)

*Vibrio alginolyticus* is a marine bacterium that causes wound infection and otitis in humans [106]. It possesses only a single flagellum that enables back-and-forth motion with a characteristic speed of  $v = 40 \dots 70 \mu\text{m s}^{-1}$  [107, 108]. From experimental observations, it was originally assumed that *V. alginolyticus* also follows the run-reverse swimming pattern of marine organisms [109].

However, recent experiments by Xie *et al.* revealed an additional “step” in the motility of *V. alginolyticus*, indicating that the bacterium performs a periodic three-step mechanism [110]:

- (1.) Forward swimming: Flagellum rotates CCW.
- (2.) Backward swimming: Flagellum rotates CW.
- (3.) Randomization of swimming direction: Flagellum “flicks”.

While the mean run times for forward and backward swimming are  $\sim 0.3 \text{ s}$ , the flick occurs much faster and its duration is therefore neglected in the following considerations.

In Ref. [110], it was stated that the diffusion coefficient of a run-reverse-flick swimmer is zero for equal mean forward and backward run times. Even without any calculations, it is hard to imagine that a run-reverse-flick swimmer should not

diffuse at all for large times, especially because the run durations are statistically distributed. This statement motivated us to determine the diffusion coefficient under the assumption of an exponential run time distribution, for which the diffusion coefficient is not zero. To generalize the two-step random walk, we introduce two persistence parameters  $\alpha$  and  $\beta$ . The persistence between a forward and backward run with  $\Delta\varphi_1 = 180^\circ$  corresponds to  $\alpha = \langle \cos \Delta\varphi_1 \rangle = -1$ ; the persistence parameter for backward run, flick event, and new forward run with  $\Delta\varphi_2 = 90^\circ$  is  $\beta = \langle \cos \Delta\varphi_2 \rangle = 0$ .

The trajectories of *V. alginolyticus* in Ref. [110] clearly contain turning angles of  $\sim 90^\circ$  due to the flick event. It is thus remarkable that its existence has not been observed earlier. Now that the flick of the flagellum has been discovered, it seems not unrealistic that more marine bacteria that have been previously classified as run-reverse swimmers, might exhibit the feature of the flick as well. Furthermore, it is still unclear why the flick occurs at all and which consequences it has for the diffusion and chemotactic drift speed of a swimmer. These consequences will be addressed in this chapter.

Our motivation to calculate the chemotactic drift speed of *V. alginolyticus* was also initiated by the statement from Ref. [111] that “*V. alginolyticus* has a threefold larger chemotactic velocity than *E. coli*”. Assuming the chemotactic response function of *E. coli*, we thus investigate whether the additional flick event in the swimming pattern is sufficient to explain a significantly larger chemotactic drift speed.

### 3.1.4 Outline of the chapter

First, in Sec. 3.2, we will analyze how a flick event affects the diffusion of a swimmer at large times. We will calculate the diffusion coefficient for a generalized random walk pattern with two alternating persistence parameters  $\alpha$  and  $\beta$ . For that purpose, we assume that the run times for forward and backward swimming are exponentially distributed with the same mean run time. Our derivation holds in two and three dimensions and will provide expressions for the directional correlation function and the mean-squared displacement. In particular, we derive an expression for the diffusion coefficient, which contains Lovely and Dahlquist’s result from Eq. (3.1) as a special case.

Second, Sec. 3.3 treats the chemotactic drift speed of *E. coli* and *V. alginolyticus* in the presence of a small external chemical gradient. To study the influence of the random walk pattern on the chemotactic drift speed, we apply the chemotactic response of *E. coli* also for *V. alginolyticus*. We close Sec. 3.3 with an outlook for alternative modeling approaches for the tumbling rate in a chemical gradient.

Third, in Sec. 3.4, we use the theoretical framework from Sec. 3.3 to explain the experimental observation that mean run times for swimming towards and away from the source of chemoattractant differ. Finally, we summarize our findings in Sec. 3.5.

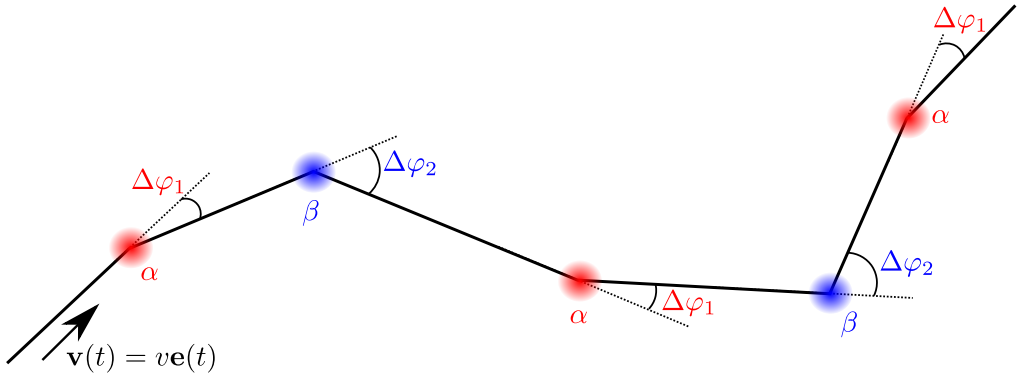


Figure 3.1 ■ Pattern of the random walk with two alternating tumbling events. The parameters  $\alpha$  and  $\beta$  correspond to the two preferred turning angles  $\Delta\varphi_1$  and  $\Delta\varphi_2$ , respectively. The walker moves with constant speed  $v$  along the direction  $\mathbf{e}(t)$ , and the run times are exponentially distributed with mean  $\tau_{\text{run}}$ .

### 3.2 Diffusion coefficient for a random walk with two alternating tumbling events

Let us first define our generalized random walk pattern in full detail. Each walker or model bacterium moves with velocity  $\mathbf{v}(t) = v \mathbf{e}(t)$ ; the speed  $|\mathbf{v}(t)| = v > 0$  is constant and the unit vector  $\mathbf{e}(t)$  denotes the direction of propagation at time  $t$ . We assume an exponential run time distribution,

$$f(t) = \lambda e^{-\lambda t}, \quad (3.2)$$

where  $\lambda$  is the tumbling rate and the mean run time reads  $\tau_{\text{run}} = \int_0^\infty dt f(t) t = \lambda^{-1}$ . We introduce two different tumbling events with preferential turning angles  $\Delta\varphi_1$ ,  $\Delta\varphi_2$ , for which we define the persistence parameters  $\alpha, \beta \in [-1, 1]$  as the ensemble averages

$$\alpha = \langle \cos \Delta\varphi_1 \rangle, \quad \beta = \langle \cos \Delta\varphi_2 \rangle. \quad (3.3)$$

We consider the following regular random walk scheme as depicted in Fig. 3.1:

- Run
- Tumbling of type  $\alpha$  at time  $t_1$ :  $\alpha = \langle \mathbf{e}(t_1^-) \cdot \mathbf{e}(t_1^+) \rangle$
- Run
- Tumbling of type  $\beta$  at time  $t_2$ :  $\beta = \langle \mathbf{e}(t_2^-) \cdot \mathbf{e}(t_2^+) \rangle$
- And so forth...

The unit vectors  $\mathbf{e}(t^\pm)$  indicate the swimming directions immediately before ( $-$ ) and after ( $+$ ) a tumbling event at time  $t$ . We assume the mean run times after both types of tumbling to be equal, and neglect the duration of tumbling. At the end of Sec. 3.2.3, we will also give an outline how to incorporate more general run time distributions.

We do not require details of the angular distribution of a tumbling event, and consider symmetric distributions around the preferential turning angles. It turns out that only the mean cosines of the turning angles,  $\alpha$  and  $\beta$ , enter the diffusion coefficient. Note that different turning angle distributions can yield the same persistence parameter. However, in the exact limiting cases of  $\alpha, \beta = \pm 1$ , only delta-peaked distributions at angles  $0$  and  $\pi$  are possible.

Our goal in the next Secs. 3.2.1 and 3.2.2 is to determine the diffusion coefficient of a random walk with two alternating tumbling events. Therefore, we first calculate the directional correlation function  $\langle \mathbf{e}(t) \cdot \mathbf{e}(t') \rangle$  for arbitrary times  $t, t'$ . The mean-squared displacement is then obtained by a double integration in time according to Eq. (2.46a), and the diffusion coefficient follows from Eq. (2.7).

### 3.2.1 Without rotational diffusion

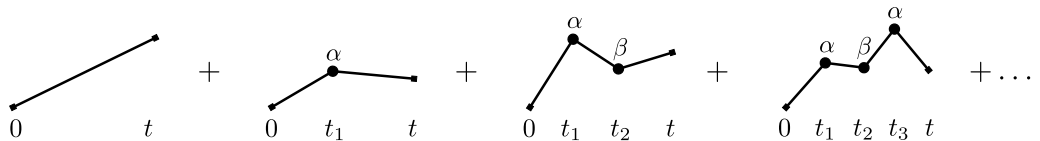
For simplicity and demonstration, we first consider a random walk without rotational diffusion during the run events. In addition to the exponential run time distribution  $f(t)$  from Eq. (3.2), we will need the “survival probability”  $F(t)$  that a run that starts at  $t = 0$  is not interrupted before time  $t$ ,

$$F(t) = 1 - \int_0^t dt' f(t') = e^{-\lambda t}. \quad (3.4)$$

Consistent with Lovely and Dahlquist [92], the preferential tumbling angles  $\Delta\varphi_1$  and  $\Delta\varphi_2$  are expressed in terms of the persistence parameters  $\alpha$  and  $\beta$ , and the directional correlation function reads:

$$\begin{aligned} & \langle \mathbf{e}(t) \cdot \mathbf{e}(0) \rangle \\ = & F(t) + \int_0^t dt_1 f(t_1) \alpha F(t - t_1) + \int_0^t dt_2 \int_0^{t_2} dt_1 f(t_1) \alpha f(t_2 - t_1) \beta F(t - t_2) \\ & + \int_0^t dt_3 \int_0^{t_3} dt_2 \int_0^{t_2} dt_1 f(t_1) \alpha f(t_2 - t_1) \beta f(t_3 - t_2) \alpha F(t - t_3) + \dots \end{aligned} \quad (3.5)$$

The interpretation of the terms on the right-hand side of Eq. (3.5) is illustrated in the following diagrams:



A run may start at  $t = 0$  and is not interrupted till  $t$ , such that the direction of motion is constant; a run may also take place from time  $0 \dots t_1$ , then tumbling of type  $\alpha$  occurs, and a second run without tumbling follows during  $t_1 \dots t$ ; the next term considers the possibility of a run  $(0 \dots t_1)$ , tumbling of type  $\alpha$  at  $t_1$ , another run  $(t_1 \dots t_2)$ , tumbling of type  $\beta$  at  $t_2$ , and one more run up to time  $t$ , etc. The emergence of products  $\alpha^{N_\alpha} \beta^{N_\beta}$  in the higher terms of Eq. (3.5) stems from the occurrence of  $N_\alpha$  and  $N_\beta$  tumbling events of type  $\alpha$  and  $\beta$ , respectively.

To calculate the infinite series in Eq. (3.5), we observe that for the exponential distribution  $f(t_1)f(t_2 - t_1) \times \dots \times f(t_n - t_{n-1})F(t - t_n) = \lambda^n e^{-\lambda t}$ . The calculation of the first emerging integrals,  $\int_0^t dt_1 = t$ ,  $\int_0^t dt_2 \int_0^{t_2} dt_1 = \frac{t^2}{2!}$ , is directly generalized to terms of higher order:

$$\underbrace{\int_0^t dt_n \int_0^{t_n} dt_{n-1} \cdots \int_0^{t_2} dt_1}_{n \text{ integrals}} = \frac{t^n}{n!}. \quad (3.6)$$

Equation (3.5) can thus be written as

$$\langle \mathbf{e}(t) \cdot \mathbf{e}(0) \rangle = e^{-\lambda t} \left[ 1 + \alpha \frac{\lambda t}{1!} + \alpha \beta \frac{(\lambda t)^2}{2!} + \alpha^2 \beta \frac{(\lambda t)^3}{3!} + \alpha^2 \beta^2 \frac{(\lambda t)^4}{4!} + \dots \right], \quad (3.7)$$

where the time-dependent terms  $e^{-\lambda t} \frac{(\lambda t)^k}{k!}$  coincide with the Poisson distribution from Eq. (2.55). Using the series expansions for the hyperbolic functions  $\sinh(x) = x + \frac{x^3}{3!} + \frac{x^5}{5!} + \dots$  and  $\cosh(x) = 1 + \frac{x^2}{2!} + \frac{x^4}{4!} + \dots$ , results in the following expression:

$$\langle \mathbf{e}(t) \cdot \mathbf{e}(0) \rangle = e^{-\lambda t} \left[ \sqrt{\frac{\alpha}{\beta}} \sinh \left( \sqrt{\alpha \beta} \lambda t \right) + \cosh \left( \sqrt{\alpha \beta} \lambda t \right) \right]. \quad (3.8)$$

Eq. (3.8) is not symmetric with respect to interchanging  $\alpha \leftrightarrow \beta$ . This reflects the fact that, so far, each random walker interrupts the first run with a tumbling event of type  $\alpha$ . However, we are interested in modeling an ensemble of walkers where the first tumbling event is either of type  $\alpha$  or  $\beta$  with the same probability.

To generalize Eq. (3.8) to an ensemble average for arbitrary times, we thus take into account that, when choosing a walker of the ensemble, the probability is  $1/2$  for the next tumbling event to be  $\alpha$  or  $\beta$ . Formally, we symmetrize Eq. (3.8) with respect to  $\alpha$  and  $\beta$ . Denoting the right-hand side of Eq. (3.8) as  $h(t)_{\alpha,\beta}$ , the correlation function becomes  $\langle \mathbf{e}(t) \cdot \mathbf{e}(t') \rangle = \frac{1}{2} [h(|t - t'|)_{\alpha,\beta} + h(|t - t'|)_{\beta,\alpha}]$ . This gives

$$\langle \mathbf{e}(t) \cdot \mathbf{e}(t') \rangle = e^{-\lambda|t-t'|} \left[ \frac{\alpha + \beta}{2\sqrt{\alpha \beta}} \sinh \left( \sqrt{\alpha \beta} \lambda |t - t'| \right) + \cosh \left( \sqrt{\alpha \beta} \lambda |t - t'| \right) \right]. \quad (3.9)$$

The following scenarios are possible:

- (i) If  $\alpha$  and  $\beta$  have the same sign,  $\sqrt{\alpha \beta}$  is real and both  $\sinh(\sqrt{\alpha \beta} \lambda |t - t'|)$  and  $\cosh(\sqrt{\alpha \beta} \lambda |t - t'|)$  are positive, such that the correlation function is always positive.

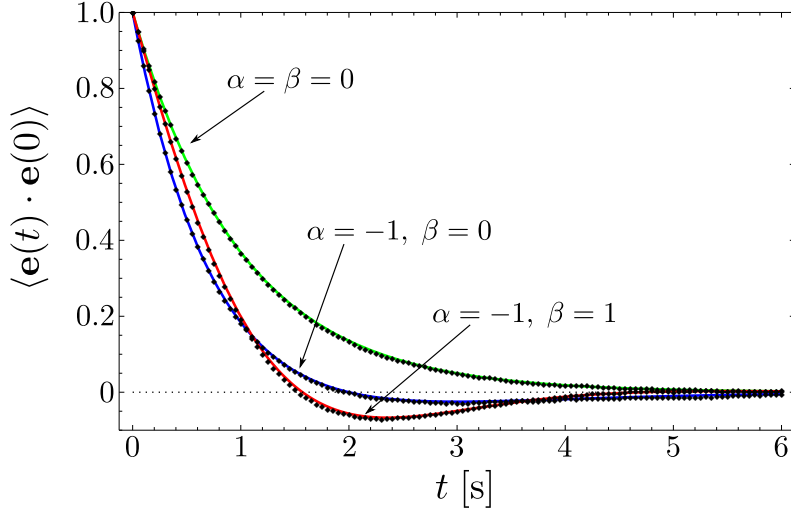


**Figure 3.2** ■ Directional correlation function  $\langle \mathbf{e}(t) \cdot \mathbf{e}(0) \rangle$  versus time  $t$  from Eq. (3.9) with  $\lambda = 1 \text{ s}^{-1}$ . For  $\alpha = \beta$ , correlations decay exponentially [Eq. (3.10)]; for the run-reverse-flick strategy ( $\alpha = -1, \beta = 0$ ), correlations become negative according to Eq. (3.11). For  $\alpha = -1$  and  $\beta = 1$ , Eq. (3.9) reduces to  $\langle \mathbf{e}(t) \cdot \mathbf{e}(0) \rangle = e^{-\lambda t} \cos(\lambda t)$ , and the negative minimum at  $t = 3\pi/(4\lambda)$  is most pronounced. The small symbols are obtained from numerical simulations and perfectly agree with the theory.

(ii) For  $\alpha = \beta$ , we obtain the well-known result of Lovely and Dahlquist [92],

$$\langle \mathbf{e}(t) \cdot \mathbf{e}(t') \rangle_{\alpha=\beta} = e^{-\lambda(1-\alpha)|t-t'|}, \quad (3.10)$$

where directional correlations decay exponentially with rate  $\lambda(1 - \alpha)$ . In the limiting case  $\alpha = \beta = 1$ , the direction of motion remains constant, and therefore  $\langle \mathbf{e}(t) \cdot \mathbf{e}(t') \rangle = 1$ .

(iii) If  $\alpha$  and  $\beta$  have opposite sign, that is successive runs are anti-correlated on average,  $\sqrt{\alpha\beta}$  is purely imaginary. Using the relations  $\sinh(ix) = i \sin(x)$  and  $\cosh(ix) = \cos(x)$  shows that the correlation function oscillates and becomes negative in particular. Negative directional correlations are also observed for  $\alpha < 0$  and  $\beta = 0$ , since

$$\langle \mathbf{e}(t) \cdot \mathbf{e}(t') \rangle_{\alpha,\beta=0} = e^{-\lambda|t-t'|} \left( 1 + \frac{\alpha\lambda}{2} |t - t'| \right). \quad (3.11)$$

To further confirm our analytical result from Eq. (3.9), we compare it to numerically obtained correlations for several combinations of  $\alpha$  and  $\beta$  in Fig. 3.2; theory and simulation fully agree.

Next, we calculate the mean-squared displacement (MSD) according to Eq. (2.46a):

$$\begin{aligned}
 & \langle [\mathbf{r}(t) - \mathbf{r}(0)]^2 \rangle \tag{3.12} \\
 &= v^2 \int_0^t dt' \int_0^{t'} dt'' \langle \mathbf{e}(t') \cdot \mathbf{e}(t'') \rangle \\
 &= \frac{v^2}{\lambda^2(1-\alpha\beta)^2} \left[ (1-\alpha\beta)(2+\alpha+\beta)\lambda t - 2(1+\alpha)(1+\beta) \right. \\
 &\quad \left. + e^{-\lambda t} \left\{ \frac{\alpha+\beta+\alpha\beta(4+\alpha+\beta)}{\sqrt{\alpha\beta}} \sinh(\sqrt{\alpha\beta}\lambda t) + 2(1+\alpha)(1+\beta) \cosh(\sqrt{\alpha\beta}\lambda t) \right\} \right].
 \end{aligned}$$

To discuss the long-time limit of Eq. (3.12), we again consider three cases:

- (i) If  $\alpha$  and  $\beta$  have the same sign,  $\sinh(\sqrt{\alpha\beta}\lambda t)$  and  $\cosh(\sqrt{\alpha\beta}\lambda t)$  asymptotically behave like  $e^{\sqrt{\alpha\beta}\lambda t}$  for  $t \rightarrow \infty$ . This implies  $e^{-\lambda t} e^{\sqrt{\alpha\beta}\lambda t} = e^{-\lambda t(1-\sqrt{\alpha\beta})} \rightarrow 0$  for large times and  $|\alpha|, |\beta| < 1$ , and only the term linear in  $t$  contributes to Eq. (3.12).
- (ii) For  $\alpha = \beta = 1$ , ballistic motion is obtained and Eq. (3.12) simplifies to  $\langle [\mathbf{r}(t) - \mathbf{r}(0)]^2 \rangle = v^2 t^2$ .
- (iii) If  $\alpha$  and  $\beta$  have opposite sign,  $\sqrt{\alpha\beta}$  is imaginary and the MSD contains oscillating functions that are suppressed by  $e^{-\lambda t}$  for large times. Hence, the MSD grows linear with time.

The diffusion coefficient of the three-dimensional random walk becomes

$$D = \lim_{t \rightarrow \infty} \frac{\langle [\mathbf{r}(t) - \mathbf{r}(0)]^2 \rangle}{6t} = \frac{v^2}{6\lambda} \frac{2+\alpha+\beta}{1-\alpha\beta}. \tag{3.13}$$

For identical tumbling events with persistence parameters  $\alpha = \beta$ , we recover Lovely and Dahlquist's result from Eq. (3.1). As expected for dimensional reasons, the diffusion coefficient scales as  $D \sim v^2/\lambda$ , while the factor containing  $\alpha$  and  $\beta$  describes the “geometric” details of the random walk. In the case of ballistic motion with  $\alpha = \beta = 1$ , the MSD scales quadratically in time and the diffusion coefficient diverges.

We can write the diffusion coefficient of Eq. (3.13) also in the form  $D = \frac{v^2}{3\lambda(1-\alpha_{\text{eff}})}$ , where the effective persistence parameter

$$\alpha_{\text{eff}} = \frac{\alpha + \beta + 2\alpha\beta}{2 + \alpha + \beta} = H(\alpha + 1, \beta + 1) - 1 \tag{3.14}$$

is expressed in terms of the harmonic mean, defined as  $H(x, y) = \frac{2xy}{x+y}$ . Alternatively, we introduce the characteristic time scale  $T$  of the random walk via  $D = v^2 T$ , which is determined by  $T^{-1} = 3\lambda[2 - H(\alpha + 1, \beta + 1)]$ . Note that our derivation of Eq. (3.13) holds in two and three spatial dimensions. In particular, the diffusion

### 3.2 Diffusion coefficient for a random walk with two alternating tumbling events

---

coefficient only depends on the mean cosine of the tumbling angles, while further details of the distributions of tumbling angles average out.

Finally, we write down explicitly the obtained quantities for the processes of run-reverse ( $\alpha = \beta = -1$ ),

$$\langle \mathbf{e}(t) \cdot \mathbf{e}(t') \rangle_{\text{run-rev}} = e^{-2\lambda|t-t'|}, \quad (3.15a)$$

$$\langle [\mathbf{r}(t) - \mathbf{r}(0)]^2 \rangle_{\text{run-rev}} = \frac{2v^2}{(2\lambda)^2} (2\lambda t - 1 + e^{-2\lambda t}), \quad D_{\alpha=\beta=-1} = \frac{v^2}{6\lambda}, \quad (3.15b)$$

and run-reverse-flick ( $\alpha = -1, \beta = 0$ ),

$$\langle \mathbf{e}(t) \cdot \mathbf{e}(t') \rangle_{\text{run-rev-flick}} = e^{-\lambda|t-t'|} \left( 1 - \frac{\lambda|t-t'|}{2} \right), \quad (3.16a)$$

$$\langle [\mathbf{r}(t) - \mathbf{r}(0)]^2 \rangle_{\text{run-rev-flick}} = \frac{v^2}{\lambda} t (1 - e^{-\lambda t}), \quad D_{\alpha=-1, \beta=0} = \frac{v^2}{6\lambda}. \quad (3.16b)$$

The correlation functions and MSDs have different functional forms for both processes; we observe that the form of the MSD for the run-reverse strategy is the same as for an active walker with rotational diffusion of the velocity direction [Eq. (2.46b)]. Correlations in the run-reverse mode decay with the time constant  $1/(2\lambda)$ , whereas in the presence of the randomizing flick event they decay twice as fast on the time scale  $1/\lambda$ . Moreover, the “anti-correlation” between the alternating tumbling events for run-reverse-flick manifests in a negative correlation function for time differences larger  $2/\lambda$ .

The most striking feature, however, is that the diffusion coefficients are identical. This means that, in a scenario without rotational diffusion, the additional flick has no effect on the diffusion coefficient of a run-reverse swimmer. To better understand this probably counterintuitive result, we imagine a trajectory of a run-reverse swimmer along a single line. In a plane, the flicking angle of  $90^\circ$  results mainly in additional path segments perpendicular to this single line. However, our result indicates that all these perpendicular contributions cancel each other for the resulting diffusion.

Indeed, an inspection of Eq. (3.13) reveals that for  $\alpha = -1$  the diffusion coefficient no longer depends on  $\beta$ ,

$$D_{\alpha=-1} = \frac{v^2}{6\lambda}, \quad \text{for all } \beta. \quad (3.17)$$

In the next section, we will see that this degeneracy in  $\beta$  will vanish if one takes into account rotational diffusion during the run events. To complete the discussion of Eq. (3.13), we point out that  $D$  does not become zero as it was concluded for the run-reverse-flick strategy in Ref. [110]. This indicates that a swimmer with arbitrary  $\alpha$  and  $\beta$  always diffuses for large times, as long as the distribution of run times is exponential. Only if there were no rotational diffusion during runs and the run times were fixed, the diffusion coefficient would be zero.

To close, we present the diffusion coefficient for *E. coli*. Estimating the persistence parameter as  $\alpha \approx 1/3$ , we arrive at

$$D_{\text{run-tumble, } E.\text{coli}} = \frac{v^2}{2\lambda}, \quad (3.18)$$

which is three times larger than for the run-reverse and run-reverse-flick process.

### 3.2.2 Rotational diffusion included

As we showed in Chapter 2.3.1, three-dimensional rotational diffusion with rotational diffusion constant  $D_r$  leads to  $\langle \mathbf{e}(t) \cdot \mathbf{e}(t') \rangle = \exp(-2D_r|t - t'|)$ . Recall that in two dimensions the factor of two in the exponential is missing. Including rotational diffusion during run events, Eq. (3.5) is modified according to

$$\begin{aligned} & \langle \mathbf{e}(t) \cdot \mathbf{e}(0) \rangle \\ &= F(t)e^{-2D_r t} + \int_0^t dt_1 f(t_1)e^{-2D_r t_1} \alpha F(t - t_1)e^{-2D_r(t-t_1)} \\ & \quad + \int_0^t dt_2 \int_0^{t_2} dt_1 f(t_1)e^{-2D_r t_1} \alpha f(t_2 - t_1)e^{-2D_r(t_2-t_1)} \beta F(t - t_2)e^{-2D_r(t-t_2)} \\ & \quad + \dots \end{aligned} \quad (3.19)$$

Compared to Eq. (3.5), Eq. (3.19) contains an additional factor of  $\exp(-2D_r t)$ . Note that this holds also true if the run times are not exponentially distributed. After symmetrization, the generalization of Eq. (3.9) becomes

$$\begin{aligned} \langle \mathbf{e}(t) \cdot \mathbf{e}(t') \rangle &= e^{-(\lambda+2D_r)|t-t'|} \\ &\times \left[ \frac{\alpha + \beta}{2\sqrt{\alpha\beta}} \sinh\left(\sqrt{\alpha\beta}\lambda|t-t'|\right) + \cosh\left(\sqrt{\alpha\beta}\lambda|t-t'|\right) \right]. \end{aligned} \quad (3.20)$$

The mean-squared displacement is given by the expression

$$\begin{aligned} & \langle [\mathbf{r}(t) - \mathbf{r}(0)]^2 \rangle \\ &= \frac{v^2}{[(1-\alpha\beta)\lambda^2 + 4D_r(\lambda + D_r)]^2} \left[ [(1-\alpha\beta)\lambda^2 + 4D_r(\lambda + D_r)][(2+\alpha+\beta)\lambda + 4D_r]t \right. \\ & \quad + \left\{ \frac{\lambda^2[\alpha+\beta+\alpha\beta(4+\alpha+\beta)] + 4D_r\lambda(\alpha+\beta+2\alpha\beta) + 4D_r^2(\alpha+\beta)}{\sqrt{\alpha\beta}} \sinh(\sqrt{\alpha\beta}\lambda t) \right. \\ & \quad \left. + 2[\lambda(1+\alpha) + 2D_r][\lambda(1+\beta) + 2D_r] \cosh(\sqrt{\alpha\beta}\lambda t) \right\} e^{-(\lambda+2D_r)t} \\ & \quad \left. - 2[\lambda(1+\alpha) + 2D_r][\lambda(1+\beta) + 2D_r] \right], \end{aligned} \quad (3.21)$$

from which we now deduce the diffusion coefficient including rotational diffusion:

$$D = \frac{v^2}{6} \frac{(2+\alpha+\beta)\lambda + 4D_r}{(1-\alpha\beta)\lambda^2 + 4D_r(\lambda + D_r)}. \quad (3.22)$$

### 3.2 Diffusion coefficient for a random walk with two alternating tumbling events

---

Eq. (3.22) constitutes our main result of this section. Setting  $\alpha = \beta$ , we recover the result of Lovely and Dahlquist from Eq. (3.1), and Eq. (3.21) simplifies to

$$\langle [\mathbf{r}(t) - \mathbf{r}(0)]^2 \rangle_{\alpha=\beta} = \frac{2v^2}{\lambda_{\text{eff}}^2} (\lambda_{\text{eff}} t - 1 + e^{-\lambda_{\text{eff}} t}) \quad \text{with } \lambda_{\text{eff}} = \lambda(1 - \alpha) + 2D_r, \quad (3.23)$$

which has again the same form as Eq. (2.46b). The significance of rotational diffusion during the run events becomes evident first of all for  $\alpha = \beta = 1$ , as the ballistic motion for  $D_r = 0$  is rendered into diffusion with  $D = \frac{v^2}{6D_r}$ , see also Ref. [86].

Taking into account rotational diffusion, the diffusion coefficients for run-reverse and run-reverse-flick change the former Eqs. (3.15b), (3.16b) into

$$D_{\text{run-rev}} = \frac{v^2}{6} \frac{1}{\lambda + D_r} = \frac{v^2 \tau_{\text{run}}}{6} \frac{1}{1 + D_r \tau_{\text{run}}}, \quad (3.24)$$

$$D_{\text{run-rev-flick}} = \frac{v^2}{6} \frac{\lambda + 4D_r}{(\lambda + 2D_r)^2} = \frac{v^2 \tau_{\text{run}}}{6} \frac{1 + 4D_r \tau_{\text{run}}}{(1 + 2D_r \tau_{\text{run}})^2}. \quad (3.25)$$

The ratio of both diffusion coefficients amounts to

$$\frac{D_{\text{run-rev-flick}}}{D_{\text{run-rev}}} = \frac{1 + 5D_r \tau_{\text{run}} + (2D_r \tau_{\text{run}})^2}{1 + 4D_r \tau_{\text{run}} + (2D_r \tau_{\text{run}})^2} \geq 1, \quad (3.26)$$

and the equality only holds for  $D_r = 0$ . In the presence of rotational diffusion, the additional flick event provides a randomizing effect of the cell movement and increases the diffusion coefficient. This result agrees with physical intuition. The effect of the flick is most pronounced for equal  $\tau_{\text{run}}$  and  $\tau_{\text{rot}} = 1/(2D_r)$ , for which the maximal ratio becomes 1.125. If the mean run time is much larger than the decorrelation time of rotational diffusion,  $\tau_{\text{run}} \gg \tau_{\text{rot}}$ ,  $D_{\text{run-rev-flick}}$  approaches  $D_{\text{run-rev}}$ .

Finally, we analyze the influence of a flick event on the diffusion coefficient from an additional perspective. We compare a random walk with a single persistence parameter  $\alpha$  to a random walk with the same  $\alpha$  and a second tumbling event, the flick, with  $\beta = 0$ . We denote the latter random walk with arbitrary  $\alpha$  and  $\beta = 0$  as “run-tumble-flick”. The ratio of diffusion coefficients  $D_{\alpha, \beta=0}$  and  $D_{\alpha, \alpha}$  becomes

$$\frac{D_{\alpha, \beta=0}}{D_{\alpha, \alpha}} = \frac{(1 - \alpha + 2D_r \tau_{\text{run}})(2 + \alpha + 4D_r \tau_{\text{run}})}{2(1 + 2D_r \tau_{\text{run}})^2}, \quad (3.27)$$

and is plotted versus  $\alpha$  in Fig. 3.3. For positive persistence parameter  $\alpha > 0$ , the flick event enhances the stochasticity of the random walk; the effective diffusion is reduced as compared to the run-and-tumble walker,  $D_{\alpha, \beta=0}/D_{\alpha, \alpha} < 1$ . For  $\alpha = 1$  and  $D_r = 0$ , the run-and-tumble motion becomes ballistic and the diffusion coefficient diverges, and therefore the ratio decays to zero. In the case of negative  $\alpha < 0$ , the additional flick event enhances diffusion as  $D_{\alpha, \beta=0}/D_{\alpha, \alpha} > 1$ .

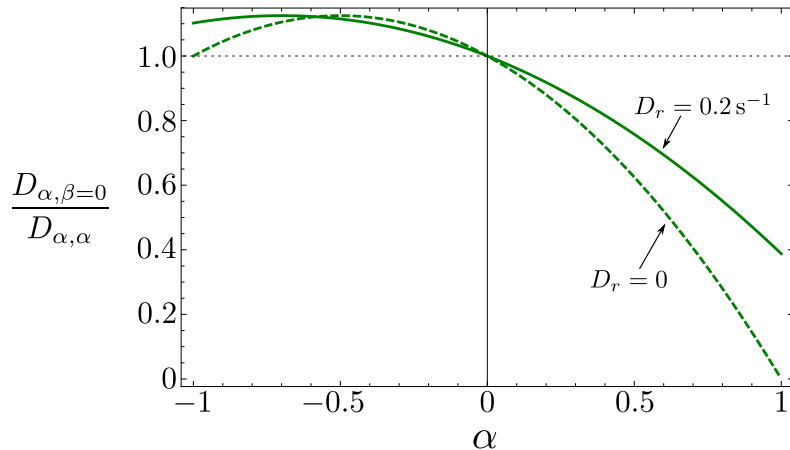


**Figure 3.3** ■ Fraction of the diffusion coefficients for the run-tumble-flick process ( $D_{\alpha,\beta=0}$ ) and standard run-and-tumble ( $D_{\alpha,\alpha}$ ). Both curves are drawn for  $\tau_{\text{run}} = 1\text{s}$ , but for different rotational diffusion constants  $D_r = 0.2\text{s}^{-1}$  and  $D_r = 0$  (dashed).

In the biologically more relevant case with  $\tau_{\text{run}} \leq 1/(2D_r)$ , the existence of the flick event maximizes the ratio  $D_{\alpha,\beta=0}/D_{\alpha,\alpha} = 1.125$  at  $\alpha = -\frac{1}{2}(1 + 2D_r\tau_{\text{run}})$ ; in the case of large rotational diffusion with  $\tau_{\text{run}} > 1/(2D_r)$ , the ratio becomes maximal for  $\alpha = -1$ .

### 3.2.3 Discussion

In Table 3.2, we summarize characteristic numbers to describe the random walk of *E. coli* and *V. alginolyticus*, taken from experimental data. A realistic rotational diffusion coefficient, which is applicable to both types of bacteria, is  $D_r = 0.2\text{s}^{-1}$  [88, 110]. With these numbers, the diffusion coefficients according to Eq. (3.22) read

$$\begin{aligned} E. \text{ } coli \quad D &= 112 \mu\text{m}^2 \text{s}^{-1}, \\ V. \text{ } alginolyticus \quad D &= 101 \mu\text{m}^2 \text{s}^{-1}. \end{aligned}$$

These values have been confirmed by our numerical simulations with very good agreement. To illustrate the influence of  $D_r$ , we present the diffusion coefficient as a function of  $D_r \in [0, 0.4\text{s}^{-1}]$  in Fig. 3.4. We realize that in this range rotational diffusion has little influence on the diffusion coefficient of *V. alginolyticus*,

	$v [\mu\text{m s}^{-1}]$	$\lambda [\text{s}^{-1}]$	$\tau_{\text{run}} [\text{s}]$	$\alpha$	$\beta$
<i>E. coli</i>	19	1	1	0.33	0.33
<i>V. alginolyticus</i>	45	3.3	0.3	-1	0

**Table 3.2** ■ Characterization of the random walks for *E. coli* and *V. alginolyticus*. Data are taken from Refs. [35, 89, 110].

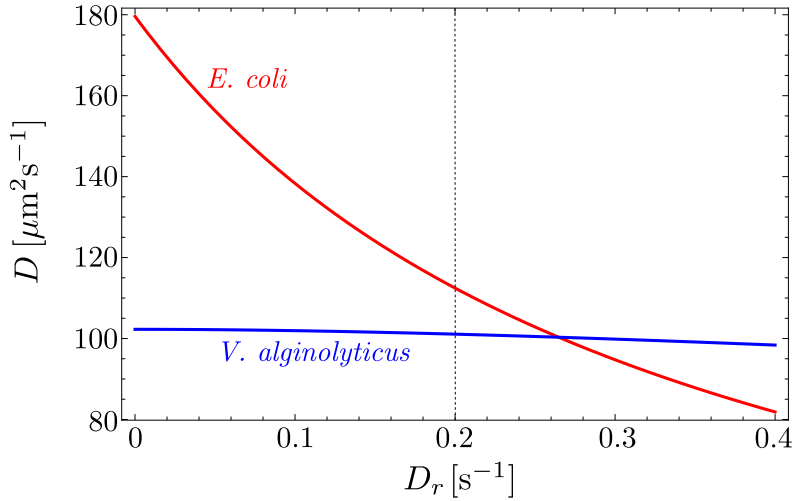


Figure 3.4 ■ Theoretical diffusion coefficient for *E. coli* and *V. alginolyticus* as function of the rotational diffusion coefficient  $D_r$ . The maximally possible  $D$  is obtained in the limiting case  $D_r = 0$  and yields  $D = 180 \mu\text{m}^2 \text{s}^{-1}$  and  $D = 102 \mu\text{m}^2 \text{s}^{-1}$ , respectively.

as the mean run time  $\tau_{\text{run}}$  is much shorter than  $\tau_{\text{rot}} = 1/(2D_r)$ , see Table 3.1. In contrast, *E. coli*'s diffusion coefficient is strongly influenced by  $D_r$ , ranging from  $D = 180 \mu\text{m}^2 \text{s}^{-1}$  for  $D_r = 0$  to the more realistic value of  $D = 112 \mu\text{m}^2 \text{s}^{-1}$  for  $D_r = 0.2 \text{s}^{-1}$  (for fixed  $v$  and  $\lambda$ ). As the values for  $D_r$  of *E. coli* vary in the literature (see Table 3.1), a reliable estimate of  $D$  requires the accurate knowledge of  $D_r$ .

We note that our exact analysis of the diffusion coefficient in Eq. (3.22) corrects simpler estimates from recent publications. In the commentary by Stocker [111], one reads: “The alternation of reversals and flicks then suggests that  $\alpha \sim -0.5$  for *V. alginolyticus* [...].” Here, a single persistence parameter  $\alpha$  has been taken as the arithmetic mean of  $\alpha = -1$  and  $\beta = 0$  in order to apply the result of Lovely and Dahlquist. For the presented values of *V. alginolyticus* with  $D_r = 0.2 \text{s}^{-1}$ , this procedure results in an overestimated diffusion coefficient of  $D = 126 \mu\text{m}^2 \text{s}^{-1}$ .

Our calculation shows that this average is not appropriate for a random walk with tumbling events of exactly alternating persistence parameters. The arithmetic mean of two different persistence parameters is only useful to describe an ensemble of two distinct random walkers, each characterized by a single parameter  $\alpha$  and  $\beta$ , respectively. The ensemble average over exponentially decaying correlations always gives a positive result, whereas in the case of periodic alternation of preferred turning angles, where  $\alpha$  and  $\beta$  have different sign, one obtains also negative correlations, see Fig. 3.2. Hence, the experimental observation of negative directional correlations and exponentially distributed run times is a hint that different tumbling events do not occur in a random series.

Our result conflicts also with Refs. [110, 112], where the authors claim that the

run-reverse-flick process with equal duration of forward and backward run times results in  $D = 0$ . For exponentially distributed run times, our result shows that the diffusion coefficient is not zero for any combination of persistence parameters, not even if rotational diffusion during the runs is completely neglected.

In this section, we have modeled the random walk with an exponential run time distribution and a single mean run time  $\tau_{\text{run}}$ . In case of different means  $\tau_r$  and  $\tau_b$  for the forward and backward run times, respectively, we showed that the diffusion coefficients read

$$D_{\text{run-rev-flick}} = \frac{v^2}{3} \frac{\tau_r^2 - \tau_r \tau_b (1 - 2D_r \tau_r) + \tau_b^2 (1 + 2D_r \tau_r)}{(\tau_r + \tau_b)(1 + 2D_r \tau_r)(1 + 2D_r \tau_b)}, \quad (3.28a)$$

$$D_{\text{run-rev-flick}} = \frac{v^2}{3} \frac{\tau_r^3 + \tau_b^3}{(\tau_r + \tau_b)^2}, \quad \text{for } D_r = 0. \quad (3.28b)$$

We emphasize that our derivation, based on immediately writing down the directional correlation function, is transparent and holds for two and three dimensions. However, it does not provide a result for arbitrary run time distributions. An interesting case besides the exponential distribution is a power-law distribution [90, 113]. Using continuous time random walks [37], it is possible to obtain the directional correlation function in Fourier-Laplace space for any kind of run time distribution; Eq. (3.28) has, for example, been derived that way [114].

In total, our results for the diffusion coefficient of a random walk with two alternating tumbling events have been derived analytically in two independent formalisms and were also confirmed by numerical simulations.

### 3.3 Chemotactic drift speed

#### 3.3.1 Chemotactic drift speed of *E. coli*

If *E. coli* is exposed to a gradient of chemoattractant, *e.g.* amino acids or sugars, with concentration  $c$ , it changes its unbiased run-and-tumble strategy in order to effectively move along the gradient. To do so, the genetic chemotactic pathway of *E. coli* extends the mean run time if the cell swims in the direction of increasing concentration,  $\nabla c$ . For motion against the gradient  $-\nabla c$ , the mean run time is only slightly decreased [59].

The response of an *E. coli* cell, exposed to a short pulse of chemoattractant, has first been measured in Ref. [93]. Several bacteria, each tethered to a surface by a single flagellum, were frequently stimulated by a delta-pulse of concentration of the amino acid aspartate. The fraction of time that the flagellum spins counterclockwise was then recorded as a function of time and revealed a biphasic response to the chemoattractant [86]. Without chemoattractant, this fraction fluctuates around a

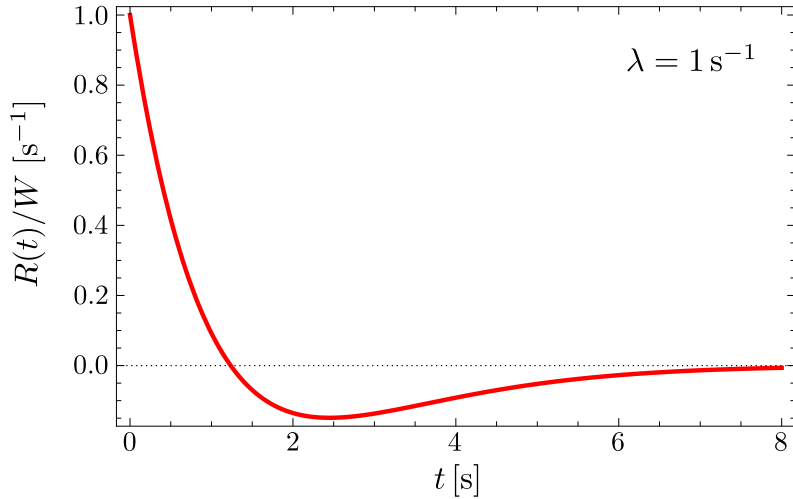


**Figure 3.5** ■ Response function of *E. coli* [Eq. (3.29)] according to Ref. [97]. The function has a zero at  $(\sqrt{5} - 1) \lambda^{-1} \approx 1.24 \lambda^{-1}$  and is minimal at  $\sqrt{6} \lambda^{-1} \approx 2.45 \lambda^{-1}$ .

“baseline”. After stimulation with the chemical pulse, the fraction quickly reaches a maximum and remains above the baseline for  $\sim 1$  s, then it falls below and finally approaches the baseline after  $\sim 4$  s.

The shape of this curve for the fraction of counterclockwise flagellar rotation motivates to introduce a shifted and rescaled response function  $R(t)$ , which is directly connected to the tumbling rate of the bacterium, as defined below in Eq. (3.30). In agreement with recent experimental results [115], there are also theoretical arguments for the analytic form of the response function  $R(t)$  [97, 88]. We take the functional form of  $R(t)$  from Refs. [96, 97], but introduce a single normalization constant  $W$  with unit of volume:

$$R(t) = W \lambda e^{-\lambda t} \left[ 1 - \frac{\lambda t}{2} - \left( \frac{\lambda t}{2} \right)^2 \right], \quad t \geq 0. \quad (3.29)$$

The tumbling rate in a homogeneous environment is given by  $\lambda$ . The response function is plotted with  $\lambda = 1 \text{ s}^{-1}$  for *E. coli* in Fig. 3.5. To account for the change of run times in gradients according to the results of Berg and Brown [59], de Gennes formulated a time-dependent tumbling rate [94]:

$$\lambda(t) = \lambda \left( 1 - \int_{-\infty}^t dt' c(t') R(t - t') \right). \quad (3.30)$$

For the special case of a delta-pulse of concentration,  $\lambda(t)$  is proportional to the response function  $R(t)$ . An important property of chemotaxis in *E. coli* is called adaptive response and corresponds to the fact that  $\int_0^\infty dt R(t) = 0$ . This means that the receptors of *E. coli* adapt to any constant level of physiological (*i.e.* “reasonable”)

concentration such that the tumbling rate recovers the “unperturbed” mean value  $\lambda$ . Note that Eq. (3.30) can only hold for small concentrations such that  $\lambda(t) \geq 0$  is ensured. Thus we add the restriction that if  $\lambda(t)$  becomes negative in Eq. (3.30), it is set to zero. In Sec. 3.3.5, we discuss alternative approaches for the tumbling rate in bacterial chemotaxis; in Sec. 3.4.1, we estimate a condition for the smallness of chemical field and gradient.

As mentioned in Sec. 2.4, the drift velocity of a particle with trajectory  $\mathbf{r}(t)$  is given by  $\mathbf{v}_{\text{drift}} = \lim_{t \rightarrow \infty} \frac{\langle \mathbf{r}(t) - \mathbf{r}(0) \rangle}{t}$ . In Ref. [96], Locsei calculated the chemotactic drift speed  $v_d = |\mathbf{v}_{\text{drift}}|$  along a gradient  $\nabla c$  for a run-and-tumble swimmer with persistence parameter  $\alpha$  and response function (3.29),

$$v_d = |\nabla c| W v^2 \frac{\lambda^2 [\lambda(5 - 2\alpha) + 4D_r] (1 - \alpha)}{6 [2D_r + \lambda(1 - \alpha)] [2D_r + \lambda(2 - \alpha)]^3}. \quad (3.31)$$

This result was obtained for small gradients by a first-order perturbation expansion in  $|\nabla c|$ . Its derivation will become clear in Secs. 3.3.2 and 3.3.4, where we perform the analogous calculation for the chemotactic drift speed of a run-reverse-flick swimmer. The validity of Eq. (3.31) was checked numerically in Ref. [96]; however, predictions in real units were not provided as the normalization  $W$  of the response function is not known.

It is our idea to estimate  $W$  as follows. We refer to recent measurements by Vupputula *et al.* [89] for the chemotactic drift speed  $v_d$  of *E. coli* in response to the amino acid serine. In the range of experimentally accessible small gradients with  $|\nabla c| = 10^{-3} \dots 10^{-2} \mu\text{M} \mu\text{m}^{-1} = 0.6 \dots 6 \mu\text{m}^{-4}$ ,  $v_d$  is estimated as  $v_d = 0.5 \dots 1.5 \mu\text{m s}^{-1}$ . Thus, we choose a “small” gradient  $|\nabla c| = 1 \mu\text{m}^{-4}$ , set  $v_d = 1 \mu\text{m s}^{-1}$  and use  $v = 19 \mu\text{m s}^{-1}$ ,  $\alpha = 0.33$ ,  $\lambda = 1 \text{s}^{-1}$ , and  $D_r = 0.2 \text{s}^{-1}$ . Solving Eq. (3.31) for  $W$  yields  $W = 0.0458 \mu\text{m}^3$ . We also calculate  $W$  for the cited values of  $D_r$  from Table 3.1.

$D_r [\text{rad}^2 \text{s}^{-1}]$	0.062	Ref. [59]	0.2	Ref. [88]	0.32	Ref. [89]
$W [\mu\text{m}^3]$	0.0248		0.0458		0.0713	

The red curve in Fig. 3.6 shows  $v_d$  from Eq. (3.31) as a function of  $\alpha$ , while the blue curve will be discussed in the next section. The graph illustrates how the chemotactic drift speed  $v_d$  increases with increasing persistence parameter  $\alpha$ , as long as  $\alpha \lesssim 0.6$ . For larger values of  $\alpha$ , the directional persistence between successive run events is so large that the response to a gradient becomes less pronounced; in the limiting case  $\alpha = 1$ ,  $v_d$  becomes zero. Note that if *E. coli* were a run-reverse swimmer with  $\alpha = -1$ ,  $v_d$  would be reduced by  $\sim 50\%$ , compared to  $v_d$  resulting from the measured persistence parameter  $\alpha = 0.33$ . As a large  $v_d$  allows *E. coli* to quickly access nutrient sources, this analysis suggests an evolutionary benefit of a positive persistence parameter  $\alpha$ .

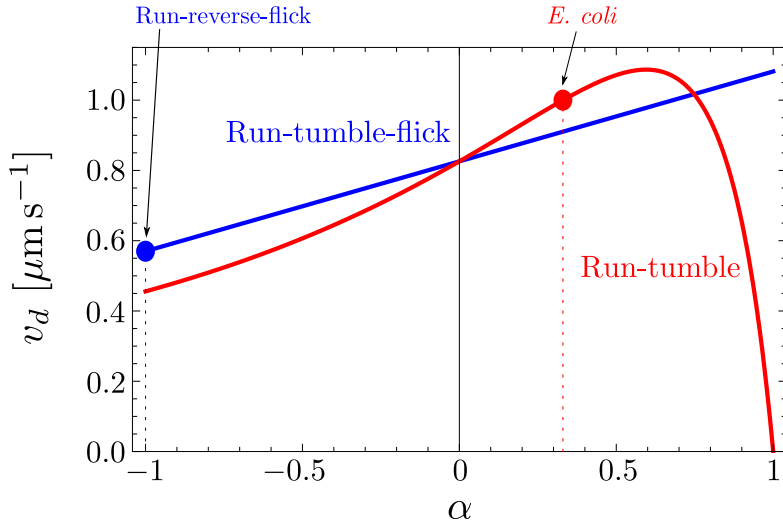


**Figure 3.6** ■ Comparison of the chemotactic drift speed  $v_d$  as a function of persistence parameter  $\alpha$  between run-tumble [Eq. (3.31)] and run-tumble-flick [Eq. (3.36)]. All parameters are adjusted to *E. coli* in the gradient  $|\nabla c| = 1 \mu\text{m}^{-4}$  with  $\lambda = 1 \text{s}^{-1}$ ,  $v = 19 \mu\text{m s}^{-1}$ ,  $D_r = 0.2 \text{s}^{-1}$ , and  $W = 0.0458 \mu\text{m}^3$ .

### 3.3.2 Chemotactic drift speed of *V. alginolyticus*

We are interested in understanding how an additional flick event in the run-and-tumble pattern influences the chemotactic drift speed  $v_d$ . For this purpose, we will first calculate  $v_d$  for the set of *E. coli* parameters in this section; in Sec. 3.3.3, we predict the chemotactic drift speed of *V. alginolyticus* and compare it to *E. coli* in absolute numbers. Here, we only give an outline of the calculation and present the results. The details of the calculation are found in Sec. 3.3.4.

As described above, we have combined Locsei's formula (3.31) and the experimental results from Vuppula *et al.* [89] to determine the chemotactic response strength. In the following, we apply the chemotactic response function of *E. coli* also for *V. alginolyticus*; though the response function of *V. alginolyticus* is not known, there is evidence that the chemotactic response of both bacteria is similar [116].

From now on, we keep the persistence parameter  $\alpha$  as a free variable, but we restrict the second persistence parameter  $\beta$  to a perfect flick event with  $\beta = 0$ ; we already referred to this pattern as run-tumble-flick. For *V. alginolyticus*, the reversal between forward and backward runs results in  $\alpha = -1$ . The run times are exponentially distributed, and we allow for different rates  $\lambda_r$  and  $\lambda_b$  for forward ( $r$ ) and backward ( $b$ ) runs, respectively.

We assume a small chemical gradient  $|\nabla c|$  in  $z$  direction, and the concentration  $c(t)$ , which is experienced by the receptors of the bacterium at position  $z(t)$ , becomes

$$c(t) = |\nabla c| z(t). \quad (3.32)$$

Next, we generalize de Gennes' approach from Eq. (3.30) for the time-dependent

rates of forward and backward runs:

$$\lambda_i(t) = \lambda_i \left( 1 - \int_{-\infty}^t dt' c(t') R_i(t-t') \right) \quad \text{for } i = r, b. \quad (3.33)$$

The adaptive response,  $\int_0^\infty dt R_i(t) = 0$ , has allowed us to set a possible constant concentration in Eq. (3.32) to zero, as it does not affect the tumbling rates in Eq. (3.33). We will use again the experimentally measured response function  $R(t)$  of *E. coli* [Eq. (3.29)], as we are primarily interested in understanding the influence of the random walk pattern on the chemotactic drift speed.

To simplify forthcoming calculations, we make use of the structure of Eq. (3.33) and consider the special case of a delta-response in time  $R_i(t) = A_i \delta(t - T_i)$  with delay time  $T_i$  and strength  $A_i$ , as it was done in Refs. [94, 96]. We denote the chemotactic drift speed for the delta-response as  $v_\delta$ . Having found this intermediate result for  $v_\delta$ , it is generalized to the “real” chemotactic drift speed  $v_d$  by integrating  $v_\delta$  with the “real” response function  $R(t)$ , according to Eq. (3.35). The procedure corresponds to writing the response function as the weighted sum of  $k$  delay times  $T_i^{(k)}$ ,  $R_i(t) = \sum_k A_i^{(k)} \delta(t - T_i^{(k)})$ , and  $v_d$  is obtained by summing  $v_\delta$  over all delay times.

We calculate  $v_\delta$  for a random walk with a flick event at  $t = 0$ . The flick totally randomizes the direction of the subsequent forward run, which is interrupted at  $t_r$ . At time  $t_r$ , the direction of motion is changed with persistence parameter  $\alpha$  and the particle performs a “backward” run of duration  $t_b$ . As every flick event destroys the directional persistence and memory of the previous random walk steps,  $v_\delta$  is calculated by considering the mean displacement along the  $z$  axis during one cycle of the run-tumble-flick process.

To obtain  $v_\delta$  in a first-order expansion of  $|\nabla c|$ , we determine the average displacement of a forward run  $\langle z_r \rangle$  and a subsequent backward run  $\langle z_b \rangle$ . As these expressions are first order in  $|\nabla c|$ , the mean duration of the cycle is given by  $\lambda_r^{-1} + \lambda_b^{-1}$ , and the chemotactic drift speed for the delta-response reads

$$v_\delta = \frac{\langle z_r \rangle + \langle z_b \rangle}{\lambda_r^{-1} + \lambda_b^{-1}}. \quad (3.34)$$

In the following, we consider equal mean run times for forward and backward motion, encoded in a single rate  $\lambda$ . We integrate  $v_\delta$  with the response function (3.29) of the same strength  $W$  for forward and backward motion,

$$v_d = \int_0^\infty dT R(T) \frac{v_\delta(T)}{A}, \quad (3.35)$$

and obtain our main result for the chemotactic drift speed:

$$\begin{aligned} v_d &= |\nabla c| W v^2 \lambda^2 \\ &\times \frac{16D_r^3(2-\alpha) + 4\lambda D_r^2(22-5\alpha) + 2\lambda^2 D_r(38+5\alpha) + \lambda^3(20+11\alpha)}{192(\lambda+D_r)^4(\lambda+2D_r)^2}. \end{aligned} \quad (3.36)$$

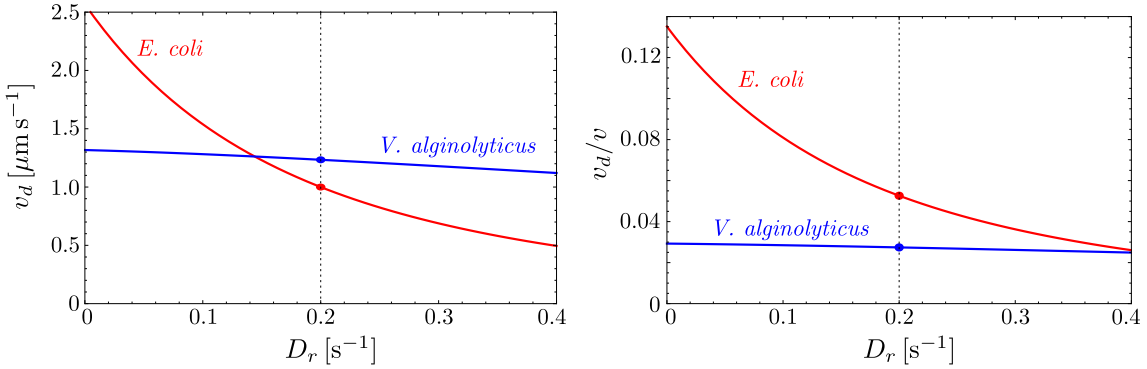


Figure 3.7 ■ Chemotactic drift speed as a function of  $D_r$  for *E. coli* and *V. alginolyticus*. The plot on the left shows  $v_d$ ; on the right, the chemotactic drift is normalized by the swimming speed as  $v_d/v$  and coincides with the chemotactic index.

We observe that  $v_d$  is always positive, in particular for the run-reverse-flick strategy with  $\alpha = -1$ . This shows that the bacterium effectively swims in the direction of the gradient in spite of the anti-correlation between each forward and following backward run. The chemotactic drift speed  $v_d$  is a linear function of  $\alpha$ , plotted as the blue curve in Fig. 3.6, whereas the red curve shows  $v_d$  for the same parameters without the flick event.

For negative persistence parameter  $\alpha$ , the additional flick event offers the random walker the opportunity to better approach the gradient: Therefore,  $v_d$  is larger with flick for  $\alpha < 0$ . For  $\alpha = 0$ , both random walk processes are equal as they have no persistence, and the curves intersect. For increasing  $\alpha > 0$ ,  $v_d$  is smaller in the presence of the randomizing flick event. Finally, there is a pronounced difference at  $\alpha = 1$ , where  $v_d = 0$  for the run-and-tumble strategy, while  $v_d$  becomes maximal for run-tumble-flick.

Note that a similar calculation for  $v_\delta$  of a run-tumble-flick swimmer without rotational diffusion is also found in Ref. [112]. Our result in Eq. (3.36) explicitly shows the influence of rotational diffusion on the chemotactic drift speed.

### 3.3.3 Comparison: *E. coli* versus *V. alginolyticus*

Now, we compare the chemotactic drift speeds of *E. coli* and *V. alginolyticus* as a function of  $D_r$ . We take the parameters from Table 3.2 and the response function  $R(t)$  and strength  $W$  from *E. coli* for both swimmers. The left plot of Fig. 3.7 shows  $v_d$  versus  $D_r$ . For the value  $D_r = 0.2 \text{ s}^{-1}$  from Sec. 3.2.3, *V. alginolyticus* has  $v_d = 1.23 \mu\text{m s}^{-1}$ , which is  $\sim 25\%$  larger than  $v_d = 1 \mu\text{m s}^{-1}$  of *E. coli*. Going to smaller values for  $D_r \lesssim 0.14 \text{ s}^{-1}$ , the chemotactic drift speed of *E. coli* exceeds that of *V. alginolyticus*. For sufficiently large  $D_r$ , the “winner of the chemotaxis race” is the run-reverse-flick swimmer *V. alginolyticus*.

However, as the bare speed of *V. alginolyticus* ( $v = 45 \mu\text{m s}^{-1}$ ) is more than twice

of *E. coli* ( $v = 19 \mu\text{m s}^{-1}$ ),  $v_d$  is not the only appropriate measure to compare the chemotactic efficiency. For that reason, we normalize  $v_d$  by the swimming speed  $v$ , shown as the right plot of Fig. 3.7. Note that the ratio  $v_d/v$  is also called the chemotactic index (CI), which compares the traveled distance of a cell in the direction of the gradient to the total path length [117, 31]. For  $D_r = 0.2 \text{ s}^{-1}$ ,  $v_d/v$  for *E. coli* (5.3%) is almost twice as large as for *V. alginolyticus* (2.7%). Moreover, the chemotactic index of *E. coli* is larger for all considered values of  $D_r$ . In this sense, the “relative” chemotaxis race is won by *E. coli*.

Ref. [111] contains the experimental observation that the chemotactic drift speed of *V. alginolyticus* is three times larger than of *E. coli*. If we assume that chemotaxis in *V. alginolyticus* is described by the same response function as in *E. coli*, our result for small gradients shows that the additional flick event does not explain the large observed difference in the chemotactic drift speed.

To support our theoretical results for the chemotactic drift speed, we performed numerical simulations for both bacteria according to the random walk approach [114]; the results from these simulations nicely agree with our predictions.

### 3.3.4 Derivation of the chemotactic drift speed for the run-tumble-flick strategy

In this section, we present the detailed calculation of the chemotactic drift speed for the run-tumble-flick process, characterized by a single persistence parameter  $\alpha$ , and  $\beta = 0$ .

We consider a random walker that starts with a flick at  $t = 0$  and initial position  $z = 0$ . We need to calculate the displacement along the direction of the gradient, the  $z$  axis, during the forward run ( $t = 0 \dots t_r$ ) and the subsequent “backward” run ( $t = t_r \dots t_r + t_b$ ). The probability density  $p_r(0 \rightarrow t_r)$  that a forward run starts at  $t = 0$  and stops at  $t_r$  is given by

$$p_r(0 \rightarrow t_r) = -\frac{d}{dt_r} \exp\left(-\int_0^{t_r} dt' \lambda_r(t')\right), \quad (3.37a)$$

$$p_b(t_r \rightarrow t_r + t_b) = -\frac{d}{dt_b} \exp\left(-\int_{t_r}^{t_r+t_b} dt' \lambda_b(t')\right), \quad (3.37b)$$

and  $p_b(t_r \rightarrow t_r + t_b)$  is the probability density that a “backward” run starts at  $t_r$  and stops at  $t_r + t_b$ . The time-dependent rates  $\lambda_i(t)$  ( $i = r, b$ ) due to chemotaxis are given in Eq. (3.33). Taking a delta-response  $R_i(t) = A_i \delta(t - T_i)$  with strength  $A_i$  and delay time  $T_i$ , and using  $c(t) = |\nabla c| z(t)$  [Eq. (3.32)], we can write the rates as

$$\lambda_i(t) = \lambda_i [1 - A_i |\nabla c| z(t - T_i)], \quad (3.38)$$

and they thus depend on the previous positions  $z(t - T_i)$ .

The mean displacement  $\langle z \rangle = \langle z_r \rangle + \langle z_b \rangle$  of the forward run  $\langle z_r \rangle$  and subsequent “backward” run  $\langle z_b \rangle$  reads

$$\langle z \rangle = \langle z_r \rangle + \langle z_b \rangle \quad (3.39a)$$

$$= \left\langle \int_0^\infty dt_r p_r(0 \rightarrow t_r) z(t_r) \right\rangle \quad (3.39b)$$

$$+ \left\langle \int_0^\infty dt_r \int_0^\infty dt_b p_r(0 \rightarrow t_r) p_b(t_r \rightarrow t_r + t_b) z(t_b) \right\rangle. \quad (3.39c)$$

The averages  $\langle \dots \rangle$  in Eq. (3.39) are taken over all possible paths due to random swimming directions after the flick event. In addition, they represent ensemble averages to account for the rotational diffusion during the runs. Without rotational diffusion, we could write the positions in Eq. (3.39) as  $z(t_i) = v_z(t_i)t_i$ , where  $v_z(t)$  is the  $z$  component of the velocity  $\mathbf{v}(t)$ . To proceed, we shift the averages  $\langle \dots \rangle$  into the integrals in Eqs. (3.39b) and (3.39c).

We start to calculate  $\langle z_r \rangle$  from Eq. (3.39b):

$$\langle z_r \rangle = \int_0^\infty dt_r \left\langle \left[ -\frac{d}{dt_r} \exp \left( - \int_0^{t_r} dt' \lambda_r(t') \right) \right] z(t_r) \right\rangle \quad (3.40a)$$

$$= \int_0^\infty dt_r \left\langle \exp \left( - \int_0^{t_r} dt' \lambda_r(t') \right) \frac{dz(t_r)}{dt_r} \right\rangle \quad (3.40b)$$

$$= \int_0^\infty dt_r e^{-\lambda_r t_r} \left( \langle v_z(t_r) \rangle + \lambda_r A_r |\nabla c| \int_0^{t_r} dt' \langle z(t' - T_r) v_z(t_r) \rangle \right). \quad (3.40c)$$

In the first step, a partial integration led us to Eq. (3.40b). Then we introduced  $v_z(t_r) = \frac{dz(t_r)}{dt_r}$  as the speed in  $z$  direction, and substituted Eq. (3.38) into (3.40b); after expanding the exponential, we only kept the first-order terms in  $|\nabla c|$  to arrive at Eq. (3.40c). The averages in this equation will be calculated without chemotaxis to remain first-order in  $|\nabla c|$ . We immediately find  $\langle v_z(t_r) \rangle = 0$ , as the direction of motion after the flick at  $t = 0$  is random. Further, we use  $z(t) = \int_0^t ds v_z(s)$  and get

$$\langle z_r \rangle = |\nabla c| A_r \int_0^\infty dt_r \lambda_r e^{-\lambda_r t_r} \int_0^{t_r} dt' \int_0^{t'-T_r} ds \langle v_z(s) v_z(t_r) \rangle. \quad (3.41)$$

Without chemotaxis, the velocity distribution is isotropic, which implies

$$\langle v_z(s) v_z(t_r) \rangle = \frac{v^2}{3} \langle \mathbf{e}(s) \cdot \mathbf{e}(t_r) \rangle, \quad (3.42)$$

and the directional correlation function reads

$$\langle \mathbf{e}(s) \cdot \mathbf{e}(t_r) \rangle = \begin{cases} e^{-2D_r(t_r-s)} & 0 \leq s < t_r, \\ 0, & \text{else.} \end{cases} \quad (3.43)$$

After inserting Eqs. (3.42) and (3.43) into Eq. (3.41), we perform the resulting integrals and obtain the mean displacement of a forward run,

$$\langle z_r \rangle = |\nabla c| A_r \frac{v^2}{3} \frac{e^{-(\lambda_r + 2D_r)T_r}}{(\lambda_r + 2D_r)^2}, \quad (3.44)$$

which is proportional to the gradient  $|\nabla c|$  and the response strength  $A_r$ . To check for consistency, we note that Eq. (3.44) agrees with Locsei's intermediate result for  $\alpha = 0$  from Ref. [96].

Now, we turn to the mean displacement of a “backward” run  $\langle z_b \rangle$  from Eq. (3.39c). We proceed in the same way as before and obtain up to first order in  $|\nabla c|$ :

$$\begin{aligned} \langle z_b \rangle = & \int_0^\infty dt_r \int_0^\infty dt_b \lambda_r e^{-\lambda_r t_r - \lambda_b t_b} \left\{ \begin{array}{l} \langle v_z(t_b) \rangle - A_r |\nabla c| \langle z(t_r - T_r) v_z(t_b) \rangle \\ + \lambda_r A_r |\nabla c| \int_0^{t_r} dt' \langle z(t' - T_r) v_z(t_b) \rangle \\ + \lambda_b A_b |\nabla c| \int_{t_r}^{t_r+t_b} dt' \langle z(t' - T_b) v_z(t_b) \rangle \end{array} \right\}. \end{aligned} \quad (3.45)$$

Again, the expectation values are calculated without chemotaxis, such that  $\langle v_z(t_r) \rangle = 0$  and Eq. (3.42) holds. Be aware that  $v_z(t_b)$  is the speed in  $z$  direction at the absolute time  $t_r + t_b$ . In the directional correlation function, we introduce different rotational diffusion coefficients,  $D_r$  and  $D_b$ ,

$$\langle \mathbf{e}(s) \cdot \mathbf{e}(t_b) \rangle = \begin{cases} e^{-2D_b t_b} \alpha e^{-2D_r(t_r-s)}, & 0 \leq s < t_r, \\ e^{-2D_b(t_r+t_b-s)}, & t_r \leq s < t_r + t_b, \\ 0, & \text{else.} \end{cases} \quad (3.46)$$

To obtain the first line of Eq. (3.46), we made the decomposition  $\langle \mathbf{e}(s) \cdot \mathbf{e}(t_b) \rangle = \langle \mathbf{e}(t_b) \cdot \mathbf{e}(t_r^+) \rangle \langle \mathbf{e}(t_r^+) \cdot \mathbf{e}(t_r^-) \rangle \langle \mathbf{e}(t_r^-) \cdot \mathbf{e}(s) \rangle$ , see also Ref. [96]. For completeness and clarification, we record the following steps of the calculation:

$$\begin{aligned} \langle z_b \rangle = & |\nabla c| \int_0^\infty dt_r \int_0^\infty dt_b \lambda_r e^{-\lambda_r t_r - \lambda_b t_b} \left\{ -A_r \langle z(t_r - T_r) v_z(t_b) \rangle \right. \\ & \left. + \lambda_r A_r \int_0^{t_r} dt' \int_0^{t'-T_r} ds \langle v_z(s) v_z(t_b) \rangle + \lambda_b A_b \int_{t_r}^{t_r+t_b} dt' \int_0^{t'-T_b} ds \langle v_z(s) v_z(t_b) \rangle \right\} \\ = & \frac{|\nabla c| v^2}{3(\lambda_r + 2D_r)^2 (\lambda_b + 2D_b)^2} \left\{ -2\alpha A_r D_r e^{-(\lambda_r + 2D_r)T_r} (\lambda_b + 2D_b) \right. \\ & + \frac{A_b(\lambda_r + 2D_r)}{\lambda_b + 2D_b - \lambda_r - 2D_r} \left[ \alpha \lambda_b (\lambda_b + 2D_b) e^{-(\lambda_r + 2D_r)T_b} \right. \\ & \left. - e^{-(\lambda_b + 2D_b)T_b} (\lambda_r + 2D_r)(\lambda_r + 2D_r + (\alpha - 1)\lambda_b - 2D_b) \right] \left. \right\}. \end{aligned} \quad (3.47)$$

Note that the dependence of  $\langle z_b \rangle$  on  $A_r$  reflects a chemotactic coupling between forward and “backward” runs. Combining all preceding results according to Eq. (3.34), we arrive at the chemotactic drift speed  $v_\delta$  in first-order in  $|\nabla c|$ :

$$\begin{aligned} v_\delta = & \frac{|\nabla c| v^2 \lambda_r \lambda_b}{3(\lambda_r + 2D_r)^2 (\lambda_b + 2D_b)^2 (\lambda_r + \lambda_b)} \\ & \times \left\{ A_r (-2\alpha D_r + \lambda_b + 2D_b) e^{-(\lambda_r + 2D_r)T_r} (\lambda_b + 2D_b) \right. \\ & + \frac{A_b (\lambda_r + 2D_r)}{\lambda_b + 2D_b - \lambda_r - 2D_r} \left[ \alpha \lambda_b (\lambda_b + 2D_b) e^{-(\lambda_r + 2D_r)T_b} \right. \\ & \left. \left. - e^{-(\lambda_b + 2D_b)T_b} (\lambda_r + 2D_r) (\lambda_r + 2D_r + (\alpha - 1)\lambda_b - 2D_b) \right] \right\}. \quad (3.48) \end{aligned}$$

Further, for  $A_r = A_b = A$ ,  $D_r = D_b$ , and  $\lambda_r = \lambda_b = \lambda$ , we obtain

$$v_\delta = A |\nabla c| v^2 \lambda e^{-(\lambda + 2D_r)T} \frac{\lambda [2 + \alpha(1 + \lambda T)] + 2D_r [2 + \alpha(\lambda T - 1)]}{6(\lambda + 2D_r)^3}. \quad (3.49)$$

The final drift speed  $v_d$  from Eq. (3.36) is obtained by integrating  $v_\delta$  with the response function  $R$  from Eq. (3.29) according to Eq. (3.35).

### 3.3.5 Different approaches for the tumbling rate

So far, we have adopted de Gennes’ approach for the tumbling rate from Eq. (3.30). However, this approach does not explicitly account for the experimental fact that runs only become longer when *E. coli* swims to the source of a chemoattractant, but remain almost constant when moving away from the source. In this section, we therefore comment on alternative and more sophisticated approaches to model the tumbling rate  $\lambda(t)$  in response to a chemoattractant.

Schnitzer suggested a modification of Eq. (3.30) in Ref. [58], where the intrinsic tumbling rate  $\lambda$  is only altered if the term  $\int_{-\infty}^t dt' c(t') R(t - t')$  is positive so that  $\lambda(t) < \lambda$  holds: A smaller tumbling rate corresponds to a larger mean run time. In Ref. [91], this non-linear effect is also taken into account, but a full analytical treatment of the resulting bacterial motion is not feasible.

Motion with velocity  $\mathbf{v}$  in the direction of the gradient  $\nabla c$  means  $\mathbf{v} \cdot \nabla c > 0$ . Thus, de Gennes also proposed the biphasic tumbling rate [94]

$$\lambda(t) = \begin{cases} \lambda \left( 1 - \int_{-\infty}^t dt' c(t') R(t - t') \right), & \text{for } \mathbf{v} \cdot \nabla c > 0, \\ \lambda, & \text{for } \mathbf{v} \cdot \nabla c \leq 0. \end{cases} \quad (3.50)$$

We briefly address the consequence of Eq. (3.50) for the chemotactic drift speed of a bacterium. De Gennes showed that for  $\alpha = 0$  and  $D_r = 0$  an additional factor

of  $1/2$  enters the result for  $v_d$ . When calculating the average displacement  $\langle z_r \rangle$  during a run along the gradient, one takes into account that each tumbling event results in a random choice of the new swimming direction  $\mathbf{v}$ . Thus, the probability that  $\mathbf{v} \cdot \nabla c > 0$  is  $1/2$ . The average over all displacements  $\langle z_r \rangle$  is split according to runs along  $\pm \nabla c$  and reads

$$\langle z_r \rangle = \frac{1}{2} (\langle z_r \rangle_{\mathbf{v} \cdot \nabla c > 0} + \langle z_r \rangle_{\mathbf{v} \cdot \nabla c \leq 0}) = \frac{1}{2} (\langle z_r \rangle_{\lambda(t)} + \underbrace{\langle z_r \rangle_{\lambda=\text{const.}}}_{=0}) = \frac{1}{2} \langle z_r \rangle_{\lambda(t)}. \quad (3.51)$$

Here, we have used that for constant  $\lambda$  the random walk is unbiased and the mean displacement during a run is zero. Therefore, the chemotactic drift speed of *E. coli* also contains the additional factor of  $1/2$ .

We now investigate the consequence of an analogous biphasic behavior for both the forward and backward tumbling rate of *V. alginolyticus*, such that Eq. (3.50) is modified to

$$\lambda_i(t) = \begin{cases} \lambda_i \left( 1 - \int_{-\infty}^t dt' c(t') R_i(t-t') \right), & \text{for } \mathbf{v} \cdot \nabla c > 0, \\ \lambda_i, & \text{for } \mathbf{v} \cdot \nabla c \leq 0, \end{cases} \quad (i = r, b). \quad (3.52)$$

To obtain a rough estimate for the resulting chemotactic drift speed, denoted as  $\tilde{v}_d$ , we assume a small rotational diffusion constant  $D_r$ , such that the swimming direction relative to the chemical gradient does not change during a run. We restrict ourselves to a run-reverse-flick swimmer, where the reverse event means  $\alpha = -1$ . If the forward run of the swimmer is towards the chemical source ( $\mathbf{v} \cdot \nabla c > 0$ ), the backward run is pointing away from it. The average displacement  $\langle z \rangle = \langle z_r \rangle + \langle z_b \rangle$  along the direction of the gradient  $\nabla c$ , the  $z$  axis, during one cycle of forward run, reverse event, and backward run reads

$$\langle z \rangle = \frac{1}{2} (\langle z_r \rangle_{\mathbf{v} \cdot \nabla c > 0} + \langle z_b \rangle_{\mathbf{v} \cdot \nabla c \leq 0}) + \frac{1}{2} (\langle z_r \rangle_{\mathbf{v} \cdot \nabla c \leq 0} + \langle z_b \rangle_{\mathbf{v} \cdot \nabla c > 0}) \quad (3.53a)$$

$$= \frac{1}{2} (\langle z_r \rangle_{\lambda_r(t)} + \langle z_b \rangle_{\lambda_b=\text{const.}}) + \frac{1}{2} (\langle z_r \rangle_{\lambda_r=\text{const.}} + \langle z_b \rangle_{\lambda_b(t)}). \quad (3.53b)$$

The first bracket in Eq. (3.53a) accounts for a forward run towards the chemical gradient ( $\langle z_r \rangle_{\mathbf{v} \cdot \nabla c > 0}$ ), which is necessarily followed by a backward run against the gradient ( $\langle z_b \rangle_{\mathbf{v} \cdot \nabla c \leq 0}$ ). To calculate  $\tilde{v}_d$ , we take the response function  $R(t)$  of *E. coli* from Eq. (3.29) and proceed as described in the previous section. We compare the chemotactic drift speed  $\tilde{v}_d$  due to a biphasic response to the former  $v_d$  from Eq. (3.36) and, for equal rates  $\lambda_r = \lambda_b = \lambda$ , obtain the ratio

$$\frac{\tilde{v}_d}{v_d} = \frac{1}{2} - \frac{8D_r}{30(4D_r + 3\lambda)} + \frac{4D_r(7D_r + 9\lambda)}{30(4D_r^2 + 6D_r\lambda + \lambda^2)}. \quad (3.54)$$

Eq. (3.54) is independent of the response strength  $W$  and valid for  $\lambda \gg 2D_r$  or  $\tau_{\text{rot}} \gg \tau_{\text{run}}$ . In Fig. 3.8, we plot  $\tilde{v}_d/v_d$  versus  $\lambda$  for different  $D_r$ . For run-and-tumble

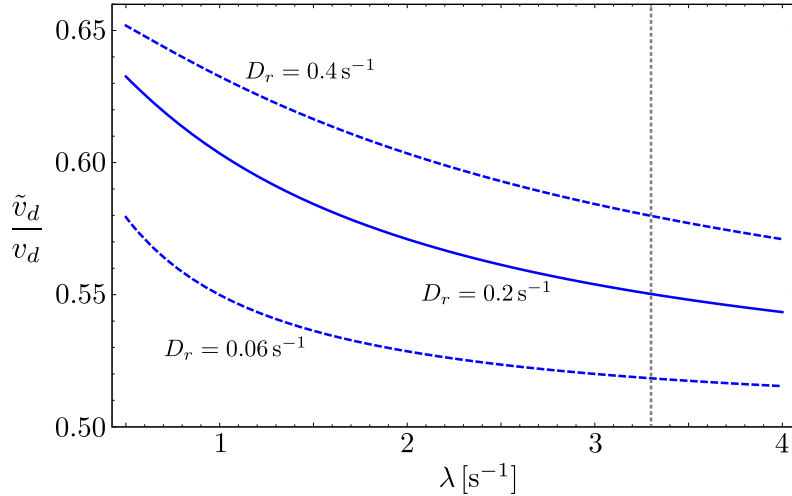


Figure 3.8 ■  $\tilde{v}_d/v_d$  from Eq. (3.54) compares the chemotactic drift speed for the biphasic tumbling rate [Eq. (3.50)] with the “standard” expression [Eq. (3.30)] for a run-reverse-flick swimmer. The approximation holds for  $\lambda \gg 2D_r$ .

dynamics of *E. coli* with  $\alpha = 0$ , we previously argued that  $\tilde{v}_d/v_d = 1/2$ . For the run-reverse-flick strategy, the biphasic tumbling rate also results in a decreased drift speed ( $\tilde{v}_d/v_d < 1$ ), but now  $\tilde{v}_d/v_d > 1/2$ . This behavior can be explained by the fact that for each run-reverse-flick cycle there is at least one run –forward or backward– in the direction of the gradient. For *V. alginolyticus*, we obtain  $\tilde{v}_d/v_d = 0.55$ ; compared to *E. coli*, the biphasic response results in a slightly less reduced chemotactic drift speed. In Sec. 3.3.3, we have calculated the drift speed of *V. alginolyticus* to be  $\sim 25\%$  larger than that of *E. coli*; using the model for the biphasic response, this “advance” of *V. alginolyticus* thus becomes larger. Note that in the limit of large  $\lambda$ , the ratio  $\tilde{v}_d/v_d$  approaches 1/2.

Finally, we comment on the fact that both the standard tumbling rate [Eq. (3.30)] as well as the biphasic rate [Eq. (3.50)] only hold for small concentrations  $c$  of chemical so that  $\lambda(t)$  remains positive. In the simplest approach, one can set  $\lambda(t) = 0$  whenever it becomes negative in Eq. (3.30). For future modeling of chemotaxis in a stationary gradient, we suggest one of the following tumbling rates:

$$\lambda(t) = \begin{cases} \lambda \exp\left(-\int_{-\infty}^t dt' c(t') R(t-t')\right) & \text{for } \mathbf{v} \cdot \nabla c > 0, \\ \lambda, & \text{for } \mathbf{v} \cdot \nabla c \leq 0. \end{cases} \quad (3.55)$$

$$\text{or } \lambda(t) = \lambda \exp\left(-\int_{-\infty}^t dt' c(t') R(t-t')\right). \quad (3.56)$$

Both expressions are positive and coincide with de Gennes’ approach after expanding the exponential for small concentrations. In particular, Eqs. (3.55) and (3.56) are appropriate to also study bacterial chemotaxis in strong chemical gradients.

The introduction of the exponential is motivated by the tumbling frequency from Chen *et al.* [118],

$$\lambda(t) = \begin{cases} \lambda \exp \left[ -\nu \frac{K_d N_t}{(K_d + c)^2} \frac{dc}{dt} \right], & \text{for } \frac{dc}{dt} > 0, \\ \lambda, & \text{for } \frac{dc}{dt} < 0, \end{cases} \quad (3.57)$$

where  $N_t$  is the number of chemoreceptors on the bacterial surface,  $K_d$  is the binding constant of the bacterial membrane receptors for chemoattractants,  $\nu$  is the signal transduction sensitivity factor, and  $\frac{d}{dt} = \partial_t + \mathbf{v} \cdot \nabla$  is the total time derivative. Recall that we sketched in Sec. 2.4.1 how the argument of the exponential in Eq. (3.57) is derived. For a stationary gradient ( $\partial_t c = 0$ ) of a small concentration field  $c$ , the first line of Eq. (3.57) thus reads  $\lambda(t) = \lambda \exp [-\text{const.} \times \mathbf{v} \cdot \nabla c]$  and has, for example, been applied in Ref. [119].

### 3.4 Mean run times in a chemical gradient

In this section, we comment again on observations for run times of *E. coli* and *V. alginolyticus*. So far, we have not mentioned the experimental result of Berg and Brown [59] that *E. coli*'s mean run time is somewhat larger in the presence of a chemical gradient as compared to a homogeneous environment. When the mean run time in a gradient,  $\langle t_r \rangle_{\text{grad}}$ , is determined, the swimming direction of the cells is arbitrary. Berg and Brown also recorded run times and distinguished whether cells swim in the direction of  $+\nabla c$  or  $-\nabla c$ . Compared to  $\langle t_r \rangle_{\text{grad}}$ , the mean run time  $\langle t_r \rangle_{+\nabla c}$  towards the gradient  $\nabla c$  is larger, while  $\langle t_r \rangle_{-\nabla c}$  for motion “against” the gradient is slightly smaller. In a gradient of the amino acid serine, they obtained the values listed in Table 3.3.

For *V. alginolyticus*, Xie *et al.* [110] present the distributions of forward and backward run times in a homogeneous environment and in a steep serine gradient. They observe a change in the run time distributions: In the absence of a gradient, both distributions have a maximum at  $\sim 0.2 \dots 0.3$  s, indicating that the distributions are not fully exponential for small times. In a gradient, a second peak at  $\sim 1$  s emerges for the forward run times, whereas the distribution of backward run times has two broad peaks close around  $\sim 1$  s.

We ask whether the two clearly separated peaks for the forward run times represent the limiting cases of motion along  $\pm \nabla c$  with  $\langle t_r \rangle_{+\nabla c} \sim 1$  s and  $\langle t_r \rangle_{-\nabla c} \sim 0.3$  s.

$\langle t_r \rangle_{\text{no gradient}}$	$\langle t_r \rangle_{\text{grad}}$	$\langle t_r \rangle_{+\nabla c}$	$\langle t_r \rangle_{-\nabla c}$
1.48 s	1.67 s	2.19 s	1.40 s

Table 3.3 ■ Mean run times of *E. coli* in a serine gradient. Data from Ref. [59].

Further, we examine whether the observation of the two close peaks of backward run times can be related to the fact that  $\langle t_b \rangle_{+\nabla c} \sim \langle t_b \rangle_{-\nabla c} \sim 1$  s. For this purpose, we apply our theory, based on the tumbling rate  $\lambda(t) = \lambda \left[ 1 - \int_{-\infty}^t dt' c(t') R(t-t') \right]$ , to explain the observed changes of the mean run times of both bacteria.

First, we show that the distribution of forward run times  $f_r(t_r)$ , averaged over all possible swimming directions of the cell, is not changed by a small gradient. Note that this statement does not contradict the fact of a non-zero chemotactic drift speed in the direction of the gradient. The following arguments hold for the run-reverse-flick strategy, as well as for run-and-tumble with  $\alpha = 0$ . To obtain  $f_r(t_r)$ , we take the probability density  $p_r(0 \rightarrow t_r)$  from Eq. (3.37a) that a run starts at  $t = 0$  and stops at  $t_r$ , and average over all possible paths as  $f_r(t_r) = \langle p_r(0 \rightarrow t_r) \rangle$ . In first order of  $|\nabla c|$ , it follows that

$$\begin{aligned} f_r(t_r) &= \left\langle \lambda_r(t_r) \exp \left( - \int_0^{t_r} dt' \lambda_r(t') \right) \right\rangle \\ &= \lambda_r e^{-\lambda_r t_r} \left( 1 - A_r |\nabla c| \underbrace{\langle z(t_r - T_r) \rangle}_{=0} + \lambda_r A_r |\nabla c| \int_0^{t_r} dt' \underbrace{\langle z(t' - T_r) \rangle}_{=0} \right) \\ &= \lambda_r e^{-\lambda_r t_r}. \end{aligned} \quad (3.58)$$

Hence, the run time distribution averaged over all possible swimming paths remains exponential with the same mean  $\lambda_r^{-1}$ . Performing the same average for the distribution of backward run times,  $f_b(t_b) = \langle \int_0^\infty dt_r p_r(0 \rightarrow t_r) p_b(t_r \rightarrow t_r + t_b) \rangle$ , gives the analogous result without a change in the mean backward run time  $\lambda_b^{-1}$ .

In Secs. 3.4.1 and 3.4.2, we estimate the mean forward and backward run time for motion along  $\pm \nabla c$ ,  $\langle t_r \rangle_{\pm \nabla c}$  and  $\langle t_b \rangle_{\pm \nabla c}$ , respectively. In the following, we neglect rotational diffusion during the runs and assume perfectly aligned motion along  $\pm \nabla c$ .

### 3.4.1 Mean run times for *E. coli*

To calculate the mean run times  $\langle t_r \rangle_{\pm \nabla c}$  of an *E. coli* bacterium that swims in the direction of  $\pm \nabla c$ , we consider a (forward) run of duration  $t_r$ , starting at  $t = 0$  and  $z = 0$ . We assume that the previous run for  $t < 0$  occurred in the plane with  $z = 0$ , so that the path of the cell reads

$$z(t) = \begin{cases} \pm vt, & 0 \leq t \leq t_r, \\ 0, & \text{else.} \end{cases} \quad (3.59)$$

The path  $z(t)$  determines the concentration  $c(t) = |\nabla c| z(t)$ . We denote the (forward) run time distribution for this particular path as  $P_r^{\pm \nabla c}$  and with the response

function from Eq. (3.29), we arrive at

$$P_r^{\pm\nabla c} = \lambda_r e^{-\lambda_r t_r} \left\{ 1 \mp v |\nabla c| W_r F(t_r, \lambda_r) \right\} \exp \left[ \pm v |\nabla c| W_r G(t_r, \lambda_r) \right], \quad (3.60)$$

where the functions  $F$  and  $G$  are defined as

$$F(t, \lambda) = \frac{e^{-\lambda t}}{4\lambda} (6e^{\lambda t} - 6 - \lambda t(6 + \lambda t)), \quad (3.61a)$$

$$G(t, \lambda) = \frac{e^{-\lambda t}}{4\lambda} ((6\lambda t - 14)e^{\lambda t} + 14 + \lambda t(8 + \lambda t)). \quad (3.61b)$$

The term in  $\{\dots\}$  brackets from Eq. (3.60) equals  $1 - \int_{-\infty}^{t_r} dt' c(t') R_r(t_r - t')$ . A positive probability distribution and tumbling rate requires it to be larger than zero for all  $t_r$ . According to Eq. (3.60),  $P_r^{-\nabla c} > 0$  always holds true, and a positive  $P_r^{+\nabla c}$  provides the condition

$$|\nabla c| v \frac{3W_r}{2\lambda_r} < 1. \quad (3.62)$$

It specifies the required smallness of gradient  $|\nabla c|$  and chemotactic strength  $W_r$ , such that Eq. (3.30) for the tumbling rate is valid. Note that the dimensionless number  $|\nabla c| v \frac{W_r}{\lambda_r}$  can also be found by scaling arguments when one requires the dimensionless gradient to be small.

Due to the exponential factor in Eq. (3.60), the distribution  $P_r^{\pm\nabla c}$  is not symmetric for  $\pm\nabla c$  around  $\nabla c = 0$ . As a consequence, the mean (forward) run times,  $\langle t_r \rangle_{\pm\nabla c} = \int_0^\infty dt_r P_r^{\pm\nabla c}(t_r) t_r$ , are not symmetric around the mean in a homogeneous environment where  $\langle t_r \rangle_{\nabla c=0} = \lambda_r^{-1}$ . We show that the theory also quantitatively explains the asymmetric shift of run times of *E. coli* from Table 3.3.

We take the experimental values from Ref. [59],  $v = 14.2 \mu\text{m s}^{-1}$ ,  $\alpha = \cos(68^\circ) = 0.37$ ,  $|\nabla c| \approx 10 \mu\text{m}^{-4}$ , and  $D_r = 0.062 \text{ s}^{-1}$ . The chemotactic drift speed  $v_d$  has not been determined in these experiments. For this reason, we assume the “large” value  $v_d = 0.74 \mu\text{m s}^{-1}$ , so that after solving Eq. (3.31) for the normalization  $W_r = 0.0019 \mu\text{m}^{-3}$ , the condition (3.62) is still satisfied. Setting  $\lambda_r = 1/\langle t_r \rangle_{\text{no gradient}} = 0.68 \text{ s}^{-1}$ , we numerically obtain the following mean run times for motion along  $\pm\nabla c$ :

$\langle t_r \rangle = 1.48 \text{ s}$	$\langle t_r \rangle_{+\nabla c} = 2.18 \text{ s}$	$\langle t_r \rangle_{-\nabla c} = 1.31 \text{ s}$
--	--	--

These values agree with the experimental data from Table 3.3. In particular, the mean run time  $\langle t_r \rangle_{-\nabla c}$  for motion along  $-\nabla c$  is close to  $\langle t_r \rangle = \lambda_r^{-1}$ . The theory thus predicts the observed asymmetric shift of mean run times  $\langle t_r \rangle_{\pm\nabla c}$  as compared to  $\langle t_r \rangle$ . We understand this result as an additional justification for the ansatz of the

tumbling rate [Eq. (3.30)], which does not depend on the cell's swimming direction with respect to the gradient.

We add a comment on the smallness of the concentration or the gradient. If we determine the response strength  $W_r$  for given  $v_d$  by Eq. (3.31), Eq. (3.62) requires

$$\frac{v_d}{v} < \frac{2\lambda_r}{3} \frac{\lambda_r^2 [\lambda_r(5 - 2\alpha) + 4D_r] (1 - \alpha)}{6 [2D_r + \lambda_r(1 - \alpha)] [2D_r + \lambda_r(2 - \alpha)]^3} \quad (3.63)$$

for our approach to be valid. Hence, we do not have to specify  $|\nabla c|$ , but the chemotactic drift speed  $v_d$  in units of the swimming speed  $v$  must not be too large. For the values from above, Eq. (3.63) gives  $v_d/v < 6.7\%$ ; for the “standard” values of this chapter, *i.e.*  $\alpha = 0.33$ ,  $\lambda_r = 1 \text{ s}^{-1}$ ,  $D_r = 0.2 \text{ s}^{-1}$ , one finds  $v_d/v < 4.0\%$ . Note that chemotactic drift speeds with a ratio up to  $v_d/v \sim 20\%$  have been experimentally observed [95]; in this situation, the chemical gradients are too large to apply the theory developed here.

### 3.4.2 Mean run times for *V. alginolyticus*

To obtain the mean forward run times along  $\pm\nabla c$  of the run-reverse-flick swimmer *V. alginolyticus*, we adopt the results from the previous section. Now, we briefly sketch how also to obtain the mean backward run times  $\langle t_b \rangle_{\pm\nabla c}$  along  $\pm\nabla c$  for *V. alginolyticus*.

By definition, a backward run along  $\pm\nabla c$  follows after a forward run along  $\mp\nabla c$ . Therefore, we calculate the distribution of backward run times

$$P_b^{\pm\nabla c} = \int_0^\infty dt_r p_r(0 \rightarrow t_r) p_b(t_r \rightarrow t_r + t_b) \quad (3.64)$$

for the specific path

$$z(t) = \begin{cases} \mp vt, & 0 \leq t \leq t_r, \\ \mp vt_r \pm v(t - t_r), & t_r \leq t \leq t_r + t_b, \\ 0, & \text{else.} \end{cases} \quad (3.65)$$

To evaluate  $p_r(0 \rightarrow t_r)$  in the integral of Eq. (3.64), we make use of Eq. (3.60) to find  $p_r(0 \rightarrow t_r) = P_r^{\mp\nabla c}$ , where the reversed sign ( $\mp\nabla c$ ) is due to the reversed direction of the forward run. The integration over  $t_r$  cannot be performed analytically, and due to the lengthy expression for  $P_b^{\pm\nabla c}$ , we only present numerical results for the mean backward run times  $\langle t_b \rangle_{\pm\nabla c} = \int_0^\infty dt_b P_b^{\pm\nabla c}(t_b) t_b$ .

For *V. alginolyticus*, we take the values from Table 3.2 with  $v = 45 \mu\text{m s}^{-1}$  and identical forward and backward rate  $\lambda = 3.3 \text{ s}^{-1}$ . As in Sec. 3.3, we adopt the

chemotactic strength  $W = 0.0458 \mu\text{m}^3$  of *E. coli* also for *V. alginolyticus*. We obtain the following mean run times for motion along  $\pm \nabla c$ :

Forward runs	$\langle t_r \rangle = 0.30 \text{ s}$	$\langle t_r \rangle_{+\nabla c} = 0.79 \text{ s}$	$\langle t_r \rangle_{-\nabla c} = 0.27 \text{ s}$
Backward runs	$\langle t_b \rangle = 0.30 \text{ s}$	$\langle t_b \rangle_{+\nabla c} = 0.54 \text{ s}$	$\langle t_b \rangle_{-\nabla c} = 0.34 \text{ s}$

We interpret these results as a possible explanation for the observations on *V. alginolyticus* from Ref. [110]. While our calculated  $\langle t_r \rangle_{+\nabla c}$  is significantly larger than  $\langle t_r \rangle$ ,  $\langle t_r \rangle_{-\nabla c}$  is only slightly smaller. The clear separation of these times might reflect the two observed peaks in the distribution of forward run times in a gradient. In contrast, for backward runs both  $\langle t_b \rangle_{\pm \nabla c}$  are larger than  $\langle t_b \rangle$  and relatively close to each other – similar to the experimental observation. The origin of this unexpected result lies in the correlation between forward and backward runs, as it manifests in the product on the right-hand side of Eq. (3.64).

We point out that the hypothesis that our results reflect the observations for *V. alginolyticus* might be daring due to several reasons. First, throughout the chapter we have adopted the chemotactic response function of *E. coli* to *V. alginolyticus* with the same strength for forward and backward runs. Second, the experiments from Ref. [110] have been performed in strong gradients, which we estimate as  $|\nabla c| \gtrsim 10^3 \dots 10^4 \mu\text{m}^{-4}$ . Third, for simplicity, we considered an exponential distribution of run times for *V. alginolyticus*, which is only a good approximation for sufficiently large times. Yet, we think that the trend of the theoretical predictions could be confirmed in future experiments with smaller gradients.

### 3.5 Summary

In this chapter, we compared different swimming strategies of bacteria in terms of their diffusion coefficient in a homogeneous environment, and their chemotactic drift speed in response to a small gradient of chemoattractant. Both the diffusion coefficient and the chemotactic drift speed serve as important measures of bacterial performance and can be determined in a straight-forward way from trajectories of swimming cells.

Whereas the run-and-tumble motion of *E. coli* and run-reverse strategy of numerous marine bacteria both constitute a two-step-process with different persistence parameter, the bacterium *V. alginolyticus* is characterized by the three-step-process run-reverse-flick. We have described these three patterns within a single random walk model, where “runs” are alternatingly interrupted by two distinct “tumbling” events. Both types of tumbling events are specified by a preferential turning angle of the walker’s velocity direction. For simplicity, the duration of tumbling is neglected

### 3.5 Summary

---

and the distribution of run times is assumed to be exponential. The random walkers move with constant speed during run events and are subjected to rotational diffusion of their velocity direction.

In summary, we obtained expressions for both the diffusion coefficient and the chemotactic drift speed for different swimming strategies. For these measures of bacterial performance, it turned out that rotational diffusion during the runs strongly affects the results, if the mean run time is comparable to the decorrelation time of rotational diffusion. In particular, we have shown that the diffusion coefficient of a run-reverse-flick swimmer is not zero, as it was stated in Refs. [110, 112]. Furthermore, if we assume the same chemotactic response function, our results indicate that the chemotactic drift speed of *V. alginolyticus* is only slightly larger than that of *E. coli*.

According to Ref. [111], the chemotactic drift speed of *V. alginolyticus* in a strong chemical gradient is three times larger than that of *E. coli*. As our calculation holds only for small gradients, we were not able to observe this behavior. To study the chemotactic drift speed numerically also in strong gradients, we suggest to apply the new model for the tumbling rate from Eqs. (3.55) and (3.56) for future investigations.

It might be also interesting to take into account fluctuations of the speed. As long as the fluctuations in the direction of motion and speed decouple, the velocity correlation function factorizes into a speed and an angular part, see Eq. (2.32). In this case, our results for the directional correlation function can be adopted without any difficulty.



# 4 Modeling an autochemotactic active walker

## 4.1 Introduction

In the following and subsequent chapter, we propose a model for microorganisms whose motion is governed by chemotactic signaling [73]. This means that microorganisms, such as bacteria, amoebae, or other cells, follow the gradient of a chemical that they produce themselves to attract or repel each other. Unlike a diffusion process, which is characterized by unbiased movement, chemotaxis results in a directed flow of particles towards regions of higher or lower concentration of a chemical substance [8]. As the chemical is produced by the microorganisms themselves, the system exhibits “autochemotaxis” and serves as a possible mechanism for communication among individuals. Two well-studied microorganisms showing autochemotaxis are the social amoeba *Dictyostelium discoideum* (*Dicty*) and the bacterium *E. coli* [63, 120, 121]. An important motivation for us to study chemotaxis is to understand the clustering of bacteria into microcolonies, which contributes to the early stage of biofilm formation [1, 122].

As mentioned in Sec. 2.4.1, the Keller-Segel model and its generalizations take a continuum approach. Here, in contrast, we explicitly describe the Langevin dynamics of individual microorganisms. In our approach, the microorganisms are treated as active particles with constant speed and rotational diffusion of their velocity directions, as presented in Sec. 2.3.1. Note that the particle speed is independent of both the absolute concentration and the gradient of the chemical. This fact constitutes a major difference to the chemotaxis models in Refs. [76, 123], where the particles are not active *per se*, as only the presence of a concentration gradient induces a non-zero mean speed. In our model, the particle speed represents an additional parameter and chemotaxis only influences the velocity direction; this kind of chemotaxis is sometimes also referred to as topotaxis [8].

Due to the complexity of a non-equilibrium system consisting of active particles, one can only address a few averaged macroscopic quantities of interest. Accordingly, calculating the long-time diffusion coefficient of interacting or self-propelled particles has been the key purpose of numerous publications; see, for instance, Refs. [76, 82, 123, 124, 125, 126, 127, 128, 129].

Our main goal of this chapter is to investigate the influence of autochemotaxis

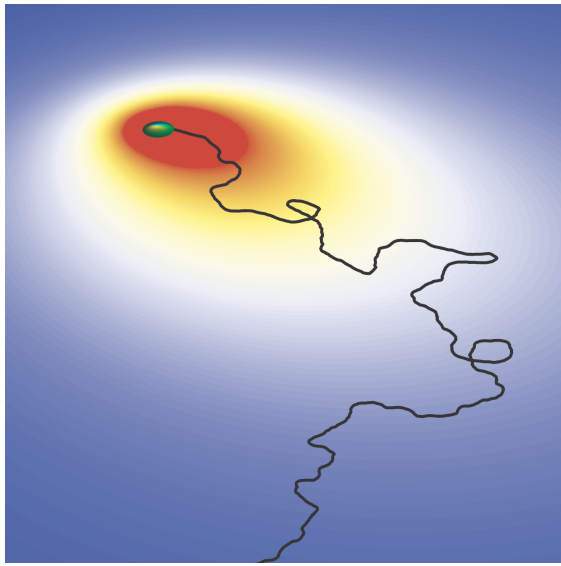


**Figure 4.1** ■ Schematic trajectory (black line) of an autochemotactic active walker. The walker continuously emits a diffusing chemical substance whose concentration field is shown as color-coded. The chemotactic feedback influences the walker to orient its velocity direction towards the red regions of high concentration.

on the diffusion coefficient of a single walker. In contrast to several approaches using perturbation theory [76, 125], our results also hold for strong chemotactic interactions. In the case of positive autochemotaxis, it is clear that the particle will be attracted to recently explored regions where it has emitted chemoattractant, as sketched in Fig. 4.1. As a consequence, the particle’s motion will be restricted in comparison to a freely diffusing non-chemotactic microorganism. So, the question arises whether the particle will eventually be trapped, in the sense that the diffusion coefficient vanishes –as is the case in a two-dimensional model by Tsori and de Gennes [130]– or whether the motion becomes diffusive in the long-time limit where the mean-squared displacement grows linearly in time [123, 126, 131]. Note that recent experimental results also inspired the study of chemotaxis models with subdiffusion and superdiffusion [113, 132, 133]. We will show that in our model even for strong chemotactic coupling the particle motion remains diffusive.

This chapter is organized as follows. In Sec. 4.2.1, we present our model for the dynamics of an autochemotactic active walker in detail, and illustrate it for the special case of a constant external chemotactic field in Sec. 4.2.2. The self-generated chemical field is modeled in Sec. 4.2.3. In Sec. 4.3, we derive analytical expressions for the diffusion coefficient of the walker and confirm our findings numerically. Finally, we summarize our results in Sec. 4.4. We will generalize our model to an ensemble of autochemotactic walkers in Chapter 5: In that system, individuals communicate with each other via the diffusing chemical, and cluster formation can be observed.

## 4.2 Model of the autochemotactic walker

### 4.2.1 Dynamic equation for the velocity direction

We model the time evolution of single trajectories of microorganisms that only move in two dimensions. The two-dimensional approach is justified because, aside from swimming, various forms of bacterial motility occur on surfaces [134]. As the historical example from Fig. 2.2 illustrates, the stochasticity in the motion of microorganisms is apparent [40]. An effective description therefore includes random forces and torques. Contributions to the stochastic terms originate from biochemical processes within a cell, *e.g.*, when a cell detects and reacts to a chemical field, as well as from stochastic interactions of the microorganisms with their environment. An example of the latter is ordinary thermal noise, which leads to Brownian motion of a micron-sized colloid and originates from collisions with the much smaller fluid particles; we presented the basics about Brownian motion in Sec. 2.1. However, in our case, there is no fluctuation-dissipation theorem for the noise. Note that our model particles should not be considered as swimming microorganisms, since they move on a surface. Nevertheless, including details of the propulsion mechanism lies beyond the scope of our coarse-grained approach.

In two dimensions, we write the velocity vector  $\mathbf{v}(t)$  of a bacterium at time  $t$  in polar coordinates, specified by the absolute value, the speed  $v(t) \geq 0$ , and the angle  $\varphi(t) \in (-\pi, \pi]$  relative to the  $x$  axis:

$$\mathbf{v}(t) = v(t) \begin{pmatrix} \cos \varphi(t) \\ \sin \varphi(t) \end{pmatrix}. \quad (4.1)$$

Experiments have demonstrated for different kinds of cells like granulocytes, monocytes, or fibroblasts that fluctuations in  $v(t)$  and  $\varphi(t)$  are independent of each other [44]. Though this property has to be checked for each experimental setup, it is reasonable to assume it in our model [45]. In addition, we will make the simplifying assumption that the speed  $v$  of our model particle is constant. In contrast to the fast fluctuating stochastic variable of the velocity direction, the speed is a slow stochastic variable. For example, as long as the microorganisms have an appropriate energy supply, there exists a speed distribution with a pronounced mean [135, 136, 137]. In the case of granulocytes, this distribution was even found to be Gaussian [44]. As explained in Sec. 3.1.1, the motility of *E. coli* is described by run-and-tumble dynamics, and during a run event the cell moves with almost constant speed. In summary, expressing the velocity vector in polar coordinates seems to be the natural choice for describing the motion of microorganisms. In contrast, most models for chemotactic bacteria have used Cartesian velocity components [76, 85, 138, 123].

In the following, we derive the equation of motion for the velocity direction of a single microorganism in response to chemotaxis. The shape of our microorganism is arbitrary, *e.g.* spherical or rod-like. However, the particle is polar and possesses

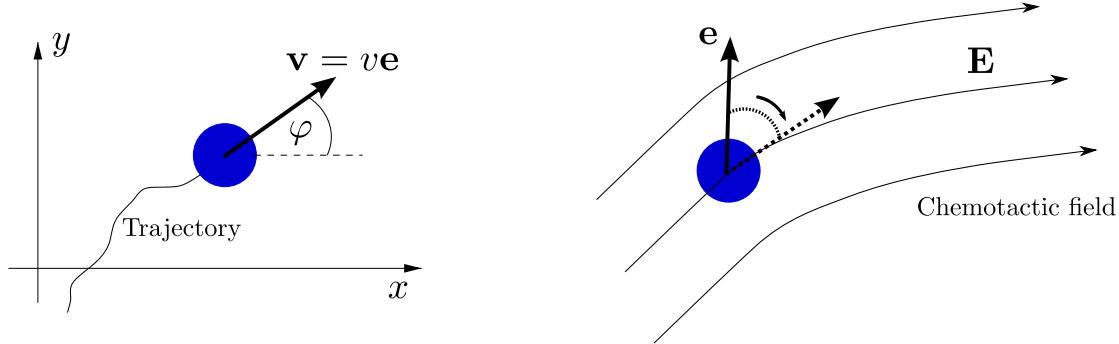


**Figure 4.2** ■ Left: Geometry of a microorganism that moves with speed  $v$  and direction of motion  $\mathbf{e}(t)$ . Right: Schematic illustration of the chemotactic torque that aligns the walker's velocity direction  $\mathbf{e}$  with the chemotactic field  $\mathbf{E}$ .

an intrinsic direction of motion that is characterized by a unit vector  $\mathbf{e}$ , say, parallel to its long axis. Furthermore, we assume that the particle always moves along this direction, so that  $\mathbf{v}(t) = v\mathbf{e}(t)$ , as sketched in the left plot of Fig. 4.2. Though this connection between velocity direction and particle orientation seems rather evident for an isolated microorganism, it is no longer valid in a suspension of microorganisms as a consequence of hydrodynamic interactions [139].

To account for chemotaxis, we introduce the potential

$$V(\mathbf{e}) = -\mathbf{e} \cdot \mathbf{E}. \quad (4.2)$$

It aligns the velocity direction  $\mathbf{e}$  with the chemotactic field  $\mathbf{E}$  that is detected at the surface of the microorganism [8]. The connection between  $\mathbf{e}$  and  $\mathbf{E}$  is sketched in the right plot of Fig. 4.2. We will specify this chemotactic field in Sec. 4.2.3 as the concentration gradient of a chemical, which is produced by the microorganisms themselves. In microfluidic devices, the chemotactic field  $\mathbf{E}$  can be imposed externally [140, 141]. For a wide range of microorganisms, the guiding field  $\mathbf{E}$  is realized by various stimuli, and examples have been given in Table 2.1: Whereas for chemotaxis the stimulus is a chemical substance, galvanotaxis refers to electric fields, and thermotaxis to temperature. Hence, in Eq. (4.2),  $\mathbf{E}$  describes the guiding field for any kind of taxis.

Certain cells use a spatial sensing mechanism to detect the gradient of a chemical field instantaneously without performing a temporal average. It is primarily found in eukaryotes, but in bacteria as well [66, 142]. By applying the rotational operator  $\mathcal{R} \equiv \mathbf{e} \times \frac{\partial}{\partial \mathbf{e}}$  to the chemotactic potential of Eq. (4.2) [56], one arrives at the chemotactic torque  $\mathbf{M}_{\text{ext}} = -\mathcal{R}V(\mathbf{e}) = \mathbf{e} \times \mathbf{E}$  that acts on the velocity direction  $\mathbf{e}$ .

We now derive the dynamic equation for  $\mathbf{e}(t)$  using Newton's equation of motion for the angular momentum  $\mathbf{L}$ ,

$$\frac{d}{dt} \mathbf{L} = -\gamma_R \boldsymbol{\Omega} + \mathbf{M}_{\text{ext}} + \boldsymbol{\Gamma}(t), \quad (4.3)$$

and the kinematic relation

$$\frac{d}{dt} \mathbf{e} = \boldsymbol{\Omega} \times \mathbf{e}, \quad (4.4)$$

which connects the angular velocity  $\boldsymbol{\Omega}$  to  $\mathbf{e}$ . In Eq. (4.3), we have introduced a frictional torque  $-\gamma_R \boldsymbol{\Omega}$ , where  $\gamma_R > 0$  is the rotational friction coefficient. The stochastic torque  $\boldsymbol{\Gamma}(t)$  is modeled as Gaussian white noise whose Cartesian components are independent of each other; the noise strength will be specified below.

In Sec. 2.2, we have argued that microorganisms swim at low Reynolds numbers, where the motion is dominated by friction compared to inertia. Therefore, we also work in the overdamped limit and employ the Debye approximation [143], which neglects the inertial term in Eq. (4.3). Taking the cross product of Eq. (4.3) with  $\mathbf{e}$ , eliminating  $\boldsymbol{\Omega}$  with Eq. (4.4), and using  $\mathbf{M}_{\text{ext}} \times \mathbf{e} = (\mathbf{e} \times \mathbf{E}) \times \mathbf{e} = (\mathbb{1} - \mathbf{e} \otimes \mathbf{e}) \mathbf{E}$ , we arrive at a Langevin equation with multiplicative noise, still valid in two and three dimensions,

$$\frac{d}{dt} \mathbf{e} = \frac{1}{\gamma_R} (\mathbb{1} - \mathbf{e} \otimes \mathbf{e}) \mathbf{E} + \frac{1}{\gamma_R} \boldsymbol{\Gamma}(t) \times \mathbf{e}, \quad (4.5)$$

where  $\mathbb{1}$  denotes the unit matrix and  $\otimes$  specifies the dyadic product. To formulate Eq. (4.5) in two dimensions, we parametrize the unit vector  $\mathbf{e}$  by  $\mathbf{e} = (\cos \varphi, \sin \varphi, 0)^T$  and let both  $\mathbf{M}_{\text{ext}}$  and  $\boldsymbol{\Gamma}(t) = (0, 0, \Gamma(t))^T$  point along the  $z$  axis. Due to the multiplicative noise, we have to choose an interpretation of the stochastic differential equation (4.5) to give it a well-defined meaning, see the discussion in Sec. 2.1.2. Since the Gaussian white noise approximates real colored noise with finite correlation time, we employ the Stratonovich interpretation [24]. As a practical consequence, the common rules of classical calculus apply, and, in particular, we have  $\frac{d}{dt} \mathbf{e} = \dot{\varphi} (-\sin \varphi, \cos \varphi, 0)^T$ . With  $\mathbf{E} = (E_x, E_y, 0)^T$ , Eq. (4.5) becomes

$$\begin{pmatrix} -\sin \varphi \\ \cos \varphi \end{pmatrix} \dot{\varphi} = \frac{1}{\gamma_R} \begin{pmatrix} \sin^2 \varphi E_x - \sin \varphi \cos \varphi E_y \\ -\sin \varphi \cos \varphi E_x + \cos^2 \varphi E_y \end{pmatrix} + \frac{1}{\gamma_R} \boldsymbol{\Gamma}(t) \begin{pmatrix} -\sin \varphi \\ \cos \varphi \end{pmatrix}, \quad (4.6)$$

from which a single Langevin equation for  $\varphi(t)$  is immediately extracted. It only has additive noise due to the restriction to two dimensions. We rescale the Gaussian white noise with zero mean  $\langle \boldsymbol{\Gamma}(t) \rangle = 0$  such that  $\langle \boldsymbol{\Gamma}(t) \boldsymbol{\Gamma}(t') \rangle = \delta(t - t')$ , introduce the noise strength  $q_\varphi > 0$ , and arrive at

$$\frac{d}{dt} \varphi(t) = -\frac{E_x}{\gamma_R} \sin \varphi(t) + \frac{E_y}{\gamma_R} \cos \varphi(t) + \sqrt{2q_\varphi} \boldsymbol{\Gamma}(t). \quad (4.7)$$

The chemotactic field  $\mathbf{E}$  is a space- and time-dependent function. In particular, it depends on the position  $\mathbf{r}(t) = (x(t), y(t))^T$  of the autochemotactic walker, which is determined by integrating  $\frac{d}{dt} \mathbf{r}(t) = \mathbf{v}(t) = v \mathbf{e}(t)$ . We emphasize that the Langevin equation (4.7) consists of a deterministic part, which tries to align  $\mathbf{e}(t)$  parallel to

the chemotactic field, and a stochastic part, which causes rotational diffusion of the velocity direction. Recall that we have discussed properties of pure rotational diffusion for  $\mathbf{E} = \mathbf{0}$  in Sec. 2.3.1.

Note that the deterministic part of Eq. (4.7) can also be derived from the Euler-Lagrange equation for  $\varphi(t)$  with the potential from Eq. (4.2) and the Rayleigh dissipation function  $W = \frac{1}{2}\gamma_R\dot{\varphi}^2$  [144]. This is seen by inserting the Lagrangian  $L = -V$  into  $\frac{d}{dt}\left(\frac{\partial L}{\partial \dot{\varphi}}\right) - \frac{\partial L}{\partial \varphi} + \frac{\partial W}{\partial \dot{\varphi}} = 0$ , which yields  $\frac{d}{dt}\varphi(t) = \frac{1}{\gamma_R}\frac{\partial}{\partial \varphi}(\mathbf{e} \cdot \mathbf{E})$ . In Ref. [145], Gruler and Franke introduced a model with a more general potential  $V(\mathbf{e}, \mathbf{E})$ ; our potential is the leading term in a Fourier expansion, linear in  $\mathbf{E}$ .

### 4.2.2 Constant chemotactic field

To get familiar with Eq. (4.7), we first consider the special case of a constant field  $\mathbf{E}$  in the absence of noise ( $q_\varphi = 0$ ). A constant chemotactic field can be realized with microfluidic techniques [140]. With  $\mathbf{E} = E\mathbf{e}_x$  ( $E > 0$ ), Eq. (4.7) reads

$$\frac{d}{dt}\varphi(t) = -\frac{E}{\gamma_R} \sin \varphi(t), \quad (4.8)$$

which we solve by separation of variables,

$$\varphi(t) = 2 \arctan \left( \tan(\varphi_0/2) e^{-t/\tau} \right), \quad (4.9)$$

with  $\tau = \gamma_R/E$ . The walker starts with an angle  $\varphi_0$  at  $t = 0$ . Its velocity direction relaxes towards the  $x$  axis and aligns along  $\mathbf{E}$  during the characteristic time  $\tau$ . Remarkably, using Eq. (4.9) in  $\frac{d}{dt}\mathbf{r}(t) = v\mathbf{e}(t)$ , one can determine the full trajectory analytically:

$$x(t) = x_0 + vt + v\tau \ln \left( \frac{1 + \tan^2(\varphi_0/2)e^{-2t/\tau}}{1 + \tan^2(\varphi_0/2)} \right), \quad (4.10a)$$

$$y(t) = y_0 + 2v\tau \left[ \arctan \left( \frac{e^{t/\tau}}{\tan(\varphi_0/2)} \right) - \arctan \left( \frac{1}{\tan(\varphi_0/2)} \right) \right]. \quad (4.10b)$$

This result confirms that in the long-time limit  $t \gg \tau$  the particle walks in  $x$  direction with speed  $v$ , while it asymptotically reaches a constant  $y$  coordinate. Three trajectories for different initial angles  $\varphi_0$  and relaxation times  $\tau$  are presented in Fig. 4.3.

Additionally, let us consider a constant torque that acts on the walker's direction of motion and mimics, for instance, a perturbation in a simplistic way. Including  $\Gamma > 0$  on the right-hand side of Eq. (4.8), we find analytically two different types of trajectories that are displayed in Fig. 4.4. For small “perturbations” with  $\Gamma\tau < 1$ , the particle moves at large times in a fixed direction which does not coincide with

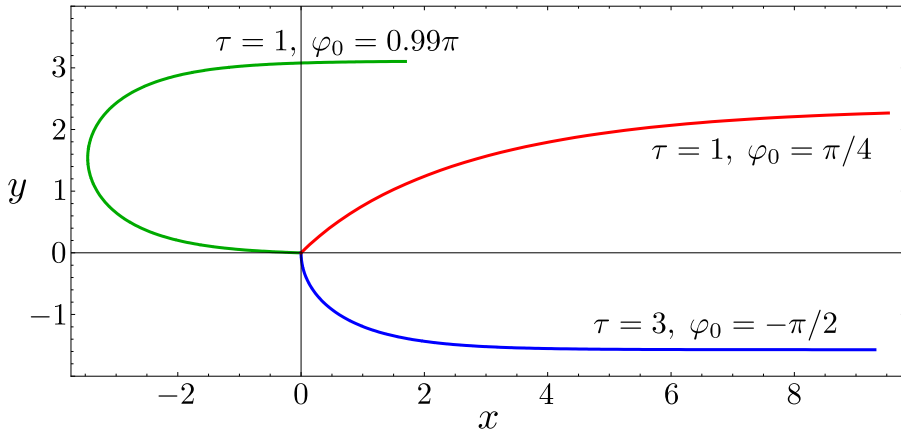


**Figure 4.3** ■ Plot in arbitrary units of three deterministic trajectories in the constant chemotactic field  $\mathbf{E} = E\mathbf{e}_x$  according to Eq. (4.10). All particles start at the origin with speed  $v = 1$  and move during the time interval  $t \in [0, 10]$ .

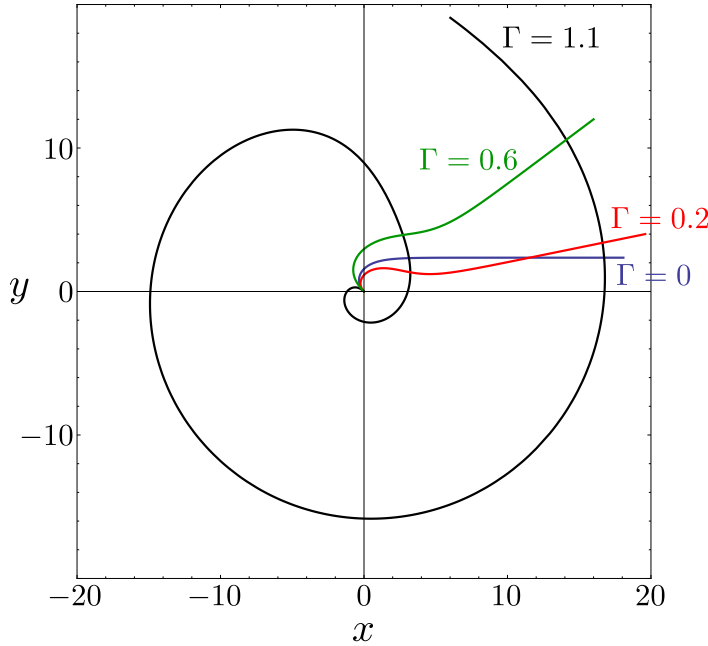


**Figure 4.4** ■ Four trajectories in the constant chemotactic field  $\mathbf{E} = E\mathbf{e}_x$  and in the presence of a constant torque  $\Gamma \in \{0, 0.2, 0.6, 1.1\}$ . Each particle starts at the origin with speed  $v = 1$ , initial direction  $\varphi_0 = 3\pi/4$ , and moves during the time interval  $t \in [0, 20]$ . The relaxation time is  $\tau = 1$ ; spiral-like trajectories are obtained for  $\Gamma\tau > 1$ .

the direction of the chemotactic field. On the contrary, for strong torques with  $\Gamma\tau > 1$ , one obtains spiral-like trajectories.

For completeness, we also discuss the consequences of the noise term  $\sqrt{2q_\varphi} \Gamma(t)$  added to Eq. (4.8) [146]. For the resulting Langevin equation, we formulate the associated Fokker-Planck equation for the probability density  $P = P(\varphi, t)$ :

$$\frac{\partial P}{\partial t} = \frac{1}{\tau} \frac{\partial}{\partial \varphi} (P \sin \varphi) + q_\varphi \frac{\partial^2}{\partial \varphi^2} P. \quad (4.11)$$

In the long-time limit,  $P(\varphi, t)$  relaxes towards the stationary solution [18],

$$P_{\text{stat}}(\varphi) = \frac{\exp\left(\frac{1}{q_\varphi \tau} \cos \varphi\right)}{2\pi I_0\left(\frac{1}{q_\varphi \tau}\right)}, \quad (4.12)$$

where a modified Bessel function of the first kind  $I_0$  has entered as a normalization factor. More general, the modified Bessel functions of the first kind and order  $n$  are given by  $I_n(z) = \int_{-\pi}^{+\pi} \frac{d\varphi}{2\pi} \cos(n\varphi) e^{z \cos \varphi}$ .  $P_{\text{stat}}(\varphi)$  is the von Mises distribution and is also known as the circular normal distribution. It is reminiscent of the Boltzmann distribution of dipoles in an external field in thermal equilibrium.  $P_{\text{stat}}(\varphi)$  is symmetric around the origin with maximum at  $\varphi = 0$  and decays to a finite value for  $\varphi \rightarrow \pm\pi$  as shown in Fig. 4.5. We quantify the average alignment of the walker along the chemotactic field by the order parameter

$$\langle \cos \varphi \rangle = \int_{-\pi}^{+\pi} d\varphi P_{\text{stat}}(\varphi) \cos \varphi = \frac{I_1\left(\frac{1}{q_\varphi \tau}\right)}{I_0\left(\frac{1}{q_\varphi \tau}\right)}. \quad (4.13)$$

For strong chemotactic field or weak noise,  $\tau \ll 1/q_\varphi$ , the order parameter approaches one (inset of Fig. 4.5), and the velocity vector is completely oriented parallel to the external field. For small chemotactic field,  $\tau \gg 1/q_\varphi$ , the order parameter increases linearly in  $1/(q_\varphi \tau)$ . Note that  $\langle \cos \varphi \rangle$  is equivalent to the averaged chemotactic index, see Sec. 3.3.3 [147]. The average drift velocity becomes  $\mathbf{v}_{\text{drift}} = v \langle \cos \varphi \rangle \mathbf{e}_x$ , which vanishes for  $\mathbf{E} = \mathbf{0}$  due to the rotational diffusion of the walker.

### 4.2.3 Chemotactic field of the autochemotactic walker

Next, we model the chemotactic field, which is generated by the walker itself. The walker or bacterium secretes a chemical substance with a constant production rate  $h$ . We assume that the chemical spreads through the environment by Gaussian diffusion with diffusion constant  $D_c$ . Due to enzymatic activity in the environment, the chemical also decays with a rate  $k$ , which we assume constant for simplicity. The concentration field of the chemical thus obeys the reaction diffusion equation

$$\frac{\partial}{\partial t} c(\mathbf{r}, t) = D_c \nabla^2 c(\mathbf{r}, t) - kc(\mathbf{r}, t) + h\delta[\mathbf{r} - \mathbf{r}_a(t)], \quad (4.14)$$

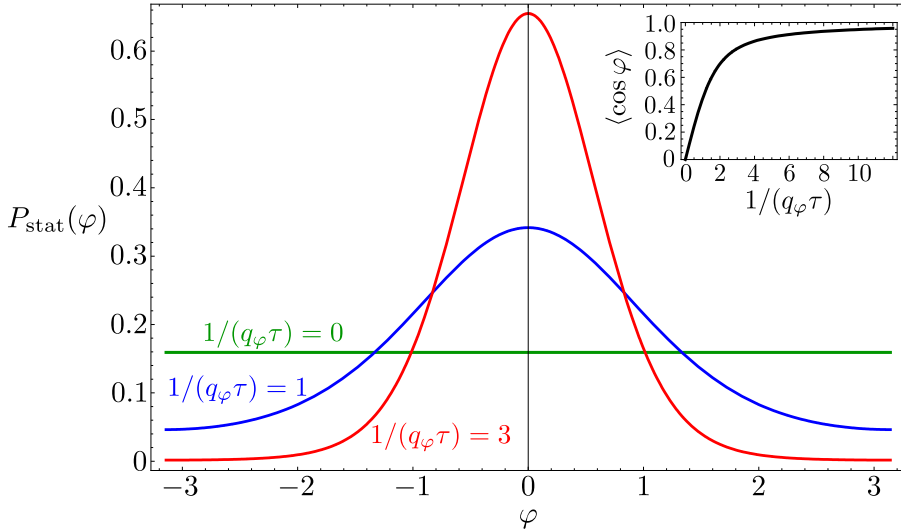


**Figure 4.5** ■ Stationary probability distribution for different chemotactic fields according to Eq. (4.12); for  $E \propto \tau^{-1} = 0$ , the distribution is constant. The inset shows the order parameter  $\langle \cos \varphi \rangle$  as a function of  $1/(q_\varphi \tau)$ .

where  $\mathbf{r}_a(t)$  is the trajectory of the walker and  $\nabla^2$  is the Laplacian in two dimensions. We already encountered Eq. (4.14) as a part of the classical Keller-Segel model (2.63); it is also found in recent chemotaxis models [76, 85, 126, 148, 149].

Assuming that the walker starts to produce the chemical at  $t = 0$ , the solution of Eq. (4.14), given in Eqs. (2.72), (2.73), is the Green's function integrated over all positions  $\mathbf{r}_a(t')$  of the walker:

$$c(\mathbf{r}, t) = \frac{h}{4\pi D_c} \int_0^t dt' \frac{e^{-k(t-t')}}{t-t'} \exp\left(-\frac{[\mathbf{r} - \mathbf{r}_a(t')]^2}{4D_c(t-t')}\right). \quad (4.15)$$

This result reveals the non-Markovian character of our system since the concentration at time  $t$  is influenced by the walker's position at times  $t' < t$ . The numerical evaluation of the integral is, however, facilitated as the exponential decay admits to reduce the integration range to times  $t'$  with  $k(t-t') \lesssim 1$ .

The chemotactic field is proportional to the gradient of the chemical:

$$\mathbf{E}(\mathbf{r}, t) = \kappa(c) \nabla c(\mathbf{r}, t). \quad (4.16)$$

The chemotactic factor or chemotactic sensitivity  $\kappa(c)$  determines the coupling strength and its sign enables one to distinguish between positive (attractive) and negative (repulsive) chemotaxis. In general, the chemotactic sensitivity  $\kappa(c)$  is a function of the concentration, for which we have given two examples in Eq. (2.64). In particular, microorganisms usually need a minimal concentration to detect the chemical. Nevertheless, here, we consider the simplest case of a constant coupling

strength  $\kappa(c) = \kappa$ . The chemotactic field entering the Langevin equation (4.7) for the walker's velocity direction is therefore given by  $\mathbf{E}(\mathbf{r}, t) = \kappa \nabla c(\mathbf{r}, t)$ , evaluated at the walker's position  $\mathbf{r}_a(t)$ .

The integrand in Eq. (4.15) diverges at the upper bound. Therefore, we introduce a regularization time  $\tau_{\text{del}} > 0$  such that the upper bound of the integral changes to  $t - \tau_{\text{del}}$  [123]. One can justify  $\tau_{\text{del}}$  as the delay time before the microorganism starts to sense the chemical. In numerical simulations, we do not regard  $\tau_{\text{del}}$  as a relevant parameter of our model and set it to the value of the time step. We point out that there are other alternatives to circumvent the introduction of  $\tau_{\text{del}}$  when evaluating the concentration  $c(\mathbf{r}_a(t), t)$  at the cell's position. For instance, we can take the finite size of the cell into account and represent the cell's observed concentration by the convolution of  $c(\mathbf{r}, t)$  with a Gaussian filter  $g$ ,

$$C(\mathbf{r}, t) = \int_{\mathbb{R}^2} d^2 r' c(\mathbf{r}', t) g(\mathbf{r} - \mathbf{r}'), \quad g(\mathbf{r}) = \frac{1}{2\pi a^2} \exp\left(-\frac{\mathbf{r}^2}{2a^2}\right). \quad (4.17)$$

The width  $a$  of the filter is given by the characteristic cell size. After inserting  $c(\mathbf{r}, t)$  from Eq. (4.15) we obtain the “filtered” concentration at the cell position,

$$C(\mathbf{r}_a(t), t) = \frac{h}{\pi} \int_0^t dt' \frac{e^{-k(t-t')}}{2a^2 + 4D_c(t-t')} \exp\left(-\frac{[\mathbf{r}_a(t) - \mathbf{r}_a(t')]^2}{2a^2 + 4D_c(t-t')}\right). \quad (4.18)$$

With  $a > 0$  the integrand does not diverge any longer at the upper bound, whereas for  $a = 0$  we recover the former expression  $c(\mathbf{r}_a(t), t)$  without convolution.

## 4.3 Diffusion coefficient of the autochemotactic walker

We consider a single autochemotactic walker that moves in its self-generated cloud of chemical. Even for this one-particle problem the non-Markovian property does not allow a full analytic treatment. We can, however, find an analytic expression for the walker's mean-squared displacement for large times, and thereby extract the effective diffusion coefficient  $D_{\text{eff}}$ . We will calculate  $D_{\text{eff}}$  analytically for weak (Sec. 4.3.1) and strong (Sec. 4.3.2) chemotactic coupling, and then compare to numerical simulations in Sec. 4.3.3.

### 4.3.1 Weak chemotactic coupling

In the following, we perform an approximate treatment of the chemotactic walker, for which we will show at the end that it is only valid for sufficiently small chemotactic coupling. Our treatment is motivated by the work of Grima in Ref. [126].

After substituting  $t - t' = ut$ , the gradient of Eq. (4.15), evaluated at the walker's position  $\mathbf{r}_a(t)$ , reads

$$\begin{aligned} \nabla c(\mathbf{r}_a(t), t) &= -\frac{h}{8\pi D_c^2} \frac{1}{t} \int_{\tau_{\text{del}}/t}^1 du \frac{\mathbf{r}_a(t) - \mathbf{r}_a(t - ut)}{u^2} \\ &\times \exp\left(-\frac{[\mathbf{r}_a(t) - \mathbf{r}_a(t - ut)]^2}{4D_c tu} - ktu\right). \end{aligned} \quad (4.19)$$

This expression cannot be evaluated in general. However, as we are interested in the mean-squared displacement for large times  $t \gg 1/k$ , we perform an asymptotic analysis with  $kt \gg 1$ . The integral in Eq. (4.19) is then dominated by the exponential function calculated at  $u \ll 1$ . With the Taylor expansion up to second order in  $u$ ,

$$\mathbf{r}_a(t) - \mathbf{r}_a(t - ut) = ut\dot{\mathbf{r}}_a(t) - \frac{(ut)^2}{2}\ddot{\mathbf{r}}_a(t) + \mathcal{O}(u^3), \quad (4.20)$$

we calculate

$$[\mathbf{r}_a(t) - \mathbf{r}_a(t - ut)]^2 = (vut)^2 + \mathcal{O}(u^4). \quad (4.21)$$

Here, we used  $\dot{\mathbf{r}}_a = v\mathbf{e}$ ,  $\mathbf{e}^2 = 1$ , and  $\dot{\mathbf{r}}_a \cdot \ddot{\mathbf{r}}_a = v^2\mathbf{e} \cdot \dot{\mathbf{e}} = 0$ . In contrast to Grima's model in Ref. [126], we will need the second-order term in Eq. (4.20) for further analysis. We use Eqs. (4.20) and (4.21) to expand  $\nabla c(\mathbf{r}_a(t), t)$  from Eq. (4.19) up to second order in  $u$  and derive from Eq. (4.7) a Langevin equation for the velocity direction, valid at large times,

$$\frac{d}{dt} \varphi(t) = \sqrt{2q_\varphi^{\text{eff}}} \Gamma(t) \quad (4.22)$$

with

$$q_\varphi^{\text{eff}} = q_\varphi/f_{\text{ch}}, \quad f_{\text{ch}} = \left(1 - \frac{\kappa h v e^{-\zeta \tau_{\text{del}}}}{16\pi \gamma_R D_c^2 \zeta}\right)^2, \quad (4.23)$$

and  $\zeta = v^2/(4D_c) + k$ . Equation (4.22) implies that in the long-time limit the particle diffuses with the effective diffusion coefficient

$$D_{\text{eff}} = \frac{v^2}{2q_\varphi^{\text{eff}}} = \frac{v^2}{2q_\varphi} f_{\text{ch}}. \quad (4.24)$$

Note that even in the limit for vanishing delay time  $\tau_{\text{del}} \rightarrow 0$  the expression for  $D_{\text{eff}}$  remains finite.

At this stage, we present the derivation of Eq. (4.22). The exponential in Eq. (4.19) is written as  $\exp(-\zeta ut + \mathcal{O}(u^3))$ , such that up to second order in  $u$ , we arrive at

$$\begin{aligned}\nabla c(\mathbf{r}_a(t), t) &= \left[ -\frac{h}{8\pi D_c^2} \int_{\tau_{\text{del}}/t}^1 du \frac{e^{-\zeta ut}}{u} \right] \dot{\mathbf{r}}_a(t) \\ &\quad + \left[ \frac{h}{16\pi D_c^2} t \int_{\tau_{\text{del}}/t}^1 du e^{-\zeta ut} \right] \ddot{\mathbf{r}}_a(t).\end{aligned}\quad (4.25)$$

Hence, the concentration gradient at position  $\mathbf{r}_a(t)$  is proportional to the velocity  $\dot{\mathbf{r}}_a(t)$  and the acceleration  $\ddot{\mathbf{r}}_a(t)$  of the walker. To proceed, we only need to take into account the integral in the second term. Due to  $kt \gg 1$  we also have  $\zeta t \gg 1$  and thus approximate  $t \int_{\tau_{\text{del}}/t}^1 du \exp(-\zeta ut) \approx \exp(-\zeta \tau_{\text{del}})/\zeta$ . Altogether, we have

$$\nabla c(\mathbf{r}_a(t), t) = [\dots] v \mathbf{e}(t) + \frac{h}{16\pi D_c^2} \frac{e^{-\zeta \tau_{\text{del}}}}{\zeta} v \dot{\mathbf{e}}(t). \quad (4.26)$$

Now, we insert the chemotactic force  $\mathbf{E}(\mathbf{r}_a(t), t) = \kappa \nabla c(\mathbf{r}_a(t), t)$  into Eq. (4.5) for the unit vector:

$$\frac{d}{dt} \mathbf{e} = \frac{1}{\gamma_R} (\mathbb{1} - \mathbf{e} \otimes \mathbf{e}) \left[ [\dots] \mathbf{e}(t) + \kappa \frac{h v e^{-\zeta \tau_{\text{del}}}}{16\pi D_c^2 \zeta} \dot{\mathbf{e}}(t) \right] + \text{“noise term”}. \quad (4.27)$$

Using the fact that  $(\mathbb{1} - \mathbf{e} \otimes \mathbf{e})$  is a projection operator onto the space perpendicular to  $\mathbf{e}$  and the property  $\mathbf{e} \perp \dot{\mathbf{e}}$ , only the second summand in Eq. (4.27) contributes. As it is proportional to  $\dot{\mathbf{e}}(t)$  we can write the equation of motion as

$$\left( 1 - \frac{\kappa}{\gamma_R} \frac{h v e^{-\zeta \tau_{\text{del}}}}{16\pi D_c^2 \zeta} \right) \frac{d}{dt} \mathbf{e}(t) = \text{“noise term”}. \quad (4.28)$$

By rewriting Eq. (4.28) in terms of the angle, we obtain the Langevin equation (4.22).

In Sec. 4.3.3, we will present numerical investigations in dimensionless quantities by using characteristic quantities of the diffusing chemical, as discussed in Chapter 2.4.1. We rescale time by the inverse decay rate,  $t_c = 1/k$ , and length by  $l_c = \sqrt{D_c/k}$ , the distance the chemical diffuses during its lifetime  $t_c$ . The rescaled model then contains three essential parameters: The effective chemotaxis strength

$$\Lambda = h \kappa \frac{t_c^2}{\gamma_R l_c^3} \quad (4.29)$$

is proportional to coupling constant  $\kappa$  and production rate  $h$ , the noise strength  $\tilde{q}_\varphi = q_\varphi t_c$ , and the speed of the walker  $\tilde{v} = v t_c / l_c$ . In addition, the rescaled delay time is  $\tilde{\tau}_{\text{del}} = \tau_{\text{del}} / t_c$ . The diffusion coefficient  $\tilde{D}_{\text{eff}} = \tilde{v}^2 / (2\tilde{q}_\varphi^{\text{eff}})$  is measured in units of the chemical’s diffusion coefficient  $D_c = l_c^2 t_c^{-1}$ . From now on, we will drop all

the tilde signs to ease the notation. Then, the rescaled diffusion coefficient from Eq. (4.24) becomes

$$D_{\text{eff}} = \frac{v^2}{2q_\varphi} \left( 1 - \frac{\Lambda}{16\pi} \frac{v}{1+v^2/4} e^{-(1+v^2/4)\tau_{\text{del}}} \right)^2. \quad (4.30)$$

For large delay times  $\tau_{\text{del}} \gg 1$ , the diffusion coefficient (4.30) equals the free diffusion coefficient  $D = \frac{v^2}{2q_\varphi}$ , since the chemical has already decayed to zero before the walker reacts to it. Also for  $v \gg 1$ , we find  $D_{\text{eff}} \rightarrow D$ , since the particle moves faster than the diffusive spread of its own chemotactic field.

In the case of large attractive or repulsive chemotactic coupling, Eq. (4.30) predicts a quadratic scaling  $D_{\text{eff}} \propto |\Lambda|^2$ . For negative autochemotaxis, this result is conceivable, whereas it is obviously wrong for attractive chemotaxis, since a strong attraction of the particle by its own secretion should reduce the diffusion coefficient. We therefore have to restrict the validity of Eq. (4.30) to  $\Lambda < \Lambda_0$ , where

$$\Lambda_0 = 16\pi \frac{1+v^2/4}{v} e^{(1+v^2/4)\tau_{\text{del}}} \quad (4.31)$$

is the coupling constant with  $D_{\text{eff}} = 0$ . Indeed, for  $0 < \Lambda < \Lambda_0$ ,  $D_{\text{eff}}$  decreases with increasing  $\Lambda$ , as expected. The validity of Eq. (4.30) breaks down for large  $\Lambda$  since in Eqs. (4.20) and (4.21) we neglected higher order terms in  $u$  when calculating the chemotactic field. This will become clearer in the next subsection.

### 4.3.2 Strong chemotactic coupling

To treat the case of strong chemotactic coupling, we rewrite the Langevin equation (4.7) as

$$\frac{d}{dt} \varphi(t) = \Omega(t) + \sqrt{2q_\varphi} \Gamma(t), \quad (4.32)$$

where the time-dependent frequency or angular drift velocity  $\Omega(t)$  is given by

$$\Omega(t) = -\frac{E_x(\mathbf{r}_a(t), t)}{\gamma_R} \sin \varphi(t) + \frac{E_y(\mathbf{r}_a(t), t)}{\gamma_R} \cos \varphi(t). \quad (4.33)$$

We now consider a sufficiently strong attractive chemotactic field and neglect noise for a moment. The walker emits the chemical and thereby creates a concentration gradient opposite to the direction of motion, with which the walker always tries to align. Hence for strong positive autochemotaxis, we expect circular trajectories with a constant circling frequency  $\Omega(t) = \omega$ . This scenario is confirmed, as the trajectory on the left of Fig. 4.6 illustrates. One might have expected that for strong chemotactic attraction the walker rests in the center of a stationary concentration

profile; however, this is not possible since the self-propelled particle always moves with constant speed.

In the following, we calculate the circling frequency  $\omega$  self-consistently for  $q_\varphi = 0$ . We describe the circular trajectory of the walker around the origin by

$$\mathbf{r}_a(t) = r_0 \begin{pmatrix} \sin \omega t \\ -\cos \omega t \end{pmatrix}, \quad (4.34)$$

where  $r_0$  is the radius and positive or negative  $\omega$  leads to counterclockwise or clockwise circling, respectively. The velocity reads

$$\mathbf{v}(t) = \dot{\mathbf{r}}_a(t) = v \begin{pmatrix} \cos \varphi(t) \\ \sin \varphi(t) \end{pmatrix}, \quad (4.35)$$

with

$$\varphi(t) = \omega t \quad \text{and} \quad v = r_0 \omega, \quad (4.36)$$

consistent with our model. After substituting Eq. (4.34) into the chemotactic field  $\mathbf{E}(\mathbf{r}_a(t), t) = \kappa \nabla c(\mathbf{r}_a(t), t)$  with  $c$  from Eq. (4.15) and using some trigonometric identities, we obtain

$$\begin{aligned} \mathbf{E}(\mathbf{r}_a(t), t) &= -\frac{\kappa h r_0}{4\pi D_c^2} \int_0^{t-\tau_{\text{del}}} dt' \frac{e^{-k(t-t')}}{(t-t')^2} \sin \left[ \frac{\omega}{2}(t-t') \right] \\ &\quad \times \begin{pmatrix} \cos[\frac{\omega}{2}(t+t')] \\ \sin[\frac{\omega}{2}(t+t')] \end{pmatrix} \exp \left( -\frac{r_0^2 \sin^2 [\frac{\omega}{2}(t-t')]}{D_c(t-t')} \right). \end{aligned} \quad (4.37)$$

Then, we insert Eq. (4.37) into Eq. (4.33), set  $\Omega(t) = \omega$ , and employ Eq. (4.36). We introduce again our reduced variables, in particular the effective chemotactic coupling strength  $\Lambda$ , and after substituting  $t - t'$  by  $ut$ , we arrive at

$$1 = \frac{\Lambda v}{4\pi\omega^2} \int_{\tau_{\text{del}}/t}^1 du \frac{1}{t} \frac{e^{-tu}}{u^2} \sin^2 \left( \frac{\omega t}{2} u \right) \exp \left( -\frac{v^2 \sin^2 (\frac{\omega t}{2} u)}{\omega^2 tu} \right). \quad (4.38)$$

This is an implicit equation for the unknown circling frequency  $\omega$ , valid at large times. Note that at short times the particle has not yet reached the circling motion. It is possible to solve Eq. (4.38) numerically for  $\omega = \omega(\Lambda, v, \tau_{\text{del}}; t)$ . For  $t \rightarrow \infty$  we can also calculate the integral in Eq. (4.38) analytically, since the exponential becomes one, the lower bound of the integral tends to zero, and the upper bound can be set to infinity due to  $e^{-tu}$ . Evaluating the resulting integral yields

$$1 \approx \frac{\Lambda v}{4\pi\omega^2} \left[ \frac{\omega}{2} \arctan \omega - \frac{1}{4} \ln(1 + \omega^2) \right], \quad (4.39)$$

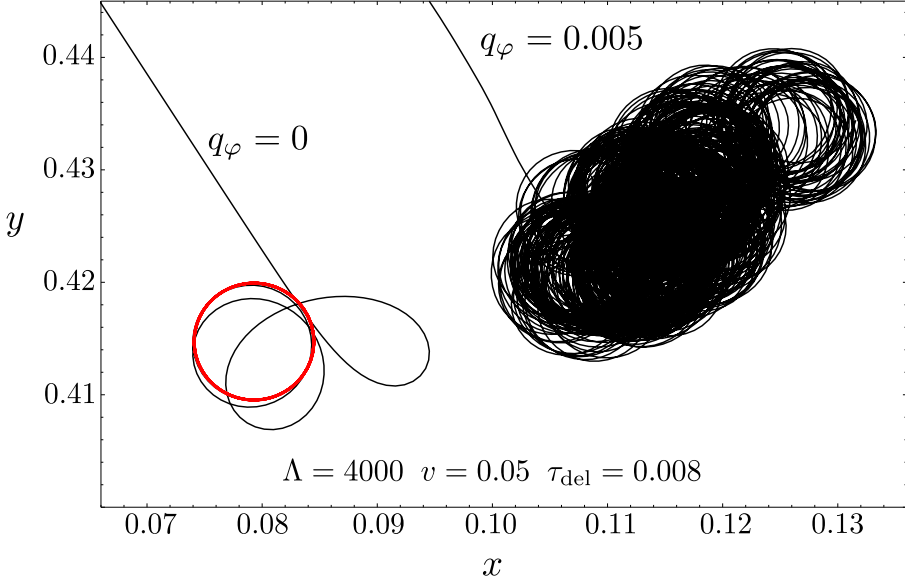


**Figure 4.6** ■ Trajectories for strong attractive chemotaxis simulated with the full model of Eq. (4.7) or (4.32). Left: Deterministic motion ( $q_\varphi = 0$ ) towards a limit cycle, shown as red circle. Right: With noise ( $q_\varphi = 0.005$ ), the circular motion is perturbed and the circle's center diffuses.

independent of the delay time  $\tau_{\text{del}}$ . From Eq. (4.39), we derive<sup>1</sup> a necessary condition for a solution  $\omega$  to exist,

$$\Lambda \gtrsim \frac{16\pi}{v}, \quad (4.40)$$

which we confirm by simulations in Sec. 4.3.3. Comparing this lower bound for  $\Lambda$  to Eq. (4.31) shows that the range of validity is complementary to the case of weak coupling.

We now include noise of strength  $q_\varphi$  in Eq. (4.32). As the trajectory on the right of Fig. 4.6 demonstrates, the noise perturbs the perfect circular motion of the walker. Since  $\varphi(t)$  but also the chemotactic field  $\mathbf{E}(\mathbf{r}_a(t), t)$  become fluctuating quantities, the angular drift velocity in Eq. (4.33) also fluctuates around  $\omega$ ,  $\Omega(t) = \omega + \delta\omega(t)$ . In Sec. 4.3.3, we will demonstrate that the fluctuations  $\delta\omega(t)$  are Gaussian distributed, so that we can replace them by an additional noise strength  $q_\omega$ . We therefore generalize  $\frac{d}{dt}\varphi(t) = \omega$  by adding Gaussian white noise of strength  $q = q_\varphi + q_\omega$ :

$$\frac{d}{dt}\varphi(t) = \omega + \sqrt{2q}\Gamma(t). \quad (4.41)$$

<sup>1</sup>A solution  $\omega$  satisfies  $\frac{4\pi}{\Lambda v}\omega^2 = \frac{\omega}{2}\arctan\omega - \frac{1}{4}\ln(1+\omega^2)$ . For large  $\omega$ , the dominant term of the r.h.s. behaves as  $\propto \frac{\pi}{2}\omega - \frac{1}{2}\ln\omega$ . The leading term is thus linear in  $\omega$  and therefore the function  $\frac{\omega}{2}\arctan\omega - \frac{1}{4}\ln(1+\omega^2)$  lies below the parabola  $\frac{4\pi}{\Lambda v}\omega^2$  on the l.h.s. For a solution to exist, both functions have to intersect and for small  $\omega$  the relation  $\frac{4\pi}{\Lambda v}\omega^2 < \frac{\omega}{2}\arctan\omega - \frac{1}{4}\ln(1+\omega^2)$  has to be fulfilled. With the Taylor expansion  $\frac{\omega^2}{4}$  for the r.h.s., we obtain  $\frac{4\pi}{\Lambda v} < \frac{1}{4}$ .

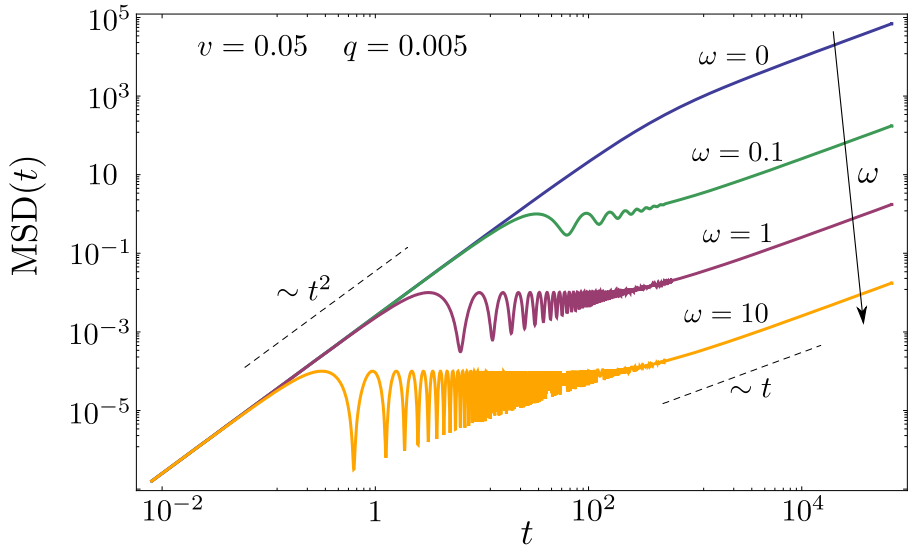


Figure 4.7 ■ Mean-squared displacement (MSD) of a circling walker with noise according to Eq. (4.42) for different frequencies  $\omega$ . Speed  $v$  and noise strength  $q$  are fixed.

In Sec. 2.3.2 [Eq. (2.52)], we have calculated the mean-squared displacement (MSD) of the particle as

$$\begin{aligned} \langle [\mathbf{r}_a(t) - \mathbf{r}_a(0)]^2 \rangle &= \frac{2v^2qt}{q^2 + \omega^2} - \frac{2v^2(q^2 - \omega^2)}{(q^2 + \omega^2)^2} \\ &\quad + \frac{2v^2e^{-qt}}{(q^2 + \omega^2)^2} \left[ (q^2 - \omega^2) \cos(\omega t) - 2q\omega \sin(\omega t) \right]. \end{aligned} \quad (4.42)$$

Figure 4.7 shows a double-logarithmic plot of the MSD. Initially, the walker moves ballistically, and then the MSD starts to oscillate when the walker performs circular motion. This is confirmed by taking the short-time limit of Eq. (4.42) for  $\omega \gg q$  at  $t \ll q^{-1}$ :  $\langle [\mathbf{r}_a(t) - \mathbf{r}_a(0)]^2 \rangle \approx \frac{4v^2}{\omega^2} \left[ \sin^2\left(\frac{\omega}{2}t\right) + qt \cos^2\left(\frac{\omega}{2}t\right) \right]$ . Finally, at large times, the walker diffuses with an effective diffusion coefficient

$$D_{\text{eff}} = D_{\text{eff}}(q, \omega) = \frac{v^2}{2q} \frac{1}{1 + (\frac{\omega}{q})^2}. \quad (4.43)$$

It is written as a product of the free diffusion coefficient and the Cauchy-Lorentz function with variable  $\omega/q$ . For fixed  $q$ ,  $D_{\text{eff}}$  is maximal in the absence of any circling for  $\omega = 0$ . For given  $\omega$ , the maximal diffusion coefficient is at  $q = |\omega|$ . So, the diffusion coefficient, as the system's response to noise, is maximal for a non-zero  $q$ . This resembles stochastic resonance, where a weak signal is amplified by noise of certain strength.

	size [ $\mu\text{m}$ ]	$v$ [ $\mu\text{m s}^{-1}$ ]	$\tau_{\text{rot}} = q_\varphi^{-1}$ [s]	$D$ [ $\text{m}^2 \text{s}^{-1}$ ]	$s_{\text{per}}$ [ $\mu\text{m}$ ]
<i>E. coli</i>	1 … 2	20	3.3	$6.6 \times 10^{-10}$	66
<i>Dicty</i>	8 … 12	0.1	500	$2.5 \times 10^{-12}$	50
	$D_c$ [ $\text{m}^2 \text{s}^{-1}$ ]	$D/D_c$	$k$ [ $\text{s}^{-1}$ ]	$l_c$ [ $\mu\text{m}$ ]	$s_{\text{per}}/l_c$
<i>E. coli</i>	$10^{-9}$	0.66	10	10	6.6
<i>Dicty</i>	$3 \times 10^{-10}$	0.01	0.09	67	0.7

Table 4.1 ■ Characteristic parameters in real units for *E. coli* and *Dicty* [35, 95, 147, 150, 151, 152]. Chemoattractants of *E. coli* are sugars or amino acids, their decay rate  $k$  is estimated. The chemoattractant of *Dicty*, cAMP, is degraded by phosphodiesterase. The directional correlation time  $\tau_{\text{rot}}$  is adjusted such that it gives the experimentally measured diffusion coefficient  $D = v^2/(2q_\varphi)$ ; for *E. coli*, it equals the duration of three run-and-tumble events. Other values are calculated from  $s_{\text{per}} = v/q_\varphi$  and  $l_c = \sqrt{D_c/k}$ .

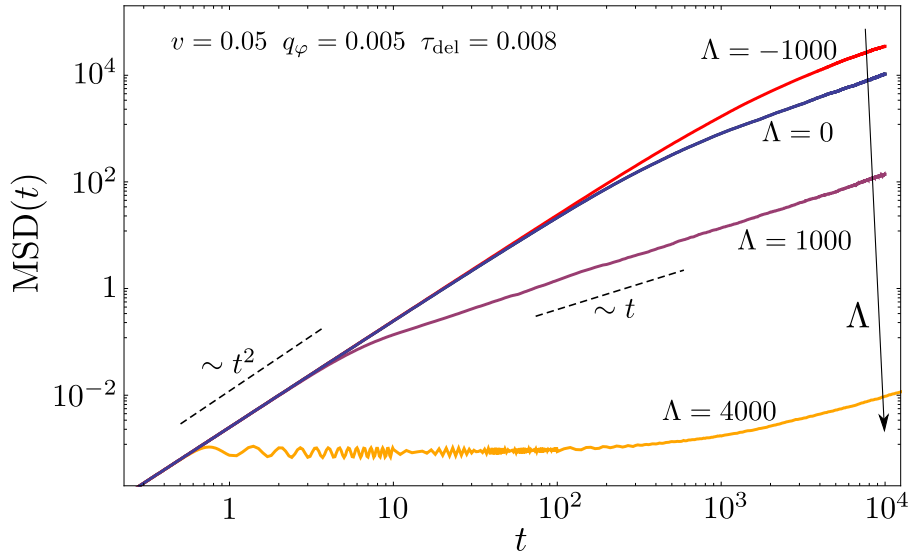
### 4.3.3 Comparison of analytical and numerical results

To check our predictions, we perform simulations of the full model in Eq. (4.7) in reduced units by averaging over at least  $10^3$  different realizations of noise for each set of parameters. In Table 4.1, we list typical experimental or estimated values for the parameters of the paradigmatic cells *E. coli* and *Dicty*. We adjust our reduced parameters introduced in Sec. 4.3.1 to agree with these experimental values. In particular, we choose  $v = 0.05$  and  $q_\varphi = 0.005$ , which yields the free diffusion coefficient  $D = v^2/(2q_\varphi) = 0.25$  and the persistence length  $s_{\text{per}} = v/q_\varphi = 10$ .

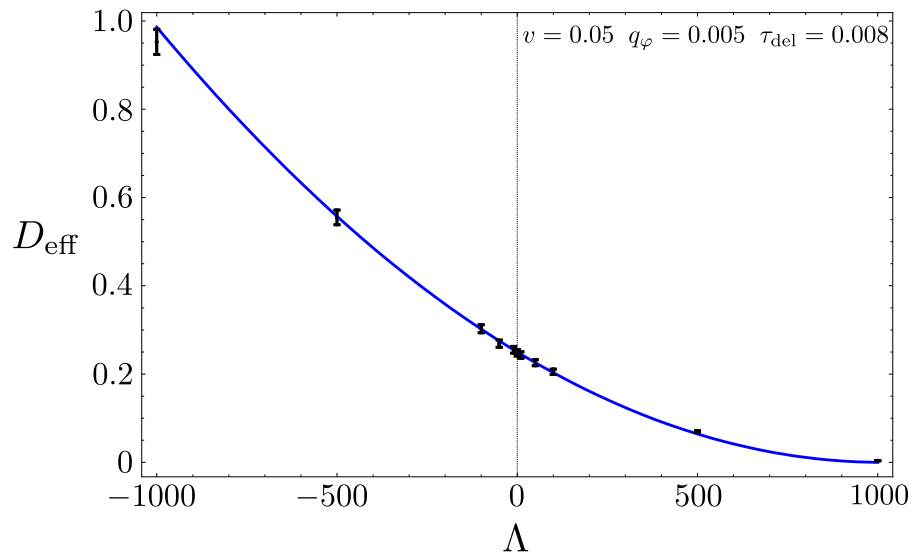
In Fig. 4.8, we plot the MSD as a function of time without chemoattractant ( $\Lambda = 0$ ), as well as for attractive ( $\Lambda > 0$ ) and repulsive ( $\Lambda < 0$ ) chemotaxis. For all values of  $\Lambda$  we observe diffusive motion at large times, and the diffusion coefficient decreases with increasing coupling strength. The lowest curve in Fig. 4.8 reveals oscillations of the MSD reminiscent of Fig. 4.7. Note that the oscillations in the MSD for  $\Lambda = 4000$  change abruptly, since at time  $t \gtrsim 10$  we change the time resolution of the graph.

Figure 4.9 plots the diffusion coefficient  $D_{\text{eff}}$  versus coupling strength  $\Lambda$  for  $\Lambda < \Lambda_0 \approx 1014$ . The analytic expression for  $D_{\text{eff}}$  in Eq. (4.30) (full line in Fig. 4.9) agrees very well with the simulated values. Note that at  $\Lambda \approx -1000$ ,  $D_{\text{eff}}$  becomes one. Since the massive microorganisms should diffuse slower than the molecules of the chemical [62, 83, 153], this restricts repulsive chemotaxis to  $\Lambda > -1000$ . We further check our theory by confirming that directional correlations decay exponentially as  $\langle \mathbf{e}(t) \cdot \mathbf{e}(0) \rangle = \exp(-q_\varphi^{\text{eff}} t)$ , where the time constant  $1/q_\varphi^{\text{eff}}$  is determined by the effective noise strength of Eq. (4.23). Numerical results for three different values of  $\Lambda$  are presented in Fig. 4.10.

For large chemotactic coupling, we employ the theory of Sec. 4.3.2, which holds for  $\Lambda > 16\pi/v \approx 1005$ , according to Eq. (4.40). Results from theory and simulations



**Figure 4.8** ■ Mean-squared displacement as a function of time for different effective chemotaxis strengths  $\Lambda$ , as obtained by simulating the full model of Eq. (4.7). Negative  $\Lambda$  correspond to a chemorepellent, positive  $\Lambda$  to a chemoattractant.



**Figure 4.9** ■ Diffusion coefficient as a function of effective chemotaxis strength  $\Lambda$  for weak coupling. The points with error bars are obtained by simulating the full model, the blue line is the analytical result from Eq. (4.30).

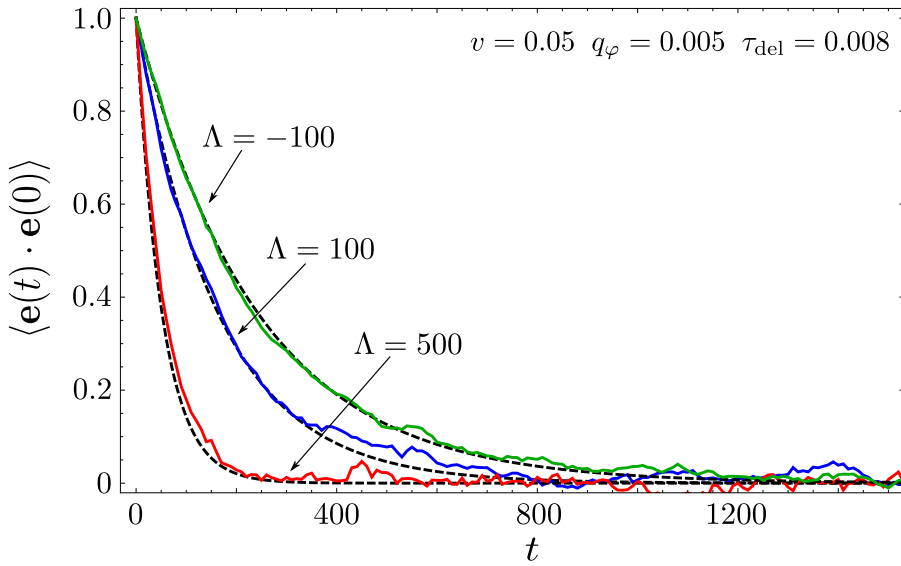


**Figure 4.10** ■ Directional correlation  $\langle \mathbf{e}(t) \cdot \mathbf{e}(0) \rangle$  versus time  $t$  for different effective chemotaxis strengths  $\Lambda$ , as obtained by simulating the full model. The simulated curves agree with the theoretical prediction of exponential decay on the characteristic time scale  $1/q_\varphi^{\text{eff}}$  (black dashed lines).

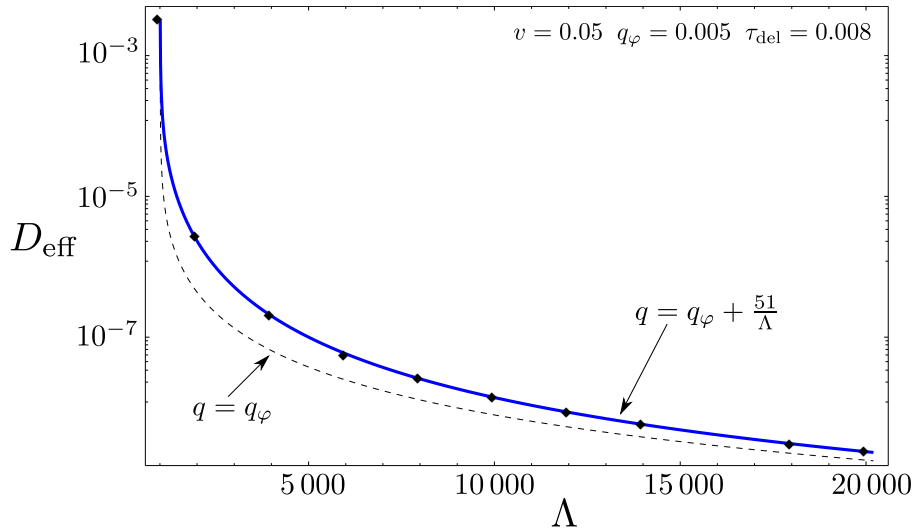


**Figure 4.11** ■ Diffusion coefficient as a function of large chemotaxis strength  $\Lambda$ . The dashed curve is the analytic expression (4.43) with noise strength  $q = q_\varphi$ ; the full line belongs to the effective noise strength  $q = q_\varphi + 51/\Lambda$ . Data points are obtained by simulating the full model.

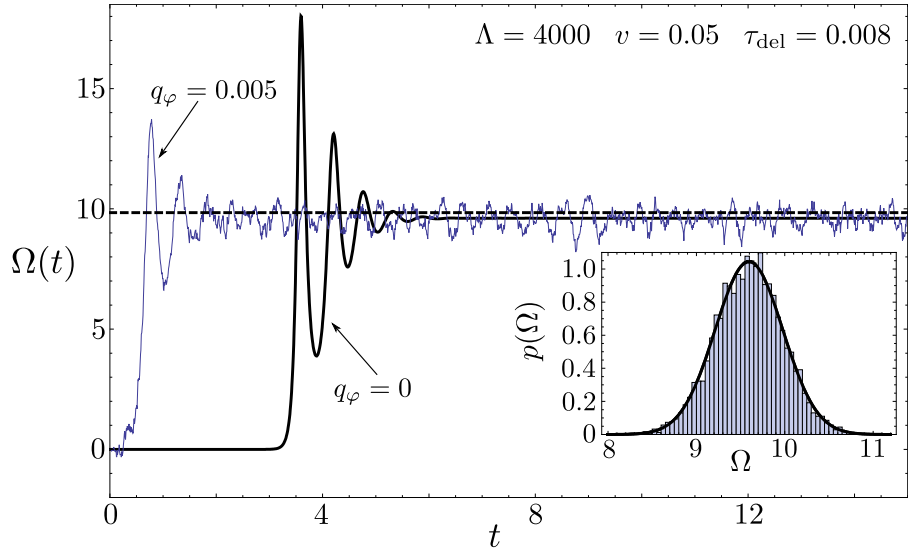


**Figure 4.12** ■ Angular drift velocity  $\Omega(t)$  for chemotactic coupling  $\Lambda = 4000$  as a function of time for  $q_\varphi = 0$  (thick line). With noise of strength  $q_\varphi = 0.005$ ,  $\Omega(t)$  fluctuates. For comparison, the dashed line indicates the self-consistently determined  $\omega$  from Eq. (4.39). The inset shows the distribution  $p(\Omega)$  of  $\Omega(t)$  values; it is well described by a Gaussian distribution (solid line).

are compared in Fig. 4.11. When we approximate the effective noise strength  $q$  of our strong-coupling model by the original noise  $q_\varphi$ , the diffusion coefficient  $D_{\text{eff}}$  is too small (dashed line in Fig. 4.11). We already noted that with noise the angular drift velocity  $\Omega(t)$  of the full model reformulated in Eqs. (4.32) and (4.33) becomes a fluctuating quantity. Therefore, we present the time evolution of  $\Omega(t)$  in Fig. 4.12. Without noise,  $\Omega(t)$  readily converges to a constant value that agrees well with the theoretical value  $\omega$  (dashed line in Fig. 4.12). With noise,  $\Omega(t)$  fluctuates around a mean value close to  $\omega$ . The distribution  $p(\Omega)$ , plotted as inset in Fig. 4.12, identifies the angular drift velocity  $\Omega(t)$  as Gaussian distributed. Thus, the Gaussian distribution of the original noise  $q_\varphi$  is inherited to the fluctuations of  $\Omega(t)$ . In our effective description of Langevin equation (4.41), we take them into account by an additional noise strength  $q_\omega$  and the total noise becomes  $q = q_\varphi + q_\omega$ . As Fig. 4.11 demonstrates, the diffusion coefficient  $D_{\text{eff}}$  of Eq. (4.43) shows a striking agreement with simulations, when we choose

$$q_\omega = q_\omega(\Lambda) = c \Lambda^{-1}, \quad (4.44)$$

where  $c \approx 51$  is a fit parameter. So far, we were not able to rigorously justify Eq. (4.44). Let us add two remarks. First, at  $\Lambda = 2000$ ,  $q_\omega \approx 0.026$  exceeds the original noise strength  $q_\varphi = 0.005$  by a factor of 5 and therefore determines the total noise  $q$ . Second,  $D_{\text{eff}}$  increases with increasing noise  $q$ , since in Eq. (4.43) we evaluate  $D_{\text{eff}}$  at  $\omega \gg q_\varphi$ .

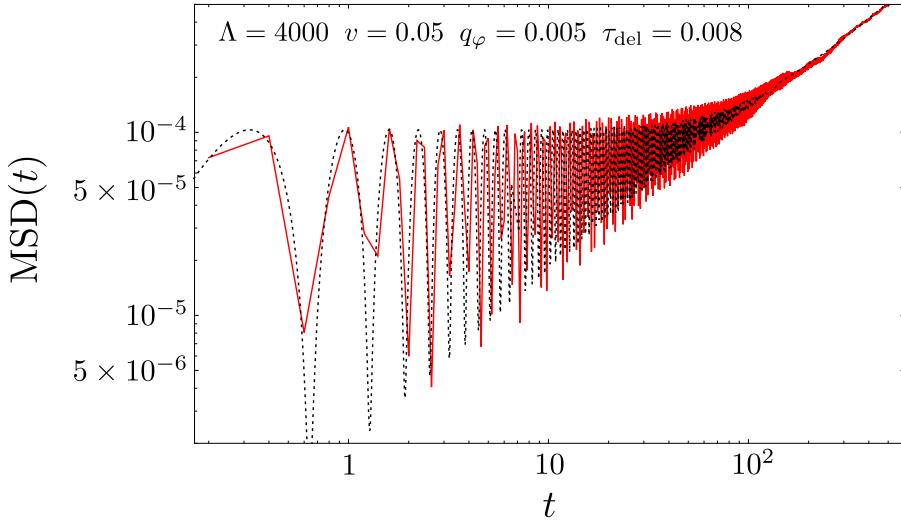


**Figure 4.13** ■ Mean-squared displacement for strong chemotactic coupling  $\Lambda = 4000$ . The solid line is obtained numerically from simulations of the full model of Eq. (4.7), and the dashed curve is the MSD from Eq. (4.42) with noise strength  $q = q_\varphi + 51/\Lambda$ .

Finally, to further confirm our strong coupling theory, we compare in Fig. 4.13 the mean-squared displacement simulated by the full model of Eq. (4.7) with the analytical expression (4.42). To obtain the ensemble average for the simulated MSD, we disregarded the initial parts of the trajectories, which had not reached the stochastic limit cycle. Both curves in Fig. 4.13 show the high frequency oscillations of the MSD at small times and the diffusive limit at large times.

## 4.4 Summary

Our model describes the dynamics of a self-propelled microorganism that shows chemotactic response to a chemical substance, which is produced by the microorganism itself. The particle moves with constant speed on a surface, while its velocity direction diffuses and tends to align along the concentration gradient of the chemical.

To study how the walker reacts to its own secreted chemical, we analyzed how the chemotactic coupling determines the long-time dynamics, which we showed to be diffusive. Our main goal was to derive analytical expressions for the diffusion coefficient and to confirm their validity by simulations. In particular, we showed that changing the effective chemotaxis strength  $\Lambda$  enables to alter the diffusion coefficient by several orders of magnitude. In nature, a variation in  $\Lambda$  might arise from environmental influences that change the production rate  $h$  of the chemical or directly the chemotactic coupling  $\kappa$ . Since we can adjust the speed  $v$  and diffusion coefficient  $D_{\text{eff}}$  independently, we expect our model to be applicable to a variety of microorganisms.

Whereas for weak chemotactic coupling, the walker's velocity direction diffuses with a modified noise strength (Sec. 4.3.1), the dynamics for strong coupling corresponds to rotational diffusion with an additional angular drift velocity (Sec. 4.3.2). However, a rigorous calculation of the effective noise strength in the second case was not possible.

In Chapter 5, we will generalize the presented model to an ensemble of autochemotactic walkers. For attractive autochemotaxis, the model describes the formation of cell clusters and thus represents a communication mechanism between microorganisms, as it is required for bacterial colonization or biofilm formation. Moreover, to make the model more realistic, we will incorporate repulsive interactions between individual walkers.

Recent experimental observations for the swimming nematode *Caenorhabditis elegans* have revealed oscillations in the MSD for small times, reminiscent of Figs. 4.7 and 4.8 [154]. The similarity to the dynamics of the autochemotactic walker for strong chemotactic coupling has raised the question whether *C. elegans* performs indeed autochemotaxis and is thus a natural realization of our autochemotactic walker. Up to now, the possibility of autochemotaxis in *C. elegans* is still debated; alternatively, the observed oscillations in the MSD might be caused by hydrodynamic interactions between the undulating nematode and the glass boundary of the experimental fluid chamber.

# 5 Collective dynamics of autochemotactic active walkers

## 5.1 Introduction

The self-organization of identical units into complex time- and space-dependent structures appears as one of the most fascinating and common features in nature [155]. Aristotle's understanding after which the whole is greater than the sum of its parts, also holds for biological systems. Many microorganisms form aggregates and ultimately constitute a multicellular organism that offers optimal living conditions for the cell community [156]. Important paradigms of multicellular communities are biofilms, formed by various species, such as the bacteria *P. aeruginosa*, *B. subtilis*, and *E. coli* [5, 157, 158]. To coordinate growth, motion, and biochemical activities, microorganisms interact and communicate with each other by physical and chemical means. For instance, direct cell-to-cell contact is a typical physical interaction [73, 159], whereas chemotaxis and quorum sensing represent examples for signaling mechanisms with the help of chemicals [160, 161].

As we have explained in detail in Sec. 2.4, chemotaxis is the directed motion of microorganisms along the gradient of a chemical substance. The bacteria *E. coli* and *S. typhimurium*, as well as the amoeba *Dicty* perform autochemotaxis: They produce chemoattractants themselves under certain living conditions and use it for chemotactic signaling [64, 77, 78, 162]. For example, the production of the chemoattractant aspartate in *E. coli* can be triggered by oxidative stress in the presence of the carbon source succinate, while *Dicty* cells start to produce the attractant cAMP under starvation.

A central aspect of current research on chemotaxis is the collective dynamics of chemotactic cells [85, 119, 152, 163, 164, 165, 166]. Further research concentrates on understanding internal signaling pathways on the biochemical level [167, 168, 169, 170], and on elucidating mathematical features of chemotaxis models [69, 171, 172]. Numerous studies more related to non-equilibrium statistical physics examine active particle systems with a special focus on clustering and collective motion [42, 49, 173, 174, 175, 176].

Here, our model from Chapter 4 for the dynamics of a single autochemotactic walker will be generalized to an ensemble of walkers, and we study, in particular, the formation of clusters and their properties. To give each walker a finite extent,

we regard it as soft disk, which is repelled by other walkers as soon as the disks overlap. Inspired by experimental results of Miyata *et al.* [177], we assume a linear relation between the velocity of the walker and the force acting on it. For simplicity, the repulsive force between two walkers is derived from a harmonic potential. For two autochemotactic walkers, we present a state diagram, where we identify free walker, metastable, and bound cluster states in terms of the chemotactic coupling strength, one of our relevant parameters. Apart from ensemble averaged quantities, such as the mean life time of a two-walker cluster, or size and asymmetry of larger aggregates, we also show typical trajectories of the model microorganisms. When the chemotactic field is not sufficiently strong, some of the two-walker clusters in the metastable state break up during simulation time. We investigate this situation in detail and compare it to Kramers' escape problem. At the end, we qualitatively study some aspects of many-walker systems. Walkers can form metastable or "hot" clusters that dissolve in time. Stable clusters relax exponentially towards their stationary circular shape after some disturbance. Several of these microcolonies coalesce into one bigger cluster. Experiments with cells, such as granulocytes or *Dicty*, have shown that clustering requires a minimal cell density [178, 179]. By tuning our model parameters in confined geometry, we confirm this experimentally observed clustering transition.

The chapter is organized as follows. In Sec. 5.2, we introduce our model of autochemotactic active walkers (Sec. 5.2.1), treat collisions between walkers by modeling them as soft disks (Sec. 5.2.2), relate our parameters to biological quantities, and introduce a rescaled version of the model (Sec. 5.2.3). We study the properties of two-walker and many-walker systems in Secs. 5.3 and 5.4, respectively. After summarizing our results in Sec. 5.5, we close with supplementary material in the appendices of Secs. 5.6 and 5.7.

## 5.2 The model

### 5.2.1 Autochemotactic active walkers

We model motile microorganisms that communicate via autochemotaxis as active walkers. As our approach is motivated in detail in Chapter 4, we just summarize it here. We consider a system of  $m$  identical walkers that move on a planar surface with velocities  $\mathbf{v}_i(t)$  ( $i = 1, \dots, m$ ). The observation that fluctuations in speed and direction of motion decouple for various cell types, suggests to express velocity in polar coordinates [44], see also Sec. 2.3. Furthermore, we keep the speed of isolated particles constant,  $|\mathbf{v}_i(t)| = v$ , so that the velocity of particle  $i$  becomes

$$\mathbf{v}_i(t) = v\mathbf{e}_i(t) = v \begin{pmatrix} \cos \varphi_i(t) \\ \sin \varphi_i(t) \end{pmatrix}. \quad (5.1)$$

The unit vector  $\mathbf{e}_i(t)$  gives an intrinsic direction along which isolated microorganisms move. When they collide, their velocities do not necessarily have to be parallel to  $\mathbf{e}_i(t)$ , as will be explained in Sec. 5.2.2. Hydrodynamic interactions in bacterial suspensions also strongly reduce the correlation between the intrinsic axis and the swimming direction [139]. Moreover, in “real” microorganisms,  $\mathbf{e}_i(t)$  does not have to be oriented along their main axis; rod-like bacteria, for example, can also move perpendicular to their long axis [174]. The trajectory  $\mathbf{r}_i(t)$  of a walker is obtained by integrating  $\frac{d}{dt} \mathbf{r}_i(t) = \mathbf{v}_i(t)$ .

Each walker emits a chemical substance with a constant production rate  $h$ . The chemical diffuses in the plane with diffusion coefficient  $D_c$  and is degraded by the environment at a constant decay rate  $k$ . The resulting reaction diffusion equation for the concentration of chemical  $c(\mathbf{r}, t)$  thus reads

$$\partial_t c(\mathbf{r}, t) = D_c \nabla^2 c(\mathbf{r}, t) - kc(\mathbf{r}, t) + h \sum_{i=1}^m \delta[\mathbf{r} - \mathbf{r}_i(t)], \quad (5.2)$$

and is the direct generalization of Eq. (4.14). To account for chemotaxis, we introduce the chemotactic field  $\mathbf{E}(\mathbf{r}, t) = \kappa \nabla c(\mathbf{r}, t)$  and a torque  $\mathbf{E} \times \mathbf{e}_i$  that tries to align the walker’s intrinsic direction  $\mathbf{e}_i(t)$  along  $\mathbf{E}$ . Again, we assume the chemotactic coupling strength  $\kappa$  to be constant. Positive  $\kappa$  represents attractive chemotaxis in response to a chemoattractant, negative  $\kappa$  means repulsive chemotaxis in response to a chemorepellent. The overdamped Langevin equation for  $\mathbf{e}_i(t)$  contains the deterministic chemotactic torque and a stochastic torque:

$$\frac{d}{dt} \varphi_i(t) = -\frac{1}{\gamma_R} [\mathbf{E}(\mathbf{r}_i(t), t) \times \mathbf{e}_i(t)]_z + \sqrt{2q_\varphi} \Gamma_i(t). \quad (5.3)$$

The cross product is oriented perpendicular to the plane along the  $z$  axis and  $\gamma_R > 0$  is the rotational friction coefficient. As usual,  $q_\varphi > 0$  denotes the strength of the Gaussian white noise,  $\Gamma_i(t)$ , characterized by a zero mean  $\langle \Gamma_i(t) \rangle = 0$  and  $\langle \Gamma_i(t) \Gamma_j(t') \rangle = \delta_{ij} \delta(t - t')$ . The noise term represents all stochastic torques acting on the walker, and thus includes non-thermal contributions.

We solve Eq. (5.2) with the help of its Green’s function and determine the chemotactic field  $\mathbf{E}(\mathbf{r}_i(t), t)$  at the particle’s position  $\mathbf{r}_i(t)$ , which enters in Eq. (5.3):

$$\begin{aligned} \mathbf{E}(\mathbf{r}_i(t), t) &= -\frac{\kappa h}{8\pi D_c^2} \int_0^{t-\tau_{\text{del}}} dt' \frac{e^{-k(t-t')}}{(t-t')^2} \\ &\quad \times \sum_{j=1}^m [\mathbf{r}_i(t) - \mathbf{r}_j(t')] \exp\left(-\frac{[\mathbf{r}_i(t) - \mathbf{r}_j(t')]^2}{4D_c(t-t')}\right). \end{aligned} \quad (5.4)$$

Here, we assume that the walkers start to emit their chemical substance at  $t = 0$ . The delay time  $\tau_{\text{del}} > 0$  regularizes the integral; it means that a walker reacts to its own emitted chemical only after a short delay. The integral representation of  $\mathbf{E}(\mathbf{r}_i(t), t)$  reveals the non-Markovian property of the autochemotactic interaction since the history of all trajectories contributes to the current value of  $\mathbf{E}(\mathbf{r}_i(t), t)$ .

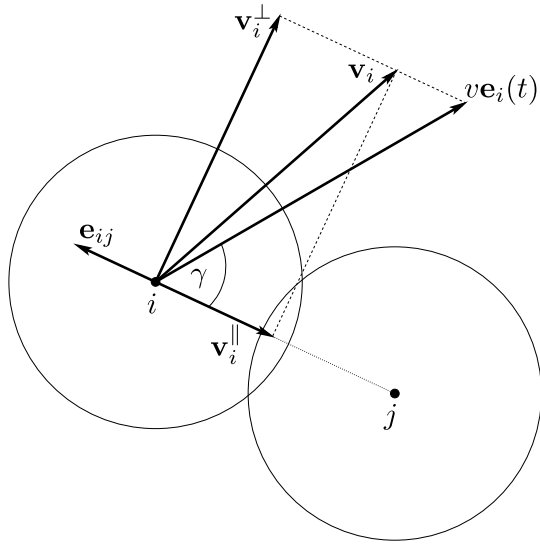


**Figure 5.1** ■ Two chemotactic walkers of radius  $a$  collide. Whereas the velocity component  $\mathbf{v}_i^\perp$  normal to the connecting line agrees with the normal component of the free velocity  $v\mathbf{e}_i$ , the parallel component  $\mathbf{v}_i^\parallel$  along the connecting line decreases according to a linear velocity-force relation illustrated in Fig. 5.2. The angle between  $\mathbf{e}_i$  and the connecting line is  $\gamma$  and  $\mathbf{e}_{ij}$  is a unit vector that points from walker  $j$  to  $i$ .

### 5.2.2 Collisions of autochemotactic walkers

So far, we have described how autochemotactic walkers interact by the chemotactic field, which they create themselves. However, “real” microorganisms are not point-like objects and if they collide with each other, their velocities change. It is known that the shape of bacteria plays a significant role for how they cluster and the resulting collective motion, see, for example, Refs. [174, 180]. Here, we are interested in clustering as a pure result of autochemotactic signaling. Therefore, instead of introducing the specific shape of the cell body, we view an autochemotactic walker in two dimensions as a circular disk of radius  $a$  whose center moves with velocity  $\mathbf{v}_i(t) = v\mathbf{e}_i(t)$ . When they touch each other, they experience some repulsive force, which then alters their velocities. In the following, we describe how we implement collisions between autochemotactic walkers.

When two walkers move against each other in a central collision, the repulsive force will slow them down until they both come to a halt at a stall force  $F_{st}$ , while still trying to walk against each other. For example, for the parasitic bacterium *Mycoplasma mobile* the relation between velocity and applied force has been measured by Miyata *et al.* [177]. They found that the bacterium’s gliding speed decreases linearly with force, until it becomes zero at the applied stall force. We will use this linear velocity-force relation for our autochemotactic walkers, as indicated by the solid line in Fig. 5.2. Each walker has an intrinsic direction  $\mathbf{e}_i$  along which it walks with speed  $v$ . During a collision with walker  $j$ , the unit vector  $\mathbf{e}_i$  does not have to

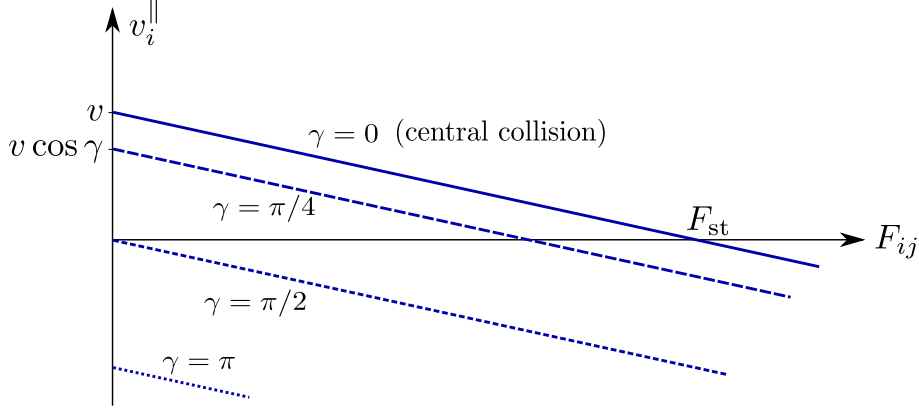


Figure 5.2 ■ Force-velocity relation for the parallel velocity component  $v_i^{\parallel}$  of walker  $i$ .  $F_{ij}$  is the force with which walker  $j$  acts on  $i$ . Each curve corresponds to a certain collision angle  $\gamma$ , which is defined in Fig. 5.1.

be parallel to the connecting line of walkers  $i$  and  $j$  (see Fig. 5.1). Normal to this line, the motion of the walkers is not hindered, and  $\mathbf{v}_i^{\perp}$  is just the normal velocity component of  $v\mathbf{e}_i$ . However, the parallel velocity component  $\mathbf{v}_i^{\parallel} = -v_i^{\parallel}\mathbf{e}_{ij}$  is slowed down by the collision so that the walker's momentary velocity  $\mathbf{v}_i = \mathbf{v}_i^{\parallel} + \mathbf{v}_i^{\perp}$  deviates from  $v\mathbf{e}_i$ . As Fig. 5.2 illustrates, we assume that at a given collision angle  $\gamma$  between  $\mathbf{e}_i$  and the connecting line, the velocity-force relation for  $v_i^{\parallel}$  has the same slope as for the central collision. So, the parallel component as a function of the central force  $F_{ij}$  becomes

$$v_i^{\parallel} = -v \frac{F_{ij}}{F_{st}} + v \cos \gamma. \quad (5.5)$$

In particular, the stall force for an oblique collision is smaller than for a central encounter. Note that a negative  $v_i^{\parallel}$  means that walker  $i$  moves away from walker  $j$ . For example, when  $\mathbf{e}_i$  changes its direction from a central ( $\gamma = 0$ ) to an oblique ( $\gamma \neq 0$ ) collision, the repulsive force  $F_{ij}$  from particle  $j$  might be strong enough that it not just stops walker  $i$ , but also reverses its parallel velocity  $\mathbf{v}_i^{\parallel}$ .

For simplicity, we assume that the repulsive force  $\mathbf{F}_{ij}$  is harmonic and only acts when the two disks of the walkers overlap,

$$\mathbf{F}_{ij} = \begin{cases} F_0 \left(1 - \frac{r_{ij}}{2a}\right) \mathbf{e}_{ij}, & r_{ij} \leq 2a, \\ 0, & r_{ij} > 2a. \end{cases} \quad (5.6)$$

Here,  $r_{ij}$  is the distance between the centers of disk  $i$  and  $j$ , and  $F_0 > 0$  is a measure for the strength of repulsion, see Fig. 5.3. The force law (5.6) was successfully applied to model the rigidity-loss transition in foams [181]. An alternative to Eq. (5.6) could be a Hertzian contact force [182]. However, we do not expect large changes of the results presented below, since the only purpose of Eq. (5.6) is to introduce some

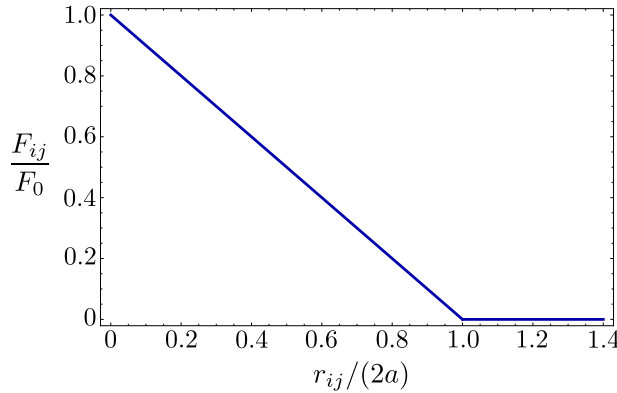


Figure 5.3 ■ The absolute value  $F_{ij} = |\mathbf{F}_{ij}|$ , normalized by  $F_0$ , of the interaction force from Eq. (5.6) as a function of particle distance  $r_{ij}/(2a)$ .

finite extension of the autochemotactic walkers. Note that the force from Eq. (5.6) is also a possible force realization in the numerical scheme of Dissipative Particle Dynamics [183]. The corresponding pair-potential from which the force is calculated as  $\mathbf{F}_{ij} = -\nabla_i U(\mathbf{r}_i, \mathbf{r}_j)$  is quadratic in the particle distance,

$$U(\mathbf{r}_i, \mathbf{r}_j) = U(r_{ij}) = F_0 \frac{(r_{ij} - 2a)^2}{4a} \Theta(2a - r_{ij}). \quad (5.7)$$

We can now write down the velocity of walker  $i$ ,  $\mathbf{v}_i = -v_i^{\parallel} \mathbf{e}_{ij} + \mathbf{v}_i^{\perp}$ , both during a collision ( $r_{ij} < 2a$ ) and when it is well separated from other walkers ( $r_{ij} > 2a$ ):

$$\mathbf{v}_i = \begin{cases} v \mathbf{e}_i + v \frac{1 - \frac{r_{ij}}{2a}}{1 - \frac{r_{st}}{2a}} \mathbf{e}_{ij}, & r_{ij} \leq 2a, \\ v \mathbf{e}_i & r_{ij} > 2a. \end{cases} \quad (5.8)$$

To arrive at the upper line, we have used  $v \mathbf{e}_i = -v \cos \gamma \mathbf{e}_{ij} + \mathbf{v}_i^{\perp}$ , together with Eqs. (5.5) and (5.6). We also introduced the stall distance  $r_{st}$ , at which two walkers come to a halt during a central collision. Setting  $F_{st} = F_{ij}(r_{st})$ , Eq. (5.6) gives  $r_{st}/2a = 1 - F_{st}/F_0$ . To account for the softness of microorganisms during collisions, we choose typical values for  $r_{st}/(2a)$  between 0.8 and 0.95 throughout our work. If a walker overlaps with several neighbors, the “correction term” in Eq. (5.8) is summed up over all neighbors, such that the upper line in Eq. (5.8) becomes

$$\mathbf{v}_i = v \mathbf{e}_i + v \sum_{j \neq i, r_{ij} \leq 2a} \frac{1 - \frac{r_{ij}}{2a}}{1 - \frac{r_{st}}{2a}} \mathbf{e}_{ij}. \quad (5.9)$$

A similar treatment of colliding active disks is found in the model of Ref. [184]; for an alternative interaction where a speed-dependent potential penalizes overlap between disks, we refer to Ref. [185]. In contrast to the cited publications, we have

given a clear physical explanation for our treatment of colliding disks, based on a harmonic interaction potential and a linear relationship between force and velocity.

We add one more comment. In the following, we make the simplifying assumption that the chemotactic substance is emitted at the disk center of each microorganism and that its diffusive spreading is not influenced by the finite extent of the autochemotactic walkers. Since the walkers or microorganisms move in a plane, the chemical can always use the third dimension to diffuse parallel to the plane. This would imply a full three-dimensional treatment for the diffusion of the chemical. Since it is more tedious and not crucial for the current considerations, we restricted ourselves to the two-dimensional case.

### 5.2.3 Rescaled units and simulation parameters

In this chapter, we rescale our model differently as it has been done for the single autochemotactic walker in Chapter 4. Now, we rescale lengths and velocities in units of the characteristic size of a microorganism, the disk radius  $a$ , and its intrinsic speed  $v$ . Within the time unit  $t_0 = a/v$ , the walker moves half its body length.

For zero chemotactic field, the velocity direction diffuses on the unit circle and directional correlations decay exponentially during the characteristic time  $\tau_{\text{rot}} = q_\varphi^{-1}$ ,  $\langle \mathbf{e}_i(t) \cdot \mathbf{e}_i(0) \rangle = \exp(-q_\varphi t)$ . Hence, the walker moves on an almost straight path with persistence length  $s_{\text{per}} = v\tau_{\text{rot}}$ . We define the persistence number  $\alpha$  –not to be mixed up with the persistence parameter  $\alpha$  from Chapter 3– as the persistence length  $s_{\text{per}}$  in units of  $a$ :

$$\alpha = \frac{s_{\text{per}}}{a} = \frac{v}{aq_\varphi} = \frac{\tau_{\text{rot}}}{t_0}. \quad (5.10)$$

Since  $\alpha$  can be rewritten as ratio of the rotational decorrelation time and the translational drift time, it was also called rotational Péclet number [186]. In the following, we use  $\alpha$  to parametrize the noise strength  $q_\varphi$ . The rotational diffusion of  $\mathbf{e}_i(t)$  leads to a translational diffusion with coefficient  $D = v^2/(2q_\varphi)$  [Eq. (2.47)]. In units of  $D_0 = a^2/t_0 = av$ , the diffusion coefficient reads  $D/D_0 = \alpha/2$ ; this means, a larger persistence number results in enhanced diffusion.

In Table 5.1, we list characteristic values for *E. coli* and *Dicty* and their chemoattractants. Since molecules of the chemoattractant are much smaller than microorganisms, the diffusion coefficient  $D_c$  of the chemoattractant satisfies  $D/D_c \ll 1$ ,  $D_0/D_c \ll 1$ . Based on the values from Table 5.1, we keep the reduced decay rate  $kt_0 = 0.1$  and the ratio  $D_0/D_c = 0.005$  constant during all simulations. During its life time  $k^{-1}$ , a chemoattractant molecule diffuses a typical length  $l_c = \sqrt{D_c/k}$ . In our simulations, we have  $l_c = 44.7a$ . Realistic values for the persistence number  $\alpha$  should be between 10 and 100, and we will set  $\alpha = 25$  in many simulations. Finally,

	$a$ [ $\mu\text{m}$ ]	$v$ [ $\mu\text{m s}^{-1}$ ]	$t_0$ [s]	$D_0$ [ $\text{m}^2 \text{s}^{-1}$ ]	$\tau_{\text{rot}}$ [s]	$\alpha$
<i>E. coli</i>	1	20	0.05	$2 \times 10^{-11}$	3.3	66
<i>Dicty</i>	5	0.1	50	$5 \times 10^{-13}$	500	10
	$D$ [ $\text{m}^2 \text{s}^{-1}$ ]	$D_c$ [ $\text{m}^2 \text{s}^{-1}$ ]	$D/D_c$	$D_0/D_c$	$k$ [ $\text{s}^{-1}$ ]	$l_c/a$
<i>E. coli</i>	$6.6 \times 10^{-10}$	$10^{-9}$	0.66	0.02	0.4	50
<i>Dicty</i>	$2.5 \times 10^{-12}$	$3 \times 10^{-10}$	0.008	0.002	0.09	11.5

Table 5.1 ■ Characteristic parameters for *E. coli* and *Dicty*, see also Table 4.1 and the discussion in Chapter 4 for references. Calculated numbers are  $t_0 = a/v$ ,  $D_0 = av$ ,  $\tau_{\text{rot}} = 2D/v^2$ ,  $\alpha = \tau_{\text{rot}}/t_0$ , and  $l_c = \sqrt{D_c/k}$ .

we introduce the dimensionless chemotactic coupling strength

$$\Lambda = \frac{\kappa h a}{D_c^2 \gamma_R}. \quad (5.11)$$

Be aware that we used a different coupling strength in Chapter 4, which is connected to  $\Lambda$  from Eq. (5.11) by  $\Lambda = a/l_c \times \Lambda_{\text{Chapter 4}}$ .

We choose the delay time  $\tau_{\text{del}}$  from Eq. (5.4) as small as possible and, therefore, set it to be equal to the time step of the simulation. Moreover, a rough estimate of  $\tau_{\text{del}}$  from the biological perspective also justifies this procedure: As the chemoattractant is emitted at the center of our model microorganism, it takes a characteristic time  $t_c$  for the chemical to diffuse over the cell body, such that it can dock at the receptors on the surface. This time  $t_c$  should be comparable to the delay time  $\tau_{\text{del}}$ . We use  $t_c \simeq a^2/D_c$  and express  $t_c$  in units of  $t_0$  as  $t_c/t_0 \simeq D_0/D_c$ . For  $D_0/D_c = 0.005$  and a time step of  $10^{-2} t_0$ ,  $t_c$  and  $\tau_{\text{del}}$  are thus of the same order of magnitude.

From now on, we give all lengths, times and velocities in units of  $a$ ,  $t_0$  and  $v$ , respectively; this holds in particular for all figures.

### 5.3 Analysis of the two-walker system

The coupled dynamics of two autochemotactic walkers is strongly influenced by the strength of their chemotactic interaction. In this section, we study typical trajectories of two walkers that start close to each other, and we illustrate some of them in Sec. 5.3.1. In particular, it is of interest if two autochemotactic microorganisms can form stable clusters where they are bound to each other. Without chemotactic coupling,  $\Lambda = 0$ , both walkers separate from each other due to translational diffusion. A small chemotactic strength  $\Lambda$  influences the walker's trajectories, but the chemotactic field is not strong enough to hold the particles together. For large  $\Lambda$ , bound states are observed. However, they will eventually break up due to stochastic

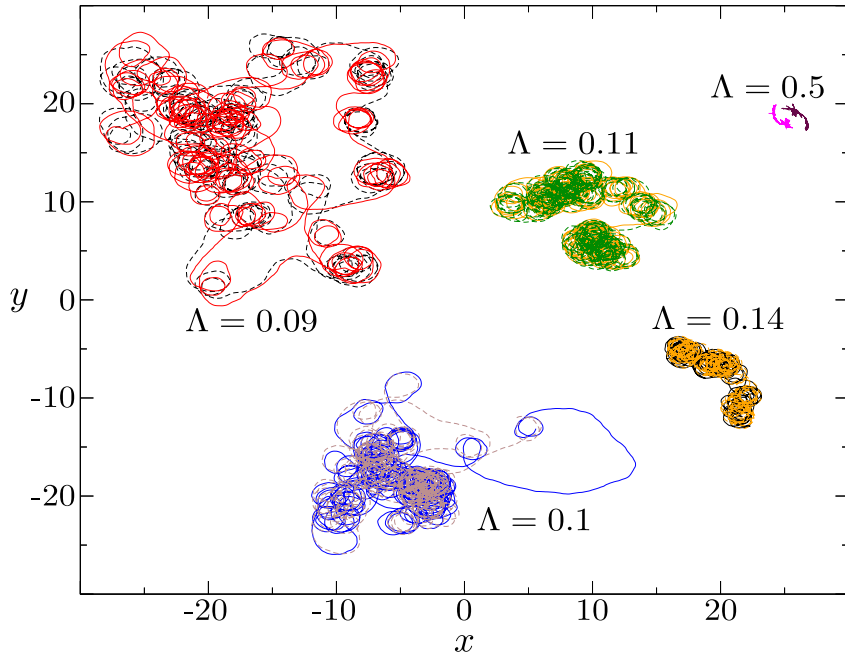
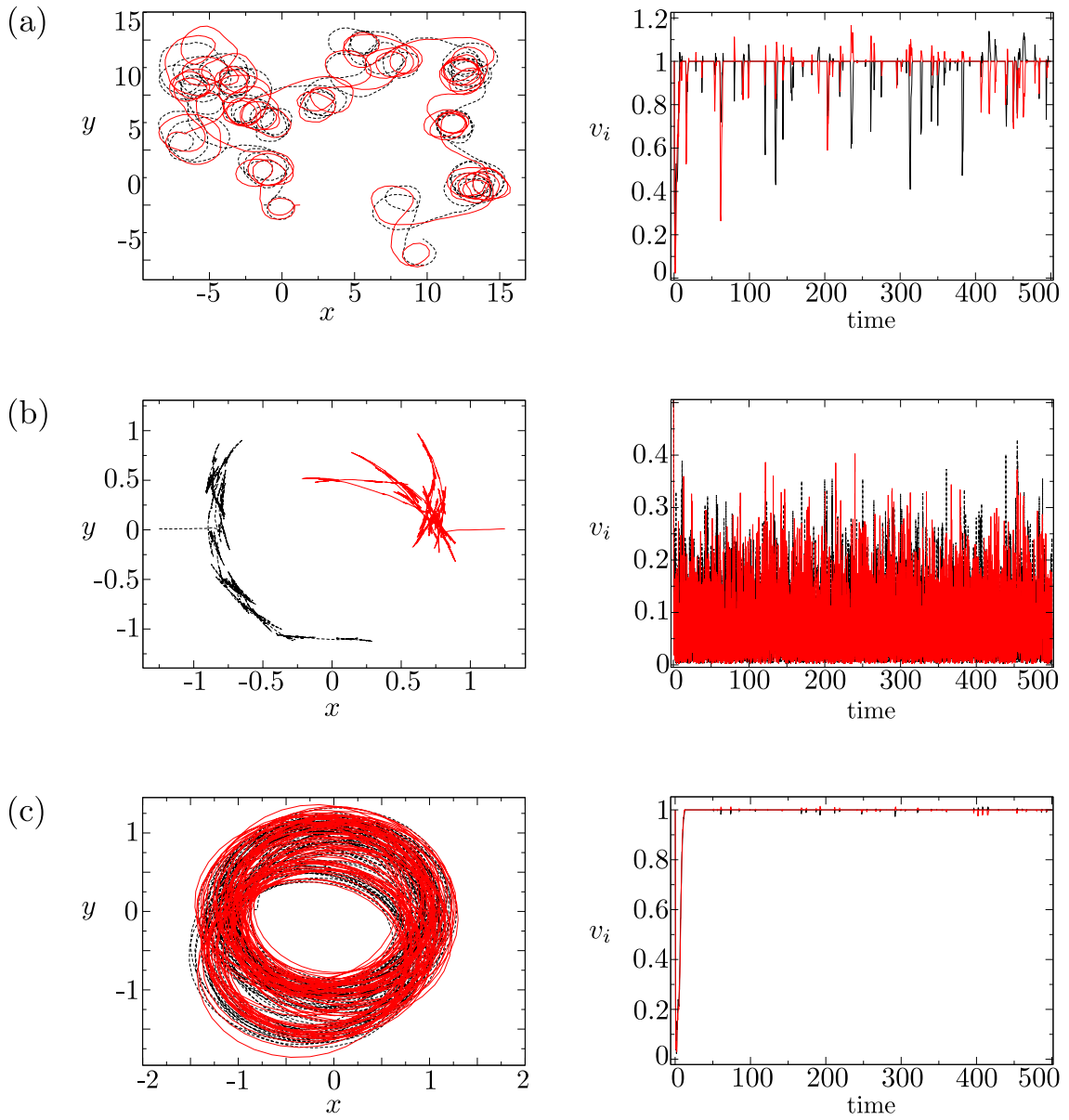


Figure 5.4 ■ Typical pairs of trajectories of two autochemotactic walkers for fixed persistence number  $\alpha = 25$  and different chemotactic strength  $\Lambda$ .

fluctuations. This is similar to Kramers' escape problem, which we have presented at the end of Sec. 2.1.2: A particle leaves a deep potential well after an average escape time, which exponentially grows with the barrier height. In Sec. 5.3.2, we introduce a state diagram as a function of chemotactic strength  $\Lambda$  and persistence number  $\alpha$ , where we distinguish between free, metastable, and bound walker states. In the bound state, all the two-walker clusters stay bound during the observation time, whereas in the metastable state for medium values of  $\Lambda$ , they coexist with free walkers. Finally, in Sec. 5.3.3, we study the mean life time of a two-particle cluster in more detail and deepen the analogy to Kramers' escape problem.

### 5.3.1 Typical trajectories

We discuss typical trajectories that illustrate the free and bound particle states. To generate these trajectories, we put two walkers close together at an initial distance  $d_0 = 2.5$  (in units of disk radius) and with random velocity directions. For small  $\Lambda \ll 0.1$ , the chemotactic coupling is so weak that both active Brownian walkers move independently from each other. Of course, when we choose the initial distance much larger than the range  $l_c$  of chemotactic interaction, the walkers would also simply separate in most cases. Figure 5.4 shows trajectories for five values of  $\Lambda$  and fixed persistence number  $\alpha = 25$ . At  $\Lambda = 0.09$  and larger values, the chemotactic interaction is so strong that the walkers are bound to each other and move strongly



**Figure 5.5** ■ Trajectories (left column) and corresponding particle speeds  $v_i$  versus time (right column) for different parameters: (a)  $\Lambda = 0.09$ ,  $\alpha = 25$ ; (b)  $\Lambda = 0.5$ ,  $\alpha = 25$ ; (c)  $\Lambda = 0.1$ ,  $\alpha = 1000$ . The speed  $v = 1$  corresponds to free walkers without contact to other individuals.

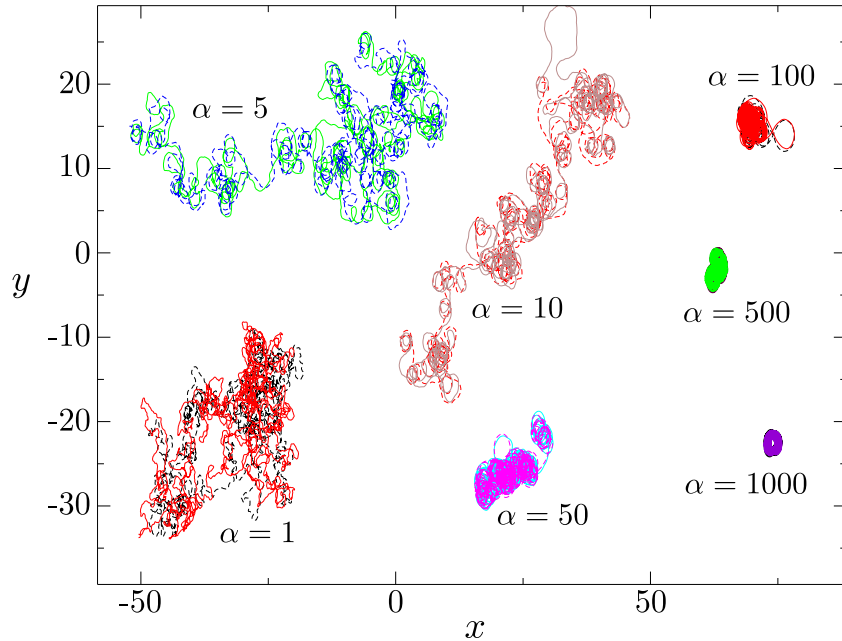


**Figure 5.6** ■ Typical pairs of trajectories of two autochemotactic walkers for fixed chemotactic strength  $\Lambda = 0.1$  and different persistence number  $\alpha$ .

correlated. At  $\Lambda \approx 0.1$ , they circle around each other, are shortly in contact, and then separate again. Occasionally, it looks as if one active walker hunts for the second. Further increase of  $\Lambda$  reduces the “hunting”. The walkers stop separating from each other and form a tightly bound cluster ( $\Lambda \approx 0.5$ ). In Fig. 5.5, we show close-ups of the trajectories for  $\Lambda = 0.09$  and  $0.5$ , together with the speed  $v$  of the walkers. At  $\Lambda = 0.09$ ,  $v$  varies between one, where the walkers are not in contact with each other, and smaller values, which indicates collisions. The speed also becomes larger than one, when one walker pushes against the other. In contrast, at  $\Lambda = 0.5$ , the walkers are firmly bound to each other and the speed is always below one.

To study the influence of the persistence number  $\alpha$ , we present trajectories for fixed  $\Lambda = 0.1$  and different values of  $\alpha$  in Fig. 5.6. Small  $\alpha$  corresponds to large noise and the coupled trajectories resemble a random walk. For increasing  $\alpha$ , the trajectories become more compact. Ultimately, the dynamics is nearly deterministic, where the active walkers circle around each other with very little contact. This is also illustrated in Fig. 5.5(c).

In Fig. 5.4, the trajectory for  $\Lambda = 0.1$  displays a big loop at the right-hand side, where one walker is clearly separated from the other walker by a large distance. If such fluctuation-induced loops become too large, the cluster of two walkers breaks up, which is indeed observed in simulations. So, in between tightly bound clusters for large  $\Lambda \gg 0.1$  and free walkers at  $\Lambda \ll 0.1$ , we find a metastable state at  $\Lambda \approx 0.1$ , where clusters may break up into free walkers during simulations. As

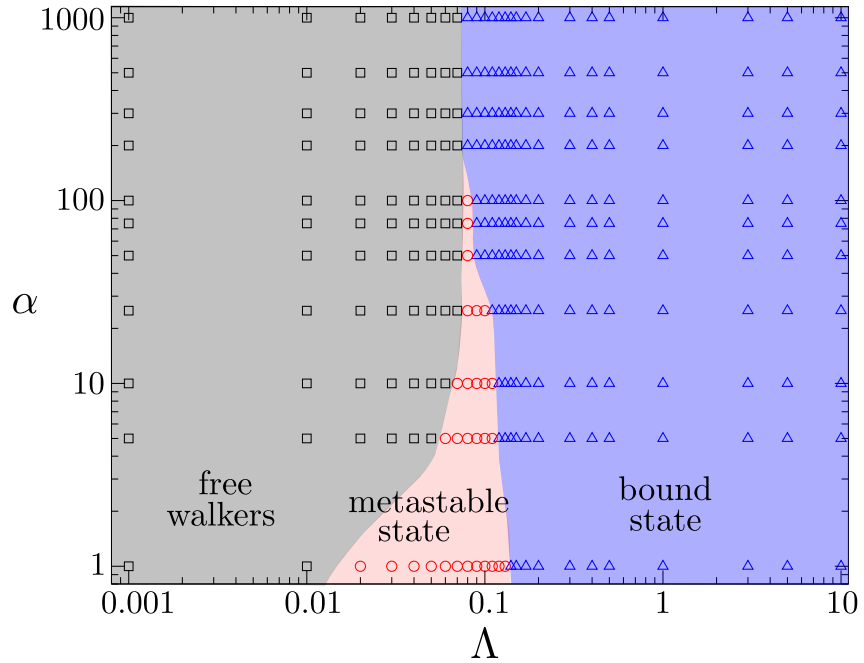


**Figure 5.7** ■ State diagram for persistence number  $\alpha$  versus chemotactic strength  $\Lambda$ . The squares indicate free walkers, triangles represent walkers in the bound state, and circles represent walkers in the metastable state.

already discussed, these clusters correspond to a Brownian particle, which escapes from a potential well. In the next section, we investigate a state diagram  $\alpha$  versus  $\Lambda$ , where we locate free, metastable, and bound states in specific parameter regions. From what we said so far, it is clear that the concept of a bound state depends on the total observation or simulation time. If this time is smaller than the mean life time of a cluster, then the cluster is in the bound state.

### 5.3.2 State diagram

To generate the state diagram in the parameter space persistence length  $\alpha$  versus chemotactic strength  $\Lambda$ , we record 100 trajectories for each parameter set. The walkers start close to each other with an initial distance  $d_0 = 2.5$  and opposing velocity directions with  $\mathbf{r}_1(0) = (-1.25, 0.01)$ ,  $\varphi_1(0) = 0.03$ ,  $\mathbf{r}_2(0) = (1.25, 0.01)$ ,  $\varphi_2(0) = \pi - 0.0001$ . As a consequence, they collide shortly after  $t = 0$  and without noise and chemoattraction they would constitute a stable cluster for all times. We choose these deterministic initial conditions to compare only the influence of  $\Lambda$  and  $\alpha$  on the cluster stability. The simulation time is  $t_{\max} = 10^4$ . In real units it corresponds to typical experimental times of several hours, *e.g.*, for *Dicty* we estimate  $t_{\max} = 13.9$  hours using values from Table 5.1. If all clusters of walkers for one parameter set ( $\Lambda, \alpha$ ) stay intact within  $t_{\max}$ , we refer to them as bound

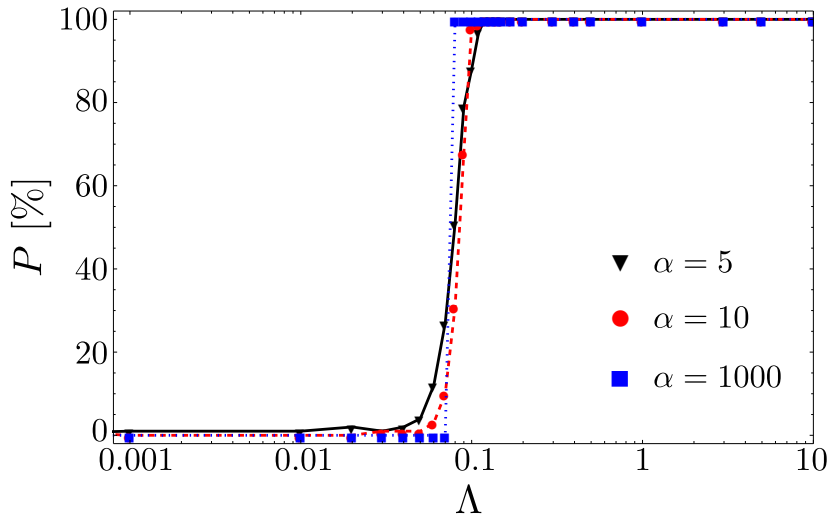
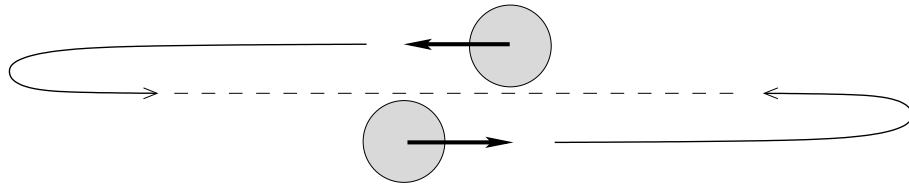


Figure 5.8 ■ Fraction  $P$  (in %) of bound clusters versus chemotactic strength  $\Lambda$  for different persistence numbers  $\alpha$ . For larger  $\alpha$ , the sigmoidal shape converts into the step function.

state. In particular, if the distances of the walkers at the end of each of the 100 trajectories are smaller than a characteristic length, we consider them as bound clusters. As characteristic length, we choose the diffusion length  $l_c = \sqrt{D_c/k} = 44.7$  of the chemical during its life time  $k^{-1}$ , since  $l_c$  gives the range of the chemotactic interaction. Besides, even using characteristic lengths 10, 20, or 40 does not change the state diagram. Once walkers end up with a final distance larger than  $l_c$  at time  $t_{\max} = 10^4$ , they are in the free state. However, with a certain probability even non-interacting random walkers will have a distance smaller than  $l_c$  at  $t_{\max}$ . In the appendix of Sec. 5.6, we estimate this probability to be 5% for  $\alpha = 1$  and keep this value also for larger  $\alpha$ . This means that in the state of free walkers less than 5% of them have a separation smaller than  $l_c$ . Finally, in the metastable state at least 5% of bound clusters coexist with free walkers. The existence of three distinct states was also reported in Ref. [187], where clustering of autochemotactic walkers in one space dimension was investigated. We stress once more that the concept of bound and metastable states always refers to the observation time  $t_{\max}$ , which in our case equals a reasonable experimental observation time.

Figure 5.7 shows the resulting state diagram. The boundary of the bound state does hardly depend on  $\alpha$ . Whereas for large persistence number  $\alpha$  the almost deterministic dynamics results in a sharp transition at  $\Lambda = 0.07$  between free and bound walkers, we obtain the metastable state for decreasing  $\alpha$  or increasing stochastic noise. This behavior is confirmed by Fig. 5.8, where we plot the fraction of bound clusters versus  $\Lambda$  for different  $\alpha$ . Increasing the chemotactic strength  $\Lambda$ , a clustering transition occurs that is smooth for small  $\alpha$ . Therefore, stronger noise favors the breakup of clusters, but also means a small diffusion constant, as reviewed in



**Figure 5.9** ■ To form stable clusters, active walkers separating from each other should turn around under the influence of the chemotactic field generated by both walkers.

Sec. 5.2.3. As a result, walkers can again form clusters after breakup and thereby clusters and free walkers coexist in the metastable state. For  $\alpha$  beyond 100, the transition becomes sharp, as illustrated by the step function. Due to negligible noise, walkers only separate from each other when the intrinsic speed  $v$  is large enough to overcome the chemotactic attraction. The probability that they meet again via diffusion is small.

The clustering transition for large  $\alpha$  occurs at a critical chemotactic strength  $\Lambda \approx 0.07$ . We present a rough estimate for this value. Clusters are stable when the chemotactic field generated by both walkers is strong enough to turn their velocity directions around when they move away from each other (see Fig. 5.9). In Sec. 4.2.2, we studied a single walker in a constant chemotactic field  $\mathbf{E} = E\mathbf{e}_x$  and found that the direction of the walker relaxes towards  $\mathbf{E}$  during the characteristic time  $t^* = \gamma_R/E$ . To form stable clusters, walkers should not separate beyond the range of the chemotactic interaction  $l_c$ , or  $vt^* < l_c$ . Using  $t^* = \gamma_R/E \propto 1/\Lambda$ , we arrive in reduced units at  $\Lambda > v/l_c$ . With  $v = 1$  and  $l_c = 44.7$  this gives  $\Lambda > 0.02$ , which is in reasonable agreement with the simulated value 0.07.

We finish with a remark for the state diagram. It is insensitive to the details of the collisions between the two walkers and therefore primarily determined by the chemotactic interaction. For example, if we vary the stall distance  $r_{st}/(2a)$  between 0.8 and 0.95 and thereby the elasticity of the walkers, the state diagram basically does not change. This is even true when we disregard collisions of the walkers and treat them as point-like objects.

### 5.3.3 Mean life time

As already discussed, the two-walker system is in the bound state when the cluster life times exceed the simulation time. Now, we will show that beyond the qualitative connection to Kramers' escape problem there is even a quantitative correspondence; for this purpose, we investigate the distribution of life times for parameter sets close to and in the transition region between the bound and the free-walker states. We choose the same initial conditions for two walkers as in Sec. 5.3.2, and define the life time  $\tau$  of a cluster as the time when the walkers' separation exceeds the distance  $l_c$  for the first time.

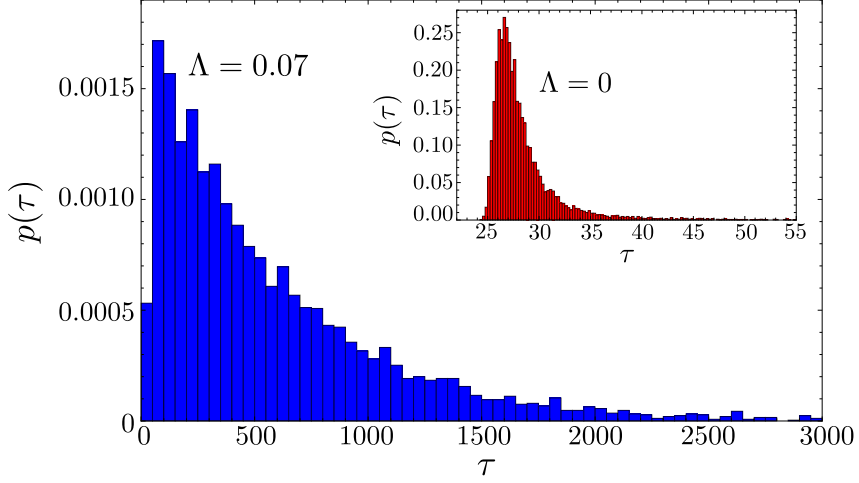


Figure 5.10 ■ Probability distributions  $p(\tau)$  of life times for  $\alpha = 100$  as obtained from simulations. The chemotactic strength is chosen as  $\Lambda = 0.07$  and  $\Lambda = 0$  (inset).

Fig. 5.10 plots the distribution of life times at  $\alpha = 100$  for  $\Lambda = 0$  (inset) and  $\Lambda = 0.07$ . For  $\Lambda = 0$ , we estimate the mean life time  $\langle \tau \rangle$  such that the mean-squared distance between the active walkers equals the characteristic distance  $l_c^2$ :  $l_c^2 \approx 4\alpha^2 (\langle \tau \rangle / \alpha - 1 + e^{-\langle \tau \rangle / \alpha})$ , cf. Eq. (2.46b). Inverting this relation for  $\langle \tau \rangle$  gives

$$\langle \tau \rangle \approx \frac{l_c^2}{4\alpha} + \alpha \left[ 1 + W \left( -e^{-1-l_c^2/(4\alpha^2)} \right) \right], \quad (5.12)$$

where  $W$  denotes the Lambert  $W$  function, which is the inverse function of  $ze^z$ . For  $\alpha = 100$ , we obtain  $\langle \tau \rangle = 33.3$ , which agrees well with the simulated value  $\langle \tau \rangle = 30.0$ . This time is smaller than the directional correlation time  $\alpha = \tau_{\text{rot}}/t_0 = 100$  and therefore the distribution remains rather narrow. On the contrary, the distribution function  $p(\tau)$  for  $\Lambda = 0.07$  yields a mean life time of  $\langle \tau \rangle = 581.8$  well above  $\alpha$  and it is relatively broad. In fact, we checked that the graph in Fig. 5.10 is well described by the inverse Gaussian distribution, which gives the distribution of the first-passage times for a one-dimensional random walk [188, 189]. The maximum of  $p(\tau)$  shifts to larger  $\tau$  for increasing  $\Lambda$  and ultimately reaches the total simulation time, meaning the system is in the bound state.

From the life time distributions for  $\alpha = 1, 5, 20, 100$ , we determined the mean value  $\langle \tau \rangle$  as a function of  $\Lambda$  in the region between the free walker and bound state. Figure 5.11 presents two plots for  $\alpha = 5$  and  $\alpha = 100$ . They clearly show that the mean life time grows exponentially in the chemotactic strength  $\Lambda$ ,  $\langle \tau \rangle \propto \exp(\Lambda/\Lambda_0)$ , reminiscent of Kramers' escape rate [Eq. (2.21)], when we identify  $\Lambda$  with the potential barrier. So, the mean life time is very sensitive to variations in  $\Lambda$ , which also means that the value of the simulation time for defining the bound state is not crucial. For example, when we interpolate the straight line for  $\alpha = 5$  to  $\langle \tau \rangle = 10^5$  in

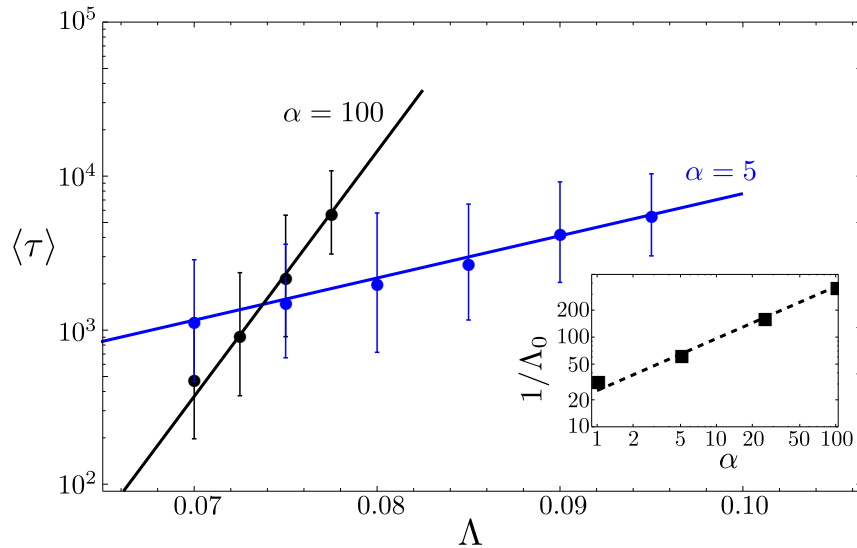


Figure 5.11 ■ Mean life times as a function of chemotactic strength  $\Lambda$  for  $\alpha = 5$  and  $\alpha = 100$ . The values with error bars are obtained numerically, and the solid lines are exponential fits. Inset: The slope or “inverse temperature”  $1/\Lambda_0$  versus persistence number  $\alpha$  obey the power law  $1/\Lambda_0 \propto \alpha^{0.58}$ .

Fig. 5.11, the bound state occurs at  $\Lambda \approx 0.14$  instead of  $\Lambda \approx 0.104$  at a simulation time of  $10^4$ .

In the exponential law  $\langle \tau \rangle \propto \exp(\Lambda/\Lambda_0)$ ,  $1/\Lambda_0$  plays the role of the “inverse temperature”. According to the inset of Fig. 5.11,  $1/\Lambda_0$  grows with the inverse noise strength  $\alpha$ , as expected, following the power law  $1/\Lambda_0 \propto \alpha^{0.58}$ . For large  $\alpha$ , when the system tends towards the deterministic regime,  $\langle \tau \rangle$  is particularly sensitive to  $\Lambda$ . The transition from the free walker to the bound state becomes more abrupt, indicating that the range of the metastable state shrinks to zero, as observed in the state diagram of Fig. 5.7.

## 5.4 Properties of a many-walker system

We study a system consisting of 50 walkers and explore some of its properties. In particular, in Sec. 5.4.1, we address different states of the system including metastable and stable cluster states as in the two-walker case. In Sec. 5.4.2, we investigate how an initially elongated cluster relaxes towards its circular stationary shape. Section 5.4.3 demonstrates how clusters or microcolonies merge due to autochemotactic signaling. Finally, we show in Sec. 5.4.4 that in a confined geometry clustering of microorganisms occurs beyond a certain area fraction.

We briefly comment on the number of walkers in the following analysis. Though we focus on systems with 50 walkers, we observe the same qualitative features for larger systems of up to 500 walkers. Going beyond this order of magnitude increases

the computational effort considerably.

### 5.4.1 State diagram and cluster stability

In analogy to Sec. 5.3.2, we investigate the stability of clusters consisting of a large number of walkers. We place them randomly, both in position and velocity, on a square with a large area fraction of 50%, so that they form a dense cluster, and let them evolve in time. Monitoring an ensemble of about 10 clusters, we identify again three different states. For sufficiently large chemotactic strength  $\Lambda$ , all the clusters stay intact and we have the bound cluster state. At small  $\Lambda$ , all the clusters dissolve and a “gas” of free chemotactic walkers results, which hardly come into contact with each other. In between, a metastable state is observed, where walkers leave and join the cluster, which itself fluctuates strongly. We therefore call it a “hot cluster”. It can happen that the fluctuations become so large that the cluster suddenly dissolves into free walkers. Figure 5.12(a) shows snapshots of such a scenario at three different times. In the supplemental material of our article [A], we provide the corresponding video, which demonstrates how the cluster dissolves.

The resulting state diagram as a function of the chemotactic strength  $\Lambda$  for constant  $\alpha = 25$  is presented in Figure 5.12(b). After rescaling  $\Lambda$  by the number of walkers  $m$ , the metastable state is situated in the same region around  $\Lambda/m \approx 0.1$  as in the two-walker case, where we found  $\Lambda \approx 0.1$ . We roughly confirmed the scaling for  $m = 50, 100$  and  $500$ . Each walker emits the chemical and thereby increases the autochemotactic field, which mediates an attraction between the walkers; this justifies the observed scaling.

We briefly refer to the Keller-Segel model for chemotactic aggregation, as discussed in Secs. 2.4.1 and 2.4.2. In its simplest form, it can generate a “chemotactic collapse”, where microorganisms collapse into a delta-peaked distribution if their density exceeds a critical value. Equivalently, for constant density the collapse occurs at a chemotactic sensitivity that scales as the inverse of the number  $m$  of microorganisms [Eq. (2.76)], in full agreement with our result. However, by taking into account the finite extent of the walkers, we prevent the unrealistic collapse and obtain stable clusters. Note that a modification of the classical Keller-Segel model also introduces a finite particle size [190]. Similarly, a stability analysis of the uniform density in the Keller-Segel model reveals a transition to pattern formation at a chemotactic sensitivity that scales again as  $1/m$  [Eq. (2.85)].

### 5.4.2 Relaxation dynamics of stable clusters

The stable clusters of walkers are circular when  $m$  is sufficiently large. To describe the size and shape of a walker distribution in a disturbed cluster, we introduce the

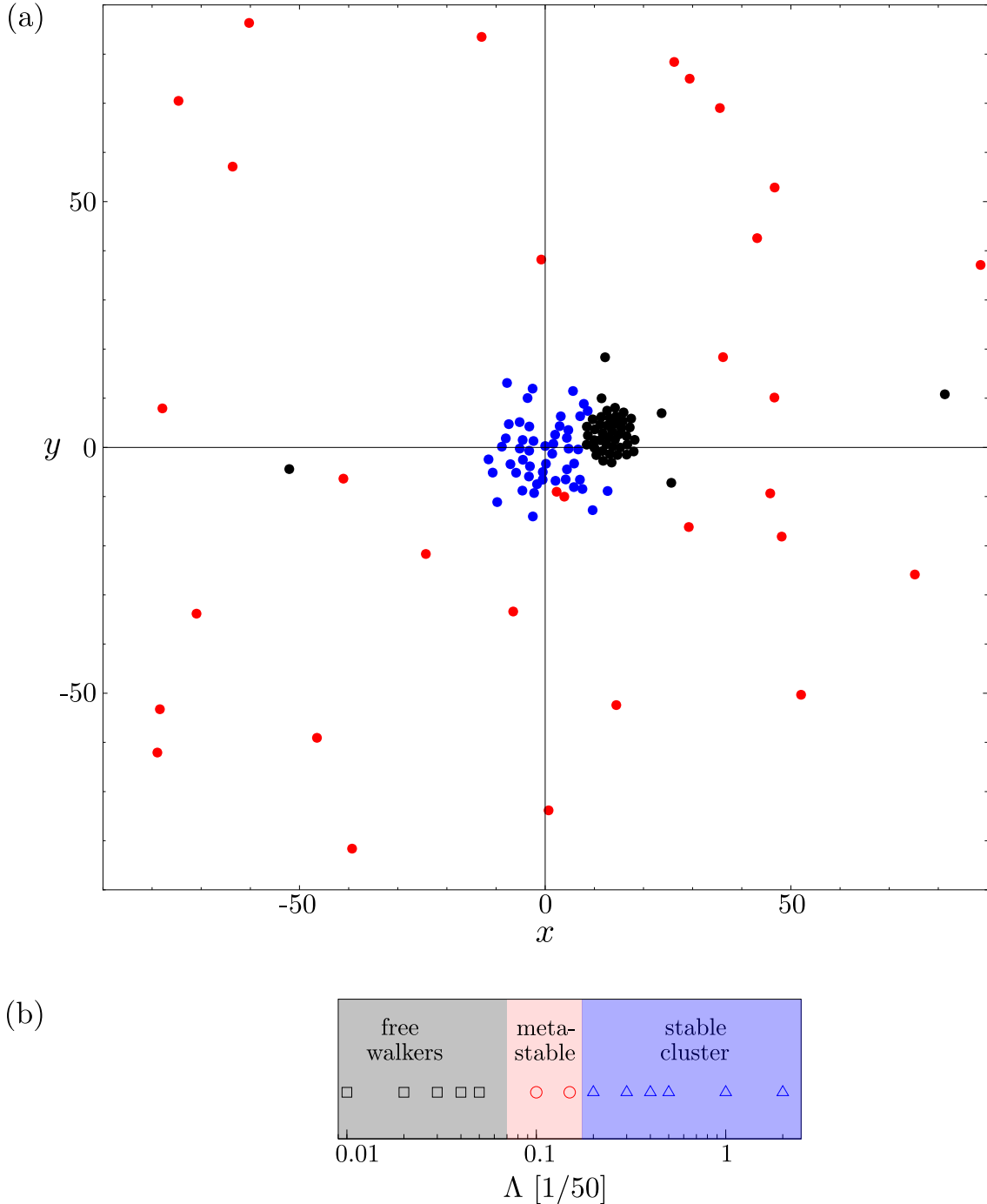


**Figure 5.12** ■ (a) A cluster of walkers in the metastable state dissolves in time. Snapshots of the walkers at three different times:  $t = 5$  (blue, disks are initially distributed on a square of side length 17.7 with area fraction 50%),  $t = 1000$  (black), and  $t = 1500$  (red). Parameters are  $\Lambda = 0.002$ ,  $\alpha = 25$ . (b) State diagram as recorded for  $m = 50$  particles with  $\alpha = 25$ .

gyration tensor  $\mathbf{Q}$ . It is defined as

$$\mathbf{Q} = \frac{1}{2m^2} \sum_{i,j=1}^m (\mathbf{r}_i - \mathbf{r}_j) \otimes (\mathbf{r}_i - \mathbf{r}_j), \quad (5.13)$$

where  $\otimes$  specifies the dyadic product [191]. Diagonalizing  $\mathbf{Q}$  yields two eigenvalues  $\lambda_1 \geq \lambda_2 \geq 0$ . An ensemble average over  $\lambda_1 + \lambda_2$ , which is the trace of  $\mathbf{Q}$ , gives the square of the radius of gyration, which is a measure for the size of the cluster:

$$R_g^2 = \frac{1}{2m^2} \sum_{i,j=1}^m \langle [\mathbf{r}_i(t) - \mathbf{r}_j(t)]^2 \rangle \quad (5.14a)$$

$$= \frac{1}{m} \sum_{i=1}^m \langle [\mathbf{r}_i(t) - \mathbf{R}(t)]^2 \rangle. \quad (5.14b)$$

Here, we have introduced the position vector of the center of mass,  $\mathbf{R} = 1/m \sum_{i=1}^m \mathbf{r}_i$ . For demonstration, we show in the appendix of Sec. 5.7 that for a hexagonal closest packing of  $m$  disks, one has the approximate scaling  $R_g^2 \propto m$ . The hexagonal closest packing looks similar to the observed structure of strongly bound clusters.

The cluster has a circular shape when both eigenvalues of  $\mathbf{Q}$  are equal,  $\lambda_1 = \lambda_2$ . To describe deviations from the spherical shape, we introduce the asymmetry parameter  $\Delta_2$  as the following ensemble average [192]:

$$\Delta_2 = \left\langle \frac{(\lambda_1 - \lambda_2)^2}{(\lambda_1 + \lambda_2)^2} \right\rangle. \quad (5.15)$$

In the limiting case, when all walkers align along one line,  $\Delta_2 = 1$ .

In the following, we demonstrate that at large chemotactic strength  $\Lambda = 0.02$ , a cluster of loosely packed walkers relaxes exponentially towards a densely packed cluster with circular shape. As Fig. 5.13(a) on the left demonstrates, we distribute 50 particles uniformly on an ellipse with asymmetry  $\Delta_2 \approx 0.15$  and area fraction 50%, and randomly choose the velocity directions. The picture on the right shows the densely packed cluster after relaxing into the stationary state. In Fig. 5.13(b), we show how the squared radius of gyration  $R_g^2$  and the asymmetry  $\Delta_2$  smoothly relax towards the circular cluster state with  $\Delta_2 \approx 0$ . The ensemble average is taken over 100 different realizations of initial conditions and noise. After subtracting the respective minimum values from  $R_g^2$  and  $\Delta_2$ , the intermediate parts of the curves in the semi-logarithmic plots in Fig. 5.13(c) are nicely fit by an exponential decay with relaxation times  $t_g = 2.4$  for the cluster's size and  $t_a = 3.4$  for its asymmetry [see the orange lines in Fig. 5.13(c)].

Note whereas the cluster size decreases continuously in Fig. 5.13(b), the asymmetry first increases due to restructuring of the cluster and then relaxes towards zero. We recorded similar curves for different persistence numbers  $\alpha = 5$  and  $\alpha = 100$ . In our simulations, the initial concentration of chemoattractant is zero. We also

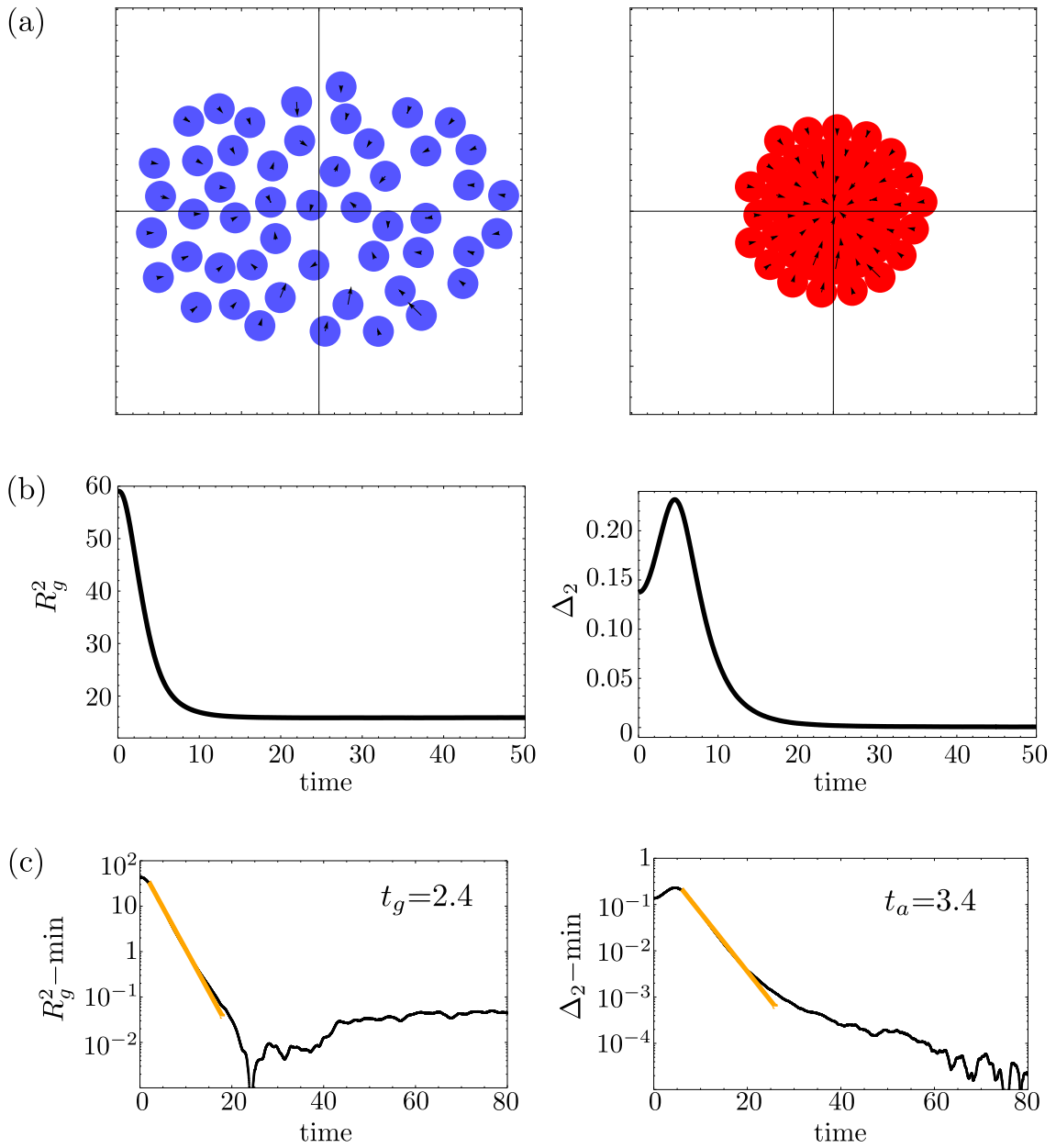


**Figure 5.13** ■ (a) The initial ellipsoidal walker distribution relaxes exponentially into a circular cluster for chemotactic strength  $\Lambda = 0.02$  (and  $\alpha = 25$ ). The arrows indicate the velocity directions of the walkers. (b) Squared radius of gyration  $R_g^2$  and asymmetry  $\Delta_2$  plotted versus time. (c) To obtain the semi-logarithmic plots, the minimum values of  $R_g^2$  and  $\Delta_2$  have been subtracted, respectively. The orange straight lines are exponential fits with respective relaxation times  $t_g = 2.4$  and  $t_a = 3.4$ .

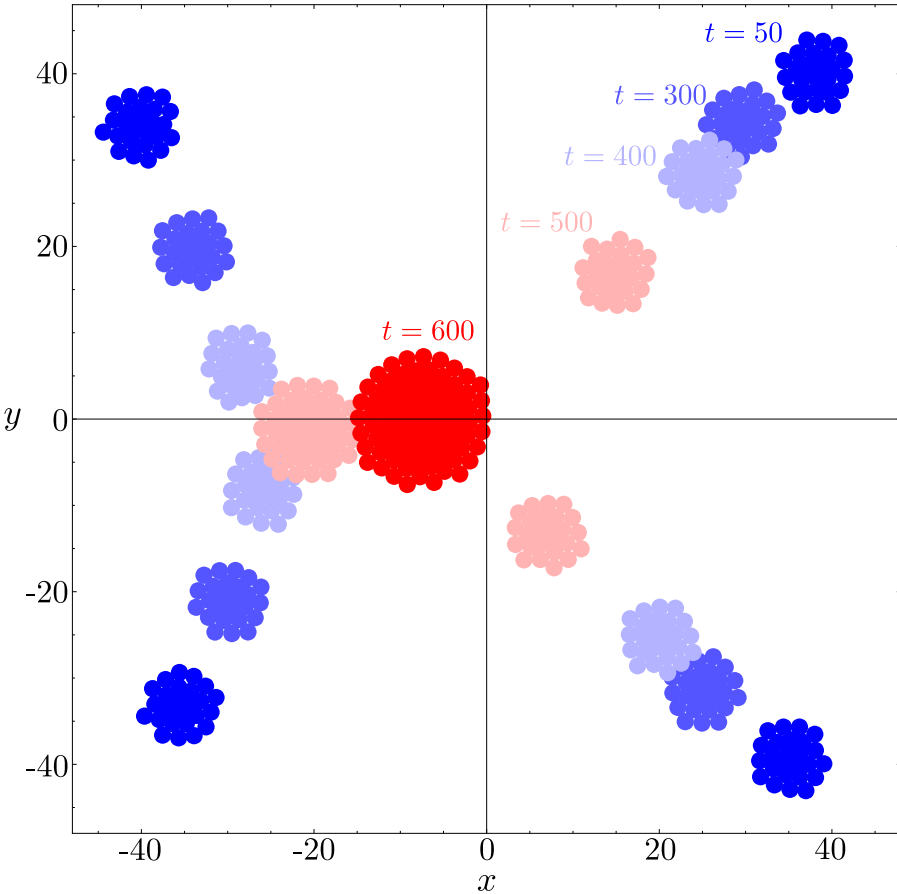


**Figure 5.14** ■ Four microcolonies, each with 25 particles, merge into a larger aggregate. The snapshots are taken at  $t = 50$  (dark blue), 300, 400, 500, and 600 (dark red). Parameters are  $\Lambda = 0.02$  and  $\alpha = 25$ .

performed a few simulations, where we initially fixed the walker positions, let the chemotactic field establish a stationary profile, and then recorded the relaxation curves for  $R_g^2$  and  $\Delta_2$ . They resemble the ones in Fig. 5.13(b). Finally, as expected, reducing the chemotactic strength  $\Lambda$  results in a weaker attraction between the walkers and thus in a less compact cluster with larger  $R_g^2$ .

The circular cluster on the right of Fig. 5.13(a) also illustrates that the velocity directions of the walkers point radially inwards towards the cluster center, where the concentration of the chemoattractant and thereby the chemotactic attraction is largest.

### 5.4.3 Microcolonies merge into a central cluster

So far, we have shown that a uniform distribution of chemotactic walkers at sufficiently large chemotactic strength  $\Lambda$  and initial area fraction forms a stable cluster,

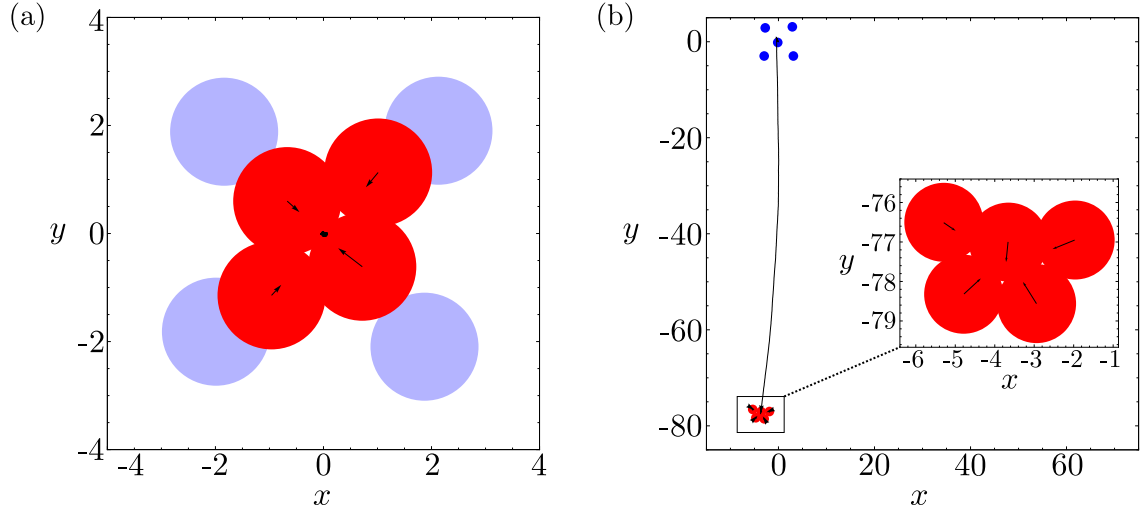


**Figure 5.15** ■ (a) A cluster of four walkers forms from an initial configuration (blue). The cluster hardly moves since the velocities of the single walkers cancel each other. (b) A cluster of five walkers is less symmetric (see blow-up) and therefore shows a noticeable drift as its trajectory shows. Both simulations are performed for the same time  $t_{\max} = 10^3$  and parameters  $\Lambda = 1$ ,  $\alpha = 25$ .

which we consider as a microcolony. Its formation can be interpreted as result of communication between individual cells mediated by the chemotactic field. On a higher level of aggregation, several microcolonies also interact via autochemotactic signaling and eventually merge into larger aggregates. The snapshots in Fig. 5.14 illustrate the scenario of four microcolonies merging into one central cluster for the parameters  $\Lambda = 0.02$  and  $\alpha = 25$ .

The drift of single clusters in the previous example is possible through an asymmetric arrangement of the walkers' velocity directions within the cluster, which add up to the center-of-mass velocity of the cluster. Geometry is important for the cluster's drift velocity. Although the stable cluster shown in Fig. 5.13 looks spherical, the small but non-zero value of the asymmetry  $\Delta_2$  generates a small drift velocity and the cluster moves around. The importance of geometry and symmetry is already realized for small clusters. Four walkers usually pack into a rhomboid [Fig. 5.15(a)] with their velocity directions pointing radially inwards so that it hardly moves. Clusters of five walkers pack into more asymmetric clusters [Fig. 5.15(b)] and exhibit a clear drift motion. The right plot of Fig. 5.16(a), to be discussed in detail below, presents another example: The walkers coalesce quickly into a cluster whose center-of-mass then moves along the thin line. Even though in clusters consisting of many walkers the cluster velocity may be several orders of magnitude smaller compared to the speed of a single active walker, it enables the cluster to explore its environment.

For clarification, we point out that even two initially perfectly symmetric clusters will merge into one aggregate due to strong chemotactic attraction. While drifting

towards each other, the internal structure will change.

#### 5.4.4 Microorganisms in confined geometry with fixed area fraction

Clustering of microorganisms in real systems due to chemotaxis requires a minimal area fraction, which is typically of the order of 5–10% and also depends on the type of cell. At low calcium concentrations, granulocytes attract each other over small distances and form clusters of actively moving cells if the density exceeds a threshold of 150–300 cells/mm<sup>2</sup> [178]. If we take the diameter of a granulocyte as  $2a = 20\mu\text{m}$  and use the cell area of  $\pi a^2$ , the critical density corresponds to a critical area fraction of  $\rho = 4.6\text{--}9.2\%$ . Aggregation of *Dicty* cells requires a minimum density of 400 cells/mm<sup>2</sup> [179]. With an estimate for an effective cell radius of  $a = 5.5\mu\text{m}$ , this threshold corresponds to  $\rho = 3.8\%$ .

We will now show that our model reproduces the experimental observation that clustering only occurs beyond a sufficiently large area fraction of microorganisms. By adjusting the parameters appropriately, in particular, the chemotactic strength  $\Lambda$ , we find clustering at an area fraction similar to experiments. We perform simulations with 50 chemotactic walkers and several area fractions  $\rho = 0.01, 0.05$ , and  $0.1$  in a circular area for which we implement a soft boundary with the help of overlapping disks [Fig. 5.16(a)]. They are non-motile, non-chemotactic, but repel the walkers with the harmonic force law of Eq. (5.6). As for the chemotactic walkers, we assume that the diffusion of the chemoattractant is not influenced by the presence of the boundary disks. Initially, the walkers are uniformly distributed over the circular area with area fraction  $\rho$  and have random velocity directions.

The effective chemotactic strength  $\Lambda$  depends on the parameters of the self-generated chemical field and on the chemotactic sensitivity  $\kappa$ , but not on the density of microorganisms. It turns out that by choosing in particular  $\Lambda = 0.003$  and for example  $\alpha = 25$ , we are able to observe the clustering transition for experimentally relevant area fractions  $\rho$  in the beginning and at the end of the simulations. For  $\rho = 0.01$ , the system remains in the gas state [on the left of Fig. 5.16(a)], whereas for  $\rho = 0.05$  [on the right of Fig. 5.16(a)] and  $\rho = 0.1$  (not shown) the walkers form a cluster in a sudden collapse shortly after the simulation starts [Fig. 5.16(b)]. Our model thus reproduces the experimental finding that clustering of microorganisms requires a minimal area fraction of the order of 5%. Note that a sudden collapse into a cluster also occurs for  $\Lambda = 0.002$ , but only after some time has passed [Fig. 5.16(b)].

The state diagram in Fig. 5.12(b) has been obtained for an open system, where the area fraction cannot be fixed. In the future, it might be interesting to determine state diagrams with specified boundary conditions that are realized in a Petri dish or microfluidic devices.

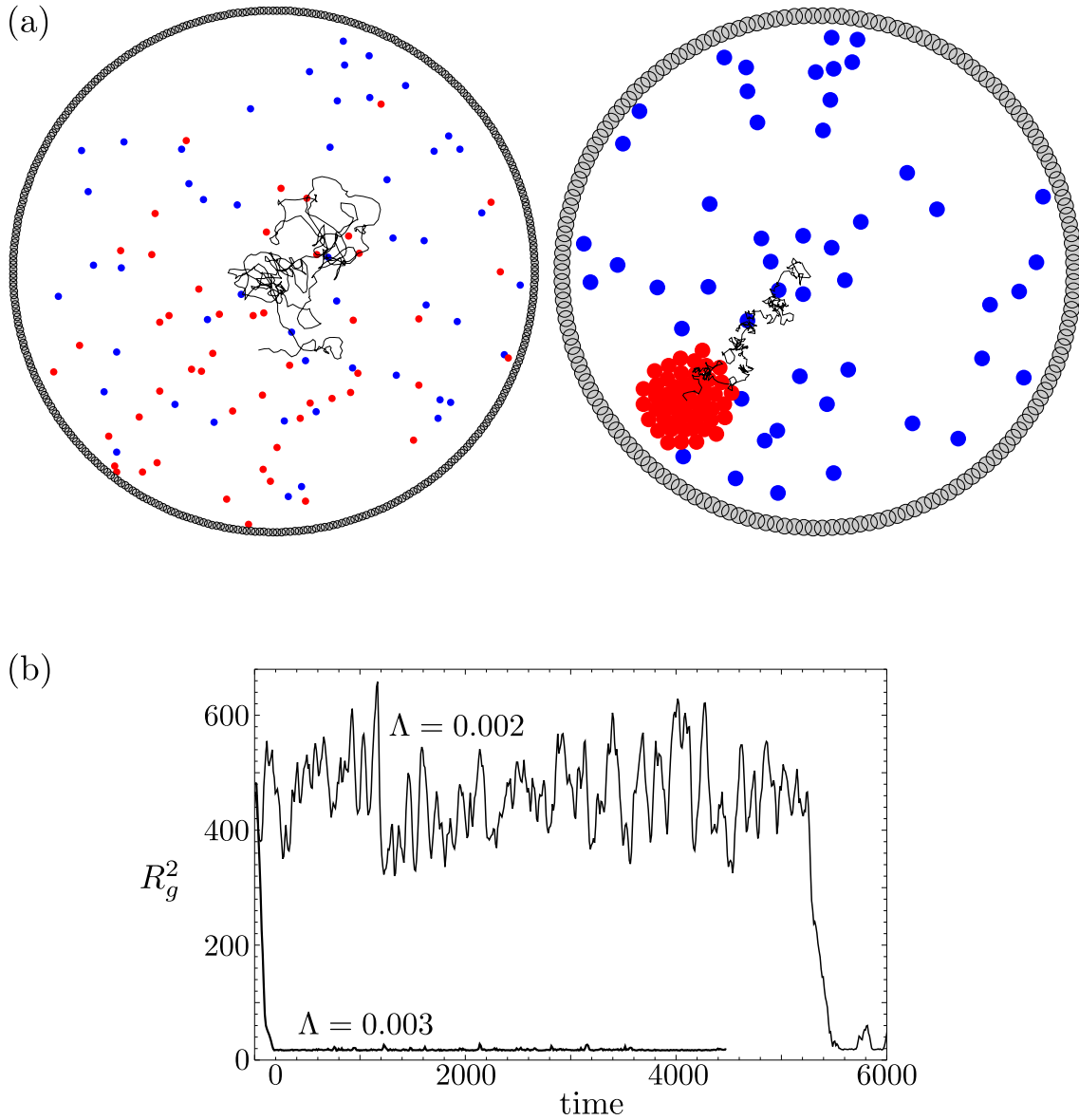


Figure 5.16 ■ (a) Simulations of 50 walkers in a circular area with soft boundary for two area fractions  $\rho$  and constant  $\Lambda = 0.003$  and  $\alpha = 25$ . Left:  $\rho = 0.01$ , right:  $\rho = 0.05$ . Blue and red circles indicate, respectively, the initial and final positions. The thin line shows the trajectory of the center of mass of all walkers,  $\mathbf{R}(t) = 1/m \sum_{i=1}^m \mathbf{r}_i(t)$ . On the right-hand side,  $\mathbf{R}(t)$  coincides with the center of the cluster. (b) Squared radius of gyration  $R_g^2$  of the walker system versus time for  $\Lambda = 0.003$  and  $\Lambda = 0.002$  (with the same  $\alpha = 25$  and  $\rho = 0.05$ ). Whereas the cluster with  $\Lambda = 0.003$  forms shortly after the simulation is started, the walkers at  $\Lambda = 0.002$  suddenly collapse into a cluster after some time.

## 5.5 Summary

We proposed a model for microorganisms that communicate via autochemotaxis. To do so, we extended the previous model for a single autochemotactic walker from Chapter 4 to a many-particle system and included a repulsive interaction between individual walkers by modeling them as soft disks. Based on a linear relationship between the harmonic repulsion force acting on a walker and its velocity, we were able to treat collisions between the autochemotactic walkers.

Already in a two-walker system, we find a rich variety of trajectories depending on the chemotactic strength  $\Lambda$ . They range from independent random walkers, to walkers that “hunt” each other, up to strongly bound clusters, where the walkers never lose contact with each other. A state diagram in terms of chemotactic coupling strength  $\Lambda$  and persistence number  $\alpha$  contains the free-walker, the metastable, and the bound state, where the latter was defined relative to the simulation time. We estimated the critical chemotactic strength for which the clustering transition to the bound state occurs. To elucidate the metastable state and the transition to stable two-particle clusters, we analyzed the distribution of cluster life times and showed that the mean life time  $\langle \tau \rangle$  in the metastable regime grows exponentially in the chemotactic strength  $\Lambda$ . The exponential law for  $\langle \tau \rangle \propto \exp(\Lambda/\Lambda_0)$  is reminiscent of Kramers’ escape rate of a trapped Brownian particle from a potential well. The “inverse temperature”  $1/\Lambda_0$  follows a power law in the inverse noise strength  $\alpha$ .

Many-walker systems show the same sequence of states for increasing chemotactic strength  $\Lambda$ . At sufficiently strong chemotactic strength, clusters or microcolonies have a circular shape. Elliptically shaped clusters relax exponentially towards the stable circular outline within a characteristic relaxation time. Small asymmetries of the cluster shape result in a drift motion of the center of mass. Finally, with our model we confirmed experimental observations that clustering requires a minimal density of microorganisms. In particular, we could adjust the chemotactic strength  $\Lambda$  such that the clustering transition occurs around an area fraction of 5%.

In conclusion, we formulated a minimal model to mimic the essential physics of chemotaxis-induced aggregation of microorganisms. For this reason, our model does not include microscopic details of the chemotaxis sensory system. For example, our model assumes an instantaneous reaction to the chemical gradient without any threshold value for the absolute concentration. We showed that even within this simple model several walkers form microcolonies and that already for two interacting walkers various motional patterns exist. Detailed experimental studies will help to determine the relevant region in the parameter space of our model and thereby test our predictions. Future theoretical investigations might improve the modeling for the spreading chemoattractant. In “real” microorganisms, it is emitted at the cell surface, where it also binds to receptors. Especially in dense bacterial systems, the free diffusion of chemical is influenced by the presence of the microorganisms and it would be interesting to study how it influences the behavior of our model system.

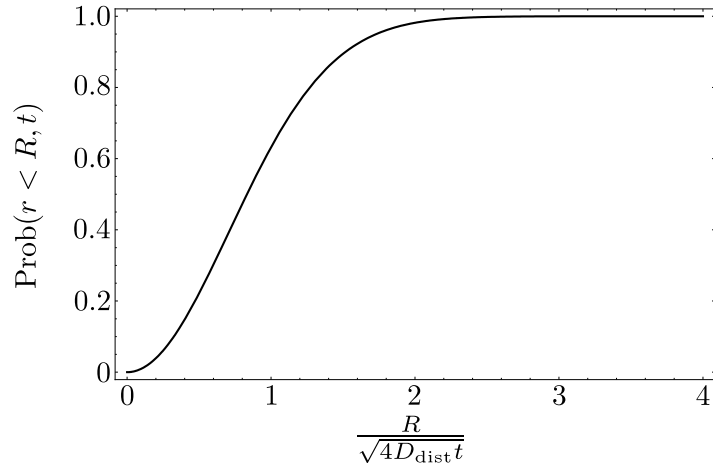


Figure 5.17 ■ Probability that the distance  $r$  between two diffusing particles at time  $t$  is smaller than  $R$  as a function of  $R/\sqrt{4D_{\text{dist}}t}$  according to Eq. (5.17).

## 5.6 Appendix I. Probability for a particle distance below a given value

We consider two independent, non-chemotactic walkers with constant speed  $v$  and rotational diffusion of their velocity directions. In the following, we estimate the probability that the particle distance  $d(t) = \sqrt{[\mathbf{r}_1(t) - \mathbf{r}_2(t)]^2}$  at time  $t > 0$  is below some value  $R$ .

For large times,  $\langle d^2(t) \rangle$  increases linearly in time and the “diffusion coefficient”  $D_{\text{dist}}$  is twice the diffusion constant  $D$  of a single walker. This is seen by noting that  $\langle \mathbf{d}^2(t) \rangle = \mathbf{d}_0^2 + 2Q_1(t)$  and the mean-squared displacement of a single walker reads  $Q_1(t) = \frac{2v^2}{q_\varphi^2} (q_\varphi t - 1 + e^{-q_\varphi t})$  [Eq. (2.46b)]. We assume that both walkers start their random walk at the origin. For large times, we thus approximate the time evolution of  $\mathbf{d}(t)$  by two-dimensional diffusion. The corresponding diffusion coefficient  $D_{\text{dist}}$  is defined by  $D_{\text{dist}} = \lim_{t \rightarrow \infty} \langle d^2(t) \rangle / (4t)$ . According to Eq. (2.26), the solution of the diffusion equation  $\partial_t P(\mathbf{r}, t | \mathbf{r}_0, t_0) = D_{\text{dist}} \nabla^2 P(\mathbf{r}, t | \mathbf{r}_0, t_0)$  with initial condition  $P(\mathbf{r}, t_0 | \mathbf{r}_0 = \mathbf{0}, t_0 = 0) = \delta(\mathbf{r})$  is given by

$$P(\mathbf{r}, t | \mathbf{r}_0 = \mathbf{0}, t_0 = 0) = \frac{1}{4\pi D_{\text{dist}} t} \exp\left(-\frac{\mathbf{r}^2}{4D_{\text{dist}} t}\right). \quad (5.16)$$

The probability  $\text{Prob}(r < R, t)$  that the particle distance  $r$  at time  $t$  is smaller than

$R$  is calculated as

$$\begin{aligned} \text{Prob}(r < R, t) &= \int_0^{2\pi} d\varphi \int_0^R dr r P(r, \varphi, t) \\ &= 1 - \exp \left[ - \left( \frac{R}{\sqrt{4D_{\text{dist}}t}} \right)^2 \right], \end{aligned} \quad (5.17)$$

and it is plotted as a function of  $R/\sqrt{4D_{\text{dist}}t}$  in Fig. 5.17. This result is intuitive as  $\sqrt{4D_{\text{dist}}t}$  corresponds to the root of the mean-squared displacement at time  $t$ . For  $R \ll \sqrt{4D_{\text{dist}}t}$ , the probability in Eq. (5.17) vanishes, whereas for  $R \gg \sqrt{4D_{\text{dist}}t}$  it approaches one.

In our rescaled model, we have  $D_{\text{dist}} = 2D = \alpha$ . For the simulation time  $t_{\text{max}} = 10^4$  and the critical distance  $l_c = 44.7$ , we obtain  $\text{Prob}(r < l_c, t_{\text{max}}) = 4.9\%$  for  $\alpha = 1$  and  $0.5\%$  for  $\alpha = 10$ . We use the former value of  $\sim 5\%$  to determine the transition between free walkers and metastable states in Sec. 5.3.2.

## 5.7 Appendix II. Radius of gyration for hexagonal closest packing of disks

In this section, we calculate the squared radius of gyration for the hexagonal closest packing of disks. This special geometry is interesting for many-walker systems, as we observe it for a strong autochemotactic attraction. A famous realization of this packing structure in nature is a honeycomb, which maximizes the area fraction of  $\pi\sqrt{3}/6 \approx 90.7\%$ . Here, we will show that for a large number of disks  $m$ ,  $R_g^2$  scales linearly with  $m$ .

We consider a fixed arrangement of unit disks as depicted in Fig. 5.18. Each disk's position  $\mathbf{r}_i$  is written as a linear combination  $\mathbf{r}_i = \alpha_i \mathbf{a} + \beta_i \mathbf{b}$  of the grid basis vectors

$$\mathbf{a} = \begin{pmatrix} 2 \\ 0 \end{pmatrix} \quad \text{and} \quad \mathbf{b} = \begin{pmatrix} 1 \\ \sqrt{3} \end{pmatrix}, \quad (5.18)$$

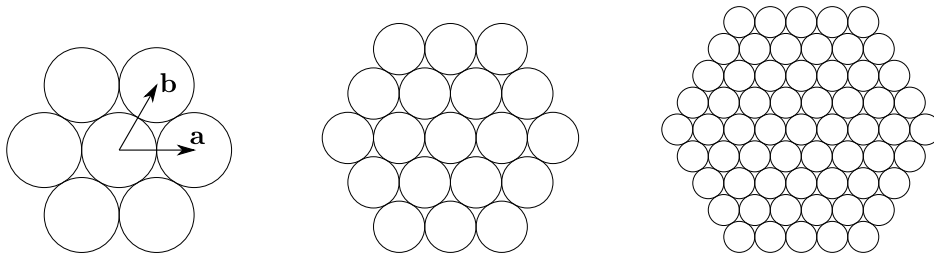


Figure 5.18 ■ Hexagonal closest packing of  $m = 7, 19, 61$  unit disks. With respect to the horizontal center line, the disk in the center of the cluster has  $z = 1, 2, 4$  neighbors on both its left and right side.

with integers  $\alpha_i, \beta_i \in \mathbb{Z}$ . We choose a coordinate system, where the center of mass is at the origin,  $\mathbf{R} = \frac{1}{m} \sum_{i=1}^m \mathbf{r}_i = \mathbf{0}$ . One particle is located at the origin and has both  $z$  left and  $z$  right neighbors with respect to the  $x$  axis. Abbreviating the position of a single particle as  $(\alpha_i, \beta_i)$ , the cluster configuration for given “neighbor parameter”  $z$  is represented by the following array:

$$\begin{array}{ccc}
 (-z, z) & \cdots & (0, z) \\
 \vdots & & \ddots \\
 (-z, 1) & & (z - 1, 1) \\
 (-z, 0) & & (z, 0) \\
 (-z + 1, -1) & & (z, -1) \\
 \ddots & & \vdots \\
 (0, -z) & \cdots & (z, -z)
 \end{array}$$

The squared radius of gyration,  $R_g^2$ , defined in Eq. (5.14), becomes

$$R_g^2 = \frac{1}{m} \sum_{i=1}^m (\mathbf{r}_i - \mathbf{R})^2 = \frac{1}{m} \sum_{i=1}^m \mathbf{r}_i^2 = \frac{1}{m} \sum_{i=1}^m \langle \alpha_i, \beta_i \rangle, \quad (5.19)$$

where we have introduced  $\mathbf{r}_i^2 = (\alpha_i \mathbf{a} + \beta_i \mathbf{b})^2 = 4(\alpha_i^2 + \alpha_i \beta_i + \beta_i^2) =: \langle \alpha_i, \beta_i \rangle$  as the squared distance of particle  $i$  to the origin. The number of disks  $m$  in dependence of the neighbor parameter  $z$  is calculated as

$$m = 1 + 2z + 2 \sum_{k=z+1}^{2z} k = 1 + 3z + 3z^2. \quad (5.20)$$

To evaluate the sum in Eq. (5.19), we split it according to the different horizontal lines of the cluster, and make use of the horizontal symmetry at the center line:

$$R_g^2 = \frac{1}{m} \left( \sum_{\text{zeroth line}} [\dots] + 2 \times \sum_{\substack{\text{k-th line,} \\ k=1, \dots, z}} [\dots] \right). \quad (5.21)$$

It follows:

$$R_g^2 = \frac{1}{m} \left( \sum_{j=-z}^z \langle j, 0 \rangle + 2 \sum_{k=1}^z \sum_{i=-z}^{z-k} \langle i, k \rangle \right) \quad (5.22a)$$

$$= \frac{4}{m} \left( 2 \sum_{j=1}^z j^2 + 2 \sum_{k=1}^z \sum_{i=-z}^{z-k} (i^2 + ik + k^2) \right) \quad (5.22b)$$

$$= \frac{z(1+z)(2+5z+5z^2)}{1+3z+3z^2}. \quad (5.22c)$$

Equation (5.22c) gives  $R_g^2$  for  $m$  disks as a function of the parameter  $z$ . To eliminate  $z$ , we solve Eq. (5.20) for  $z = -\frac{1}{2} + \sqrt{\frac{1}{4} + \frac{m-1}{3}}$ , and arrive at

$$R_g^2 = \frac{5}{9}m - \frac{4}{9} - \frac{1}{9m}. \quad (5.23)$$

For large clusters with  $m \gg 1$ , the squared radius of gyration for the hexagonal closest packing thus scales linearly with the particle number  $m$ . Note that the parameter  $z$  is an integer and the considered geometry allows only for distinct values of  $m = 7, 19, 37, 61, 91, \dots$  according to Eq. (5.20). To obtain the general scaling, we thus interpolate  $R_g^2 \propto m$  for integer  $m$ .



# 6 Kinetic equation for autochemotactic walkers

In this chapter, we develop a many-body theory for our model of autochemotactic walkers from the previous chapter. Instead of dealing with Langevin equations of single particles, we now obtain a kinetic equation, resembling a Fokker-Planck equation, for the probability density  $P_i(\mathbf{r}, \varphi, t)$  to find walker  $i$  with position  $\mathbf{r}$  and velocity orientation  $\varphi$  at time  $t$ . We consider a system of  $m$  microorganisms that are treated as point particles and interact exclusively via chemotactic signaling.

The following approach has been inspired by several works: Kinetic equations of many-particle systems with chemotactic interactions are formulated in Refs. [76, 82, 193]. Hydrodynamic equations of self-propelled particles are found in Refs. [194, 195, 196]. As already emphasized, our model combines the physics of autochemotactic interactions with the concept of active particles.

The motivation for this chapter is twofold: Whereas Langevin equations are easily implemented on a computer, the kinetic equation might provide analytical understanding of the model. Further, for very large systems with many individuals, it is neither feasible nor interesting to solve the Langevin equations of all particles. For the thermodynamic limit, where the number of particles  $m$  satisfies  $m \gg 1$ , a stochastic description in terms of a cell density seems more appropriate. In Chapter 2.4.1, we have pointed out that the model of Newman and Grima [76] for the overdamped Langevin dynamics of autochemotactic particles reduces to the Keller-Segel equations for chemotaxis in a mean-field approximation.

## 6.1 Kinetic equation

We summarize the Langevin equations for the dynamics of active walker  $i$ ,

$$\frac{d}{dt} \varphi_i(t) = -\frac{E_x(\mathbf{r}_i(t), t)}{\gamma_R} \sin \varphi_i(t) + \frac{E_y(\mathbf{r}_i(t), t)}{\gamma_R} \cos \varphi_i(t) + \sqrt{2q_\varphi} \Gamma_i(t), \quad (6.1a)$$

$$\frac{d}{dt} \mathbf{r}_i(t) = v \begin{pmatrix} \cos \varphi_i(t) \\ \sin \varphi_i(t) \end{pmatrix}, \quad (6.1b)$$

where the chemotactic field  $\mathbf{E}(\mathbf{r}_i(t), t)$  is evaluated at the particle's position  $\mathbf{r}_i(t)$ , and  $\Gamma_i(t)$  denotes normalized Gaussian white noise. In Eq. (5.4), we presented the

explicit solution of  $\mathbf{E}(\mathbf{r}, t) = \kappa \nabla c(\mathbf{r}, t)$ ; using the Green's function of Eq. (2.72) in two dimensions ( $d = 2$ ), we now write the regularized chemotactic field  $\mathbf{E}(\mathbf{r}, t)$  as

$$\mathbf{E}(\mathbf{r}, t) = \kappa h \int_0^{t-\tau_{\text{del}}} dt' \int_{\mathbb{R}^2} d^2 r' [\nabla_r G(\mathbf{r} - \mathbf{r}', t - t')] \sum_{j=1}^m \delta[\mathbf{r}' - \mathbf{r}_j(t')]. \quad (6.2)$$

We first define the one-particle probability density  $P_i(\mathbf{r}, \varphi, t)$  to find the fixed particle  $i$  at time  $t$  with position  $\mathbf{r} = (x, y)$  and velocity orientation  $\varphi$  as the ensemble average

$$P_i(\mathbf{r}, \varphi, t) = \langle \delta[\mathbf{r} - \mathbf{r}_i(t)] \delta[\varphi - \varphi_i(t)] \rangle. \quad (6.3)$$

Next, we introduce the two-particle probability density  $P_{i,j}$  to find particle  $i$  at time  $t$  with position  $\mathbf{r}$  and orientation  $\varphi$  and particle  $j$  at time  $t'$  with position  $\mathbf{r}'$  and unspecified orientation:

$$P_{i,j}(\mathbf{r}, \varphi, t; \mathbf{r}', t') = \langle \delta[\mathbf{r} - \mathbf{r}_i(t)] \delta[\varphi - \varphi_i(t)] \delta[\mathbf{r}' - \mathbf{r}_j(t')] \rangle. \quad (6.4)$$

In Sec. 6.2, we will show that taking the time derivative of  $P_i(\mathbf{r}, \varphi, t)$  and using Eqs. (6.1), (6.2) provides the following kinetic equation:

$$\begin{aligned} & \partial_t P_i(\mathbf{r}, \varphi, t) + v \cos \varphi \partial_x P_i(\mathbf{r}, \varphi, t) + v \sin \varphi \partial_y P_i(\mathbf{r}, \varphi, t) - q_\varphi \partial_\varphi^2 P_i(\mathbf{r}, \varphi, t) \\ &= \frac{\kappa h}{\gamma_R} \partial_\varphi \int_0^{t-\tau_{\text{del}}} dt' \int d^2 r' (\sin \varphi [\partial_x G(\mathbf{r} - \mathbf{r}', t - t')] - \cos \varphi [\partial_y G(\mathbf{r} - \mathbf{r}', t - t')]) \\ & \quad \times \sum_{j=1}^m P_{i,j}(\mathbf{r}, \varphi, t; \mathbf{r}', t'). \end{aligned} \quad (6.5)$$

Eq. (6.5) is exact, however, as it is typical for many-body problems, the equation for  $P_i$  is not closed, since it is expressed in terms of the two-particle distribution  $P_{i,j}$ . If we derive an equation for  $P_{i,j}$  as well, it will be expressed in terms of the three-particle distribution, and so on. To handle this infinite hierarchy of many-particle probability distributions, one needs some closure relation. The easiest way to do so is a mean-field ansatz, which we will discuss in Sec. 6.3. In mean-field theory, we will also obtain an equation for the full distribution function

$$f(\mathbf{r}, \varphi, t) = \sum_{i=1}^m P_i(\mathbf{r}, \varphi, t), \quad (6.6)$$

which is the probability density to find a particle, which is not labeled or specified any more, at time  $t$  with position  $\mathbf{r}$  and orientation  $\varphi$ .

The two-particle distribution  $P_{i,j}$ , as defined in Eq. (6.4), contains information about correlations between two particles  $i$  and  $j$ . Even in a one-particle system,  $P_{i,i}$  contains non-trivial correlations due to the particle's interaction with the self-generated chemical field: The past trajectory determines where chemical has been

emitted, and in turn the chemical influences the future trajectory, as the walker tends to explore spatial regions of higher or lower concentration.

The kinetic equation (6.5) reveals the important “ingredients” of the model at a glance; we quickly check it for consistency by considering two trivial cases. If the particles do not move ( $v = 0$ ) and do not interact with each other ( $\kappa = 0$ ), we are only left with rotational diffusion of the velocity direction. In this case, particles that are initially located at positions  $\mathbf{r}_i^{(0)}$  with velocity directions  $\varphi_i^{(0)}$  according to  $P_i(\mathbf{r}, \varphi, t = 0) = \delta[\mathbf{r} - \mathbf{r}_i^{(0)}] \delta[\varphi - \varphi_i^{(0)}]$ , remain localized at the initial positions, while the velocity directions diffuse on the unit circle according to Eq. (2.37a):

$$P_i(\mathbf{r}, \varphi, t) = \delta[\mathbf{r} - \mathbf{r}_i^{(0)}] \left( \frac{1}{2\pi} + \frac{1}{\pi} \sum_{m=1}^{\infty} e^{-m^2 q_\varphi t} \cos[m(\varphi - \varphi_i^{(0)})] \right). \quad (6.7)$$

In the second special case without rotational diffusion  $q_\varphi = 0$  and without chemotactic coupling  $\kappa = 0$ , one obtains ballistic motion along the initial directions  $\varphi_i^{(0)}$ :

$$P_i(\mathbf{r}, \varphi, t) = \delta[x - x_i^{(0)} - vt \cos \varphi_i^{(0)}] \delta[y - y_i^{(0)} - vt \sin \varphi_i^{(0)}]. \quad (6.8)$$

The more general situation without chemotaxis ( $\kappa = 0$ ) gives the model of independent active particles with speed  $v$  and rotational diffusion of the velocity direction, parametrized by the noise strength  $q_\varphi$ . Though we know the directional correlation function and mean-squared displacement for this case (see Chapter 2.3.1), it is not clear what the probability distribution  $P_i$  looks like. Note that after transforming the position variable  $\mathbf{r}$  into Fourier space and expanding the direction  $\varphi$  into discrete Fourier modes with index  $n$ , Eq. (6.5) takes the form of a “tridiagonal recurrence relation”, which can presumably be solved in terms of continued fractions [18].

## 6.2 Derivation of the kinetic equation

We briefly sketch how the kinetic equation (6.5) is derived. We start with the definition of  $P_i$  from Eq. (6.3) and differentiate it with respect to time:

$$\begin{aligned} & \frac{\partial}{\partial t} P_i(\mathbf{r}, \varphi, t) \\ &= -\frac{\partial}{\partial x} \langle \dot{x}_i(t) \delta[x - x_i(t)] \delta[y - y_i(t)] \delta[\varphi - \varphi_i(t)] \rangle \\ &\quad -\frac{\partial}{\partial y} \langle \dot{y}_i(t) \delta[x - x_i(t)] \delta[y - y_i(t)] \delta[\varphi - \varphi_i(t)] \rangle \\ &\quad -\frac{\partial}{\partial \varphi} \langle \dot{\varphi}_i(t) \delta[x - x_i(t)] \delta[y - y_i(t)] \delta[\varphi - \varphi_i(t)] \rangle. \end{aligned} \quad (6.9)$$

To arrive at Eq. (6.9), we used the “chain rule”  $\frac{\partial}{\partial t} \delta[w - z(t)] = -\dot{v}(t) \frac{\partial}{\partial w} \delta[w - z(t)]$  for an arbitrary function  $z(t)$ , which is readily proven with help of the Fourier representation of the delta function,  $\delta(x) = \int_{-\infty}^{\infty} \frac{dk}{2\pi} e^{ikx}$ . Next, we insert the derivatives  $\dot{x}_i(t)$ ,  $\dot{y}_i(t)$ , and  $\dot{\varphi}_i(t)$  from Eq. (6.1), and after rewriting the arguments of  $\mathbf{E}$  due to the properties of the delta function, we obtain

$$\begin{aligned} & \frac{\partial}{\partial t} P_i(\mathbf{r}, \varphi, t) \\ = & -v \cos \varphi \frac{\partial}{\partial x} \langle \delta[\mathbf{r} - \mathbf{r}_i(t)] \delta[\varphi - \varphi_i(t)] \rangle - v \sin \varphi \frac{\partial}{\partial y} \langle \delta[\mathbf{r} - \mathbf{r}_i(t)] \delta[\varphi - \varphi_i(t)] \rangle \\ & + \frac{\partial}{\partial \varphi} \left\langle \frac{E_x(\mathbf{r}, t)}{\gamma_R} \sin \varphi \delta[\mathbf{r} - \mathbf{r}_i(t)] \delta[\varphi - \varphi_i(t)] \right\rangle \\ & - \frac{\partial}{\partial \varphi} \left\langle \frac{E_y(\mathbf{r}, t)}{\gamma_R} \cos \varphi \delta[\mathbf{r} - \mathbf{r}_i(t)] \delta[\varphi - \varphi_i(t)] \right\rangle \\ & - \sqrt{2q_\varphi} \frac{\partial}{\partial \varphi} \langle \Gamma_i(t) \delta[\mathbf{r} - \mathbf{r}_i(t)] \delta[\varphi - \varphi_i(t)] \rangle. \end{aligned} \quad (6.10)$$

The first two terms of Eq. (6.10) contain simply spatial derivatives of  $P_i(\mathbf{r}, \varphi, t)$ . The evaluation of the last term is known from deriving the Fokker-Planck equation from a Langevin equation with additive noise, *e.g.* via path integrals [20], and yields

$$- \sqrt{2q_\varphi} \frac{\partial}{\partial \varphi} \langle \Gamma_i(t) \delta[\mathbf{r} - \mathbf{r}_i(t)] \delta[\varphi - \varphi_i(t)] \rangle = q_\varphi \frac{\partial^2}{\partial \varphi^2} P_i(\mathbf{r}, \varphi, t). \quad (6.11)$$

Here, we analyze the first remaining term containing the chemotactic field. Using Eq. (6.2) for  $\mathbf{E}(\mathbf{r}, t)$  introduces the two-particle distribution  $P_{i,j}$  from Eq. (6.4):

$$\begin{aligned} & \left\langle \frac{E_x(\mathbf{r}, t)}{\gamma_R} \sin \varphi \delta[\mathbf{r} - \mathbf{r}_i(t)] \delta[\varphi - \varphi_i(t)] \right\rangle \\ = & \frac{\kappa h}{\gamma_R} \sin \varphi \int_0^{t-\tau_{\text{del}}} dt' \int d^2 r' [\partial_x G(\mathbf{r} - \mathbf{r}', t - t')] \\ & \times \sum_{j=1}^m \underbrace{\langle \delta[\mathbf{r} - \mathbf{r}_i(t)] \delta[\varphi - \varphi_i(t)] \delta[\mathbf{r}' - \mathbf{r}'_j(t)] \rangle}_{=P_{i,j}(\mathbf{r}, \varphi, t; \mathbf{r}', t')} . \end{aligned} \quad (6.12)$$

Combining all preceding results leads to the kinetic equation (6.5).

### 6.3 Mean-field approximation and discussion

In the following, we truncate the infinite hierarchy from Eq. (6.5) by a mean-field approximation, as it was performed in Ref. [76]. From the definition of the conditional probability  $P_{i,j}(\mathbf{r}, \varphi, t | \mathbf{r}', t')$  we have

$$P_{i,j}(\mathbf{r}, \varphi, t; \mathbf{r}', t') = P_{i,j}(\mathbf{r}, \varphi, t | \mathbf{r}', t') P_j(\mathbf{r}', t'). \quad (6.13)$$

The mean-field assumption means that the conditional probability for finding particle  $i$  at time  $t$  at position  $\mathbf{r}$  with orientation  $\varphi$  is independent of the full history of all particles  $j$ , that is

$$P_{i,j}(\mathbf{r}, \varphi, t | \mathbf{r}', t') = P_i(\mathbf{r}, \varphi, t). \quad (6.14)$$

The spatial density for particle  $i$  reads  $P_i(\mathbf{r}, t) = \int_{-\pi}^{+\pi} d\varphi P_i(\mathbf{r}, \varphi, t)$ , and the spatial density of all particles,  $\rho(\mathbf{r}, t)$ , is obtained by integrating  $f(\mathbf{r}, \varphi, t)$  [Eq. (6.6)] over the angle:  $\rho(\mathbf{r}, t) = \int_{-\pi}^{+\pi} d\varphi f(\mathbf{r}, \varphi, t)$ . The mean-field ansatz provides a closed equation for  $P_i(\mathbf{r}, \varphi, t)$ ; summing Eq. (6.5) over all particles finally gives the equation for  $f(\mathbf{r}, \varphi, t)$ :

$$\begin{aligned} & \partial_t f(\mathbf{r}, \varphi, t) + v \cos \varphi \partial_x f(\mathbf{r}, \varphi, t) + v \sin \varphi \partial_y f(\mathbf{r}, \varphi, t) - q_\varphi \partial_\varphi^2 f(\mathbf{r}, \varphi, t) \\ &= \frac{\partial}{\partial \varphi} \left[ f(\mathbf{r}, \varphi, t) \left( \frac{\tilde{E}_x(\mathbf{r}, t)}{\gamma_R} \sin \varphi - \frac{\tilde{E}_y(\mathbf{r}, t)}{\gamma_R} \cos \varphi \right) \right]. \end{aligned} \quad (6.15)$$

Here, the smooth chemotactic field  $\tilde{\mathbf{E}}(\mathbf{r}, t)$  has been obtained after an ensemble average over Eq. (6.2) and reads

$$\tilde{\mathbf{E}}(\mathbf{r}, t) = \kappa h \int_0^{t-\tau_{\text{del}}} dt' \int_{\mathbb{R}^2} d^2 r' [\nabla_r G(\mathbf{r} - \mathbf{r}', t - t')] \rho(\mathbf{r}', t'), \quad (6.16)$$

and the concentration field  $\tilde{c}(\mathbf{r}, t)$  is given by

$$\tilde{c}(\mathbf{r}, t) = h \int_0^{t-\tau_{\text{del}}} dt' \int_{\mathbb{R}^2} d^2 r' G(\mathbf{r} - \mathbf{r}', t - t') \rho(\mathbf{r}', t'). \quad (6.17)$$

The densities for cells  $\rho(\mathbf{r}, t)$  and chemical  $\tilde{c}(\mathbf{r}, t)$  thus automatically satisfy the former balance equation:

$$\partial_t \tilde{c}(\mathbf{r}, t) = D_c \nabla^2 \tilde{c}(\mathbf{r}, t) - k \tilde{c}(\mathbf{r}, t) + h \rho(\mathbf{r}, t). \quad (6.18)$$

To obtain an equation for  $\rho$ , we integrate Eq. (6.15) over the direction. Due to the periodicity in  $\varphi$  of  $f(\mathbf{r}, \varphi, t)$  and  $\partial_\varphi f(\mathbf{r}, \varphi, t)$ , the terms containing  $\partial_\varphi$  derivatives vanish. Introducing the velocity field

$$\mathbf{u}(\mathbf{r}, t) = \frac{v}{\rho(\mathbf{r}, t)} \int_{-\pi}^{+\pi} d\varphi f(\mathbf{r}, \varphi, t) \begin{pmatrix} \cos \varphi \\ \sin \varphi \end{pmatrix}, \quad (6.19)$$

we realize that the cell density obeys the continuity equation

$$\partial_t \rho + \nabla \cdot (\rho \mathbf{u}) = 0. \quad (6.20)$$

The mean-field model of our autochemotactic walkers is captured by Eqs. (6.15) and (6.18). In contrast to the Keller-Segel equations, which have been derived by a mean-field approximation in Ref. [76], this set of equations still depends on the velocity orientation. Note that a uniform and stationary distribution  $f(\mathbf{r}, \varphi, t) = \rho_0/(2\pi)$  solves the equations. In the future, it will be of interest to study the stability of the homogeneous state. A spatial dependence of  $f(\mathbf{r}, \varphi, t)$  corresponds to pattern formation, whereas a dependence on the direction of motion  $\varphi$  would indicate collective motion.

## 6.4 Conclusion and outlook

In this short chapter, we reformulated our model for the Langevin dynamics of autochemotactic point particles in terms of a kinetic equation, which resembles a Fokker-Planck equation. However, one does not directly obtain an equation for the full density  $f(\mathbf{r}, \varphi, t)$  to find a particle at time  $t$  at position  $\mathbf{r}$  with velocity direction  $\varphi$ , but instead ends up with coupled equations for the probability density  $P_i(\mathbf{r}, \varphi, t)$  of a fixed particle  $i$ .

In Sec. 6.1, we have presented the kinetic equation that contains the autochemotactic interactions between the active walkers; we checked the validity of the kinetic equation for two trivial cases. The derivation of the kinetic equation is sketched in Sec. 6.2. As it is well-known from many-particle systems, solving this equation requires a truncation of the infinite hierarchy of probability distributions. In Sec. 6.3, we therefore adopted a mean-field approximation in the spirit of Ref. [76].

The resulting set of mean-field equations may serve as the starting point for a “hydrodynamic” study of our model in a continuum version. This will in particular be of interest if the Langevin dynamics of the autochemotactic microorganisms are to be averaged over a large number of individuals, *i.e.* in the thermodynamic limit. For instance, pattern formation of active particles has recently been analyzed for continuum models in Refs. [197, 198].

# 7 Pili-induced clustering of *N. gonorrhoeae* bacteria

The first step of colonization of *Neisseria gonorrhoeae* bacteria, the etiological agent of gonorrhea, is the attachment to human epithelial cells. The bacterial cells are known to cluster rapidly and form microcolonies that are considered to be the infection unit of the disease. This surface attachment and subsequent clustering are mediated by filamentous cell appendages, called type IV pili (Tfp). In this chapter, we study how *N. gonorrhoeae* cells, initially dispersed over a surface, agglomerate into spherical microcolonies within hours. Our analysis suggests that the clustering is driven entirely by the Tfp dynamics without any additional chemotactic signaling. We support our hypothesis by a “pili-taxis” model for the pili-mediated attraction between cells.

In Sec. 7.1, we give an introduction to *N. gonorrhoeae* and properties of Tfp. We first present our experimental results in Sec. 7.2, and then introduce a model for “pili-taxis” in Sec. 7.3. Afterwards, in Sec. 7.4, we compare the experimental results to numerical simulations. A summary and outlook are given in Sec. 7.5. We close with an appendix in Sec. 7.6, where we suggest a different model for the pili-mediated interaction between cell clusters.

## 7.1 Basics about gonococci and type IV pili

The micrometer-sized bacterium *N. gonorrhoeae*, also termed gonococcus, is the pathogen, which causes the sexually transmitted disease gonorrhea. Usually, one observes a dumbbell-shaped aggregate of two cells as the smallest unit, called diplococcus.

In contrast to the bacteria discussed in Chapter 3, gonococci cannot swim, because they lack flagella and the corresponding propulsion mechanism. However, they possess a form of motility that enables them to crawl over surfaces. As this kind of motion looks rather jerky, it is called “twitching” [199, 200]. Twitching motility is driven by type IV pili (Tfp), which are 5...9 nm thin filamentous appendages present over the whole cell body of *N. gonorrhoeae* [11]. Cycles of elongation and retraction of Tfp also enable the attachment of gonococci to abiotic surfaces and cells [201]. According to Bradley’s retraction model [10], a pilus is “thrown” like an

anchor, attaches to a surface (or cell), and by retraction pulls the cell forward.

The force generated by Tfp is one of the strongest in the microbial world: The retraction of a single pilus can generate a force up to 100 pN, which corresponds to roughly 10 000 times the bodyweight of *N. gonorrhoeae* [202]. Summing up the forces due to bundle formation of  $\sim 10$  pili produces a total force in the nanonewton range [203]. The distribution for the length of Tfp is exponential with a mean of  $0.9 \mu\text{m}$  [204], and pili as long as  $30 \mu\text{m}$  have been witnessed [203].

A gonorrhea infection comes along with the attachment of gonococci to the epithelial cells of the urethra. The bacteria do not only interact with the infected host cells by biochemical means, but also exert physical stress [205]. As a consequence, the stress triggers gene expression, rearrangements of the cytoskeleton, and the production of “cortical plaques”, *i.e.* the local recruitment of various proteins underneath microcolonies.

Higashi *et al.* investigated the clustering dynamics of gonococci in their natural environment on human epithelial cells [205]. They observed that within a few hours, symmetric, dome-shaped microcolonies formed, which were still motile. Contrary observations are made for mutants lacking Tfp: Gonococci without pili do not form any microcolonies; they do not interact with each other and move only as a result of thermal fluctuations [206]. This strongly suggests that Tfp indeed provide the only means of motility for *N. gonorrhoeae* cells.

These observations also indicate that the clustering is driven by Tfp. For this reason, we experimentally analyze the aggregation of wild-type cells on a surface. We address the question, whether “pili-taxis”, namely the pili-induced attraction between cells, is sufficient for explaining the clustering dynamics of gonococci, and chemotaxis is not required in particular. Our experimental findings will be supported by modeling and numerical simulations.

## 7.2 Experimental setup and results

Dr. Nicolas Biais and I designed and performed the experiments in the biological lab of Prof. Michael Sheetz at Columbia University. Bacteria are grown on GCB (gonococcal broth) medium agar plates in an incubator at  $37^\circ\text{C}$  and 5% CO<sub>2</sub> for 15 to 17 hours. Before an experiment, cells are resuspended in liquid GCB medium and their density is assessed by an optical densitometry measurement. Cells are then diluted in DMEM liquid medium at the concentration of  $5 \times 10^7$  cells in 2 ml. This volume of 2 ml is added in the 35 mm well of a six-well plate. The number of  $5 \times 10^7$  bacteria on a circular area with 35 mm diameter yields an initial cell density of  $0.052 \mu\text{m}^{-2}$ . Idealizing a single bacterium as a disk of radius  $a_0 = 0.6 \mu\text{m}$  (and area  $\pi a_0^2 = 1.13 \mu\text{m}^2$ ) gives an initial area fraction of  $\rho_0 \sim 6\%$ . Bacteria are observed with an optical microscope and the observation area usually comprises a region of  $350 \mu\text{m} \times 262 \mu\text{m}$ . The analysis of images and movies is performed with

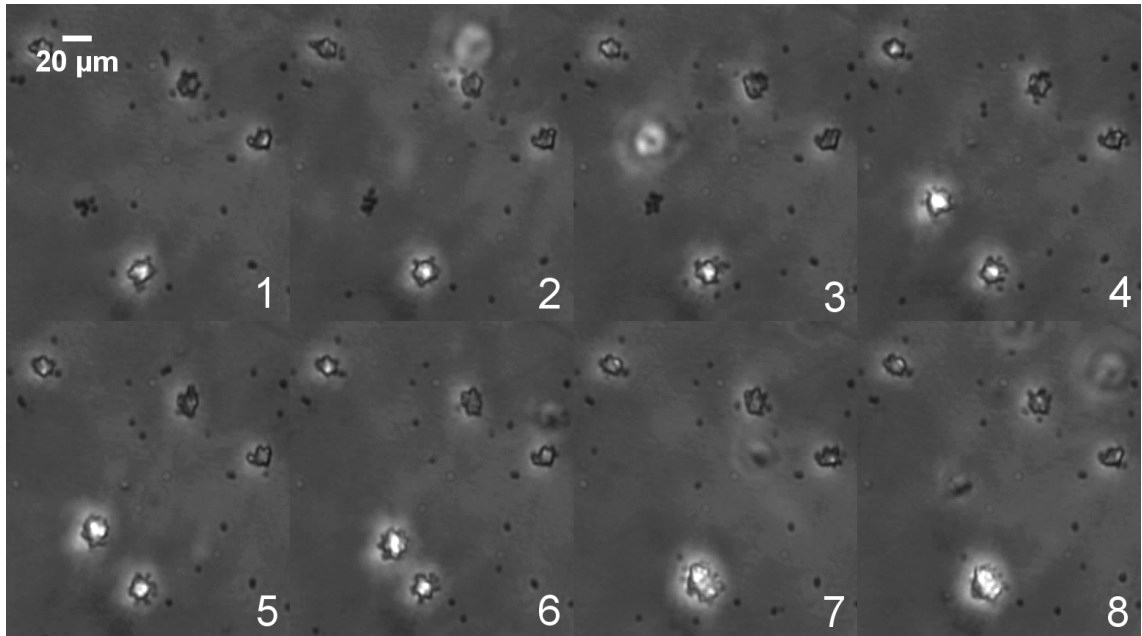


**Figure 7.1** ■ A microcolony of *N. gonorrhoeae* cells comes “from the third dimension” above the focal plane, settles down to the surface, and merges into a larger aggregate. The entering microcolony first emerges on the top right of the second frame. The time interval between two images is 5 s.

the software ImageJ [207]; we describe technical details in Sec. 7.2.2. To obtain a quasi-two-dimensional system, the bacteria are sedimented by centrifugating the plate at  $4000 \times g$  for 5 min. The snapshots in Fig. 7.1 are recorded without prior sedimentation: A cluster of gonococci suddenly emerges “from the third dimension” above the focal plane and settles down to the surface, where it merges with another microcolony into a larger, spherically symmetric aggregate.

Note that the pili-mediated forces are so strong that clustering is not prevented during centrifugation. As a consequence, when microscopy starts, clustering has already begun, and small aggregates of several diplococci already exist. Moreover, as we adjust the microscope’s focus manually after the first  $\sim 30$  min of observation, for all presented data the time  $t = 0$  corresponds to that readjustment; therefore, we observe even fewer small aggregates of *N. gonorrhoeae* cells.

### 7.2.1 Clustering dynamics

Figure 7.2 shows the clustering at three different times  $t = 0$ , 74.2 min, and 174.5 min. After about three hours of observation, we obtain a distribution of rather circular symmetric microcolonies. We focus on the time evolution of three observables: The mean cluster size, number of aggregates, and area fraction covered by the cells. These observables are shown as functions of time on the right of Fig. 7.2. The mean

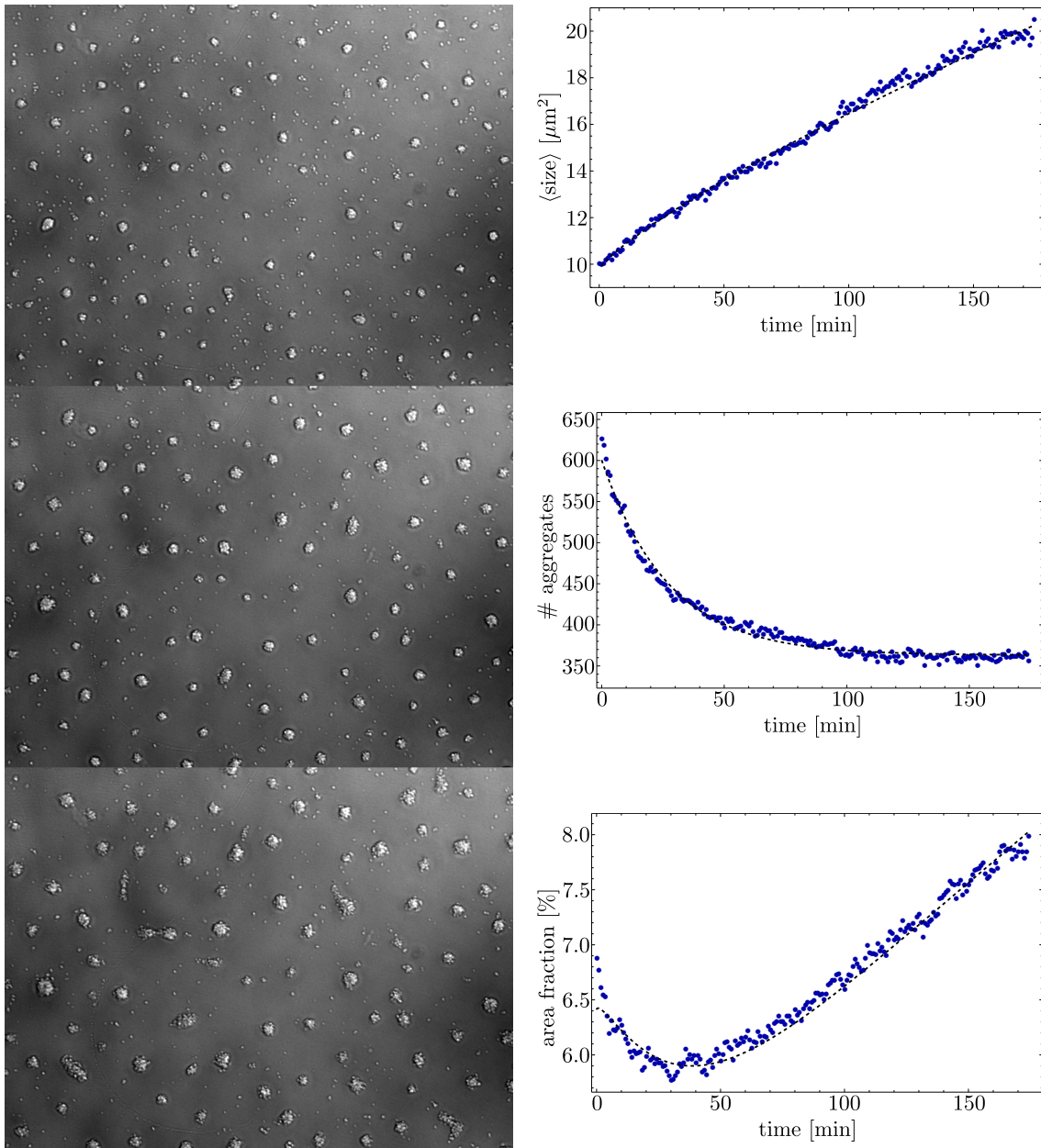
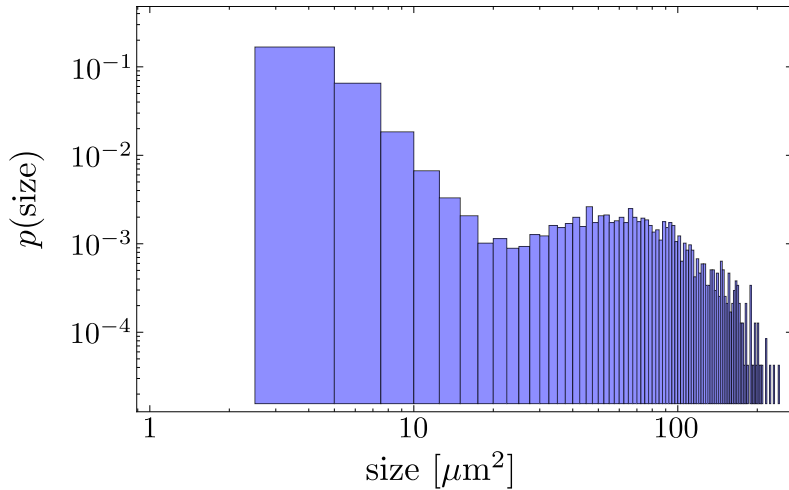


Figure 7.2 ■ Left: Formation of microcolonies of *N. gonorrhoeae* cells. The snapshots on a rectangle of size  $350 \mu\text{m} \times 262 \mu\text{m}$  are taken at times  $t = 0, 74.2 \text{ min}, 174.5 \text{ min}$  (from top to bottom). Right: Mean cluster size, number of aggregates, and area fraction are plotted as functions of time. The dashed lines are fitting functions:  $\langle \text{size} \rangle \sim 0.16 \times t^{0.81} + 9.78$ ;  $\# \text{ aggregates} \sim 237.4 \times e^{-t/27.1} + 363.1$  (notation without units). The fit of the area fraction is given by the product of the first two curves divided by the area  $350 \mu\text{m} \times 262 \mu\text{m}$ .



**Figure 7.3** ■ Probability density for the cluster size, as obtained by analyzing 20 different spatial regions of interest of one sample. For a typical distribution of aggregates, see the bottom picture of Fig. 7.2.

cluster size increases monotonically, whereas the total number of aggregates decays and finally reaches a steady state after  $t \sim 110$  min. The area fraction is the product of the mean cluster size and the number of aggregates, divided by the total area  $350 \mu\text{m} \times 262 \mu\text{m}$ . The area fraction has a minimum at  $t \sim 30$  min; it first decreases due to the formation of three-dimensional microcolonies, reaches a minimal value, and continuously increases afterwards. As the total number of aggregates does not increase, this increase of area fraction has to be due to cell growth.

Note that the mean cluster size is approximately fitted by a power law with exponent smaller one, see the dashed line in Fig. 7.2. In contrast, the decay in the number of aggregates can be described by a shifted exponential and gives a characteristic relaxation time of  $\sim 27$  min for the clustering process.

To obtain a better statistics for the distribution of cluster sizes, we repeated the experiment and after three hours recorded images of 20 different spatial regions. The normalized probability distribution of cluster sizes is shown as a double-logarithmic plot in Fig. 7.3. It contains a large peak corresponding to relatively small aggregates of size  $\lesssim 10 \mu\text{m}^2$ . In addition, we observe a second peak at  $\sim (50 \dots 60) \mu\text{m}^2$ ; it corresponds to the average size of the microcolonies, which are clearly visible by eye in Fig. 7.2. The large standard deviation  $32.3 \mu\text{m}^2$  compared to the mean cluster size of  $17.2 \mu\text{m}^2$  reflects the width of the distribution.

### 7.2.2 Image analysis

In this section, we briefly sketch how we analyzed the experimental data with the help of the software ImageJ [207]. Our experiments with *N. gonorrhoeae* were per-

formed with the strain MS11. Imaging was achieved by performing phase contrast microscopy with an inverted Olympus IX81 microscope set-up with a coolsnap digital camera, providing grayscale images as shown on the left of Fig. 7.2.

To obtain data for the number and sizes of aggregates, the images need to be converted to binary pictures. To arrive at a sufficient quality, several ImageJ processes were systematically run and manually optimized. For image manipulation, we applied the following options: “smooth”, “find edges”, “subtract background”, and “make binary”. Afterwards, a combination of the procedures “fill holes”, “dilate”, and “erode” was used. This processing is necessary to determine the correct area covered by clusters. Large clusters are often captured by donut-shaped objects. The total area of the cluster would then be determined incorrectly, and only after filling the “donut’s hole” the correct area is found. Finally, the graphs of Fig. 7.2 were generated with the software Mathematica.

To obtain the mean-squared displacement of clusters, as required for the diffusion coefficients from Fig. 7.4 below, we recorded movies of several minutes duration with a time resolution of 50 Hz. After the conversion to binary images, particle tracking was done with the ImageJ plugin MTrack2, which enables the tracking of clusters within a certain size range.

## 7.3 Modeling of “pili-taxis”

In the following, we construct a model, based on the diffusion and aggregation of clusters, to understand the dynamics of the experimentally observed clustering of *N. gonorrhoeae* cells.

Our model microcolonies are spheres that move on a flat surface and appear as disks in a two-dimensional projection. Each particle or bacterial aggregate  $i$  is represented by its position vector  $\mathbf{r}_i = (x_i, y_i)$  and radius  $a_i$ . We assume that the motion of each particle is described by an overdamped Langevin equation [Eq. (2.23)],

$$\frac{d}{dt} \mathbf{r}_i(t) = \sqrt{2D_i} \boldsymbol{\Gamma}_i(t), \quad (7.1)$$

where  $\boldsymbol{\Gamma}_i(t)$  is uncorrelated Gaussian white noise with  $\langle \boldsymbol{\Gamma}_i(t) \rangle = \mathbf{0}$  and  $\langle \Gamma_i^\alpha(t) \Gamma_j^\beta(t') \rangle = \delta_{ij} \delta_{\alpha\beta} \delta(t - t')$ . In general, the diffusion coefficient  $D_i$  of each aggregate depends on its radius  $a_i$ .

### 7.3.1 Diffusion coefficient as a function of cluster size

In analogy to the Stokes-Einstein relation for a freely diffusing Brownian particle,  $D = k_B T / (6\pi\eta a)$  [Eq. (2.8)], one might first assume the scaling  $D_i = D_0 a_0 / a_i$ . Here, we consider  $D_0$  as the diffusion coefficient of a single particle with size  $a_0$ , and  $D_0$  is not necessarily related to the thermal energy any longer.

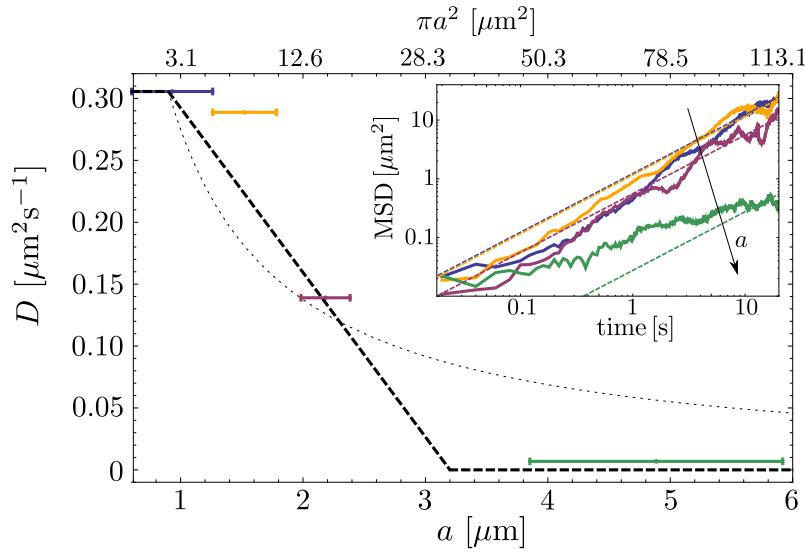


**Figure 7.4** ■ Diffusion coefficient  $D$  as a function of cluster radius  $a$ . The thick dashed line is the linear function from Eq. (7.2) with  $D_0 = 0.31 \mu\text{m}^2 \text{s}^{-1}$ ,  $a_s = 0.9 \mu\text{m}$ , and  $a_{\text{cut}} = 3.2 \mu\text{m}$ . For comparison, the thin dashed line is the Stokes-Einstein scaling  $\sim a^{-1}$ . The inset shows the corresponding mean-squared displacements versus time  $t$ , which are fitted by  $4Dt$  (dashed lines).

However, a quick estimate of the diffusion coefficients for the experimentally observed cluster sizes reveals that the Stokes-Einstein scaling predicts too large values for big cell aggregates. According to Fig. 7.3, the minimal and maximal cluster sizes are approximately  $A_{\min} \sim 1 \mu\text{m}^2$  and  $A_{\max} \sim 200 \mu\text{m}^2$ , respectively. Assuming circular aggregates of radius  $a = \sqrt{A/\pi}$ , the corresponding radii are  $a_{\min} \sim 0.5 \mu\text{m}$  and  $a_{\max} \sim 8 \mu\text{m}$ , and the ratio of diffusion coefficients becomes  $D_{\max}/D_{\min} \sim a_{\max}/a_{\min} \sim 16$ . On the contrary, our analysis, summarized in Fig. 7.4, shows that diffusion decreases more quickly with radius and the ratio of diffusion coefficients clearly exceeds this order of magnitude.

We have estimated the diffusion coefficients  $D$  in Fig. 7.4 from a linear fit of the mean-squared displacement (see inset) of several cells, whose radii were binned in distinct intervals. For larger clusters with  $a \gtrsim 6 \mu\text{m}$ , the quality and amount of our experimental data is not sufficient to determine the cell diffusivity, as it becomes very small. Note that we assumed normal diffusion when fitting the mean-squared displacement and it is far beyond our scope to rule out subdiffusion. We emphasize that our goal only is to show that the diffusion coefficient  $D(a)$  decays more rapidly than with  $\sim a^{-1}$  according to the Stokes-Einstein scaling. A maximal diffusion coefficient of small clusters with  $a \lesssim 1.3 \mu\text{m}$  is estimated as  $D_0 = 0.31 \mu\text{m}^2 \text{s}^{-1}$ . This value is consistent with recent measurements for single cells of *N. gonorrhoeae* [208].

Instead of the Stokes-Einstein relation, we suggest a linear dependence for the diffusion coefficient that fits well the experimental data, and where the diffusion

coefficient  $D = D(a)$  becomes zero above the cut-off radius  $a_{\text{cut}} = 3.2 \mu\text{m}$ ,

$$D(a) = \begin{cases} D_0, & a \leq a_s, \\ D_0 \frac{a - a_{\text{cut}}}{a_s - a_{\text{cut}}}, & a_s \leq a \leq a_{\text{cut}}, \\ 0, & a > a_{\text{cut}}; \end{cases} \quad (7.2)$$

this dependence is plotted as the thick dashed line in Fig. 7.4. In this approximation, aggregates larger than  $\pi a_{\text{cut}}^2 \sim 32 \mu\text{m}^2$  are completely immobile and do not diffuse.

### 7.3.2 Cell growth

To take into account the growth of cells, we introduce the growth rate  $\lambda$  with which the total bacterial mass  $M$  increases exponentially according to

$$M(t) = M_0 e^{\lambda t}. \quad (7.3)$$

Using the mass density  $\rho_m$  and writing  $M \propto \rho_m a^3$ , the “radius”  $a(t)$  grows like

$$a(t) = a_0 e^{\frac{\lambda}{3}t}, \quad (7.4)$$

and the area fraction  $\propto a^2$  increases exponentially with rate  $\frac{2}{3}\lambda$ . In the following, each sphere of our model with radius  $a(t)$  will grow according to  $\frac{d}{dt} a(t) = \frac{\lambda}{3} a(t)$ , which is equivalent to Eq. (7.4). Hence, we need to know the growth rate  $\lambda$ .

According to Fig. 7.2, the number of aggregates is almost constant at times larger than 120 min. So, the increase of area fraction is due to cell growth. Within an interval of  $\Delta t = 50$  min, the area fraction changes from about 7% to 8%, which corresponds to an increase of 14.3%. Solving  $e^{\frac{2}{3}\lambda\Delta t} \sim 1.143$  for  $\lambda$ , we find the growth rate

$$\lambda \sim 6.7 \times 10^{-5} \text{ s}^{-1} \quad \text{or} \quad \lambda^{-1} \sim 249 \text{ min}. \quad (7.5)$$

This value is roughly consistent with an optical densitometry measurement; it provided the estimate that the cell density increases by about 20...30% within  $T \sim 3$  hours. Solving Eq. (7.3) for  $\lambda$ , i.e.  $e^{\lambda T} = 1.2 \dots 1.3$ , gives  $\lambda^{-1} \sim (686 \dots 987)$  min.

### 7.3.3 Merging rule for pili-mediated interaction

We propose a merging rule that respects mass and volume conservation in three dimensions. Note that mass conservation is the reason why each cell aggregate on the surface is better represented as a three-dimensional sphere instead of a two-dimensional disk. To mimic a uniform distribution of pili on the cell surface, we introduce a “shell” of width  $l_i$  around particle  $i$ , where  $l_i$  represents the length of pili. As the length of pili is exponentially distributed [204], we assume a constant

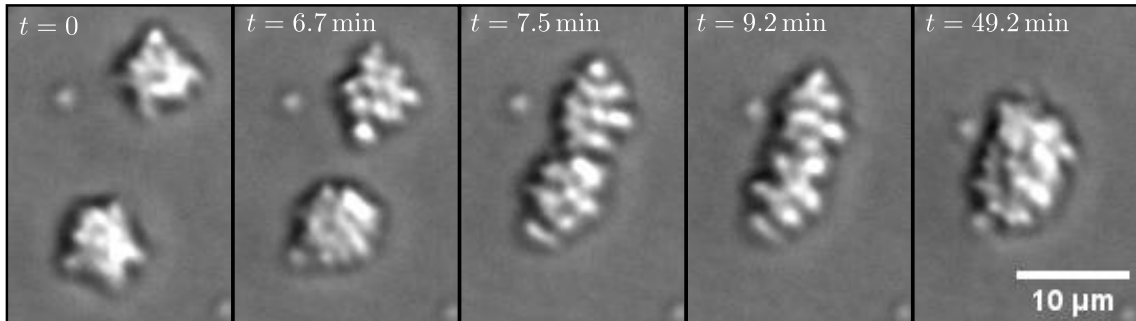


Figure 7.5 ■ Two large microcolonies merge into an aggregate that finally tends to an almost spherical shape.

pilus length  $l_0$  for simplicity. The pili-mediated merging of colonies occurs as follows. If the shells of two particles, labeled as 1 and 2, are in contact,

$$|\mathbf{r}_1 - \mathbf{r}_2| < a_1 + a_2 + 2l_0 , \quad (7.6)$$

both particles can merge into a new sphere with radius

$$a_{12} = \sqrt[3]{a_1^3 + a_2^3} , \quad (7.7)$$

whose center-of-mass  $\mathbf{r}_{12}$  is given by the weighted average

$$\mathbf{r}_{12} = \frac{a_1}{a_1 + a_2} \mathbf{r}_1 + \frac{a_2}{a_1 + a_2} \mathbf{r}_2 . \quad (7.8)$$

Note that volume conservation in three dimensions implies that –in a system without cell growth– the area fraction during clustering is not conserved. Next, we take into account that clustering does not happen instantaneously, as the growth of pili requires a characteristic time after which cells can merge. In other words, the cells need some “time for shaking hands” and merging becomes a dynamical process. For two aggregates in contact, we therefore introduce a waiting time as a random variable with exponential distribution and mean waiting time  $T_w$ . If two aggregates satisfy Eq. (7.6), the probability  $P$  of merging within a small time interval  $\Delta t \ll T_w$  becomes

$$P = \Delta t / T_w . \quad (7.9)$$

We will determine  $T_w$  to match simulation and experimental results, which is in the order of minutes. Altogether, exponentially distributed waiting times imply that merging occurs only with a certain probability, and two nearby aggregates can also separate again by diffusion without having merged.

To proceed, we comment on additional observations on the clustering. The first picture of Fig. 7.5 shows two large microcolonies whose distance between the outer

edges is  $\sim 8 \mu\text{m}$ . We notice that both aggregates remain relatively immobile for quite a long time until the cells attract and start to merge into one larger cluster. Figure 7.5 also shows a tiny aggregate, the small spot left from the upper microcolony, which hardly moves, and in particular, does not merge with the nearby cluster. Further observations also suggest that binding of small aggregates to a large microcolony is not always irreversible.

The large number of non-merging, small aggregates is also visible in Fig. 7.2 and strongly dominates the size distribution in Fig. 7.3. Therefore, we will include this fact into our model as well; to keep the interactions between cells as simple as possible, we will fix a certain number  $m_p$  of small aggregates as immobile that are unable to merge at all, but grow with the same rate as the common cells. These “passive” cells amount to  $\sim 45\%$  of all cells.

## 7.4 Comparison of experimental and numerical results

We perform numerical simulations of our model with periodic boundary conditions on a rectangular surface of the same size as in the experiment ( $350 \mu\text{m} \times 262 \mu\text{m}$ ), and for the same duration of 3 hours. The initial configuration for  $t = 0$  is generated from the initial experimental data, and we approximate each aggregate of area  $A$  by a sphere of radius  $a = \sqrt{A/\pi}$ . Simulations start with a total number of  $m_0 = 629$  aggregates, and we select the smallest  $m_p = 285$  particles as the “passive” ones. The diffusion coefficient of cell aggregates is modeled using the linear estimate, as presented in Fig. 7.4.

To match the experimental data, we adjusted the waiting time as  $T_w = 16.7 \text{ min}$  and the pili length as  $l_0 = 3.2 \mu\text{m}$ . The simulation results are shown in Fig. 7.6. The curves for the mean cluster size, number of aggregates, and area fraction demonstrate a nice agreement between simulation and experiment. In particular, our model features the plateau in the number of aggregates for large times, which –together with the monotonically increasing mean cluster size– results in a minimum of the area fraction at small intermediate times. Yet, in the simulation, the minimum of the area fraction is less pronounced and shifted to a slightly larger time. In addition to the agreement of the final mean cluster size  $\sim (20 \dots 21) \mu\text{m}^2$  between simulation and experiment, the spatial distributions of aggregates also look similar, see Fig. 7.2 and Fig. 7.6.

Finally, we note that our simulation also includes the merging between large clusters. This effect is illustrated by the corresponding snapshots in Fig. 7.7, which strongly resembles the experimentally observed process from Fig. 7.5. As the merging probability according to Eq. (7.9) makes clustering a dynamical process, the aggregates merge only after some time.

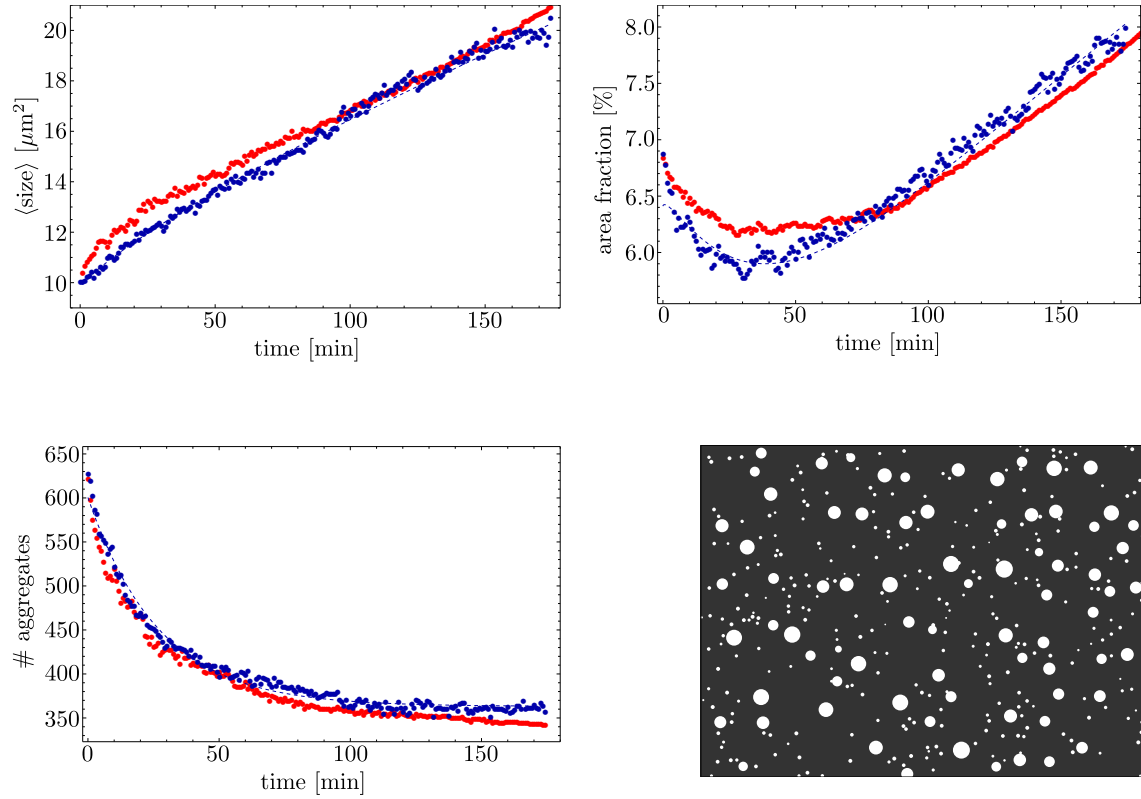


**Figure 7.6** ■ Comparison of simulation results (red curves) to the experimental data points (blue). The spatial distribution of aggregates from the simulation is shown for the maximal time  $t = 180$  min. The initial conditions for simulations are taken from the experiment with 629 particles, with 344 “active” and  $m_p = 285$  “passive” particles. Parameters:  $\lambda = 6.7 \times 10^{-5} \text{ s}^{-1}$ ,  $D_0 = 0.3 \mu\text{m}^2 \text{ s}^{-1}$ ,  $a_s = 0.9 \mu\text{m}$ ,  $a_{\text{cut}} = 3.2 \mu\text{m}$ ,  $l_0 = 3.2 \mu\text{m}$ ,  $T_w = 16.7$  min.

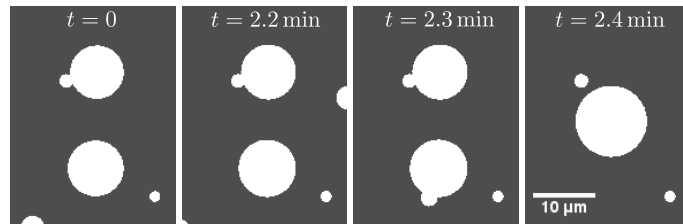


**Figure 7.7** ■ Merging of two large microcolonies as observed in the same simulation for which the clustering dynamics is analyzed in Fig. 7.6. Note that each snapshot also contains two “passive” particles, which are completely immobile and unable to merge.

## 7.5 Summary

We studied the cluster formation of *N. gonorrhoeae* bacteria on a plastic surface. Prerequisites for clustering are the surface attachment and motility of cells; both are provided by type IV pili.

The analysis of our experimental data was focused on the time evolution of the mean cluster size, total number of clusters, and area fraction covered by the cells. Motivated by the experimental results, we wanted to test whether we could account for the observed clustering only by the pili-mediated attraction between cells. We built a physical model based on various experimental results and a few simplifying assumptions; the model features the diffusive motion of small aggregates, cell growth, and a merging rule to account for the clustering dynamics. Our simulation results agree well with the experiment.

As the experimentally observed clusters predominantly show spherical symmetry, we restricted our model to spherical or disk-like aggregates. Recall that we have already encountered spherical aggregates of microorganisms in this thesis; in Chapter 5.4, we have seen that a strong autochemotactic attraction also results in the formation of symmetrical clusters. Here, our “pili-taxis” model was able to reproduce the observed clustering of *N. gonorrhoeae* cells. We therefore consolidate the hypothesis that clustering in *N. gonorrhoeae* is mediated by type IV pili. Yet, to complete the “proof”, follow-up experiments with non-chemotactic mutants are required. Only if the same dynamics is observed, chemotaxis can definitely be ruled out. However, it will be challenging to create a totally chemotactic-free mutant, as each strain of *N. gonorrhoeae* has plenty of different chemotactic pathways, which are still regularly discovered [206]. In contrast, experiments with pili-lacking mutants will be less appropriate, as those cells cannot even attach to the surface.

Though our model already explains the experimental data, our study offers several experimental and theoretical follow-up projects to provide a more detailed understanding of the clustering dynamics. It will be interesting to accurately relate the motion of clusters to their size. In a detailed study, one should first determine whether the diffusive motion of large clusters is indeed normal or anomalous. One might investigate how the pili create “friction” with the surface, and how it affects motility as a function of cluster size.

Further progress can be made on the model assumptions. The introduced characteristic waiting time for merging depends probably on the cluster size. One could develop microscopic models for the interaction between pili. In the appendix of Sec. 7.6, we sketch a possible realization, where two cells with a given distance merge due to pili contact only with a certain probability. On the experimental side, one should determine the fraction of immobile or “passive” cells. In the future, it will also be interesting to resolve the dynamics of individual pili, and thus study the clustering process on a more fundamental level.

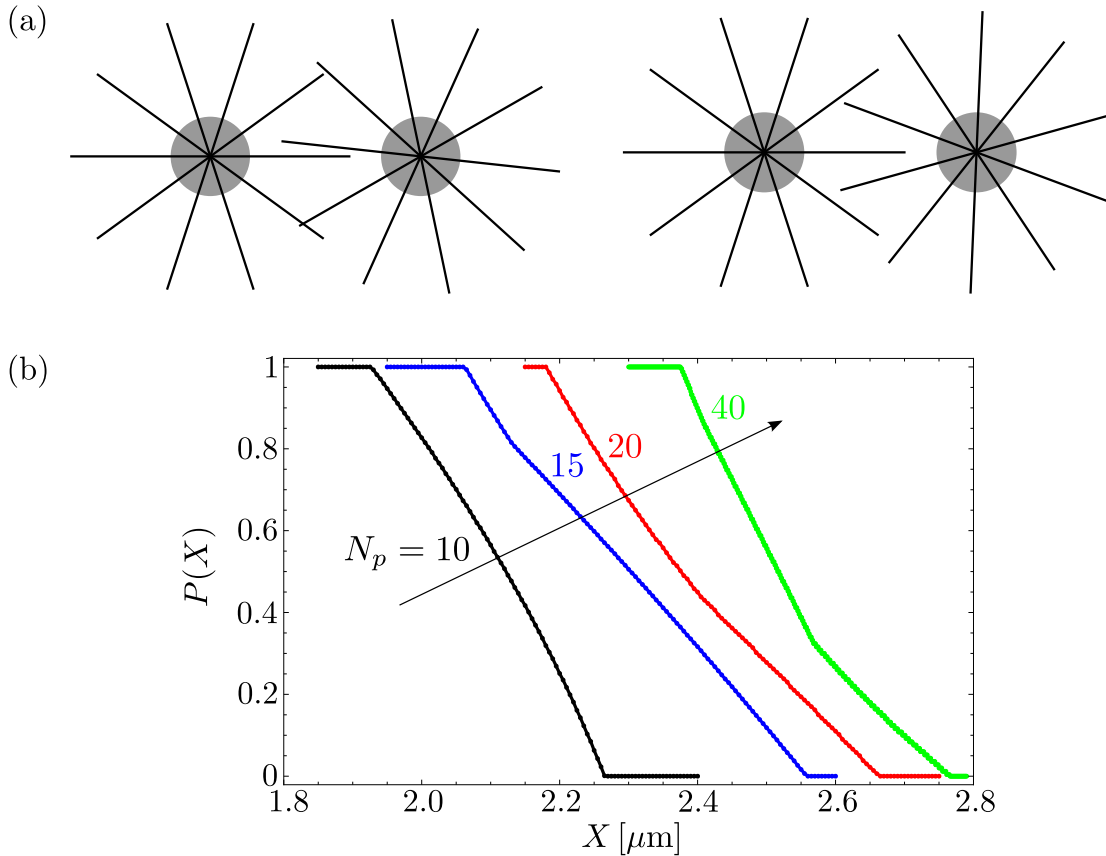


Figure 7.8 ■ (a) Two different configurations of cells with (left) and without (right) contact of pili for  $N_p = 10$  and  $X = 2.12 \mu\text{m}$ . (b) The probability  $P(X)$  of pili intersection as a function of distance  $X$  is shown for different number of pili  $N_p = 10, 15, 20, 40$ , while  $a_0 = 0.4 \mu\text{m}$  and  $l_0 = 1 \mu\text{m}$  are constant.

## 7.6 Appendix: A different model for pili-mediated cluster interaction

Here, we propose a more detailed model for the interaction between pili. For two cells with a certain distance, we determine the probability that at least one pair of pili is in contact, such that the cells merge into a larger cluster.

We consider two gonococci as disks with minimal radius  $a_0$  and assume that  $N_p$  pili of length  $l_0$  are uniformly distributed over the surface of each disk. As sketched in Fig. 7.8(a), a pilus is a straight line, which is fixed perpendicular to the surface. For given distance  $X$  between the two disks, it depends on the relative orientation of all pili whether at least one pair intersects. Considering the relative orientation as a randomly distributed angle, we determine the probability  $P(X)$  for pili intersection as a function of the distance  $X$ . The model is thus based

on the geometrical arrangement of pili. In Fig. 7.8(b), we plot  $P(X)$  for  $a_0 = 0.4 \mu\text{m}$  and  $l_0 = 1 \mu\text{m}$  and vary the number of “effective pili”  $N_p = 10, 15, 20, 40$ . The probability approximately increases linearly with decreasing particle distance; a larger  $N_p$  clearly enhances the probability for intersection at larger distances. For a larger pilus length,  $l_0 = 2 \mu\text{m}$ , the probabilities look similar and are shifted to larger distances (not shown).

As an outlook, we generalize this approach for larger cells and clusters. So far, the distance between two neighboring pili on a disk’s surface is  $s_0 = \frac{2\pi}{N_p} a_0$ . If we require a constant density of pili, *i.e.*  $s_0$  is constant for all cell sizes, we end up with a size-dependent pili number  $N_p a_N = N_p a_0 \sqrt[3]{N}$ , where  $N$  is the number of single cells in a cluster of radius  $a_N$ . In the future, the presented probabilities can be implemented in our model, and replace the merging probability, which we introduced phenomenologically in Eq. (7.9).

# 8 Conclusions

This thesis contributes to the understanding of the initial stages of biofilm formation. The formation of a biofilm is a complex interplay of numerous biological, chemical, and physical processes. Therefore, we analyzed fundamental aspects independently from a perspective of statistical physics.

The swimming strategies of freely diffusing bacteria are described as random walks: “run-and-tumble” of *E. coli*, “run-reverse” of the biofilm-forming pathogen *P. aeruginosa*, or the recently discovered “run-reverse-flick” of *V. alginolyticus*. To capture these diverse patterns in a single model, we developed a generalized random walk, where “runs” are alternately interrupted by two distinct “tumbling” events. For this generalized strategy, we were able to analytically determine the mean-squared displacement of a swimmer and its diffusion coefficient. Thereby, our rigorous calculation corrects former simpler estimates for the diffusion coefficient of *V. alginolyticus* [110, 111, 112]. As a distinctive feature of the generalized random walk, we derived an analytical expression for the directional correlation function. Using our result, the analysis of an experimentally obtained correlation function may help to deduce the swimming strategy of a bacterial species.

Cells that swim in the gradient of a chemical substance can perform chemotaxis and move to regions of higher or lower chemical concentration, *e.g.* towards food sources. Temporal sensing of the concentration and a genetic chemotactic pathway make the cells swim along the gradient with a “chemotactic drift velocity”, which serves as a common measure for the chemotactic efficiency of cells. While the chemotactic drift speed for “run-and-tumble” motion was determined in Refs. [94, 96], we computed the chemotactic drift of a “run-tumble-flick” swimmer perturbatively for a small gradient. As conclusion, there is no significant difference in the resulting chemotactic drift speed for both swimming strategies.

Once microorganisms have attached to a surface, communication among the cells initiates the formation of microcolonies. Certain cells produce chemicals themselves, to which they respond chemotactically. Prominent examples for “autochemotaxis” comprise the bacteria *E. coli*, *S. typhimurium*, and the amoeba *D. discoideum*. They inspired us to construct a model for autochemotactic microorganisms. We treat them as active walkers, which align their velocity direction along the gradient of a self-generated chemical field. Our model for autochemotactic signaling between cells allows for the formation of microcolonies, as observed in experiments for different

## 8 Conclusions

---

microorganisms. We showed that a large chemotactic attraction results in the formation of spherical cell aggregates. Furthermore, the microorganisms of our model require a minimal cell density to start clustering, which is fully consistent with experimental results as well. To investigate the stability of a two-particle cluster, we determined its “mean life time” and found a remarkable analogy to Kramers’ escape rate. We created the basis for future studies of a large number of autochemotactic microorganisms, *i.e.* for the thermodynamic limit, by deriving a kinetic equation, upon which a continuum version of the model is established.

In the literature, the question was posed whether “self-trapping” of a single autochemotactic cell occurs, if it is attracted to its own secreted chemical. Our autochemotactic walker was found to always diffuse for large times, though the diffusion coefficient may be reduced by several orders of magnitude for strong coupling. Moreover, we worked out two theories, for weak and strong chemotactic coupling strength, that describe the non-Markovian dynamics of an isolated microorganism. Thereby, we obtained analytical expressions for the diffusion coefficient of the walker, which are in very good agreement with our numerical results. For a strong coupling to the chemoattractant, the walker’s trajectory consists of noisy circles. Interestingly, similar dynamics have recently been reported for the swimming nematode *C. elegans* [154]; it is thus fascinating to check whether *C. elegans* could be a natural realization of our autochemotactic walker.

The communication between cells via diffusing chemicals is not the only process that results in the formation of cell aggregates. Cell appendages, type IV pili, enable the bacterium *N. gonorrhoeae* to firmly attach to and move on surfaces by means of “twitching motility”. The medical interest in *N. gonorrhoeae* bacteria is evident as microcolonies attached to the human urethra cause the disease gonorrhea; from a scientific point of view, *N. gonorrhoeae* serves as a model system for studying type IV pili. We hypothesize that cluster formation in *N. gonorrhoeae* can be solely explained by local cell-to-cell interactions via pili, and no chemotaxis is required. If this holds true, it might motivate to develop alternative strategies to prevent surface attachment of *N. gonorrhoeae* that take into account the physics of pili instead of biochemistry.

To test our hypothesis, we performed experiments with *N. gonorrhoeae* cells that are initially spread on a surface and form microcolonies after several hours. In addition to mapping the mean cluster size and total number of aggregates over time, our analysis provided an estimate how the motility of a cluster decreases with its increasing size. To investigate whether clustering is solely explained by a pili-mediated interaction, we developed a “pili-taxis” model for cell aggregation and performed numerical simulations. Inserting the parameters measured in our experiments, the model reproduces the experimentally obtained clustering dynamics. Although subsequent experiments with non-chemotactic mutants are required to confirm our hypothesis, our result strongly suggests that the pili-mediated inter-

---

action is sufficient to explain cluster formation in *N. gonorrhoeae* bacteria.

In conclusion, we studied random walk strategies of swimming bacteria, chemotactic signaling between model microorganisms, and pili-induced clustering of bacterial cells. All these aspects have a strong impact on early stages of biofilm formation. In the future, we hope that our approaches and results contribute to a larger, comprehensive picture of biofilm formation that is firmly based on a statistical physics description.



# List of Publications

## Related to this work

- [A] Johannes Taktikos, Vasily Zaburdaev, and Holger Stark  
Collective dynamics of model microorganisms with chemotactic signaling  
Physical Review E **85**, 051901 (2012)
- [B] Johannes Taktikos, Vasily Zaburdaev, and Holger Stark  
Modeling a self-propelled autochemotactic walker  
Physical Review E **84**, 041924 (2011)

## Other publications

- [C] Johannes Taktikos and Hans Behringer  
Dry and wet interfaces: Influence of solvent particles on molecular recognition  
Physical Review E **79**, 041908 (2009)
- [D] Maximilian Zieringer, Marçal Casas Cartagena, Ewelina Burakowska,  
Johannes Taktikos, Katja Neuthe, Heinz Bandmann, Frank-Gerrit Klärner,  
and Rainer Haag  
Polyglycerol-tagged molecular clips as receptors in protic solvents  
European Journal of Organic Chemistry **2013**, 362 (2013)

## Diploma thesis

- [E] Johannes Taktikos  
Einfluss von Lösungsmittelteilchen bei molekularen Erkennungsprozessen  
Diplomarbeit, Fakultät für Physik, Universität Bielefeld (2008)



# Bibliography

- [1] L. Hall-Stoodley, J. W. Costerton, and P. Stoodley. Bacterial biofilms: From the natural environment to infectious diseases, *Nature Reviews Microbiology*, **2**, 95–108, (2002).
- [2] G. O'Toole, H. B. Kaplan, and R. Kolter. Biofilm formation as microbial development, *Annual Review of Microbiology*, **54**, 49–79, (2000).
- [3] R. M. Donlan and J. W. Costerton. Biofilms: Survival mechanisms of clinically relevant microorganisms, *Clin. Microbiol. Rev.*, **15**, 167–193, (2002).
- [4] R. Singh, D. Paul, and R. K. Jain. Biofilms: Implications in bioremediation, *Trends in Microbiology*, **14**, 389–397, (2006).
- [5] E. Karunakaran, J. Mukherjee, B. Ramalingam, and C. Biggs. “Biofilmology”: A multidisciplinary review of the study of microbial biofilms, *Applied Microbiology and Biotechnology*, **90**, 1869–1881, (2011).
- [6] H.-C. Flemming and J. Wingender. The biofilm matrix, *Nature Reviews Microbiology*, **8**, 623–633, (2010).
- [7] C. Fux, J. Costerton, P. Stewart, and P. Stoodley. Survival strategies of infectious biofilms, *Trends in Microbiology*, **13**, 34–40, (2005).
- [8] M. Eisenbach, *Chemotaxis*. Imperial College Press, (2004).
- [9] M. B. Miller and B. L. Bassler. Quorum sensing in bacteria, *Annual Review of Microbiology*, **55**, 165–199, (2001).
- [10] D. E. Bradley. A function of *Pseudomonas aeruginosa* PAO polar pili: Twitching motility, *Canadian Journal of Microbiology*, **26**, 146–154, (1980).
- [11] A. J. Merz, M. So, and M. P. Sheetz. Pilus retraction powers bacterial twitching motility, *Nature*, **407**, 98–102, (2000).
- [12] P. Watnick and R. Kolter. Biofilm, city of microbes, *J. Bacteriol.*, **182**, 2675–2679, (2000).
- [13] O. Wanner and W. Gujer. A multispecies biofilm model, *Biotechnology and Bioengineering*, **28**, 314–328, (1986).

## Bibliography

---

- [14] E. Alpkvist, C. Picioreanu, M. C. van Loosdrecht, and A. Heyden. Three-dimensional biofilm model with individual cells and continuum EPS matrix, *Biotechnology and Bioengineering*, **94**, 961–979, (2006).
- [15] J. K. G. Dhont, *An Introduction to Dynamics of Colloids*. Elsevier, (1996).
- [16] C. Gardiner, *Stochastic Methods: A Handbook for the Natural and Social Sciences*. Springer, 4 ed., (2009).
- [17] N. Pottier, *Nonequilibrium Statistical Physics*. Oxford University Press, (2010).
- [18] H. Risken, *The Fokker-Planck Equation*. Springer, 2 ed., (1996).
- [19] D. Zwillinger, *Handbook of Differential Equations*. Academic Press, 3 ed., (1997).
- [20] F. Schwabl, *Statistische Mechanik*. Springer, (2000).
- [21] S. I. Denisov, W. Horsthemke, and P. Hänggi. Generalized Fokker-Planck equation: Derivation and exact solutions, *EPJ B*, **68**, 567–575, (2009).
- [22] J. Dunkel and P. Hänggi. Relativistic Brownian motion, *Physics Reports*, **471**, 1–73, (2009).
- [23] J. Honerkamp, *Stochastic Dynamical Systems: Concepts, numerical methods, data analysis*. Wiley, (1994).
- [24] W. Horsthemke and R. Lefever, *Noise-Induced Transitions*. Springer, (1984).
- [25] P. E. Kloeden and E. Platen, *Numerical Solution of Stochastic Differential Equations*. Springer, (1992).
- [26] Y. L. Klimontovich. Nonlinear Brownian motion, *Physics Uspekhi*, **164**, 737–766, (1994).
- [27] H. A. Kramers. Brownian motion in a field of force and the diffusion model of chemical reactions, *Physica*, **7**, 284–304, (1940).
- [28] W. Paul and J. Baschnagel, *Stochastic Processes: From Physics to Finance*. Springer, (2000).
- [29] P. Langevin. Sur la théorie du mouvement brownien, *C. R. Acad. Sci.*, **146**, 530–533, (1908).
- [30] B. Øksendal, *Stochastic Differential Equations: An Introduction with Applications*. Springer, 6 ed., (2003).

- 
- [31] G. Amselem, M. Theves, A. Bae, E. Bodenschatz, and C. Beta. A stochastic description of Dictyostelium chemotaxis, *PLoS ONE*, **7**, e37213, (2012).
  - [32] D. Selmeczi, S. Mosler, P. H. Hagedorn, N. B. Larsen, and H. Flyvbjerg. Cell motility as persistent random motion: Theories from experiments, *Biophys. J.*, **89**, 912–931, (2005).
  - [33] K. Przibram. Über die ungeordnete Bewegung niederer Tiere, *Pflügers Archiv European Journal of Physiology*, **153**, 401–405, (1913).
  - [34] J. Perrin. Mouvement brownien et réalité moléculaire, *Annales de Chimie et de Physique*, **8**, 5–114, (1909).
  - [35] H. C. Berg, *Random Walks in Biology*. Princeton University Press, (1993).
  - [36] E. Lauga and T. R. Powers. The hydrodynamics of swimming microorganisms, *Reports on Progress in Physics*, **72**, 096601, (2009).
  - [37] R. Metzler and J. Klafter. The random walk’s guide to anomalous diffusion: A fractional dynamics approach, *Physics Reports*, **339**, 1–77, (2000).
  - [38] M. Weiss, M. Elsner, F. Kartberg, and T. Nilsson. Anomalous subdiffusion is a measure for cytoplasmic crowding in living cells, *Biophys. J.*, **87**, 3518–3524, (2004).
  - [39] I. Y. Wong, M. L. Gardel, D. R. Reichman, E. R. Weeks, M. T. Valentine, A. R. Bausch, and D. A. Weitz. Anomalous diffusion probes microstructure dynamics of entangled F-actin networks, *Phys. Rev. Lett.*, **92**, 178101, (2004).
  - [40] E. A. Codling, M. J. Plank, and S. Benhamou. Random walk models in biology, *J. R. Soc. Interface*, **5**, 813–834, (2008).
  - [41] F. Schweitzer, W. Ebeling, and B. Tilch. Complex motion of Brownian particles with energy depots, *Phys. Rev. Lett.*, **80**, 5044–5047, (1998).
  - [42] F. Schweitzer, *Brownian Agents and Active Particles. Collective Dynamics in the Natural and Social Sciences*. Springer, (2003).
  - [43] P. Romanczuk, M. Bär, W. Ebeling, B. Lindner, and L. Schimansky-Geier. Active Brownian particles, *EPJ ST*, **202**, 1–162, (2012).
  - [44] M. Schienbein and H. Gruler. Langevin equation, Fokker-Planck equation and cell migration, *Bull. Math. Biol.*, **55**, 585–608, (1993).
  - [45] F. Peruani and L. G. Morelli. Self-propelled particles with fluctuating speed and direction of motion in two dimensions, *Phys. Rev. Lett.*, **99**, 010602, (2007).

## Bibliography

---

- [46] T. Vicsek, A. Czirók, E. Ben-Jacob, I. Cohen, and O. Shochet. Novel type of phase transition in a system of self-driven particles, *Phys. Rev. Lett.*, **75**, 1226–1229, (1995).
- [47] N. Shimoyama, K. Sugawara, T. Mizuguchi, Y. Hayakawa, and M. Sano. Collective motion in a system of motile elements, *Phys. Rev. Lett.*, **76**, 3870–3873, (1996).
- [48] M. R. D’Orsogna, Y. L. Chuang, A. L. Bertozzi, and L. S. Chayes. Self-propelled particles with soft-core interactions: Patterns, stability, and collapse, *Phys. Rev. Lett.*, **96**, 104302, (2006).
- [49] F. Ginelli, F. Peruani, M. Bär, and H. Chaté. Large-scale collective properties of self-propelled rods, *Phys. Rev. Lett.*, **104**, 184502, (2010).
- [50] S. Ramaswamy. The mechanics and statistics of active matter, *Annual Review of Condensed Matter Physics*, **1**, 323–345, (2010).
- [51] J. Toner, Y. Tu, and S. Ramaswamy. Hydrodynamics and phases of flocks, *Annals of Physics*, **318**, 170–244, (2005).
- [52] T. Vicsek and A. Zafeiris. Collective motion, *Physics Reports*, **517**, 71–140, (2012).
- [53] S. J. Ebbens and J. R. Howse. In pursuit of propulsion at the nanoscale, *Soft Matter*, **6**, 726–738, (2010).
- [54] I. Theurkauff, C. Cottin-Bizonne, J. Palacci, C. Ybert, and L. Bocquet. Dynamic clustering in active colloidal suspensions with chemical signaling, *Phys. Rev. Lett.*, **108**, 268303, (2012).
- [55] Y. Hong, M. Diaz, U. M. Cordova-Figueroa, and A. Sen. Light-driven titanium-dioxide-based reversible microfireworks and micromotor/micropump systems, *Advanced Functional Materials*, **20**, 1568–1576, (2010).
- [56] M. Doi and S. F. Edwards, *The theory of polymer dynamics*. Oxford University Press, (2001).
- [57] A. Abragam, *Principles of Nuclear Magnetism*. Oxford University Press, (1983).
- [58] M. J. Schnitzer. Theory of continuum random walks and application to chemotaxis, *Phys. Rev. E*, **48**, 2553–2568, (1993).
- [59] H. C. Berg and D. A. Brown. Chemotaxis in *Escherichia coli* analysed by three-dimensional tracking, *Nature*, **239**, 500–504, (1972).

- 
- [60] M. Polin, I. Tuval, K. Drescher, J. P. Gollub, and R. E. Goldstein. Chlamydomonas swims with two “gears” in a eukaryotic version of run-and-tumble locomotion, *Science*, **325**, 487–490, (2009).
  - [61] C. A. Condat, J. Jäckle, and S. A. Menchón. Randomly curved runs interrupted by tumbling: A model for bacterial motion, *Phys. Rev. E*, **72**, 021909, (2005).
  - [62] J. D. Murray, *Mathematical Biology I. An Introduction*. Springer, 3 ed., (2001).
  - [63] N. Mittal, E. O. Budrene, M. P. Brenner, and A. van Oudenaarden. Motility of Escherichia coli cells in clusters formed by chemotactic aggregation, *PNAS*, **100**, 13259–13263, (2003).
  - [64] D. Woodward, R. Tyson, M. Myerscough, J. Murray, E. Budrene, and H. Berg. Spatio-temporal patterns generated by Salmonella typhimurium, *Biophys. J.*, **68**, 2181–2189, (1995).
  - [65] K. F. Swaney, C.-H. Huang, and P. N. Devreotes. Eukaryotic chemotaxis: A network of signaling pathways controls motility, directional sensing, and polarity, *Annual Review of Biophysics*, **39**, 265–289, (2010).
  - [66] R. Thar and M. Kühl. Bacteria are not too small for spatial sensing of chemical gradients: An experimental evidence, *PNAS*, **100**, 5748–5753, (2003).
  - [67] E. F. Keller and L. A. Segel. Initiation of slime mold aggregation viewed as an instability, *J. Theor. Biol.*, **26**, 399–415, (1970).
  - [68] E. F. Keller and L. A. Segel. Model for chemotaxis, *J. Theor. Biol.*, **30**, 225–234, (1971).
  - [69] T. Hillen and K. Painter. A user’s guide to PDE models for chemotaxis, *J. Math. Biol.*, **58**, 183–217, (2009).
  - [70] M. J. Tindall, S. L. Porter, P. K. Maini, G. Gagli, and J. P. Armitage. Overview of mathematical approaches used to model bacterial chemotaxis I: The single cell, *Bull. Math. Biol.*, **70**, 1525–1569, (2008).
  - [71] M. J. Tindall, P. K. Maini, S. L. Porter, and J. P. Armitage. Overview of mathematical approaches used to model bacterial chemotaxis II: Bacterial populations, *Bull. Math. Biol.*, **70**, 1570–1607, (2008).
  - [72] M. A. Rivero, R. T. Tranquillo, H. M. Buettner, and D. A. Lauffenburger. Transport models for chemotactic cell populations based on individual cell behavior, *Chemical Engineering Science*, **44**, 2881–2897, (1989).

## Bibliography

---

- [73] E. Ben-Jacob, I. Cohen, and H. Levine. Cooperative self-organization of microorganisms, *Advances in Physics*, **49**, 395–554, (2000).
- [74] R. Grima, Multiscale modeling of biological pattern formation in *Multiscale Modeling of Developmental Systems* (S. Schnell, P. K. Maini, S. A. Newman, and T. J. Newman, eds.), vol. 81 of *Current Topics in Developmental Biology*, pp. 435–460, Academic Press, (2008).
- [75] H. G. Othmer and T. Hillen. The diffusion limit of transport equations II: Chemotaxis equations, *SIAM Journal on Applied Mathematics*, **62**, 1222–1250, (2002).
- [76] T. J. Newman and R. Grima. Many-body theory of chemotactic cell-cell interactions, *Phys. Rev. E*, **70**, 051916, (2004).
- [77] E. O. Budrene and H. C. Berg. Complex patterns formed by motile cells of *Escherichia coli*, *Nature*, **349**, 630–633, (1991).
- [78] E. O. Budrene and H. C. Berg. Dynamics of formation of symmetrical patterns by chemotactic bacteria, *Nature*, **376**, 49–53, (1995).
- [79] M. P. Brenner, L. S. Levitov, and E. O. Budrene. Physical mechanisms for chemotactic pattern formation by bacteria, *Biophys. J.*, **74**, 1677–1693, (1998).
- [80] R. Tyson, S. R. Lubkin, and J. D. Murray. Model and analysis of chemotactic bacterial patterns in a liquid medium, *J. Math. Biol.*, **38**, 359–375, (1999).
- [81] P. M. Lushnikov. Critical chemotactic collapse, *Physics Letters A*, **374**, 1678–1685, (2010).
- [82] P.-H. Chavanis and C. Sire. Kinetic and hydrodynamic models of chemotactic aggregation, *Physica A*, **384**, 199–222, (2007).
- [83] M. Luca, A. Chavez-Ross, L. Edelstein-Keshet, and A. Mogilner. Chemo-tactic signaling, microglia, and Alzheimer’s disease senile plaques: Is there a connection?, *Bull. Math. Biol.*, **65**, 693–730, (2003).
- [84] M. Abramowitz and I. Stegun, eds., *Handbook of Mathematical Functions*. Dover Publications, (1972).
- [85] P. Romanczuk, U. Erdmann, H. Engel, and L. Schimansky-Geier. Beyond the Keller-Segel model: Microscopic modelling of bacterial colonies, *EPJ ST*, **157**, 61–77, (2008).
- [86] H. C. Berg, *E. coli in motion*. Springer, (2004).

- [87] L. Turner, W. S. Ryu, and H. C. Berg. Real-time imaging of fluorescent flagellar filaments, *J. Bacteriol.*, **182**, 2793–2801, (2000).
- [88] A. Celani and M. Vergassola. Bacterial strategies for chemotaxis response, *PNAS*, **107**, 1391–1396, (2010).
- [89] R. R. Vuppula, M. S. Tirumkudulu, and K. V. Venkatesh. Chemotaxis of *Escherichia coli* to L-serine, *Physical Biology*, **7**, 026007, (2010).
- [90] E. Korobkova, T. Emonet, J. M. G. Vilar, T. S. Shimizu, and P. Cluzel. From molecular noise to behavioural variability in a single bacterium, *Nature*, **428**, 574–578, (2004).
- [91] Y. Kafri and R. A. da Silveira. Steady-state chemotaxis in *Escherichia coli*, *Phys. Rev. Lett.*, **100**, 238101, (2008).
- [92] P. S. Lovely and F. W. Dahlquist. Statistical measures of bacterial motility and chemotaxis, *J. Theor. Biol.*, **50**, 477–496, (1975).
- [93] J. E. Segall, S. M. Block, and H. C. Berg. Temporal comparisons in bacterial chemotaxis, *PNAS*, **83**, 8987–8991, (1986).
- [94] P.-G. de Gennes. Chemotaxis: The role of internal delays, *European Biophysics Journal*, **33**, 691–693, (2004).
- [95] H. C. Berg and L. Turner. Chemotaxis of bacteria in glass capillary arrays. *Escherichia coli*, motility, microchannel plate, and light scattering, *Biophys. J.*, **58**, 919–930, (1990).
- [96] J. Locsei. Persistence of direction increases the drift velocity of run and tumble chemotaxis, *J. Math. Biol.*, **55**, 41–60, (2007).
- [97] D. A. Clark and L. C. Grant. The bacterial chemotactic response reflects a compromise between transient and steady-state behavior, *PNAS*, **102**, 9150–9155, (2005).
- [98] G. M. Barbara and J. G. Mitchell. Bacterial tracking of motile algae, *FEMS Microbiology Ecology*, **44**, 79–87, (2003).
- [99] J. G. Mitchell, L. Pearson, S. Dillon, and K. Kantalis. Natural assemblages of marine bacteria exhibiting high-speed motility and large accelerations, *Applied and Environmental Microbiology*, **61**, 4436–4440, (1995).
- [100] R. H. Luchsinger, B. Bergersen, and J. G. Mitchell. Bacterial swimming strategies and turbulence, *Biophys. J.*, **77**, 2377–2386, (1999).

## Bibliography

---

- [101] M. H. Rashid and A. Kornberg. Inorganic polyphosphate is needed for swimming, swarming, and twitching motilities of *Pseudomonas aeruginosa*, *PNAS*, **97**, 4885–4890, (2000).
- [102] N. C. Caiazza, J. H. Merritt, K. M. Brothers, and G. A. O'Toole. Inverse regulation of biofilm formation and swarming motility by *Pseudomonas aeruginosa* PA14, *J. Bacteriol.*, **189**, 3603–3612, (2007).
- [103] M. Klausen, A. Heydorn, P. Ragas, L. Lambertsen, A. Aaes-Jørgensen, S. Molin, and T. Tolker-Nielsen. Biofilm formation by *Pseudomonas aeruginosa* wild type, flagella and type IV pili mutants, *Molecular Microbiology*, **48**, 1511–1524, (2003).
- [104] D. E. Whitworth, ed., *Myxobacteria: Multicellularity and Differentiation*. ASM Press, (2008).
- [105] Y. Wu, A. D. Kaiser, Y. Jiang, and M. S. Alber. Periodic reversal of direction allows myxobacteria to swarm, *PNAS*, **106**, 1222–1227, (2009).
- [106] P. A. West. The human pathogenic vibrios - a public health update with environmental perspectives, *Epidemiol. Infect.*, **103**, 1–34, (1989).
- [107] Y. Magariyama, S.-y. Masuda, Y. Takano, T. Ohtani, and S. Kudo. Difference between forward and backward swimming speeds of the single polar-flagellated bacterium *Vibrio alginolyticus*, *FEMS Microbiology Letters*, **205**, 343–347, (2001).
- [108] T. Nakai, M. Kkikuda, Y. Kuroda, and T. Goto. Speed, trajectory and increment in the number of cells of singly flagellated bacteria swimming close to boundaries, *Journal of Biomechanical Science and Engineering*, **4**, 2–10, (2009).
- [109] Y. Magariyama, M. Ichiba, K. Nakata, K. Baba, T. Ohtani, S. Kudo, and T. Goto. Difference in bacterial motion between forward and backward swimming caused by the wall effect, *Biophys. J.*, **88**, 3648–3658, (2005).
- [110] L. Xie, T. Altindal, S. Chattopadhyay, and X.-L. Wu. Bacterial flagellum as a propeller and as a rudder for efficient chemotaxis, *PNAS*, **108**, 2246–2251, (2011).
- [111] R. Stocker. Reverse and flick: Hybrid locomotion in bacteria, *PNAS*, **108**, 2635–2636, (2011).
- [112] T. Altindal, L. Xie, and X.-L. Wu. Implications of three-step swimming patterns in bacterial chemotaxis, *Biophys. J.*, **100**, 32–41, (2011).

- [113] F. Matthäus, M. Jagodic, and J. Dobnikar. *E. coli* superdiffusion and chemotaxis-search strategy, precision, and motility, *Biophys. J.*, **97**, 946–957, (2009).
- [114] V. Zaburdaev, (2012). Private communication.
- [115] J.-B. Masson, G. Voisinne, J. Wong-Ng, A. Celani, and M. Vergassola. Non-invasive inference of the molecular chemotactic response using bacterial trajectories, *PNAS*, **109**, 1802–1807, (2012).
- [116] T. Altindal, S. Chattopadhyay, and X.-L. Wu. Bacterial chemotaxis in an optical trap, *PLoS ONE*, **6**, e18231, (2011).
- [117] P. J. van Haastert and M. Postma. Biased random walk by stochastic fluctuations of chemoattractant-receptor interactions at the lower limit of detection, *Biophys. J.*, **93**, 1787–1796, (2007).
- [118] K. C. Chen, R. M. Ford, and P. T. Cummings. Cell balance equation for chemotactic bacteria with a biphasic tumbling frequency, *J. Math. Biol.*, **47**, 518–546, (2003).
- [119] T. V. Kasyap and D. L. Koch. Chemotaxis driven instability of a confined bacterial suspension, *Phys. Rev. Lett.*, **108**, 038101, (2012).
- [120] H. Levine. The dynamics of Dictyostelium development, *Physica A*, **249**, 53–63, (1998).
- [121] M. T. Keating and J. T. Bonner. Negative chemotaxis in cellular slime molds, *J. Bacteriol.*, **130**, 144–147, (1977).
- [122] Q. Wang and T. Zhang. Review of mathematical models for biofilms, *Solid State Communications*, **150**, 1009–1022, (2010).
- [123] A. Sengupta, S. van Teeffelen, and H. Löwen. Dynamics of a microorganism moving by chemotaxis in its own secretion, *Phys. Rev. E*, **80**, 031122, (2009).
- [124] H. Löwen and G. Szamel. Long-time self-diffusion coefficient in colloidal suspensions: Theory versus simulation, *J. Phys.: Condens. Matter*, **5**, 2295, (1993).
- [125] D. S. Dean and A. Lefèvre. Self-diffusion in a system of interacting Langevin particles, *Phys. Rev. E*, **69**, 061111, (2004).
- [126] R. Grima. Strong-coupling dynamics of a multicellular chemotactic system, *Phys. Rev. Lett.*, **95**, 128103, (2005).

## Bibliography

---

- [127] B. Lindner. The diffusion coefficient of nonlinear Brownian motion, *New Journal of Physics*, **9**, 136, (2007).
- [128] B. Lindner. Diffusion coefficient of a Brownian particle with a friction function given by a power law, *Journal of Statistical Physics*, **130**, 523–533, (2007).
- [129] C. Bracher. Eigenfunction approach to the persistent random walk in two dimensions, *Physica A*, **331**, 448–466, (2004).
- [130] Y. Tsori and P.-G. de Gennes. Self-trapping of a single bacterium in its own chemoattractant, *EPL*, **66**, 599, (2004).
- [131] R. Grima. Phase transitions and superuniversality in the dynamics of a self-driven particle, *Phys. Rev. E*, **74**, 011125, (2006).
- [132] T. A. M. Langlands and B. I. Henry. Fractional chemotaxis diffusion equations, *Phys. Rev. E*, **81**, 051102, (2010).
- [133] S. Fedotov. Subdiffusion, chemotaxis, and anomalous aggregation, *Phys. Rev. E*, **83**, 021110, (2011).
- [134] D. B. Kearns. A field guide to bacterial swarming motility, *Nature Reviews Microbiology*, **8**, 634–644, (2010).
- [135] L. H. Cisneros, J. O. Kessler, S. Ganguly, and R. E. Goldstein. Dynamics of swimming bacteria: Transition to directional order at high concentration, *Phys. Rev. E*, **83**, 061907, (2011).
- [136] E. Sackmann, F. Keber, and D. Heinrich. Physics of cellular movements, *Annual Review of Condensed Matter Physics*, **1**, 257–276, (2010).
- [137] J. P. Armitage, T. P. Pitta, M. A.-S. Vigeant, H. L. Packer, and R. M. Ford. Transformations in flagellar structure of Rhodobacter sphaeroides and possible relationship to changes in swimming speed, *J. Bacteriol.*, **181**, 4825–4833, (1999).
- [138] F. Schweitzer and L. Schimansky-Geier. Clustering of active walkers in a two-component system, *Physica A*, **206**, 359–379, (1994).
- [139] A. Sokolov, I. S. Aranson, J. O. Kessler, and R. E. Goldstein. Concentration dependence of the collective dynamics of swimming bacteria, *Phys. Rev. Lett.*, **98**, 158102, (2007).
- [140] T. Ahmed, T. S. Shimizu, and R. Stocker. Microfluidics for bacterial chemotaxis, *Integr. Biol.*, **2**, 604–629, (2010).

- [141] D. Fuller, W. Chen, M. Adler, A. Groisman, H. Levine, W.-J. Rappel, and W. F. Loomis. External and internal constraints on eukaryotic chemotaxis, *PNAS*, **107**, 9656–9659, (2010).
- [142] P. A. Iglesias and P. N. Devreotes. Navigating through models of chemotaxis, *Current Opinion in Cell Biology*, **20**, 35–40, (2008).
- [143] W. T. Coffey, Y. P. Kalmykov, and J. T. Waldron, *The Langevin Equation: With Applications to Stochastic Problems in Physics, Chemistry and Electrical Engineering*. World Scientific, (1998).
- [144] H. Goldstein, C. P. Poole, and J. L. Safko, *Classical Mechanics*. Addison Wesley, 3 ed., (2001).
- [145] H. Gruler and K. Franke. Automatic control and directed cell movement. Novel approach for understanding chemotaxis, galvanotaxis, galvanotropism, *Zeitschrift für Naturforschung*, **45c**, 1241–1249, (1990).
- [146] M. Schienbein, K. Franke, and H. Gruler. Random walk and directed movement: Comparison between inert particles and self-organized molecular machines, *Phys. Rev. E*, **49**, 5462–5471, (1994).
- [147] R. G. Endres and N. S. Wingreen. Accuracy of direct gradient sensing by single cells, *PNAS*, **105**, 15749–15754, (2008).
- [148] A. Czirók, E. Ben-Jacob, I. Cohen, and T. Vicsek. Formation of complex bacterial colonies via self-generated vortices, *Phys. Rev. E*, **54**, 1791–1801, (1996).
- [149] P.-H. Chavanis. A stochastic Keller-Segel model of chemotaxis, *Communications in Nonlinear Science and Numerical Simulation*, **15**, 60–70, (2010).
- [150] Y.-X. Li, R. Lukeman, and L. Edelstein-Keshet. Minimal mechanisms for school formation in self-propelled particles, *Physica D*, **237**, 699–720, (2008).
- [151] J.-L. Martiel and A. Goldbeter. A model based on receptor desensitization for cyclic AMP signaling in Dictyostelium cells, *Biophys. J.*, **52**, 807–828, (1987).
- [152] D. S. Calovi, L. G. Brunnet, and R. M. C. de Almeida. cAMP diffusion in Dictyostelium discoideum: A Green’s function method, *Phys. Rev. E*, **82**, 011909, (2010).
- [153] H. Berg and E. Purcell. Physics of chemoreception, *Biophys. J.*, **20**, 193–219, (1977).
- [154] J.-S. Park and D. A. Weitz, (2012). Private communication.

## Bibliography

---

- [155] E. Ben-Jacob and H. Levine. The artistry of nature, *Nature*, **409**, 985–986, (2001).
- [156] J. A. Shapiro. Thinking about bacterial populations as multicellular organisms, *Annual Review of Microbiology*, **52**, 81–104, (1998).
- [157] T. Romeo, ed., *Bacterial Biofilms*, vol. 322 of *Current Topics in Microbiology and Immunology*. Springer, (2008).
- [158] M. Klausen, A. Aaes-Jørgensen, S. Molin, and T. Tolker-Nielsen. Involvement of bacterial migration in the development of complex multicellular structures in *Pseudomonas aeruginosa* biofilms, *Molecular Microbiology*, **50**, 61–68, (2003).
- [159] D. Bray, *Cell movements: From molecules to motility*. Garland Publishing, 2 ed., (2001).
- [160] J. Wingender, T. R. Neu, and H. C. Flemming, eds., *Microbial Extracellular Polymeric Substances*. Springer, (1999).
- [161] C. M. Waters and B. L. Bassler. Quorum sensing: Cell-to-cell communication in bacteria, *Annual Review of Cell and Developmental Biology*, **21**, 319–346, (2005).
- [162] P. Fey, A. S. Kowal, P. Gaudet, K. E. Pilcher, and R. L. Chisholm. Protocols for growth and development of *Dictyostelium discoideum*, *Nature Protocols*, **2**, 1307–1316, (2007).
- [163] P. M. Lushnikov, N. Chen, and M. Alber. Macroscopic dynamics of biological cells interacting via chemotaxis and direct contact, *Phys. Rev. E*, **78**, 061904, (2008).
- [164] A. Sengupta, T. Kruppa, and H. Löwen. Chemotactic predator-prey dynamics, *Phys. Rev. E*, **83**, 031914, (2011).
- [165] B. M. Friedrich and F. Jülicher. Chemotaxis of sperm cells, *PNAS*, **104**, 13256–13261, (2007).
- [166] M. Inoue and K. Kaneko. Conditions for self-consistent aggregation by chemotactic particles, *Phys. Rev. E*, **77**, 041916, (2008).
- [167] A. Celani, T. Shimizu, and M. Vergassola. Molecular and functional aspects of bacterial chemotaxis, *Journal of Statistical Physics*, **144**, 219–240, (2011).
- [168] Y. V. Kalinin, L. Jiang, Y. Tu, and M. Wu. Logarithmic sensing in *Escherichia coli* bacterial chemotaxis, *Biophys. J.*, **96**, 2439–2448, (2009).

- [169] F. Matthäus, M. S. Mommer, T. Curić, and J. Dobnikar. On the origin and characteristics of noise-induced Lévy walks of *E. coli*, *PLoS ONE*, **6**, e18623, (2011).
- [170] M. J. Tindall, S. L. Porter, P. K. Maini, and J. P. Armitage. Modeling chemotaxis reveals the role of reversed phosphotransfer and a bi-functional kinase-phosphatase, *PLoS Comput. Biol.*, **6**, e1000896, (2010).
- [171] M. Herrero, Chapter 2: The mathematics of chemotaxis. vol. 3 of *Handbook of Differential Equations: Evolutionary Equations*, pp. 137–193, North-Holland, (2007).
- [172] D. Horstmann. From 1970 until present: The Keller-Segel model in chemotaxis and its consequences, *I. Jahresberichte DMV*, **105**, 103–165, (2003).
- [173] G. Grégoire, H. Chaté, and Y. Tu. Moving and staying together without a leader, *Physica D*, **181**, 157–170, (2003).
- [174] F. Peruani, A. Deutsch, and M. Bär. Nonequilibrium clustering of self-propelled rods, *Phys. Rev. E*, **74**, 030904, (2006).
- [175] H. P. Zhang, A. Be'er, E.-L. Florin, and H. L. Swinney. Collective motion and density fluctuations in bacterial colonies, *PNAS*, **107**, 13626–13630, (2010).
- [176] S. Henkes, Y. Fily, and M. C. Marchetti. Active jamming: Self-propelled soft particles at high density, *Phys. Rev. E*, **84**, 040301, (2011).
- [177] M. Miyata, W. S. Ryu, and H. C. Berg. Force and velocity of Mycoplasma mobile gliding, *J. Bacteriol.*, **184**, 1827–1831, (2002).
- [178] H. Gruler, U. Dewald, and M. Eberhardt. Nematic liquid crystals formed by living amoeboid cells, *EPJ B*, **11**, 187–192, (1999).
- [179] P. v. Sengbusch, *Molekular- und Zellbiologie*. Springer, (1979).
- [180] I. S. Aranson, A. Sokolov, J. O. Kessler, and R. E. Goldstein. Model for dynamical coherence in thin films of self-propelled microorganisms, *Phys. Rev. E*, **75**, 040901, (2007).
- [181] D. J. Durian. Foam mechanics at the bubble scale, *Phys. Rev. Lett.*, **75**, 4780–4783, (1995).
- [182] K. L. Johnson, *Contact Mechanics*. Cambridge University Press, (1987).
- [183] P. Español. Hydrodynamics from dissipative particle dynamics, *Phys. Rev. E*, **52**, 1734–1742, (1995).

## Bibliography

---

- [184] B. Szabó, G. J. Szöllösi, B. Gönci, Z. Jurányi, D. Selmeczi, and T. Vicsek. Phase transition in the collective migration of tissue cells: Experiment and model, *Phys. Rev. E*, **74**, 061908, (2006).
- [185] F. Peruani, A. Deutsch, and M. Bär. A mean-field theory for self-propelled particles interacting by velocity alignment mechanisms, *EPJ ST*, **157**, 111–122, (2008).
- [186] I. O. Götze and G. Gompper. Mesoscale simulations of hydrodynamic squirmer interactions, *Phys. Rev. E*, **82**, 041921, (2010).
- [187] M. Inoue and K. Kaneko. Condition for intracellular adaptive dynamics for chemotaxis, *Phys. Rev. E*, **74**, 011903, (2006).
- [188] J. L. Folks and R. S. Chhikara. The inverse Gaussian distribution and its statistical application - a review, *J. R. Statist. Soc. B*, **40**, 263–289, (1978).
- [189] S. Redner, *A Guide to First-Passage Processes*. Cambridge University Press, (2001).
- [190] K. J. Painter and T. Hillen. Volume-filling and quorum-sensing in models for chemosensitive movement, *Canadian Applied Mathematics Quarterly*, **10**, 501–543, (2002).
- [191] J. W. Cannon, J. A. Aronovitz, and P. Goldbart. Equilibrium distribution of shapes for linear and star macromolecules, *J. Phys. I France*, **1**, 629–645, (1991).
- [192] B. Maier and J. O. Rädler. Shape of self-avoiding walks in two dimensions, *Macromolecules*, **34**, 5723–5724, (2001).
- [193] P. H. Chavanis. Exact diffusion coefficient of self-gravitating Brownian particles in two dimensions, *EPJ B*, **57**, 391–409, (2007).
- [194] E. Bertin, M. Droz, and G. Grégoire. Hydrodynamic equations for self-propelled particles: Microscopic derivation and stability analysis, *J. Phys. A*, **42**, 445001, (2009).
- [195] C. F. Lee. Fluctuation-induced collective motion: A single-particle density analysis, *Phys. Rev. E*, **81**, 031125, (2010).
- [196] A. Baskaran and M. C. Marchetti. Enhanced diffusion and ordering of self-propelled rods, *Phys. Rev. Lett.*, **101**, 268101, (2008).
- [197] F. D. C. Farrell, M. C. Marchetti, D. Marenduzzo, and J. Tailleur. Pattern formation in self-propelled particles with density-dependent motility, *Phys. Rev. Lett.*, **108**, 248101, (2012).

- [198] D. Saintillan and M. J. Shelley. Instabilities and pattern formation in active particle suspensions: Kinetic theory and continuum simulations, *Phys. Rev. Lett.*, **100**, 178103, (2008).
- [199] J. Henrichsen. Twitching motility, *Annual Review of Microbiology*, **37**, 81–93, (1983).
- [200] J. S. Mattick. Type IV pili and twitching motility, *Annual Review of Microbiology*, **56**, 289–314, (2002).
- [201] J. M. Skerker and H. C. Berg. Direct observation of extension and retraction of type IV pili, *PNAS*, **98**, 6901–6904, (2001).
- [202] B. Maier, L. Potter, M. So, H. S. Seifert, and M. P. Sheetz. Single pilus motor forces exceed 100 pN, *PNAS*, **99**, 16012–16017, (2002).
- [203] N. Biais, B. Ladoux, D. Higashi, M. So, and M. Sheetz. Cooperative retraction of bundled type IV pili enables nanonewton force generation, *PLoS Biol.*, **6**, e87, (2008).
- [204] C. Holz, D. Opitz, L. Greune, R. Kurre, M. Koomey, M. A. Schmidt, and B. Maier. Multiple pilus motors cooperate for persistent bacterial movement in two dimensions, *Phys. Rev. Lett.*, **104**, 178104, (2010).
- [205] D. L. Higashi, S. W. Lee, A. Snyder, N. J. Weyand, A. Bakke, and M. So. Dynamics of Neisseria gonorrhoeae attachment: Microcolony development, cortical plaque formation, and cytoprotection, *Infect. Immun.*, **75**, 4743–4753, (2007).
- [206] N. Biais, (2012). Private communication.
- [207] C. A. Schneider, W. S. Rasband, and K. W. Eliceiri. NIH Image to ImageJ: 25 years of image analysis, *Nature Methods*, **9**, 671–675, (2012).
- [208] V. Zaburdaev and N. Biais. *Unpublished results*, (2012).



# Acknowledgments

I am indebted to Prof. Holger Stark for supervising this work as my Doktorvater and providing excellent research conditions. Further, I am thankful for the continuous support from my second mentor Dr. Vasily Zaburdaev and the collaborations with Dr. Nicolas Biais, Matthias Theves and Prof. Carsten Beta. I thank Prof. David A. Weitz for the warm hospitality during my stay in his group at Harvard University. In addition, I appreciate numerous discussions with my colleagues, in particular Dr. Reinhard Vogel, Andreas Zöttl, Philipp Kählitz, Christopher Prohm, Dr. Katrin Wolff, and Dr. Maximilian Zieringer.

This work was funded by the Deutsche Forschungsgemeinschaft through the Research Training Group GRK 1558, “Nonequilibrium Collective Dynamics in Condensed Matter and Biological Systems”.



# Zusammenfassung

Ansammlungen von Bakterien auf Oberflächen werden als Biofilme bezeichnet, deren Entstehung durch zahlreiche biologische, chemische und physikalische Prozesse beeinflusst wird. In dieser Arbeit untersuchen wir mit Methoden der Statistischen Physik Aspekte, die im frühen Entwicklungsstadium von Biofilmen relevant sind.

Die Fortbewegungsstrategien von Bakterien lassen sich als Zufallsbewegungen charakterisieren: “Run-and-tumble” für das Darmbakterium *E. coli*, “Run-reverse” für den Krankheitserreger *P. aeruginosa* oder “Run-reverse-flick” für das Meeresbakterium *V. alginolyticus*. Zum quantitativen Vergleich dieser unterschiedlichen Bewegungsmuster entwickeln wir eine verallgemeinerte Zufallsbewegung, für die wir analytisch den Diffusionskoeffizienten als Maß der Zellmotilität bestimmen. In inhomogener Umgebung können Mikroorganismen ihre Bewegung entlang eines chemischen Gradienten ausrichten, was als Chemotaxis bezeichnet wird. Um die chemotaktische Effizienz zu vergleichen, berechnen wir die chemotaktische Driftgeschwindigkeit, mit der sich ein “Run-tumble-flick”-Bakterium einer Nahrungsquelle nähert.

Sobald Mikroorganismen sich auf einer Oberfläche anlagern, aktiviert “Kommunikation” zwischen einzelnen Zellen die Bildung von Mikrokolonien und damit die Entstehung eines Biofilms. Coli-Bakterien, Salmonellen oder Amöben können selbst chemische Stoffe produzieren, auf die die jeweilige Zellpopulation chemotaktisch reagiert. Diese Mikroorganismen inspirieren unser Modell für aktive, “autochemotaktische” Teilchen. Wir zeigen, dass die chemotaktische Wechselwirkung bei unseren Modellorganismen die Bildung von Zellaggregaten bewirkt, was im Einklang mit zahlreichen Experimenten steht. Für die diffusive Langzeitdynamik eines isolierten Modellteilchens geben wir den Diffusionskoeffizienten analytisch an.

Physikalische Wechselwirkungen zwischen Zellen können ebenfalls die Bildung von Mikrokolonien verursachen. Gonokokken-Bakterien (*N. gonorrhoeae*), Erreger der sexuell übertragbaren Krankheit Gonorrhoe, weisen Zellfortsätze auf, sogenannte Typ-IV-Pili, die den Zellen Oberflächenhaftung und “Twitching Motility” als Art der Fortbewegung ermöglichen. Unserer Hypothese nach erfolgt die Bildung von Mikrokolonien von *N. gonorrhoeae* ausschließlich über die Wechselwirkung der Pili, wofür insbesondere keine Chemotaxis notwendig ist. Ein von uns durchgeführtes Experiment demonstriert, wie anfänglich auf einer Oberfläche verteilte Zellen binnen Stunden aggregieren. Für die Dynamik der Zellaggregation entwickeln wir ein auf der Pili-Wechselwirkung basierendes Modell, das die experimentellen Beobachtungen gut reproduziert.